A thesis of

6.7 GHz methanol masers and the early phases of massive star formation

submitted by

Sonu Tabitha Paulson

in partial fulfillment for the award of the degree of

Doctor of Philosophy

Department of Earth and Space Sciences
Indian Institute of Space Science and Technology
Thiruvananthapuram, India

April 2022

Certificate

This is to certify that the thesis titled ***6.7 GHz methanol masers and the early phases of massive star formation*** submitted by **Sonu Tabitha Paulson**, to the Indian Institute of Space Science and Technology, Thiruvananthapuram, in partial fulfillment for the award of the degree of **Doctor of Philosophy** is a bona fide record of the original work carried out by her under my supervision. The contents of this thesis, in full or in parts, have not been submitted to any other Institute or University for the award of any degree or diploma.

Dr. Jagadheep D. Pandian	Dr. Rama Rao Nidamanuri
Associate Professor	Professor & Head

Place: Thiruvananthapuram
Date: April 2022

Declaration

I declare that this thesis titled ***6.7 GHz methanol masers and the early phases of massive star formation*** submitted in partial fulfillment for the award of the degree of **Doctor of Philosophy** is a record of the original work carried out by me under the supervision of **Dr. Jagadheep D. Pandian**, and has not formed the basis for the award of any degree, diploma, associateship, fellowship, or other titles in this or any other Institution or University of higher learning. In keeping with the ethical practice in reporting scientific information, due acknowledgments have been made wherever the findings of others have been cited.

Place: Thiruvananthapuram Sonu Tabitha Paulson
Date: April 2022 (SC15D009)

This thesis is dedicated to
my beloved parents,
who always picked me up on time
and encouraged me to go on every adventure
especially this one ...

Acknowledgements

First and foremost, I would like to express the deepest appreciation to my research advisor, Dr. Jagadheep D. Pandian, who has the attitude and substance of a genius, for his generous guidance and persistent help. He continually and convincingly conveyed a spirit of adventure in regard to research. He has always encouraged me to work independently, helping me to become more of an independent and responsible researcher. Without his steadfast support, this thesis would not have been possible.

I would also like to thank my doctoral committee members, Dr. Anandamayee Tej, Dr. Samir Mandal, Dr. S. Murugesh, Dr. Bhaswathi Mookerjea (TIFR) and Dr. Nissim Kanekar (NCRA-TIFR) for their useful suggestions, that has helped towards improving the quality of my work.

Many thanks to all my fellow graduate students with whom I have shared moments of deep anxiety but also of big excitement. They have made my PhD life more exciting and lively. Special thanks to Anu Kuriakose, for all those stimulating discussions and philosophical discourse.

I also extend my heartfelt gratitude to my parents, who have always supported me to pursue my passion. You have been there at all my highs and lows, strengthening me spiritually and emotionally. I also wish to thank my brother, Samuel, for his endless support, love and cheers.

A very special word of thanks goes to my in-laws, who have been great over the years and never raised an eyebrow when I claimed my thesis would be finished 'in the next two weeks' for nearly a year.

I am eternally grateful to my better half, Aditya, for his unceasing support and for keeping me sane over the past few years. Thank you for being my muse, editor, proofreader, and sounding board. But most of all, thank you for being my best friend. I owe you everything.

Last but not the least, I thank God Almighty for the wisdom he bestowed upon me, the strength, motivation and good health in order to finish this research. . .

Sonu Tabitha Paulson

Abstract

Methanol masers at 6.7 GHz are the brightest of Class II methanol masers and have been found almost exclusively towards massive star forming regions. These masers can thus be used as an ideal tool to probe the early phases of massive star formation. The primary goal of this thesis was to investigate the evolutionary stage of the young stellar objects that excite 6.7 GHz methanol masers. Even though there have been several studies in this regard, they were either limited by small sample size or lack of data in the far-infrared. This work has made use of the entire sample from the Methanol Multibeam Survey (MMB) – the largest unbiased Galactic plane survey for 6.7 GHz methanol masers, FIR data from the Herschel Infrared Galactic plane survey (Hi-GAL) and millimetre wave spectroscopic data from the MALT90 survey. We investigated the evolutionary states of 6.7 GHz maser hosts from two perspectives: (1) studying the physical properties of the methanol maser sources (2) probing the chemical environments of maser hosts. For the first case, we obtained the spectral energy distributions (SEDs) from 870 to 70 μm for 320 6.7 GHz methanol maser sources, and used the best-fit parameters of the SED fits to derive the maser clump properties. A comparison of the mass–luminosity diagram of the sample with evolutionary tracks from the turbulent core model suggests that most methanol masers are associated with massive young stellar objects, with over 90 percent in early evolutionary stages where they are accreting matter. However, there also appears to be a small population of sources that are likely to be associated with intermediate- or low-mass stars, suggesting that the association between high-mass star formation and methanol maser emission is not exclusive.

We also studied the chemical properties of the sources associated with the masers using the molecular line observations from the MALT90 survey. This study was carried out for a sample of 68 out of the 320 methanol masers of the first study, with the selection based on data availability and the signal-to-noise ratio of the molecular lines. We used the line intensities and abundances of four molecular transitions: N_2H^+(1-0), HCN(1-0), HNC(1-0) and HCO^+(1-0) since they are bright and are good tracers of dense gas. The molecular spectra were modelled using radiative transfer under the assumption of local thermodynamic equilibrium (LTE). The excitation temperatures and column densities were compared to models that solve for time dependent astrochemistry in star forming cores. The molecular abundances and integrated line intensities agree well with the typical values found towards high-mass star forming regions. The HCN/HNC, N_2H^+/HCO^+, HNC/HCO^+ and N_2H^+/HNC ratios of column density and integrated intensity suggest that methanol masers are at an earlier evolutionary state than H II regions, but more evolved than the quiescent phase – much in agreement with previous dust continuum studies. This thesis work thus gives strong evidence that along a timeline for massive star formation, the 6.7 GHz methanol maser phase originates in massive young stellar objects that are more evolved than infrared dark clouds, and is quenched by the time the sources evolve into ultracompact H II regions.

Contents

List of Figures

List of Tables

O Star, (the fairest one in sight),
We grant your loftiness the right
To some obscurity of cloud —
It would not do to say of night,
Since dark is what brings out your light
Some mystery becomes the proud.
But to be wholly taciturn
In your reserve is not allowed.
Say something to us we can team
By heart and when alone repeat
Say something! And it says "I burn."
But say with what degree of heat
Talk Fahrenheit, talk Centigrade.
Use language we can comprehend.
Tell us what elements you blend.
It gives us strangely little aid,
But does tell something in the end.
. . .

Robert Frost

Chapter 1

Introduction

Stars are the fundamental luminous units of the Universe. The process of star formation is often quite intricate and requires different types of astronomical observations. At present times, we have a relatively better understanding on how low mass stars form (Shu et al., 1987b). However, many aspects of the mechanisms through which high-mass stars ($M \geq 8\ M_{\odot}$) form still remains elusive. Massive stars play a vital role in the evolution of the Galaxy. They act as principal sources of heavy elements and contribute towards the chemical enrichment of the universe. The outflows, stellar winds, expansion of H II regions and supernova explosions are a significant source of the turbulence in the interstellar medium of the Galaxy. In order to better comprehend the physical, chemical and morphological structure of the galaxies, the processes involved in the formation of massive stars and their subsequent impact on their local environment should be well studied (Kennicutt Jr, 1998; Kennicutt, 2005). However, the study of massive star formation poses several observational constraints. This is mainly due to the fact that they spend the majority of their life deeply embedded in their natal cloud, making observations difficult. We therefore rely on emission at millimetre/submillimetre and IR wavelengths for probing the evolutionary stages of massive star formation. Massive stars are also extremely rare. The number of stars formed per unit mass interval is roughly proportional to $M^{-2.35}$ (e.g. Salpeter, 1955; Kroupa, 2002; Lamb et al., 2013; Dib et al., 2017), making them scarcer than low mass stars. Furthermore, their short-life and clustered environments make their study even more formidable.

The early stages of massive star formation has been a subject of intense research for many years. Since massive star formation is a quick process, their initial stages are even more ephemeral. Almost three decades ago, regions of photoionization around massive stars (otherwise called H II regions) were considered to be the main signposts of the early stages of massive star formation. Since H II regions expand as the time proceeds, their size is taken as an indicator for their age, with younger H II regions being more compact. Later, with the advent of millimeter interferometers, Hot Molecular Cores (HMCs) were regarded as the observational signpost of early stages of massive star formation. HMCs are small ($d \lesssim 0.5$ pc) pockets of gas, characterized physically by high gas densities ($> 10^6 cm^{-3}$) and elevated temperatures of both gas and dust ($\sim$100−500 K). They are also the precursors of H II regions. The gaseous chemical composition is distinct from that of cold molecular clouds, due to the freeze-out of gas-phase species onto dust grains and the grain surface reactions in the cold collapsing pre-protostellar phase, and the evaporation of the grain mantle material and the subsequent gas-phase reactions in the hot protostellar phase (e.g., Millar, 1993; Nomura & Millar, 2004). HMCs are also considered as the most chemically rich sources in the Galaxy (Rivilla et al., 2017). Preceding the hot core phase in the high-mass star formation sequence is, unsurprisingly, the cold core phase. These massive ($10^2 - 10^3$), cold ($T < 20$ K) cores lack mid-infrared counterparts and have the potential to eventually collapse and form massive stars (Garay et al., 2004). They are often found embedded in infrared dark clouds (IRDCs) –extinction features identified against the bright Galactic mid-infrared emission. This hot and cold core phase typically constitute the early stages of high-mass star formation, and can be detected by mid-infrared and far-infrared/sub-mm surveys, respectively.

One of the effective ways to probe the hot core phase in particular is by observing interstellar masers. They serve as the most readily detectable indicators of the star forming regions, with the masing action initiated by the infrared photons emitted by the heated dust. Masers are ideal for investigating the kinematics and physical conditions within the massive star forming region at milli-arcsecond resolution, owing to their high brightness temperatures ($T_b > 10^9$ K) and compact sizes. The most common types of masers are those of the molecules of hydroxyl (OH), water (H_2O), methanol (CH_3OH) and silicon monoxide (SiO). Different species of masers inhabit different regions within a given source, which is often reflected in the differences in pumping requirements of the various transitions and molecules. While water masers are found in both low-mass and high-mass star-forming regions, OH masers are found towards both high-mass star forming regions and evolved stars (for e.g. AGB stars). Unlike OH and water masers, the methanol masers are shown to uniquely trace earlier phases of massive star formation. Methanol masers in star-forming regions can be divided into two distinct types, Classes I and II. Class I masers are collisionally pumped and Class II masers are characterized by radiative pumping. While Class I masers are believed to form away from the central protostar, Class II masers are found in close vicinity of the protostar.

This thesis aims at studying the early stages of massive star formation using 6.7 GHz methanol maser emission as probes. Class II methanol masers, of which the 6.7 GHz maser is the strongest, are commonly found towards massive star forming regions. One of the key questions concerning 6.7 GHz methanol masers is whether they are indeed exclusively associated with massive star formation. In order to address this problem, we study the maser sample provided by Methanol Multibeam survey (the largest blind survey of Class II methanol masers, conducted using a 7-beam receiver on the Parkes radio telescope. The survey covers the entire Galactic plane with a latitude coverage of $|b| \leq 2°$ and the catalogue comprises of a total of 972 sources), utilizing the high resolution data of Hi-GAL survey. Another key question concerns the evolutionary stage of the young stellar objects that excite 6.7 GHz methanol masers. This is done in a physical as well as chemical perspective. We rely on spectral energy distributions (SEDs) of 6.7 GHz maser hosts to study their physical properties. This is complimented by a chemical study where we perform molecular line studies of the emissions from HCN, HNC, N_2H^+ and HCO^+, with the data taken from the MALT90 survey. MALT90 is a large international project carried out with the Mopra Spectrometer (MOPS) arrayed on the Mopra 22 m telescope, with the aim to characterize physical and chemical properties of massive star formation in our Galaxy. The survey is targeted towards 2014 compact sources detected in the ATLASGAL survey covering Galactic longitude ranges $300° < l < 357°$ and $3° < l < 20°$. We thus try to provide a more holistic view of the characteristics of sources that host 6.7 GHz methanol masers.

Outline of the thesis

This thesis is structured as follows.

- A brief discussion on the theory of star formation, with special emphasis given to massive star formation and their evolutionary phases is given in chapter 2.
- A detailed description of astronomical masers and their phenomenological theory is presented in chapter 3.
- Chapter 4 presents a discussion of methanol masers, their classification and properties of the different classes. Theoretical models of 6.7 GHz methanol masers and observational studies are also discussed.
- In Chapter 5 we investigate the physical properties of early stages of massive star formation with the help of SEDs, using 6.7 GHz methanol masers as probes.

- Chapter 6 presents an astrochemical study of 6.7 GHz methanol maser hosts using millimetre wave spectroscopy of dense gas tracers.
- Chapter 7 will present the summary of the thesis along with prospects for future work.

Chapter 2

Star formation: An overview

2.1 Giant Molecular Clouds

Giant Molecular Clouds (GMCs) are regarded as the cradles of star formation within the Galaxy (Myers et al., 1986; Shu et al., 1987b; Scoville & Good, 1989). They are also the most massive individual objects of the Galaxy, with masses ranging from $\sim 10^2$ $M_\odot$ for small clouds at high Galactic latitudes (e.g., Magnani et al., 1985) and in the outer disk of the Milky Way (e.g., Brand & Wouterloot, 1995; Heyer et al., 2001) up to giant $\sim 10^7$ $M_\odot$ clouds in the central molecular zone of the Galaxy (Oka et al., 2001). The predominant constituent of a GMC is molecular hydrogen ($n(H_2) \sim 50$ cm^{-3}) (Blitz, 2000), followed by He ($\sim$ 26% by mass) and HI gas (Fukui & Kawamura, 2010). GMCs extend to about 100 pc, with masses in the range $10^4 - 10^6$ $M_\odot$ (e.g. Beuther et al., 2007). Their typical average surface density is found to be $\Sigma \sim 0.02$ gm cm^{-2} in local galaxies (Solomon et al., 1987; Bolatto et al., 2008). Figure 2.1 depicts the giant molecular cloud, W51, at different wavelengths.

Several mechanisms have been proposed in regard to the formation of GMCs. These include (1) converging flows driven by stellar feedback or turbulence, (2) agglomeration of smaller clouds, (3) gravitational and magneto-gravitational instability, and (4) instability involving differential buoyancy (Dobbs et al., 2014). The real phenomenon, however, might be a combination of all these mechanisms, with different processes dominating in different galactic environments. Nonetheless, it is widely accepted that GMCs form in the disk of the Milky Way as the molecular gas enters the spiral wave pattern of the gravitational potential energy of the Galactic disk (Elmegreen, 1994). The gravitational collapse occurs more rapidly in the spiral arms than the interarm regions owing to the weaker tidal shear forces in the former (Luna et al., 2006). This is supported observationally, as GMCs are seen to be constrained to the spiral arms of the Milky Way (Stark & Lee, 2005). The GMCs are broken

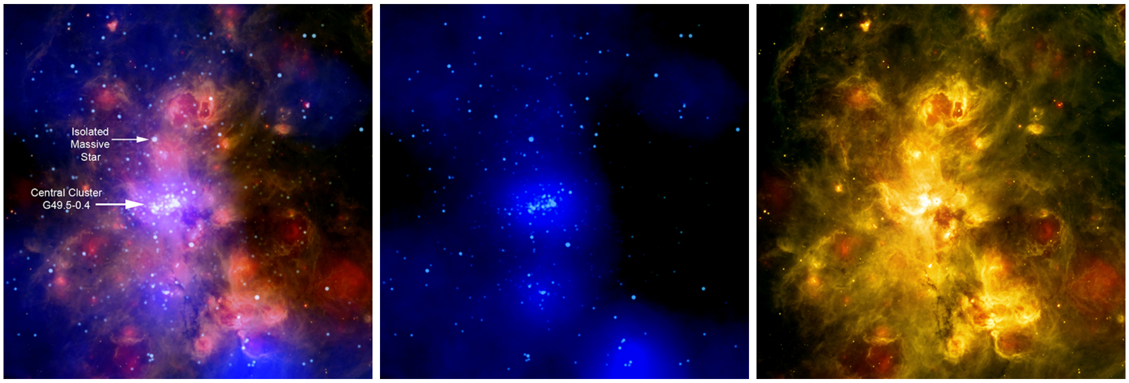

Figure 2.1: The image of W51 giant molecular cloud. The left most panel illustrates the composite image with X-ray data from Chandra (blue) and Spitzer (orange and yellow-green). The image in X-ray alone is shown in the middle panel. The right most panel depicts the infrared image. W51 is just 17,000 light years away from Earth. The Chandra data show that the X-ray sources in the field are found in small clumps, with a clear concentration of more than 100 sources in the central cluster, called $G49.5-0.4$. This cluster harbours two massive star-forming clumps bound by a Roche lobe potential (Nanda Kumar et al., 2004). Image credit: X-ray: NASA/CXC/PSU/L. Townsley et al. (2014); Infrared: NASA/JPL-Caltech.

down to substructures “clumps” and “cores”, based on their sizes and number densities. This hierarchical naming convention for the fragmentation within the clouds is propounded by Williams et al. (2000). Clumps have number densities, $n(H_2) \sim 10^3\,cm^{-3}$ (Larson, 2003) whereas “cores” are denser with number densities, $n(H_2) \sim 10^5\,cm^{-3}$ (Churchwell, 2002). The cores are the sites of star formation which can generate single, binary, multiple stellar systems. As for the formation of massive stars, it occurs in regions with elevated molecular gas density, roughly coincident with the line of sight tangent to spiral arms (Luna et al., 2006). GMCs harbour most of the massive star formation in the Galaxy (Luna et al., 2006; Mac Low & Klessen, 2004; McKee & Ostriker, 2007; Zinnecker & Yorke, 2007). However, it is worth noting that a vast majority of the gas in GMC does not contribute to star formation. This is attributed to the small fraction of gas present in dense clumps (Padoan, 1995; Hartmann et al., 1998; Zinnecker, 2002), and the turbulence and magnetic field effects that support molecular clouds on large scales against collapse (McKee & Ostriker, 2007).

2.2 Low mass star formation

2.2.1 Cloud collapse and formation of protostars

In this section, we discuss the formation of pre-nuclear-burning objects known as protostars from interstellar molecular clouds. For a star with $M \leq 8\ M_{\odot}$, this phenomenon is relatively well understood. For a spherical cloud in hydrostatic equilibrium,

$$\frac{dP}{dr} = -\frac{G\rho(r)m(r)}{r^2} \tag{2.1}$$

where $m(r)$ is the enclosed mass, P is the pressure, r is the radius, $\rho(r)$ is the density of the gas at radius r and G is the gravitational constant. The cloud becomes unstable when the kinetic energy of the gas pressure fail to balance the potential energy of the internal gravitational force. Isothermal clouds are stable when their mass is below a critical mass. However, the cloud begins a process of runaway contraction once it exceeds a critical mass, and this will continue until some other force can impede the collapse. This critical mass is defined as Jeans mass M_J (Shu et al., 1987b)

$$M_J = \left(\frac{5k_bT}{\mu m_H G}\right)^{3/2}\left(\frac{3}{4\pi\rho}\right)^{1/2} \tag{2.2}$$

where ρ and T are the density and temperature of the cloud, m_H is the mass of the hydrogen atom, μ is the mean molecular weight and G is the gravitational constant. The gravity remains dominant, once it has overcome gas pressure (Zinnecker & Yorke, 2007). A uniform sphere of gas with no pressure support will collapse on a timescale given by the free fall timescale,

$$t_{ff} = \left(\frac{3\pi}{32G\rho}\right)^{1/2} \tag{2.3}$$

For a cloud of typical density $\sim 10^2$ cm^{-3}, the free fall timescale is of the order $\sim 10^5$ years. As long as the original density of the spherical molecular cloud is uniform, all parts of the cloud will take the same amount of time to collapse, and the density will increase at the same rate everywhere. On the other hand, if the cloud is somewhat centrally condensed when the collapse begins ($\rho \propto r^{-2}$), the free-fall time will be shorter for material near the centre than for material farther out (Larson, 2003). This onsets the formation of a central protostar within the collapsing core. During the gravitational collapse, the centrifugal forces increase due to the conservation of angular momentum, leading to the formation of a disc

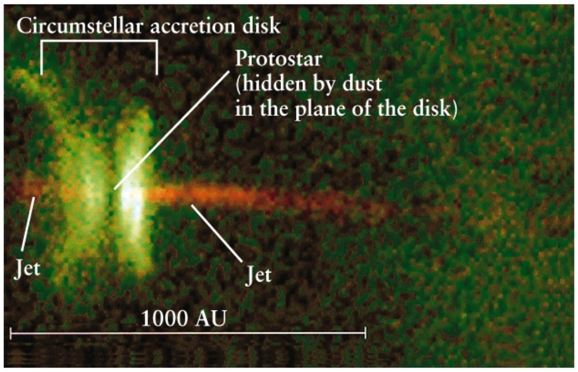

Figure 2.2: This view of a protostellar object called HH-30 reveals an edge-on disk of dust encircling a newly forming star. Light from the forming star illuminates the top and bottom surfaces of the disk, making them visible, while the star itself is hidden behind the densest parts of the disc. Image credit and copyright: C. Burrows (STScI & ESA), J. Hester (Arizona State University), J. Morse/STScI and NASA.

structure around the central protostar (Zinnecker & Yorke, 2007). The material is then accreted through this disc in to the central core (e.g. Shu et al., 1987a). The accretion rate is believed to be more rapid in the earlier stages of protostar formation (Larson, 2003). The accreting matter that feeds the circumstellar disc also generates a highly collimated bipolar jet and the magnetic forces in the accretion disc instigate the initial outflow (McKee & Ostriker, 2007). Outflows are regarded as a ubiquitous feature of low mass star formation (Arce & Sargent, 2006). As for the low mass stars, the accretion halts when the star enters the hydrogen burning phase, as the strong stellar winds produced thwart further accretion of matter. The bipolar jet and circumstellar disc of the protostellar object HH-30 is illustrated in Figure 2.2.

2.3 High Mass star formation

Although high-mass stars ($M \geq 8\ M_\odot$) dominate the luminosity, chemistry, and energy input in galaxies, their formation mechanisms still remain unclear. This is in contrast to low mass star formation, where the paradigm is relatively well understood. One of the key hindrances in understanding massive star formation is that they form in clusters, deeply embedded in high density gas and dust (Lada & Lada, 2003). This obscures their observation in optical and near-infrared wavelengths. Further, the clustered environments put additional constraints on their study, as each member of the cluster can be in different evolutionary phase or can possess different masses. High-mass stars can begin burning hydrogen while the outer envelope is still collapsing. Furthermore, high-mass stars are

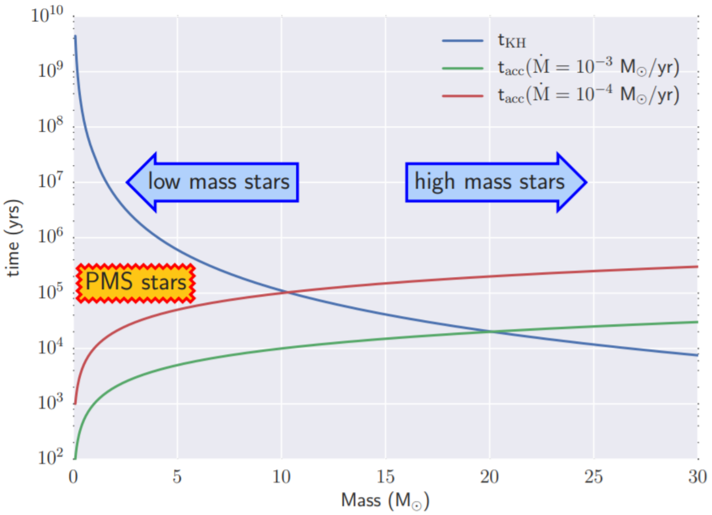

Figure 2.3: Kelvin-Helmholtz timescale vs. accretion timescale of high mass stars vs. low mass stars, for varying accretion rates. Unlike low-mass stars, high mass stars do not have a pre-main sequence phase where they have stopped accreting. It can also be seen that for any reasonable accretion rates, the Kelvin-Helmholtz contraction time is less than the accretion time for high mass stars (Schilke, 2015).

much rarer (due to the steep dependence on mass in the initial mass function) and their formation is an ephemeral process. All these are in stark contrast to low mass star formation, as these objects are much more ubiquitous, formed in relative isolation and are long-lived. The difference in formation timescales of high and low mass stars can be ascribed to the variations in their accretion and Kelvin-Hemholtz timescale. The accretion timescale is given by,

$$t_{acc} = \frac{M_*}{\dot{M}_*} \tag{2.4}$$

where M_* is the mass of the core and $\dot{M}_*$ is the mass accretion rate. The time required to radiate the current gravitational binding energy of the star at its current luminosity is called the Kelvin-Hemholtz timescale,

$$t_{KH} \approx \frac{GM^2}{RL} \tag{2.5}$$

where R, L and M are stellar radius, luminosity and mass respectively. This is the timescale on which the star would contract if its nuclear energy sources were turned off. For high mass stars $t_{KH} < t_{acc}$ (Figure 2.3). This is due to the fact that t_{KH} is luminosity dependent and $L \propto M^\alpha$ (where $\alpha > 2$). A lower Kelvin-Helmholtz timeline implies that the fusion commences before the object has stopped accreting. The resulting luminosity generates an extreme outward radiation pressure, which thwarts further accretion of matter (Beuther et al., 2007). This effect may limit the upper mass of stars (~ 30 M$_\odot$) that can form by accretion (Palla & Stahler, 1993). However, observations show that stars with masses 150 M$_\odot$ and above exist (Figer et al., 2005; Crowther et al., 2010), and their formation mechanism still remains highly debated.

Several theoretical models have been proposed to shed light on the formation of massive stars. The three main theories amongst them are: monolithic collapse of a massive quasi-hydrostatic core (McKee & Tan, 2003); competitive accretion (Bonnell et al., 2001; Bonnell & Bate, 2006) and stellar collisions (Bonnell et al., 1998).

2.3.1 Monolithic collapse

McKee & Tan (2003) envisage the massive star formation as a scaled up version of low mass star formation via the monolithic collapse of massive prestellar cores that are supported by turbulence rather than thermal motions. Therefore, this model is also called turbulent core model. The stability of the prestellar cores are characterized by their virial parameter, α_{vir},

$$\alpha_{vir} = \frac{5\sigma_{1D}^2 R_c}{G M_c} \tag{2.6}$$

where σ_{1D} is the core's 1D velocity dispersion, M_c and R_c are the core mass and radius, respectively (Bertoldi & McKee, 1992). When $\alpha_{vir} \gtrsim 1$, the core is said to be stable against gravitational collapse, whereas cores with $\alpha_{vir} < 1$ are unstable to collapse. Here, we have neglected the effect of external pressure and magnetic fields. The turbulent core model suggests that the cores that form high-mass stars are highly supersonically turbulent, i.e, $\alpha_{vir} \sim 1$. The resulting formation timescale is several times the core free-fall timescale ($t_{ff} \lesssim 10^5$ yr), and the high degree of turbulence causes clumping, resulting in high accretion rates ($\dot{M}_{acc} \sim 10^{-4} - 10^{-3}$ M$_\odot$ s^{-1}) that can overcome the radiation pressure associated with the star's large luminosity (McKee & Tan, 2003; Rosen et al., 2019). This has also been supported observationally, as massive cores are found to live in highly pressurized environments and are characterized by nonthermal turbulent motions that dominate over thermal motions (e.g., Tan et al., 2013; Zhang & Tan, 2015; Liu et al., 2018). Moreover, the high angular momentum of the core leads to the formation of an optically thick accretion disc around the accreting massive star as the core collapses and delivers material at high rates via gravitational torques to the star (Yorke & Sonnhalter, 2002). The monolithic collapse model requires the presence of stable, massive starless cores, possibly up to of order 10^2 Jeans masses (Tan et al., 2014) – with more massive stars

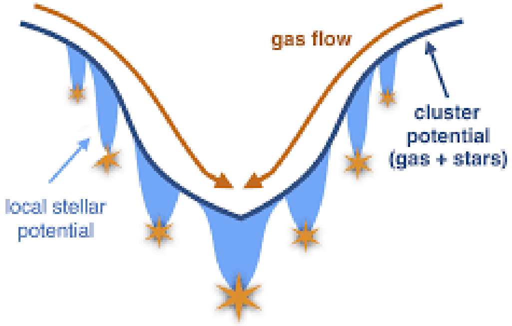

Figure 2.4: The gravitational potential of the forming star cluster, due to both the gas and the stars, funnels gas flow towards the centre of the potential (Wright, 2015).

formed from more massive cores. Although this model successfully explains the formation of isolated massive stars, there are no conclusive detections of starless massive cores, yet (e.g. Motte et al., 2018; Massi et al., 2019).

2.3.2 Competitive accretion

The competitive accretion, as the name suggests, is a gravitational competition for gas within dense stellar clusters (Bonnell et al., 2001). According to this model, the gravitational potential energy of the entire star forming region will be greatest at the centre, resulting in an enhanced accretion rate towards the centre. Thus, the stars that are located near the cluster centres become more massive, primarily due to their location. The central protostars grow through Bondi-Hoyle accretion, where the accretion rate is given as

$$\dot{M} \simeq \pi R^2 \rho v \tag{2.7}$$

where ρ is the ambient density, v is the object's velocity, R is the Bondi radius, defined as $2GM/c_s^2$. Competitive accretion requires a distributed gas reservoir with initially low velocity dispersion, as expected in a turbulent medium*. This model can explain how the total stellar mass of a cluster is related to the most massive star within. It can further shed light on the distribution of stellar masses, the mass segregation of young stellar clusters, and the high binary frequency and properties of massive stars. A schematic illustrating the competitive accretion process is shown in Figure 2.4. One of the main challenges faced by

---

*The velocity dispersion of dense regions in turbulent media is typically lower due to (i) smaller physical size of the region (ii) anti-correlation between density and velocity (e.g. Offner et al., 2009)

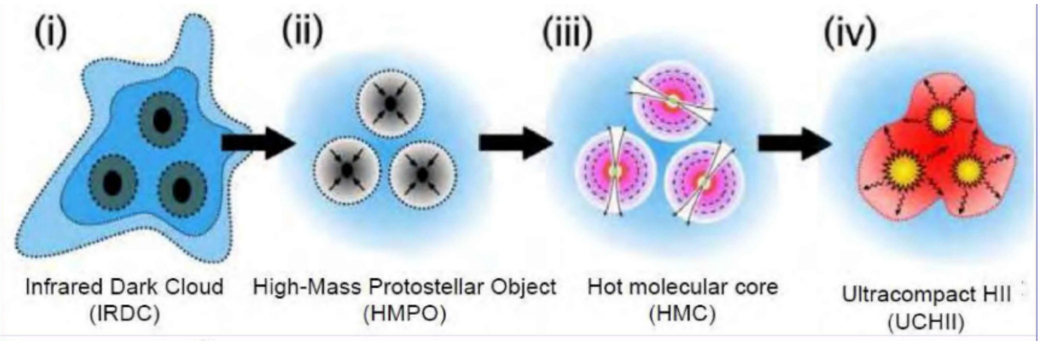

Figure 2.5: Schematic of evolutionary stages of high mass star formation. Image credit: Cormac Purcell

this process is the effects of radiation pressure, which puts major constraints on Bondi-Hoyle accretion, especially for stars with $M > 10\ M_\odot$ (Edgar & Clarke, 2004).

2.3.3 Stellar collisions

It is also proposed that high mass stars can form via the collision and merging of two or more stars in dense systems (Bonnell et al., 1998; Bonnell, 2002). This theory was primarily put forward to account for the gas accretion despite extreme radiation pressure. Although, the radiation pressure problem in the context of accretion was resolved with the help of disc structures, stellar collisions are shown to contribute to the formation of some massive cores observed (Takahira et al., 2014). A collisional build-up of high-mass stars is more feasible for the most massive stars in extremely dense clusters ($\sim 10^8\ \mathrm{pc}^{-3}$) (Tan, 2007). However, such clusters are not generally observed. The N-body simulations performed by Baumgardt & Klessen (2011) bolster accretion as the favourable mechanism for massive star formation, with stellar collisions playing a minor role.

2.4 Evolutionary phases of high-mass star formation

For sun-like stars, the observed pre-main sequence evolutionary stages have been divided into four major classes: Class 0, I, II and III, based on the shape of their spectral energy distributions (SEDs) from near-infrared to submillimeter wavelengths (André, 2011). Class 0 sources ($T_{bol} \leq 70$ K) are low mass protostars, whose SEDs peak longward of 100 μm in the submillimeter domain, and have very weak emission (and are often undetected) at near- and mid-infrared wavelengths. These sources are surrounded by a massive envelope and a disc. The ages of Class 0 protostars are just a few $\times\ 10^4$ years. Class I sources belong to the late accretion phase, where they are slowly accreting the rest of the final stellar mass. Similar to Class 0 sources, the Class I objects are surrounded by a remnant envelope and massive circumstellar disk. They peak at mid-and far-infrared wavelengths and lasts few $\times\ 10^5$ years. Class II sources are devoid of any envelope, but possess an optically thick accretion disc, generating the observed excess infrared emission. Most of the classical T Tauri stars belong to this class. Class III stars are post-accretion but still pre-main sequence stars. They are also called weak lined T Tauri stars. Unlike the case for low-mass stars, high-mass star formation lacks a firmly established observational evolutionary sequence. This is mainly due to the fact that massive stars, still deeply embedded in their natal cloud, undergo collapse and accretion while burning hydrogen in their core. Therefore, massive stars do not have an observable pre-main-sequence phase. Despite the lack of an evolutionary sequence, there are certain objects that indicate the evolutionary stages of high-mass star formation. A brief discussion on each of these evolutionary indicators is presented in the following subsections.

2.4.1 Early stages

IR dark clouds

Infrared dark clouds (IRDCs) are the coldest and densest regions of giant molecular cloud. They were first discovered by the Infrared Space Observatory (Kessler et al., 1996) and the Midcourse Space Experiment (Price et al., 2001) as dark extinction features against the bright mid-infared galactic background emission (Perault et al., 1996; Egan et al., 1998; Hennebelle et al., 2001). These structures are ubiquitous throughout the Galaxy (Simon et al., 2006) and are believed to be the progenitors of massive protostellar and cluster formation. IRDCs host complexes of cold ($T < 20$ K), dense ($n > 10^5\ \mathrm{cm}^{-3}$), and massive ($M \gtrsim 100\ M_\odot$) clumps and can exhibit compact or filamentary morphologies (Lada & Lada, 2003; Pillai et al., 2006). They are usually assumed to lie at the near kinematic distance, since a strong mid-IR background is required to make them appear in absorptions (Rathborne et al., 2006). There are also cases where a more evolved star forming region provide the background emission for IRDCs, allowing us to observe them at far distances too (Giannetti et al., 2015). They also contain jet-like outflows (Wang et al., 2011) and extended green objects (EGOs) (Yu & Wang, 2013), both of which are indicators of massive young stellar objects. The internal structure of IRDCs are best studied in millimeter/submillimeter wavelengths, as their thermal emission peaks at those wavelengths due to their low temperatures. This allows to trace column density and mass more accurately, as millimetre dust emission is

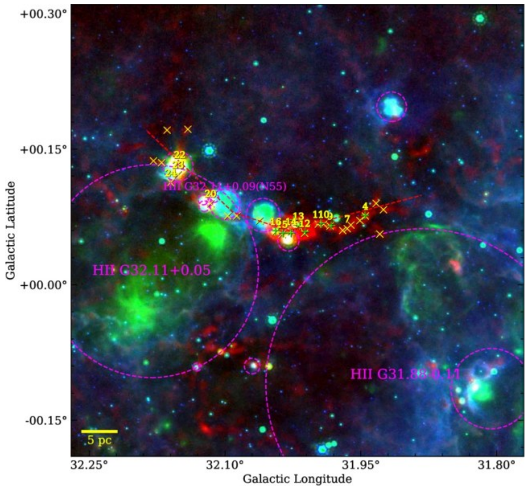

Figure 2.6: The three-colour image for IRDC G31.97+0.07 at large scale, red: JPS 850 µm, green: MIPSGAL 24 µm, blue: GLIMPSE 8 µm. Red dashed lines indicate the filamentary structure. The positions of H II regions identified by Anderson et al. (2014) are represented by the magenta dashed circles. Green and yellow crosses represent the positions of millimetre cores and compact sources, respectively. Image credit: Zhou et al. (2019).

optically thin.

HMPOs and HMCs

High Mass protostellar objects are observationally characterized by high luminosities ($L > 10^6\,L_\odot$), strong dust emission, and very weak or no detectable free-free emission (from ionized gas) at centimetre wavelengths (Beuther et al., 2002; Sridharan et al., 2002). This categorizes them as one of the earliest stages of high mass star formation. HMPOs are usually formed in clusters, deeply enshrouded in gas clouds. This impedes the formation of a detectable H II region, despite their high luminosities. They are believed to harbour unresolved internally heated gas cores at their centre. HMPOs have masses and sizes ranging from a few 100 to a few 1000 $M_\odot$ and 0.25−0.5 pc respectively, similar to that of IRDCs. However, their temperatures (~ 22 K) and densities ($n > 10^6$ cm^{-3}) are higher than what is observed in IRDCs.

Hot molecular cores (HMCs) (Kurtz et al., 2000; Cesaroni, 2005) are considered as the precursors of high-mass stars. They are also known for their rich chemistry, a consequence of the evaporation of dust grain mantles by the strong radiation of the deeply embedded early-type stars (Beltrán & Rivilla, 2018). HMCs are small (diameters ≤ 0.1 pc), dense ($n \geq 10^7$ cm^{-3}), hot ($T \geq 100$ K), and dark ($A_v \geq 100$ mag) molecular cloud cores (Nomura & Millar, 2004). The observed high molecular densities are believed to be an indicator

Table 2.1: Physical parameters of H II regions (Kurtz, 2005a).

Class of region	Size (pc)	Density (cm^{-3})	Emis.Meas. (pc cm^{-6})	Ionized mass $M_\odot$
Hypercompact	≤ 0.03	$\geq 10^6$	$> 10^{10}$	$\sim 10^{-3}$
Ultracompact	≤ 0.1	$\geq 10^4$	$\geq 10^7$	$\sim 10^{-2}$
Compact	≤ 0.5	$\geq 5 \times 10^3$	$\geq 10^7$	~ 1
Classical	~ 10	~ 100	~ 100	$\sim 10^5$
Giant	~ 100	~ 30	$\sim 5 \times 10^5$	$10^3 - 10^6$
Supergiant	> 100	~ 10	$\sim 10^5$	$10^6 - 10^8$

of luminous high mass star formation, which yields a large mass of high temperature gas. HMCs are characterized by actively accreting protostars, prior to the formation of ultracompact H II regions (e.g., Kurtz et al., 2000; Beuther et al., 2006b).

2.4.2 Evolved stage

H II regions

H II regions are formed when hydrogen is ionized in the gas clouds. The conversion of HI to H II occurs when they are exposed to intense UV radiation beyond the Lyman limit (13.6 eV). Since, only high mass stars are capable of generating significant amount of Lyman continuum photons, H II regions are considered as a tracer of massive star formation (Hoare et al., 2007). They are best observed in radio and IR wavelengths, as they are characterized by thermal emission from surrounding warm dust and free-free radiation.

H II regions are classified as Hypercompact (HC), Ultracompact (UC) (Kurtz, 2005a; Hoare et al., 2007), compact and classical/extended regions (Mezger et al., 1967; Yorke, 1986). Table 2.1 shows the properties of each of these regions. Both HC and UC H II regions represent small, growing pockets of ionized gas around newly formed massive stars. HC H II regions are much smaller compared to UC H II regions, indicating that the former represents ionized gas around a single star in contrast to the latter which corresponds to a stellar cluster (Kurtz, 2005b). Compact and classical H II regions, on the other hand, are manifestations of hydrodynamical expansion of the entire gas, leading to the disruption of the parent molecular cloud. This reveals the embedded high-mass and low mass stars, that can be observed in optical and near-IR wavebands (Carpenter et al., 1990; Zinnecker et al., 1993). Classical H II Regions are diffuse ionized nebulae surrounding hot O and B stars. Initially, UC H II phase was considered as the transition phase between the HMC and the compact H II regions, until Gaume et al. (1995) identified the first hypercompact H II region. However, there is an ongoing research to understand if HC H II regions indicate an evolutionary stage prior to the formation of UC H II region, or instead represent a different class of objects.

Although short-lived (a few million years), H II regions play a profound role in the propagation of star formation through molecular clouds. Star formation can be triggered in H II regions either due to the compression of pre-existing clumps due to shock waves propagating from supernovae ('globule squeezing'), accumulation of gas into a dense shell leading to the gravitational collapse into cores ('collect and collapse') or due to the gravitational instabilities prompted by the collision of clouds (Elmegreen, 1998). The 'collect and collapse' model is one of the simplest models of triggered star formation, where an expanding H II region sweeps up a dense shell of molecular material, allowing the formation of massive molecular fragments. However, it has to be noted that events such as expanding H II regions can sometimes quench star formation by causing the dispersion of gas and dust; depending on the gas structure amongst many other factors (Shima et al., 2017).

2.5 Probing massive star forming regions

Massive star forming regions of our galaxy are known to be the sites of complex physical and chemical processes, particularly involving dust grains. The earliest stages of massive star formation, prior to the formation of any embedded heating source, are characterized by strong cold dust and gas emitters at FIR/sub-millimeter wavelengths, and weak or non-detections in the mid-infrared (MIR) because they have not yet heated a warm dust cocoon (Beuther et al., 2006a). The eventual collapse and heating up of the cold, dense cores, marks the beginning of the hot core phase. The mid-infrared, provides the only access to rovibrational transitions and molecules with no permanent dipole moment, and probes hot core material closest to embedded protostars. Hence, high mass star forming regions can be probed by blind surveys at different wavelengths. The cold and massive molecular cloud cores, that constitute the early stages of high-mass star formation, are best detected by an unbiased, large survey at far-infrared and sub-millimetre wavelengths. The HMPOs are identified by mid-infrared surveys. Typically, in this stage, the objects are not yet surrounded by larger amounts of ionized hydrogen. The ultra-compact H II regions emit strongly at radio wavelengths, hence, these objects can be best found by radio continuum surveys. Apart from these large surveys, another effective way to trace high-mass star formation is by observing astronomical masers. They are the microwave analogue of lasers, occurring naturally in interstellar space. Since different masers need different physical conditions for them to get excited, they signpost different evolutionary stages of massive star formation, including the very elusive early stages (Ellingsen, 2004). Masers are bright and compact sources, making them ideal for investigating the kinematics and physical conditions within the massive star forming region at milli-arcsecond resolution. A more detailed discussion on astronomical masers is provided in the upcoming chapters of this thesis.

Chapter 3

Astronomical Masers

3.1 Introduction

Maser stands for ‘Microwave Amplification by the Stimulated Emission of Radiation’. Maser, like its optical counterpart (Laser), involves coherent emission of radiation but at microwave or radio frequencies. The emission is amplified through population inversion of molecular energy levels. When masers occur naturally in interstellar space instead of laboratory environments, we call them astronomical masers. The maser phenomenon in the cosmos was an unexpected discovery when an emission from an unknown source at a frequency of 1665 MHz was observed. This was soon identified as simultaneous detections of four OH lines that were not in thermal equilibrium with each other, resulting in anomalous radiation patterns (Weinreb et al., 1963; Weaver et al., 1965). Soon it became evident that owing to the relatively low densities, equilibrium distributions of level populations are the exception rather than the norm in interstellar clouds. Deviations from thermal equilibrium are likely to cause population inversion, which results in maser amplification. This phenomenon is not limited to OH molecule and has been detected in many more molecular species such as H_2O, SiO, CH_3OH, NH_3, CH_2O, CH and HCN. A general description of the theory of maser emission, pumping mechanisms, saturated and unsaturated masers are presented in this chapter. We also introduce the basic concepts of transfer of radiation through interstellar and intergalactic space. Most of the material discussed here are taken from Rybicki & Lightman (1985) and Elitzur (1992).

3.2 Some basic concepts

3.2.1 Radiative Transfer

The variation of the intensity of radiation propagating through space is described by the equation of radiative transfer,

$$\frac{dI_\nu}{dl} = -\alpha_\nu I_\nu + j_\nu \tag{3.1}$$

where I_ν represents the specific intensity of photons at a given frequency ν, passing through an area dA, with direction within solid angle $d\Omega$, travelling along a distance l. The attenuation per unit length at frequency ν is given by the absorption coefficient α_ν (cm^{-1}), while the intensity generated per unit length is described by the volume emission coefficient j_ν (erg cm^{-3} s^{-1} ster^{-1} Hz^{-1}). In free space,

$$\frac{dI_\nu}{dl} = 0 \tag{3.2}$$

3.2.2 Optical Depth

Equation (3.1) takes a much simpler form if, instead of l, we use another variable τ_ν called the optical depth, defined by

$$d\tau_\nu = \alpha_\nu dl \tag{3.3}$$

or

$$\tau_\nu = \int_0^l \alpha_\nu(l) dl \tag{3.4}$$

Optical depth is measured along the path of a travelling ray where τ_ν increases backwards along the path l and has the value zero at the observer. If $\tau_\nu \gg 1$, the medium is said to be optically thick or opaque, implying that no emission beyond that region is reaching the observer. On the other hand, when $\tau_\nu < 1$, the medium is said to be optically thin or transparent, with all emission reaching the observer.

The transfer equation, after dividing by α_ν, can be written as,

$$\frac{dI_\nu}{d\tau_\nu} = -I_\nu + S_\nu \tag{3.5}$$

where

$$S_\nu = j_\nu / \alpha_\nu \tag{3.6}$$

is the source function. The radiative transfer equation can be solved by regarding all quantities of Equation (3.1) as functions of the optical depth τ_ν instead of l and integrating over an entire region,

$$I_\nu(\tau_\nu) = I_\nu(0)e^{-\tau_\nu} + \int_0^{\tau_\nu} e^{-(\tau_\nu - \tau'_\nu)} S_\nu(\tau'_\nu) d\tau'_\nu \tag{3.7}$$

where $I_\nu(0)$ is the original intensity of the radiation located away from the observer.

3.2.3 Einstein relations

Consider a two level atom (levels 1 and 2) with energies E_1 and $E_2 > E_1$ and a radiatively allowed transition between the two states with exchange energy $h\nu_0 = E_2 - E_1$. Let g_1 and g_2 be the degeneracy factors in populating that state with electrons (statistical weights). Assume that the transition has some finite width in frequency defined by some functional form called the normalized line profile function ϕ_ν. Following the assumption that I_ν does not vary significantly across $\Delta\nu$, we must recognize that the energy difference between the two levels is not infinitely sharp but is described by a line profile function ϕ_ν, which is sharply peaked at $\nu = \nu_0$ and which is conveniently taken to be normalized:

$$\int d\nu \phi_\nu = 1 \tag{3.8}$$

There are three types of radiative transitions that are possible: spontaneous emission, absorption and stimulated emission. Their probability of transition from state 2 to 1 (state 1 to 2 in the case of absorption) are given by A_{21}, B_{12} and B_{21} respectively. These are called Einstein's coefficients. A simple sketch illustrating the same is given in Figure 3.1.

In thermal equilibrium,

$$\frac{\partial n_2}{\partial t} = J_\nu(\nu_0)B_{12} - n_2 J_\nu(\nu_0)B_{21} - n_2 A_{21} = 0 \tag{3.9}$$

where n_1 and n_2 are the number densities of atoms in levels 1 and 2 respectively. J_ν is the specific intensity averaged over all solid angles:

$$J_\nu = \frac{1}{4\pi} \int I_\nu d\Omega \tag{3.10}$$

Solving for J_ν and plugging in the Boltzmann relation,

$$\frac{n_1}{n_2} = \frac{g_1}{g_2} e^{\frac{(E_2 - E_1)}{kT}} \tag{3.11}$$

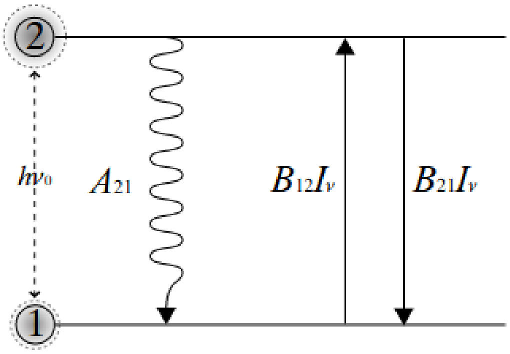

Figure 3.1: Illustration of Einstein's two level atom.

we obtain,

$$J_\nu(\nu_0) = \frac{A_{21}/B_{21}}{(g_1/g_2)(B_{12}/B21)e^{h\nu_0/kT} - 1} \tag{3.12}$$

For $\tau_\nu \longrightarrow \infty$,

$$J_\nu \longrightarrow B_\nu = \frac{2h\nu^3/c^2}{e^{h\nu_0/kT} - 1} \tag{3.13}$$

Equating the coefficients, we obtain the Einstein relations,

$$\frac{A_{21}}{B_{21}} = \frac{2h\nu_0^3}{c^2} \quad and \quad \frac{g_1 B_{12}}{g_2 B_{21}} = 1 \tag{3.14}$$

3.3 Maser Theory

3.3.1 The two level model and Rate equations

Finding solutions to the level population problem is a formidable task in itself, as many of the levels are coupled either directly, or indirectly. A basic idea of exchange of population between different levels can be obtained if we study a simple, isolated two level system. We discuss here a two level system with energy separation ΔE, with n_1 and n_2 being the number density of particles in lower and upper levels, respectively. The rate equation for such a system is defined as,

$$\frac{\partial n_1}{\partial t} = -\frac{\partial n_2}{\partial t} = n_2(C_{21} + A_{21}) - n_1 C_{12} + \bar{J}(n_2 B_{21} - n_1 B_{12}) \tag{3.15}$$

Here, B_{12}, B_{21} and A_{21} are the Einstein coefficients, $\bar{J}$ describes the radiation field and C_{12} and C_{21} are the collision rates. Population inversion can't be produced from the rate equations derived above, as they only describe particle exchange between two levels with rates that obey detailed balance relations. It can only occur as a result of particle cycling through other levels. A description of the maser effect therefore requires a generalization of the rate equations to include also system gains and losses due to population exchange with other levels that do not directly interact with the maser radiation. We introduce a loss rate Γ (s^{-1}) and a pump rate per unit volume P_i (cm^{-3} s^{-1}), for each of the two maser levels. These terms describe the interaction with all other levels that are omitted from the maser model since they do not couple to the maser photons. Because the particles in those other levels are unaffected by the maser radiation, the corresponding frequency distributions can be expected to follow the Doppler profile,

$$\phi(\nu) = \frac{1}{\Delta\nu_D\sqrt{\pi}} e^{-x^2} \tag{3.16}$$

where $x = (\nu - \nu_0)/\Delta\nu_D$ and $\Delta\nu_D = \nu_0(\Delta\nu_D/c)$. The density of those particles whose transition frequency has been shifted to ν from their original frequency ν_0 as a result of their random velocity - when the populations are distributed by the Doppler profile - is denoted by $n_{i\nu}$ (cm^{-3}Hz^{-1}), where $n_{i\nu} = n_i\phi(\nu)$. Let the pump rates into the frequency interval [ν, $\nu + d\nu$] are $P_{i\nu} = P_i\phi(\nu)$ (cm^{-3} s^{-1} Hz^{-1}). Then the rate equations for the upper and lower levels are,

$$\frac{\partial n_{2\nu}}{\partial t} = P_{2\nu} - \Gamma_2 n_{2\nu} - A_{21}n_{2\nu} - J_\nu(n_{2\nu}B_{21} - n_{1\nu}B_{12}) - (n_{2\nu}C_{21} - n_{1\nu}C_{12}) \tag{3.17}$$

$$\frac{\partial n_{1\nu}}{\partial t} = P_{1\nu} - \Gamma_1 n_{1\nu} + A_{21}n_{2\nu} - J_\nu(n_{1\nu}B_{12} - n_{2\nu}B_{21}) - (n_{1\nu}C_{12} - n_{2\nu}C_{21}) \tag{3.18}$$

where J_ν is the angle averaged maser intensity. We can assume steady state, i.e, $\frac{\partial}{\partial t} = 0$, as astronomical masers are stable over periods much longer than any timescale in the rate equations. The quantities relevant for maser gain are the populations per sub-level, $\tilde{n}_{i\nu} = n_{i\nu}/g_i$. To make the algebra even more simple, we will assume equal statistical weights and loss rates, i.e. $g_1 = g_2 \equiv g$ and that $\Gamma_1 = \Gamma_2 \equiv \Gamma$. With the aid of Equation (3.13) and using the fact that $g_1C_{12} = g_2C_{21}\exp(-\Delta E/kT)$, the steady state level population equations for the maser become,

$$0 = p_{2\nu} - \Gamma\tilde{n}_{2\nu} - A_{21}\tilde{n}_{2\nu} - B_{21}J_\nu(\tilde{n}_{2\nu} - \tilde{n}_{1\nu}) - C_{21}\left[\tilde{n}_{2\nu} - \tilde{n}_{1\nu}e^{-\Delta E/kT}\right] \tag{3.19}$$

$$0 = p_{1\nu} - \Gamma\tilde{n}_{1\nu} + A_{21}\tilde{n}_{2\nu} + B_{21}J_\nu(\tilde{n}_{2\nu} - \tilde{n}_{1\nu}) + C_{21}\left[\tilde{n}_{2\nu} - \tilde{n}_{1\nu}e^{-\Delta E/kT}\right] \tag{3.20}$$

where $p_i = P_i/g_i$ are the pump rates per sub-level.

Adding the above two equations and cancelling out the exchange terms between the two levels, the overall population of the maser system becomes,

$$\tilde{n}_\nu \equiv \tilde{n}_{1\nu} + \tilde{n}_{2\nu} = \tilde{n}\phi(\nu) \tag{3.21}$$

where $\tilde{n} = (p_1 + p_2)/\Gamma$. Equation (3.21) tells us that the overall population is distributed according to the thermal profile, irrespective of the maser intensity.

3.3.2 Population Inversion

In order to study the interaction of the maser particles with the radiation they generate, we can solve Equation (3.20) for the population difference,

$$\Delta\tilde{n}_\nu = \tilde{n}_{2\nu} - \tilde{n}_{1\nu} \tag{3.22}$$

Here we are not taking into account the spontaneous decays and collisional exchange terms provided A_{21} and C_{21} are much less than Γ. With these simplifications, the population difference $\Delta\tilde{n}_\nu$ can be derived by subtracting Equations (3.19) and (3.20).

$$\Delta\tilde{n}_\nu = \frac{\Delta\tilde{n}_0}{1 + \frac{J_\nu}{J_s}}\phi(\nu), \tag{3.23}$$

where

$$\Delta\tilde{n}_0 = \Delta p/\Gamma, \quad \Delta p = p_2 - p_1, \quad J_s = \Gamma/2B_{21} \tag{3.24}$$

When the maser is so intense that $J_\nu \gg J_s$, the frequency dependence of $\Delta\tilde{n}_\nu$ can deviate from the profile shape $\phi(\nu)$.

For the population inversion and maser action to occur, it is required that the pump rate per sub-level of the upper state must exceed that of the lower state. In other words, $p_2 > p_1$. The efficiency of the inversion process is characterized by the parameter

$$\eta = \frac{p_2 - p_1}{p_2 + p_1} = \frac{\Delta\eta_0}{\tilde{n}}; -1 \leq \eta \leq 1 \tag{3.25}$$

One can derive an excitation temperature T_{x0} from Δn_0, the population difference in the absence of maser emission ($J_\nu = 0$), which is negative for an inverted population.

$$e^{-h\nu/kT_{x_0}} = \frac{\tilde{n}_{2\nu}}{\tilde{n}_{1\nu}} = \frac{p_2}{p_1} \quad \Rightarrow \left|T_{x_0}\right| = \frac{h\nu}{k}\frac{1-\eta}{2\eta} \tag{3.26}$$

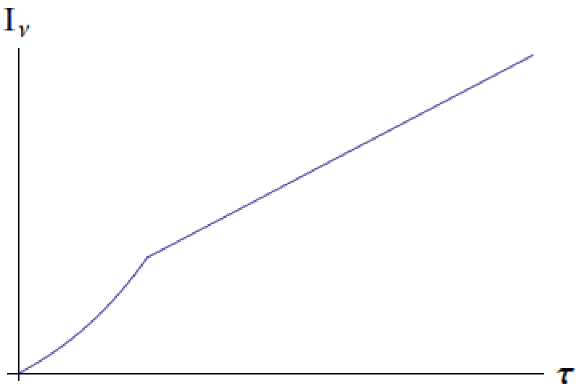

Figure 3.2: Maser intensity plotted against optical depth.

The excitation temperature is independent of the pumping rate and is exclusively determined by the inversion efficiency η. $\left|T_{x_0}\right|$ becomes smaller as the pumping becomes more efficient ($\eta \longrightarrow 1$). In other words, strong inversion corresponds to small $\left|T_{x_0}\right|$.

The absorption coefficient depends on the population difference and is given by

$$\alpha_\nu = (\tilde{n}_1 - \tilde{n}_2) g_2 B_{21} h\nu\phi(\nu)/4\pi \tag{3.27}$$

Hence, we can write the absorption coefficient for the maser as

$$\alpha_\nu = \frac{\alpha_{0\nu}}{1 + J_\nu/J_s}, \quad \alpha_{0\nu} = \Delta\tilde{n}_0 g_2 B_{21} h\nu\phi(\nu)/4\pi \tag{3.28}$$

Note that the absorption coefficient is negative and α_ν must be written as $|\alpha_\nu|$, as there is population inversion. The frequency dependence of the opacity ($\rho\kappa_\nu = \alpha_\nu$) can deviate from the profile of $\phi(\nu)$ when the intensity is high enough such that $J_\nu \gg J_s$, as in the case of population difference.

3.3.3 Unsaturated Vs Saturated Masers

Masers have two operational modes - unsaturated and saturated. For unsaturated masers, the maser intensity grows exponentially with the path length whereas for saturated ones, the growth in intensity is linear. A maser remains unsaturated as long as the pumping processes can maintain the population inversion against the growing losses by stimulated emission. Mathematically, for the case of unsaturated masers, the population difference $\Delta\tilde{n}_\nu$ becomes independent of the maser radiation field and $\alpha_\nu = \alpha_{0\nu}$, when $J_\nu \ll J_s$. Hence, the intensity of maser grows in proportion to $\mathrm{e}^{\alpha_{0\nu} l}$. Once $J_\nu \gg J_s$, the conversion efficiency $(J_\nu/(J_\nu+J_s))$

of inversions to maser photons approaches unity and the maser saturates. The sequence of events that might lead to maser saturation can be described as follows:

Consider a two level system with a large number of atoms in state 2. If a photon that has energy $E_2 - E_1$ interacts with one of these atoms, we get two identical photons. Both of these photons can then interact with other atoms in state 2 giving 4 photons. This leads to an exponential amplification of the number of photons. If this increasing number of photons continues to propagate through the atoms, a point will eventually be reached where there are more photons with energy $E_2 - E_1$ then there are atoms in state 2 for them to interact with. This means that we transition from an exponential amplification (from photon doubling) to a linear amplification (from continuing to travel through a medium with some density of atoms in state 2). This is called saturation. Figure 3.2 shows intensity I_ν as a function of optical depth τ. The discontinuity in the derivative on the graph is the saturation point.

3.3.4 Pumping in masers

If we have maser emission, there must be a population inversion in the source, so that light amplifies through it. Maintenance of the inversion requires a pumping mechanism. Three types of mechanism can contribute to the overall pump: collisions with partner atoms and molecules, which, in astrophysics, usually means a mixture of atomic and molecular hydrogen plus helium; radiation, usually of far-infrared (FIR) wavelengths; and chemical reactions, which, when forming the maser molecule, leave it in the upper state of a maser transition (Gray, 1999).

In order to comprehend the pumping mechanism better, consider a “three” level energy model (Figure 3.3), that describes the population of each energy level causing a maser transition. Here, level 3 actually represents all levels above level 2. The values P_i and Γ_i represent the pumping from all other energy levels in to the maser levels and energy loss from maser levels in to any other energy, respectively.

In collisional pumping, collisions with other species in the ISM must occur with different collision cross-sections, for the population inversion to take place. This leads to either the depletion of population in level 1 or transitions from level 3 into level 2, causing an over population in the upper maser energy level. However, too high an amount of collision would result in the thermalization of the gas and stop the maser. In other words, collisional pumping can be limited by the collision rates.

In radiative pumps, the main mechanism that causes the population inversion is radiation from an external source. Considering the energy level system shown in Figure 3.3, under

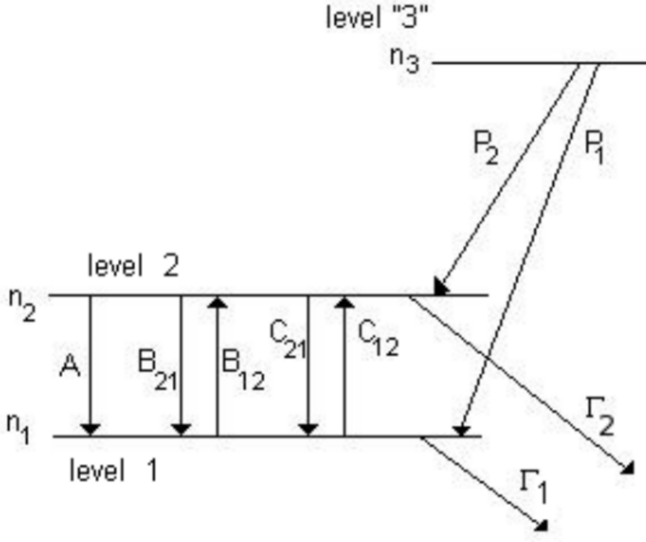

Figure 3.3: Illustration of a simple “three” level model for maser emission (Reid & Moran, 1988).

normal conditions a population inversion due to radiation should not be possible. In other words, pumping radiation is behaving like a black body. On the other hand, if the radiation deviates from this distribution, population inversion can occur. One possibility is maser molecules mixed with optically thin dust where the intensity is frequency dependent, i.e, the optical depths for particular transitions may be different, causing the population inversion by which more level 1 molecules are excited to level 3.

3.4 Maser Linewidths

As discussed in section 3.3.3, unsaturated maser intensity grows in proportion to $\mathrm{e}^{\alpha_{0\nu} l}$. The amplification is stronger at the line-centre frequency than at the line wings, since $\alpha_{0\nu}$ is sharply peaked there. The amplified line is also narrower than the input line. For instance, consider amplification when the maser gain is Doppler-shaped and the input signal has a Gaussian frequency distribution with some width $\Delta\nu_0$. That is,

$$I_\nu = I_0 e^{-x^2/\delta_0^2} \quad \tau_\nu = \tau_0 e^{-x^2} \tag{3.29}$$

where x is the dimensionless frequency shift from line centre given by $x = (\nu - \nu_0)\Delta\nu_D$ ($\Delta\nu_D$ is the Doppler linewidth) and $\delta_0 = \Delta\nu_0/\Delta\nu_D$. The intensity of the amplified line then

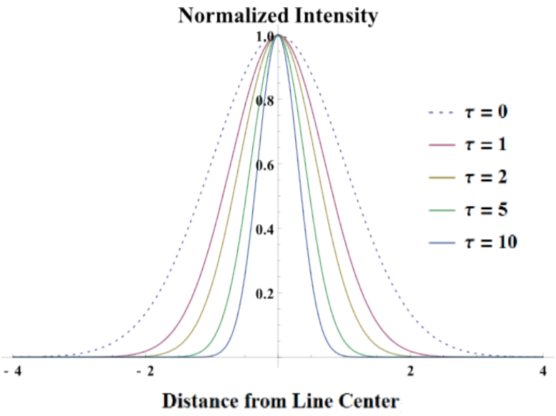

Figure 3.4: Simulated line narrowing of a Gaussian Doppler broadened spectrum at low saturation (Gentry, 2013).

becomes,

$$
\begin{aligned}
I_\nu &= I_0 \exp[-x^2/\delta_0^2 + \tau_0 \exp(-x^2)] \qquad (3.30)\\
&\simeq I_0 \exp(\tau_0) \exp[-x^2(1/\delta_0^2 + \tau_0)] \qquad (3.31)
\end{aligned}
$$

The linewidth of this distribution is,

$$\Delta\nu = \frac{\Delta\nu_D}{(1/\delta_0^2 + \tau_0)^{1/2}} \qquad (3.32)$$

Thus, during unsaturated amplification:

1. Input continuous radiation ($\delta_0 \rightarrow \infty$) will be processed into a line whose width is $\Delta\nu_D/\tau_0^{1/2}$
2. A Doppler-shaped line ($\delta_0 = 1$) will become narrower by the amount $(1 + \tau_0)^{1/2}$
3. The profile of an extremely narrow input signal ($\delta_0^2 \ll 1/\tau_0$) will remain unchanged.

Figure 3.4 illustrates the line arrowing, when the amplifying gas has the same temperature (and thus the same velocity dispersion) as the radiation source gas (i.e, $\delta_0 = 1$). Such line narrowing has been clearly seen narrowing spectral features by at least a factor of 2–3. In the scenario where there are two gas clouds with the same thermal velocity dispersion, an emission line emanating from one cloud will have a narrower width after it passes through the other only if there has been population inversion. A value of $\alpha_{0\nu}l \approx 16 - 25$ is required to provide enough gain to explain the observed brightness temperatures for many masers.

Hence, the line widths of unsaturated masers should be narrower, by a factor of 4 to 5, compared to the thermal line width (Bouton et al., 2012). For example, the unsaturated 1.667 OH maser linewidth is $\leq$ 0.24 km s^{-1} (Wright et al., 2004), whereas the thermal linewidth of OH molecule is typically 0.57 km s^{-1} (Bains et al., 2003).

It has to be noted that narrowing cannot continue indefinitely. When the maser emission saturates, the intensity at resonant frequency grows linearly with depth, and the wings grow exponentially. Here, the line ceases to narrow further, and the wings grow relative to the peak, which leads to rebroadening of the spectral line.

Chapter 4

Methanol masers

4.1 Introduction

The methanol molecule (CH_3OH) is an asymmetric top molecule. The chemical structure of the molecule is shown in Figure 4.1.

Methanol has been observed abundantly in both the gas phase (Friberg et al., 1988; Turner, 1998; Parise et al., 2002; Bergman et al., 2011; Wirström et al., 2011; Guzmán et al., 2013; Öberg et al., 2014; Taquet et al., 2015) and the solid state (Grim et al., 1991; Allamandola et al., 1992; Skinner et al., 1992; Chiar et al., 1996; Dartois et al., 1999; Gibb et al., 2000; Pontoppidan et al., 2003; Taban et al., 2003; Boogert et al., 2008; Bottinelli et al., 2010). The formation of methanol is thought to be most efficient by solid state interactions on icy grain mantles. Chemical models that simulate the formation of methanol through gas phase chemistry provide abundances orders of magnitude below the observed fractional abundance of the methanol molecule (Garrod et al., 2006; Geppert et al., 2006). On the other hand, solid state laboratory studies show that CH_3OH is efficiently formed in CO-rich

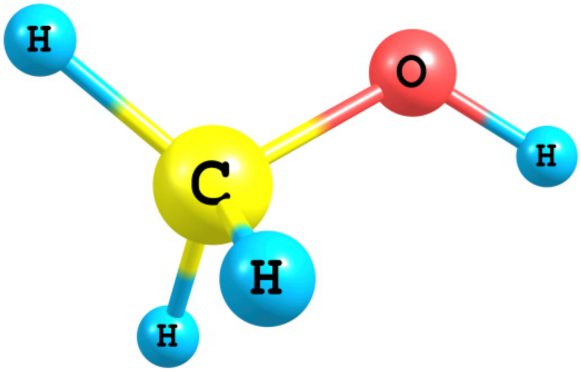

Figure 4.1: Chemical structure of a methanol molecule.

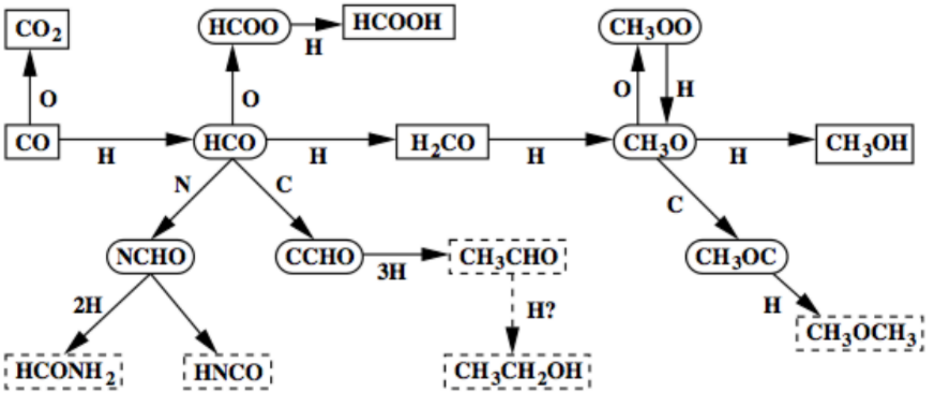

Figure 4.2: Synthesis of methanol molecule via grain-surface reactions. Solid boxes show molecules observed in interstellar ices, whereas dashed boxes show those observed in gas phase (van Dishoeck & Hogerheijde, 1999).

ices through sequential hydrogenation of CO (Hiraoka et al., 1994; Watanabe & Kouchi, 2002; Fuchs et al., 2009). Figure 4.2 illustrates the formation of methanol molecule via hydrogenation of CO the molecule (van Dishoeck & Hogerheijde, 1999). These findings are also in agreement with spectroscopic observations that show the coexistence of CO and CH_3OH in CO-rich and H_2O-poor interstellar ices (Cuppen et al., 2011; Boogert et al., 2015; Penteado et al., 2015). It has also been discovered that methanol is an important precursor in the formation of larger species (Qasim et al., 2018). The methanol molecule fragments into smaller components upon UV irradiation, which then recombine to form complex organic molecules (Öberg et al., 2009).

Methanol molecules exist in two symmetry states, denoted by A and E, which differ in the total spin (I) state of the hydrogen nuclei in the CH_3. Species A is characterized by the symmetric spin function (I = 3/2) and E species by the asymmetric spin function (I = 1/2). These two species are considered independent, as the normal radiative and collisional processes do not interconvert these symmetry states. A and E species are assumed to be equally abundant, except at very low temperatures, where the A species becomes more dominant (Cragg et al., 2005; Rabli & Flower, 2010). The methanol transition is written in the form J_K in terms of labelling, where J is the rotational quantum number (selection rule allow $\Delta J = 0, \pm 1$), K represents the alignment of angular momentum with respect to the molecular axis. The symmetry state of the methanol transition is also indicated in the label. The A-symmetry species has a non-negative K and has close pairing of levels, which are labelled by a ± symmetry label (related to the parity quantum number). The E-species

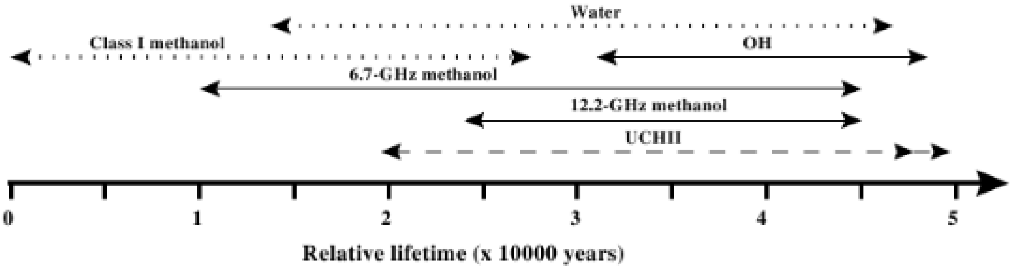

Figure 4.3: Schematic diagram of the evolutionary sequence for different maser species (Breen et al., 2010).

levels, on the other hand, are labelled by a signed K (Lees & Baker, 1968).

Methanol offers a rich selection of maser activity, which must be sorted out in some fashion before any meaningful modelling can be attempted. A scheme that divides methanol maser sources to two classes was put forward by (Batrla et al., 1987). According to this scheme, methanol masers are split into two classes; class A and class B. Class A sources were observed at typically large offsets from known tracers of star formation (UCH II regions and strong infrared sources), whereas class B sources were observed towards the centre of star forming regions (Batrla et al., 1987). This scheme of classification was later refined by Slysh et al. (1994), based on the differences in their excitation mechanisms. Class I and Class II methanol masers previously called as class A and class B, respectively) were found to be collisionally and radiatively pumped, respectively (Cragg et al., 1992). It was also found that both Class I and Class II masers trace star formation (Menten, 1991). The spatial coincidence of Class I and Class II maser emission is still not clear and is an area of ongoing research. Class I masers, that include a series of transitions near 25 GHz, as well as 36, 44, 84 and 95 GHz, are found typically offset from IR–bright areas of star formation regions and OH or H_2O masers, by up to 1 pc (Ellingsen, 2006a). Class II masers are detected towards star forming regions, where they are associated with ultracompact H II regions and OH/H_2O masers (Norris et al., 1987; Kemball et al., 1988; Koo et al., 1988; Menten et al., 1988; Norris et al., 1988). While more than 20 transitions of Class II methanol masers have been observed (Müller et al. 2004, and references therein), transitions near 12.2 GHz and 6.7 GHz has been extensively studied, owing to its high brightness temperatures.

The evolutionary sequence for different maser species is shown in Figure 4.3 (Breen et al., 2010). One has to note that this is only an approximate evolutionary sequence, and the timescales between the onset and shut off of masers are still under research.

Transition	Frequency (MHz)
$9_{-1} \rightarrow 8_{-2}$-E	9936
$10_1 \rightarrow 9_2$-A^-	23445
$3_2 \rightarrow 3_1$-E	24929
$4_2 \rightarrow 4_1$-E	24933
$2_2 \rightarrow 2_1$-E	24934
$5_2 \rightarrow 5_1$-E	24959
$6_2 \rightarrow 6_1$-E	25018
$7_2 \rightarrow 7_1$-E	25125
$8_2 \rightarrow 8_1$-E	25294
$9_2 \rightarrow 9_1$-E	25541
$10_2 \rightarrow 10_1$-E	25878
$12_2 \rightarrow 12_1$-E	26847
$13_2 \rightarrow 13_1$-E	27473
$14_2 \rightarrow 14_1$-E	28169
$15_2 \rightarrow 15_1$-E	28906
$16_2 \rightarrow 16_1$-E	29637
$17_2 \rightarrow 17_1$-E	30308
$4_{-1} \rightarrow 3_0$-E	36169
$7_0 \rightarrow 6_1$-A^+	44069
$5_{-1} \rightarrow 4_0$-E	84521
$8_0 \rightarrow 7_1$-A^+	95169
$11_{-1} \rightarrow 10_{-2}$-$E$	104300
$6_{-1} \rightarrow 5_0 E$	132891
$9_0 \rightarrow 8_1$-A^+	146618
$4_2 \rightarrow 3_1$-E	218440
$8_{-1} \rightarrow 7_0\ E$	229758
$9_{-1} \rightarrow 8_0$-E	278305

Table 4.1: Different transitions of interstellar Class I methanol maser known to date (Leurini et al., 2016).

4.2 Class I methanol masers

Class I methanol masers are collisionally excited and are believed to form away from the central protostar, at distances typically larger than 10^4 AU. These masers are often detected towards Extended Green Objects (EGOs), sources that show extended emission in the 4.5 μm band of GLIMPSE (Cyganowski et al., 2009; Chen et al., 2009). As EGOs are produced by shock-excited H_2 and CO (Cyganowski et al., 2008), Class I masers are thought to be associated with shocked material in protostellar outflows. Such outflows are expected to be most energetic and prevalent during the infall/accretion phase of star formation, and hence it has been speculated that sources with associated Class I methanol masers may signpost an earlier phase of high-mass star formation than those without (Ellingsen, 2005). Later, Kalenskii et al. (2010) reported that these masers are also detected from outflows associated with low and intermediate mass protostars. However, Class I methanol masers do not exclusively probe molecular outflows (Leurini et al., 2016). Astronomical environments that encompass shocked gas, such as regions where supernova remnants interact with the molecular cloud (e.g., Szczepanski et al., 1989; Haschick et al., 1990;

Pihlström et al., 2011), cloud-cloud collisions (e.g., Sobolev, 1992), and layers where expanding H II regions interact with the ambient molecular environment (Voronkov et al., 2010), also harbour Class I emission.

All the known Class I methanol maser transitions have been shown in Table 4.1 (Leurini et al., 2016). The transitions at 44 GHz ($7_0 \rightarrow 6_1 - A^+$) and 95 GHz ($8_0 \rightarrow 7_1 - A^+$) are regarded as the most widespread and strongest of them all (e.g., Haschick et al., 1990; Val'tts et al., 2000), followed by the transitions at 36 GHz ($4_{-1} \rightarrow 3_0 - E$) and 84 GHz ($5_{-1} \rightarrow 4_0 - E$) (e.g., Haschick & Baan, 1989; Kalenskiĭ et al., 2001; Voronkov et al., 2014). Different transitions of Class I maser have been suggested to represent different evolutionary stages of the source. Pratap et al. (2008) surveyed the 36 and 44 GHz Class I maser transition towards a sample of star forming regions and found that the 36 GHz emission trace colder, less dense environments than the latter. They categorized the objects having a 44 to 36 GHz line ratio > 5 being more evolved and the ones having the ratio < 5 to be indicative of colder less evolved state with no associated UCH II regions. However, modelling maser emission is highly complicated. Therefore, the temperatures and densities provided by the models are rather estimates than exact values.

4.3 Class II methanol masers

Class II methanol masers, unlike Class I masers, are found in close vicinity of star forming regions and OH/H_2O masers (Norris et al., 1987; Kemball et al., 1988; Koo et al., 1988; Menten et al., 1988; Norris et al., 1988). Initial studies showed that Class I and Class II maser transitions are mutually exclusive (Menten et al., 1986). This was further explained qualitatively by Cragg et al. (1992) through statistical equilibrium calculations. According to their study, the collisionally pumped Class I masers are produced when the local continuum radiation is lower than the gas kinetic temperature, whereas the Class II radiatively excited transitions dominate when the continuum radiation temperature becomes greater than the kinetic temperature of the gas. Later, Ellingsen (2005), detected 95 GHz Class I methanol masers towards half of a sample of 6.7 GHz Class II methanol masers, implying that Class I and Class II emissions could coincide in star forming regions. However, it is worth noting that the objects that cause Class I maser emission is different from those that are responsible for producing Class II methanol masers.

The transitions at 12.2 GHz and 6.7 GHz are the two strongest Class II methanol maser transitions. The $5_1 \rightarrow 6_0\, A^+$ line of methanol at 6.7 GHz maser emission is known to produce the brightest emission both observationally and theoretically (Sobolev et al., 2005).

Transition	Frequency (MHz)
$5_1 \rightarrow 6_0\ A^+$	6668.5
$2_0 \rightarrow 3_{-1}\ E$	12178.6
$2_1 \rightarrow 3_0\ E$	19967.4
$9_2 \rightarrow 10_1\ A^+$	23121
$4_0 \rightarrow 3_1\ E$	28316
$8_2 \rightarrow 9_1\ A^-$	28970
$7_{-2} \rightarrow 8_{-1}\ E$	37703.7
$6_2 \rightarrow 5_3\ A^-$	38293.3
$6_2 \rightarrow 5_3\ A^+$	38452.7
$7_2 \rightarrow 8_1\ A^-$	80993.3
$13_{-3} \rightarrow 14_{-2}\ E$	84423.7
$6_{-2} \rightarrow 7_{-1}\ E$	85568.1
$7_2 \rightarrow 6_3\ A^-$	86615.6
$7_2 \rightarrow 6_3\ A^+$	86902.9
$8_3 \rightarrow 9_2\ E$	94541.8
$3_1 \rightarrow 4_0\ A^+$	107013.8
$0_0 \rightarrow 1_{-1}\ E$	108893.9
$7_2 \rightarrow 8_1\ A^+$	111289.6
$8_0 \rightarrow 8_{-1}\ E$	156488.9
$2_1 \rightarrow 3_0\ A^+$	156602.3
$7_0 \rightarrow 7_{-1}\ E$	156828.5
$5_0 \rightarrow 5_{-1}\ E$	157179
$4_0 \rightarrow 4_{-1}\ E$	157246

Table 4.2: List of Class II methanol maser transitions

The transition at 6.7 GHz was first discovered by Menten (1991), in observations towards known star formation regions in the Northern Hemisphere. All the detected 6.7 GHz masers had 12.2 GHz counterparts (Menten, 1991). Further observations showed that the 6.7 GHz transition was more extensive than the 12.2 GHz methanol masers (e.g. Caswell et al., 1995). Moscadelli et al. (2002) showed that the transitions at 6.7 GHz and 12.2 GHz are co-spatial to within a few milliarcseconds, particularly where their spectra are similar. It was later found out that the 6.7 GHz and 12.2 GHz maser emission happens in similar physical conditions (Cragg et al., 2005). However, there is also a large fraction of 6.7 GHz methanol masers lacking 12.2 GHz methanol maser counterparts, suggesting that they do not cover exactly the same regions.

Blaszkiewicz & Kus (2003) detected 12.2 GHz counterparts at the 6.7 GHz transition in all except one source of their sample, with 12.2 GHz emission being less luminous. The estimated lifetime of 6.7 GHz methanol maser is $2.5 \times 10^4 - 4.5 \times 10^4$ years (van der Walt, 2005) and that of 12.2 GHz maser is $1.4 \times 10^4 - 2.7 \times 10^4$ years (Breen et al., 2010). Breen et al. (2010) studied the association of 12.2 GHz masers with 6.7 GHz masers and suggested that the 12.2 GHz methanol masers “switch on” sometime after the onset of 6.7 GHz methanol maser emission. Table 4.2 shows a list of Class II methanol maser transitions (Cragg et al., 2005).

4.4 Pumping mechanisms in 6.7 GHz methanol masers

Maser emission at both 6.7 and 12.2 GHz are a result of underlying radiative processes. Class II methanol masers appears only when the brightness temperature of the external radiation is greater than the kinetic temperature in the source itself (Cragg et al., 1992; Zeng, 1992; Peng & Whiteoak, 1993). The brightness temperatures of Class II methanol masers often exceed 10^{10} K. The high intensities of 12.2 GHz masers was modelled by Sobolev & Deguchi (1994) using radiative transfer in the large velocity gradient (LVG) approximation. The masers were considered to be strongly beamed. H II regions provide the seed radiation for the maser to amplify. The kinetic temperature of the gas was assumed to be 20−50 K. The actual pumping is attributed to the warm dust (100−200 K) which surrounds the regions where methanol is abundant, providing an infrared continuum source to pump the first and second torsionally excited states of methanol. Based on the above models, the general conditions required for strong 12.2 GHz masers are the following:

- Hydrogen number densities (n_{H_2}) should be larger than 10^8 cm^{-3}.
- Methanol abundance (relative to H_2) must exceed 7×10^{-7}.
- The kinetic temperature should be less than 50 K.
- The masers should be beamed (beaming factor, $\epsilon^{-1} > 3$)

The $5_1 \rightarrow 6_0\, A^+$ methanol line at 6.7 GHz is the brightest of Class II masers with a brightness temperature $> 10^{12}$ K. Sobolev et al. (1997) applied the model for 12.2 GHz masers described above, for the A species of methanol, in an attempt to explain the extremely bright 6.7 GHz masers. They found that the $5_1 \rightarrow 6_0\, A^+$ transition is pumped by the infrared emission from local warm dust of T > 150 K which acts to excite the first and torsionally excited states of methanol. The de-excitation happen in such a way that the spontaneous decay favours downward transitions to levels of the ground state with K quantum number different from that of the initial state, causing the appearance of masers. The generation of 6.7 GHz methanol masers require gas densities of $3 \times 10^3 < n_{\mathrm{H_2}} < 10^9$ cm^{-3} (Cragg et al., 2005; Sobolev et al., 1997) and methanol column densities exceeding 2×10^{15} cm^{-2} (Sobolev et al., 1997), for them to get excited.

4.5 6.7 GHz methanol masers and massive star formation

Since its discovery in 1991, the 6.7 GHz methanol masers have been associated with the earliest stages of massive star formation. Several unbiased and targeted surveys for 6.7 GHz methanol masers have been carried out in the past decades. The targeted surveys were mostly performed towards the infrared sources or star-forming regions associated with other known tracers of massive star formation, such as H_2O or OH masers (e.g., Menten, 1991; MacLeod & Gaylard, 1992; Caswell et al., 1995; Caswell, 1996; Ellingsen et al., 1996; Ellingsen, 2007). The advantage of blind surveys over targeted surveys is that they detect maser emissions from multiple regions that are otherwise missed by the latter. Ellingsen et al. (1996) conducted the first blind survey of the Galactic plane for 6.7 GHz methanol masers. The survey covered a longitude range of $325° - 335°$, latitude range of $-0.53° - 0.53°$ and detected a total of 50 masers, 26 of which were new detections. An unbiased blind survey of a region at $20° \leq \ell \leq 40°$, $|b| \leq 0°$, carried out by Szymczak et al. (2002), detected 100 6.7 GHz methanol masers, among which 26 were new. Later, Pandian et al. (2007) conducted a sensitive blind survey of a portion of the Galactic plane that is visible to the Arecibo radio telescope, in search of 6.7 GHz methanol masers. They surveyed an area at $35.2° \leq \ell \leq 53.7°$, $|b| \leq 0.41°$ and detected a total of 86 sources, 48 of which were new detections. An unbiased, blind Galactic plane survey for 6.7 GHz methanol masers, the Methanol Multibeam (MMB) Survey, was conducted using the Parkes telescope. The survey covered a relatively wide region of the Galactic plane ($186° \leq \ell \leq 60°$and $|b| \leq 2°$) and detected 954 sources, including 344 new detections (Green et al., 2009, 2010, 2012; Caswell et al., 2010, 2011; Breen et al., 2015). The MMB survey constitutes the most extensive blind survey for the strong widespread maser emission from the 6.7 GHz $5_1 \rightarrow 6_0\, A^+$ transition of methanol. A total of approximately 1000 Galactic methanol masers have been detected so far at the 6.7 GHz transition.

Several studies have been carried out in search of a potential association of 6.7 GHz methanol masers with radio-continuum emission. High angular resolution ($\sim 0.01'' - 1''$) observations (Caswell, 1996; Phillips et al., 1998; Walsh et al., 1998; Minier et al., 2000) have shown that methanol masers are generally not directly associated with the Ultra compact H II regions. The targeted observations for 6.7 GHz methanol maser emission undertaken by Walsh et al. (1998) shows that only $\sim 25\%$ of methanol masers are associated with UC H II regions. For the cases where the 6.7 GHz methanol maser is associated with UC H II region, the size of the latter was observed to be smaller, implying that such regions are possibly younger. Further evolution of UC H II region occurs following the destruction of the maser

(Hill et al., 2005). Caswell (1997), in their study comparing the sites of OH masers at 6.035 GHz with that of 6.7 GHz masers and UC H II regions, found that UC H II regions are preferentially associated with the sources exhibiting excited OH masers. This bolsters the idea that 6.7 GHz methanol masers exist at a very early evolutionary stage of massive star formation. It was also shown that methanol masers are associated with sub-millimetre continuum emission, suggesting that they are excited by cold and deeply embedded objects (Walsh et al., 2003). Ellingsen (2006b) investigated the association between a statistically complete sample of 6.7 GHz methanol masers with GLIMPSE and MSX sources and found that the majority of their Class II methanol masers are associated with sources embedded within IRDCs. Later, Pandian et al. (2010), based on the spectral energy distributions of 6.7 GHz methanol masers, concluded that the masers are associated with rapidly accreting massive stars, mostly prior to the formation of an UC H II region. However, an alternative hypothesis was put forward by Phillips et al. (1998) to explain the lack of UC H II region detections towards 6.7 GHz maser sites. According to them, the maser emission may arise from intermediate mass non-ionising stars, that can produce sufficient IR photons to pump the masing transition, but insufficient UV photons to produce UC H II region. On the other hand, Hill et al. (2005), detected sub-millimetre continuum from warm dust emission towards majority (> 95%) of the 6.7 GHz methanol masers. Breen et al. (2010) reported the onset of methanol masers prior to the H_2O and OH maser emission. Urquhart et al. (2015) mapped thermal emission from cool dust towards 77 Class II 6.7 GHz methanol masers and found strong evidence for the ubiquitous association of methanol masers with compact dense clumps– showing them to be excellent signposts for identifying massive star-forming regions.

The maser distribution is typically found to extend between 100 and 2000 AU, when studied at high angular resolutions. They are also known to show different morphologies (Norris et al., 1988; Minier et al., 2002). High resolution observations of the 6.7 GHz methanol maser transition undertook by Phillips et al. (1998), showed that 17 of the 45 maser sources observed, displayed a linear or curved morphology. This suggests that methanol maser sources could be probing edge on circumstellar discs. Pestalozzi et al. (2009), also supported the idea of differentially rotating disc being the location of the 6.7 GHz methanol maser. Pandian et al. (2011), however, found that many of the linear distributions are part of a larger and more complex distribution, which is detected at shorter baselines. High resolution VLBI observations of Bartkiewicz et al. (2009), found that 9 of 31 6.7 GHz methanol maser sources selected from a blind survey, exhibited elliptical morphology. Thus, it was propounded that masers occur in ring-like structure with exciting sources at its centre. The fact that the detected elliptical sources were devoid of any cm continuum emission suggests that the sources are at an earlier evolutionary stage prior to any free-free emission.

While most of the 6.7 GHz methanol masers are closely associated with high-mass star forming regions, there has been an instance where the masers are detected towards low/intermediate-mass protostars–the low-luminosity 6.7 GHz methanol maser towards the Orion B region (NGC 2024:FIR 4) detected by Minier et al. (2003). They suggested that FIR 4 harbours an intermediate/high mass protostar. Later, Choi et al. (2015), using archival data sets from the Very Large Array, identified FIR 4 as a low mass protostar. High resolution maser spot studies were also carried out in an attempt to find the lower mass limit of sources that host 6.7 GHz methanol masers. The VLBI maps of 6.7 GHz methanol masers revealed elongated structures with linear velocity gradients (e.g Minier et al., 1998). This was attributed to the molecular gas lying within a rotating disk. Assuming Keplerian motion within the disk, they estimated the lower mass limit of the sources associated with 6.7 GHz masers to be less than 8 $M_\odot$ (e.g Minier et al., 2000; Goddi et al., 2011). However, this could likely be due to seeing a fraction of the rotating disk around young massive stars, thus underestimating the enclosed mass. Later, Bourke et al. (2005) estimated the minimum luminosity of a source that is associated with 6.7 GHz maser emission and found it to be somewhat lower than the 10^3 $L_\odot$. The mechanism by which 6.7 GHz methanol masers are excited by low-mass protostars is still enigmatic. For low-mass protostellar objects, the dust temperatures required to pump the line are expected to be at distances where the H_2 number density is high enough to quench maser action (Pandian et al., 2008). Thus, we need to resort to high-sensitivity and high resolution instruments in conjunction with improved distance estimates to the high-mass star forming regions, to properly quantify the physical processes at play.

Chapter 5

Probing the early phases of high-mass star formation with 6.7 GHz methanol masers

5.1 Introduction*

6.7 GHz methanol masers serve as a unique tool to detect and probe the early phases of massive star formation. Since the first detection reported by Menten et al. (1992), there have been numerous targeted and blind surveys for 6.7 GHz methanol masers, the largest being the Methanol Multibeam survey (MMB; Caswell et al. 2010). Targeted searches for 6.7 GHz methanol masers towards low-mass young stellar objects and hot corinos have not yielded any detections (Minier et al., 2003; Bourke et al., 2005; Xu et al., 2008; Pandian et al., 2008). Urquhart et al. (2013a) studied the properties of 577 ATLASGAL (Schuller et al., 2009) clumps associated with 6.7 GHz methanol masers and concluded that over 90% of their sample are associated with massive young stars. However, they also concluded that a few 6.7 GHz methanol masers may be associated with clumps that may form only intermediate-mass stars. While the study of Urquhart et al. (2013a) covers a significant fraction of the 6.7 GHz methanol masers that have been detected using the Methanol Multibeam Survey, it used only the 870 μm ATLASGAL data and derived the properties of the clumps hosting methanol masers assuming the dust temperature to be 20 K. Based on the spectral energy distributions of 6.7 GHz methanol masers, Pandian et al. (2010) conclude that the masers are associated with rapidly accreting massive stars, mostly prior to the formation of an ultracompact H II (UCH II) region. However, this study is limited by the small sample size,

---

*This chapter is based on the published paper: Pauslon & Pandian 2020 [Sonu Tabitha Paulson, Jagadheep D Pandian, Probing the early phases of high-mass star formation with 6.7 GHz methanol masers, Monthly Notices of the Royal Astronomical Society, Volume 492, Issue 1, February 2020, Pages 1335–1347]. The paper is reproduced here with minor changes.

and the lack of data in the far-infrared. De Villiers et al. (2015) studied the association of 6.7 GHz methanol masers with molecular outflows traced by ^{13}CO and concluded that the masers turn on in hot core sources that have already developed outflows and turn off during the UCH II phase.

While earlier studies such as Urquhart et al. (2013a) and Pandian et al. (2010) were constrained by the lack of data in the far-infrared, the availability of data from the Herschel Infrared Galactic Plane Survey (Hi-GAL; Molinari et al. 2010) allows us to do a more systematic study of the SEDs of the sources exciting methanol masers. In this chapter, we present the SEDs of 320 6.7 GHz methanol masers from 870 μm to 70 μm using data from ATLASGAL and Hi-GAL surveys.

5.2 Source Selection

Our methanol maser sample has been selected from the catalog of the Methanol Multibeam survey. The MMB survey covers the entire Galactic plane with a latitude coverage of $|b| \leq 2°$ and the catalog comprises of a total of 972 sources. We have restricted our analysis to sources that have been covered by the Hi-GAL survey ($|l| \leq 60°$, $|b| \leq 1°$). This limits the number of masers in our sample to 630. Determination of physical parameters such as mass, size and luminosity of the sources requires a knowledge of the distances to the sources; and this brings the sample size to 602 sources. The distances are taken from Urquhart et al. (2013b), Reid et al. (2014), Pandian et al. (2009) and Green et al. (2017). The distances for a majority of the sources are determined from their kinematics using the observed radial velocity, with a smaller sample of sources having more accurate distance estimates through trigonometric parallax. Green et al. (2017) also report distances to the full MMB sample using a parallax based approach of Reid et al. (2016) wherein sources are assigned to spiral arms using a Bayesian approach. However, for this work we prefer to use the kinematic distances since a large fraction of our sample is in the fourth Galactic quadrant where parallax measurements are limited. The method of Reid et al. (2016) is expected to be more accurate in the northern hemisphere where deviations in the kinematics of the star forming regions from pure Galactic rotation are modelled using observed parallax distances. An examination of the new distances reported by Green et al. (2017) indeed shows a large number of sources to be not associated with any spiral arm. A discussion on the variation of the results when adopting the new parallax based distances is presented in section 5.9.

We have discarded sources that are either saturated in the Hi-GAL data or are in very crowded fields where reliable photometry is difficult (especially at 500 μm where source

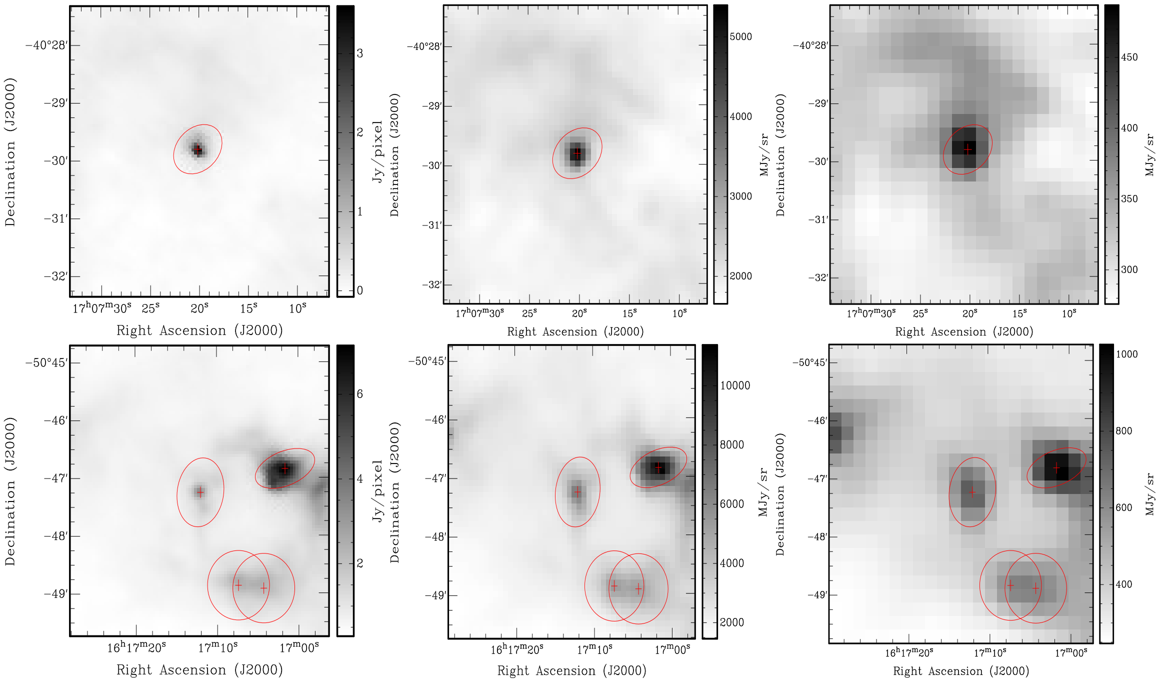

Figure 5.1: Source identification and apertures used by HYPER for doing photometry. The two rows show the 160, 250 and 500 μm data for G346.036+0.048 and G332.560−0.148 respectively, the latter showcasing a slightly crowded field.

blending in such fields is severe). We have also taken into account only sources that have ATLASGAL counterparts. This gave a final methanol maser sample of 320 sources, among which the integrated flux densities of 311 methanol maser sources are taken from Breen et al. (2015).

5.3 Data Analysis

We have determined the spectral energy distributions from 870 μm to 160 μm of the sources hosting methanol masers using data from ATLASGAL and Hi-GAL surveys. Fluxes from 870 to 70 μm have been determined from aperture photometry of the ATLASGAL and Hi-GAL images (level 2.5 images in the Herschel archive). The 870 μm ATLASGAL data have a resolution of 19”, while the Hi-GAL data have a resolution of 36.9”, 25.3”, 18.0”, 11.6” and 10.2” at 500, 350, 250, 160 and 70 μm respectively.

5.3.1 Source Photometry

Aperture photometry of Hi-GAL data is extremely challenging due to the complex structure of background emission and the crowded fields. An additional complication is that the resolution is different at different wavelength bands. We carried out aperture photometry using HYPER, an IDL based software package (Traficante et al., 2015). HYPER first detects sources in each band based on the supplied threshold. The photometry is then carried out using the sources detected in the reference band that is specified by the user. First, small cutouts are made around each source. After masking the central pixels containing emission from the source, the background is estimated by fitting a two-dimensional polynomial up to fourth order. The order of the polynomial is decided such that the residual after subtraction of the background is minimized. In the case of crowded fields where emission from multiple sources overlap, the size of the cutout is chosen to include all overlapping sources. A more detailed description of the procedure can be found in Traficante et al. (2015).

The shape of the aperture used for performing photometry is elliptical and is determined by fitting a two-dimensional Gaussian to the data at the reference wavelength. In the case of blended sources, a simultaneous multi-Gaussian fit is done to separate between the target source and its companions. The size of the aperture is related to the measured size of the source by a user supplied factor. This factor is selected such that most of the flux is recovered while minimizing contamination from nearby sources in crowded fields. The same aperture is then used to determine the fluxes in all bands. This allows us to obtain the integrated flux from the same volume of gas and dust at different wavelengths. We have used 250 μm as a reference wavelength for aperture photometry since the resolution and morphology of emission at 250 μm is very similar to that at 870 μm while the signal to noise ratio is much better. Figure 5.1 shows an example of photometry for an isolated and a slightly crowded field.

It is to be noted that the aperture photometry above will not recover the total flux from the source, especially at 350 and 500 μm, unless the size of the aperture is very large. However, the use of a large aperture factor is detrimental to the quality of photometry due to the effect of residuals from the background subtraction and contamination from other sources in crowded fields. Hence, the scale factor between the size of the source and that of the aperture used for photometry is kept to a moderate value, and the total flux is determined from the flux obtained by HYPER by incorporating a wavelength dependent correction factor. The correction factor is determined by simulating sources of different sizes, convolving the simulated data to the resolution of the Hi-GAL and ATLASGAL

Table 5.1: Flux densities of sources hosting 6.7 GHz methanol masers from 870 to 70 μm. The uncertainties in the measured flux densities are given in parentheses.

Name	Flux Values (Jy)					
	870 μm	500 μm	350 μm	250 μm	160 μm	70 μm
G345.131-0.174	4.14 (0.11)	17.52 (0.77)	49.45 (1.56)	97.06 (2.64)	125.80 (4.46)	60.30 (2.92)
G345.576-0.225	1.90 (0.06)	6.71 (0.40)	19.95 (0.80)	29.80 (1.02)	33.28 (0.90)	3.85 (0.30)
G345.807-0.044	0.84 (0.05)	3.92 (0.32)	8.03 (0.48)	11.70 (0.65)	9.75 (0.48)	0.54 (0.15)
G345.824+0.044	2.85 (0.09)	5.40 (0.82)	21.25 (2.15)	44.66 (2.92)	61.32 (3.30)	44.96 (2.74)
G309.384-0.135	7.22(0.29)	34.35 (1.04)	104.22 (2.65)	210.16 (5.33)	376.29 (11.26)	270.82 (7.67)
G005.618-0.082	4.31 (0.15)	20.19 (0.48)	53.77 (1.19)	94.64 (2.18)	98.20 (3.26)	17.61 (0.33)
G016.855+0.641	1.80 (0.06)	8.25 (0.37)	23.47 (0.78)	40.89 (1.05)	55.24 (1.68)	18.91 (0.69)
G010.724−0.334	4.05 (0.16)	18.46 (0.98)	55.74 (1.99)	81.11 (2.97)	112.08 (3.70)	39.01 (1.67)

*The full table is given in Appendix A.1

surveys, and comparing the actual flux with those determined by HYPER.

Table 5.1 shows the flux densities of the sources from 870 μm to 70 μm. The uncertainties in the flux densities quoted in Table 5.1 only account for random errors in the data and do not incorporate systematic effects such as the accuracy of flux calibration in the ATLASGAL and Hi-GAL surveys. A small fraction ($<$ 10%) of the sources are resolved into multiple sources at 160 and 70 μm even though they appear as single sources at 250 μm. In these cases, the procedure of aperture photometry used by HYPER will determine the combined fluxes of the multiple sources at shorter wavelengths since the aperture ellipse used for photometry is identical to that at 250 μm. The same result would have been obtained if the data at shorter wavelengths were convolved to the same resolution as that of the reference wavelength.

Another point to note is that there are alternate algorithms for carrying out aperture photometry in the Galactic plane region. While a detailed list of these algorithms can be found in Traficante et al. (2015), it is of interest to compare our results with that of the CUTEX algorithm, which is used for photometry of the catalogue released by the Hi-GAL team (e.g. Elia et al. 2017). While the CUTEX algorithm is relatively insensitive to background contamination for identification of point sources, the photometry is done independently in each band by fitting the source with a 2D Gaussian. Since the beam size of Herschel changes by more than a factor of 4 over the different bands, the process of aperture photometry requires integrating flux from larger areas at long wavelengths. This results in a bias which is corrected by rescaling the fluxes according to the ratio of deconvolved source sizes using 250 μm as a reference (Elia et al., 2017). A comparison of our fluxes with those of Elia et al. (2017) shows consistency to within 15% although the 500 μm fluxes

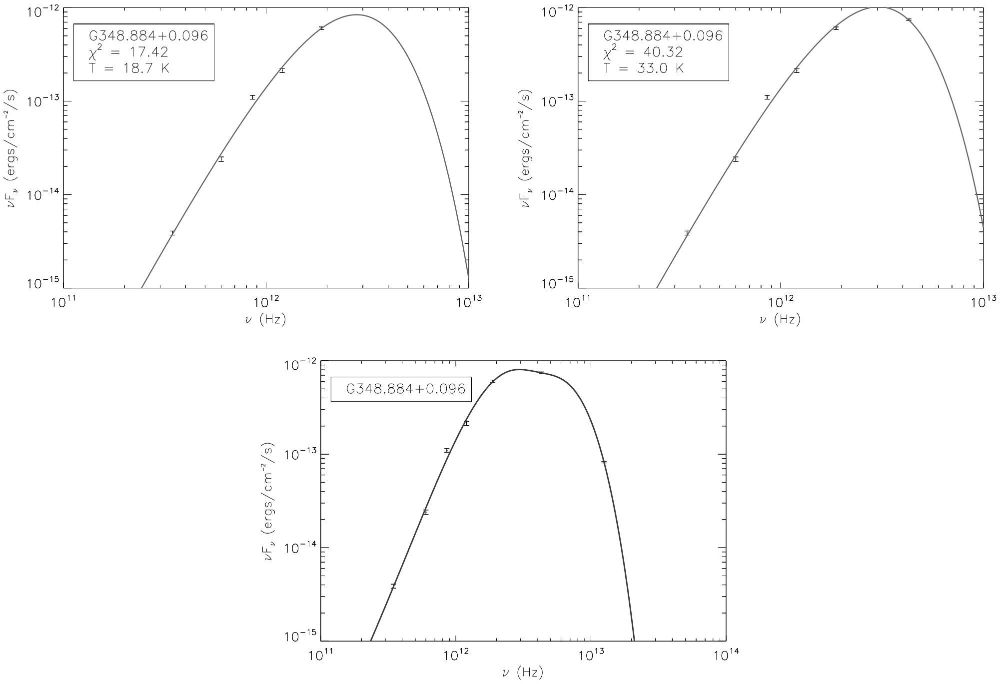

Figure 5.2: SED fits at different wavelength ranges.The upper left panel: The grey body fit for the wavelength range 70-870 μm. The upper right panel: grey body fit for the wavelength range 160-870 μm. Lower panel: SED fit taking into account both the cold and warm dust emission (excluding the contribution of 70 μm towards the cold dust emission).

show a mean variation of 30%. In most cases where there is significant variation between the HYPER and CUTEX fluxes, the source sizes are seen to be significantly different. Moreover, the source sizes are seen to be significantly larger at 500 μm compared to shorter wavelengths. Hence, we conclude that the discrepancy is mostly due to blending of sources due to the relatively poor resolution at 500 μm. This highlights the limitation of the CUTEX algorithm due to its treatment of the different bands independently.

5.3.2 Fitting the SED

We have fit the SED of the sources from 870 μm to 160 μm using a grey body to model the cold dust emission:

$$F_\nu = \Omega_c B_\nu(T_c)(1 - e^{-\tau_\nu}) \tag{5.1}$$

$$\tau_\nu = \tau_0 \left(\frac{\nu}{\nu_0}\right)^\beta \tag{5.2}$$

Here, Ω_c is the deconvolved solid angle of the source derived from the aperture used by HYPER for doing photometry (deconvolution is done using the Hi-GAL beam size at 250 μm – i.e. 18″), T_c is the temperature of the cold dust, τ_0 is the optical depth at frequency ν_0 (chosen to be 500 μm wavelength) and β is the dust emissivity index which is assumed to be $1 < \beta < 3$. The fitting was carried out using the nonlinear least squares Marquardt-Levenberg algorithm.

The emission at 70 μm is not likely to be attributable to a single dust component (Compiègne et al., 2010; Battersby et al., 2011). Rather, the 70 μm flux is expected to have contributions from both cold and warm dust. In order to test this hypothesis, we first compare the single component fit to the SED of a source with and without including the 70 μm flux. As shown in the left and right panels of Figure 5.2 for a typical source (G348.884+0.096 in this case), the fit including the 70 μm data gives a higher dust temperature with a significantly poorer χ^2 goodness of fit. We then carried out a two component fit to the SED including the the 24 μm flux from the MIPSGAL catalogue (Gutermuth & Heyer, 2014), with the second component being modelled as a black body:

$$F_\nu = \Omega_w B_\nu(T_w) \tag{5.3}$$

where Ω_w and T_w are the solid angle and the temperature of the warm dust respectively. In this fit (bottom panel of Figure 5.2), almost 60% of the 70 μm flux arose from the warm dust emission, confirming the hypothesis of the 70 μm emission arising from both cold and warm dust. Hence, for most sources, the grey body fit for cold dust was restricted to the 870−160 μm data.However, there are a few sources where the temperature of the cold dust is high enough that the peak of the black body is at wavelengths significantly shorter than 160 μm. In such cases, it is not possible to determine the dust temperature by fitting the 870−160 μm data alone since these wavelengths lie in the Rayleigh-Jeans part of the spectrum. In such cases, we have included the 70 μm data to fit the SED.

5.4 Physical properties of the clumps

We have fit the cold dust emission for 318 sources from 870−160 μm and 2 sources from 870−70 μm. The fits to SEDs of characteristic sources are shown in Figure 5.3 and the fit parameters for the sources listed in Table 5.1 are shown in Table 5.2. The uncertainty in the temperature of cold dust from the SED fit is typically less than 15%. The properties of the clumps hosting methanol masers such as radii, hydrogen column densities, masses, surface

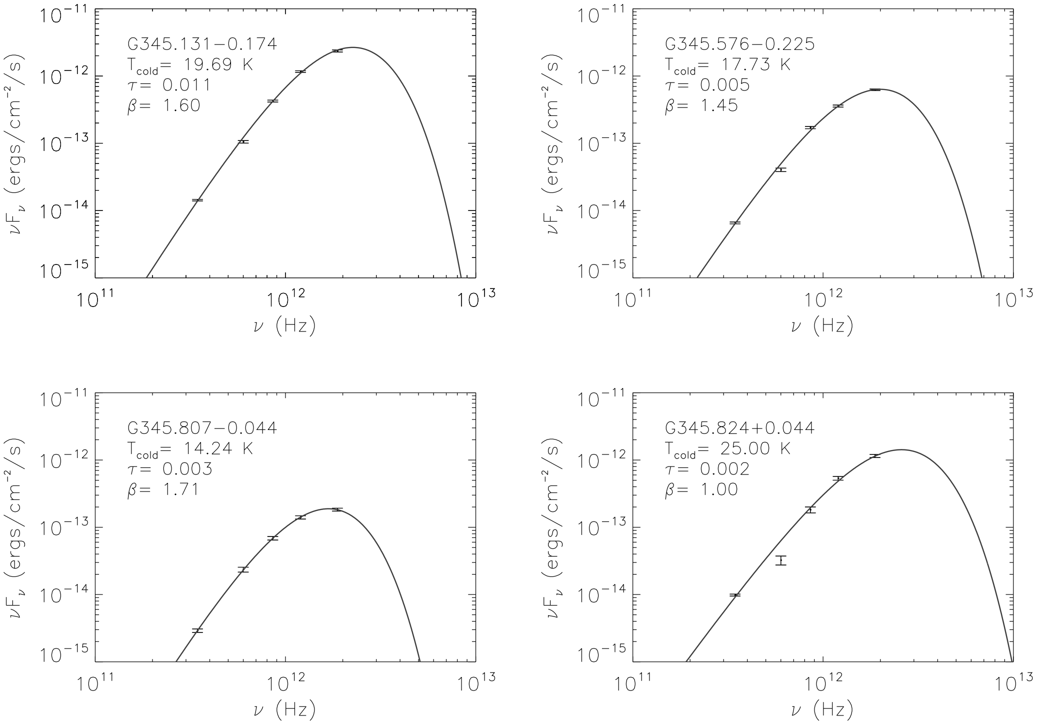

Figure 5.3: Single component fits to the SEDs of characteristic sources. The inset shows the source name, temperature of cold dust, dust optical depth at 500 μm and the dust spectral index. Fits to the SEDs of the entire 320 maser sources are given in Appendix A.1

Table 5.2: The best fit parameters of characteristic sources. The columns show the source name, distance, temperature of the cold dust component, the solid angle of cold dust as seen in aperture photometry, optical depth of dust at 500 μm and the dust spectral index, β.

Name	Distance (kpc)	T_c (K)	Ω_c (sr)	τ	β
G345.131−0.174	3.05	19.69	8.54×10^{-9}	0.024	1.6
G345.576−0.225	5.5	17.79	1.05×10^{-8}	0.010	1.5
G345.807−0.044	10.8	14.29	1.13×10^{-8}	0.006	1.7
G345.824+0.044	10.9	25.04	1.36×10^{-8}	0.005	1.0
G005.618−0.082	5.1	15.06	6.15×10^{-9}	0.092	2.0
G010.724−0.334	5.2	18.47	7.25×10^{-9}	0.003	1.7
G016.855+0.641	13.79	17.40	3.04×10^{-9}	0.049	1.8
G309.384−0.135	5.4	24.24	6.90×10^{-9}	0.039	1.6

*The full table is given in Appendix A.2.

densities and luminosities were determined from the SED parameters. These properties are described in subsections below. Table 5.3 lists the physical properties of each clump, while the global statistics are summarized in Table 5.4.

5.4.1 Source sizes

The effective radius of the sources have been estimated following the formulation of Rosolowsky et al. (2010):

$$\theta_R = \eta\left[\left(\sigma_{maj}^2 - \sigma_{beam}^2\right)\left(\sigma_{min}^2 - \sigma_{beam}^2\right)\right]^{1/4} \tag{5.4}$$

where σ_{beam} is related to the FWHM θ_{beam} by $\sigma_{beam} = \theta_{beam}/\sqrt{8\log 2}$. Since the aperture photometry is carried out using 250 μm as the reference wavelength, θ_{beam} is the FWHM size of the Hi-GAL beam at 250 μm (i.e. 18.0”). The factor η accounts for the relationship between rms size of the emission distribution and angular radius of the object, and is taken to be 2.4 as in Rosolowsky et al. (2010). Excluding sources that are close to being unresolved (for which deconvolution is not meaningful), the effective radius ranges from 0.07 to 1.99 pc, the median value being 0.69 pc. The distribution of the source radius is shown in Figure 5.4. Bergin & Tafalla (2007) suggest the nominal boundary between cores and clumps to be 0.125 pc and the boundary between clumps and clouds to be 1.25 pc. Under this nomenclature, three methanol masers are in cores, 273 are in clumps, and 33 are

Table 5.3: The physical properties derived from best fit parameters of characteristic sources. The columns show the source name, clump Mass, Hydrogen column density,effective radius,surface density and FIR Luminosity.

Name	Clump Mass ($M_\odot$)	N_{H_2} (cm^{-2})	Radius (pc)	Σ (g cm^{-2})	L_{FIR} ($L_\odot$)
G345.131−0.174	2.13×10^2	1.20×10^{24}	0.307	0.150	8.42×10^2
G345.576−0.225	3.77×10^2	5.30×10^{23}	0.618	0.065	6.68×10^2
G345.807−0.044	9.18×10^2	3.11×10^{23}	1.321	0.035	7.45×10^2
G345.824+0.044	1.35×10^3	3.75×10^{23}	1.508	0.039	6.192×10^3
G005.618−0.082	1.04×10^3	2.91×10^{23}	0.333	0.622	1.45×10^3
G010.724−0.334	6.79×10^2	1.55×10^{24}	0.462	0.210	1.95×10^3
G016.855+0.641	2.53×10^3	1.95×10^{24}	0.549	0.554	6.53×10^3
G309.384−0.135	8.82×10^2	1.96×10^{24}	0.450	0.288	9.51×10^3

*The full table is given in Appendix A.3.

Table 5.4: Summary of derived parameters

Parameter	Mean	Std. dev	Median	Min	Max
Dust temperature (K)	21.54	5.29	20.86	10.86	47.59
Dust emissivity	1.83	0.29	1.83	1.00	2.85
Effective radius (pc)	0.69	0.41	0.61	0.07	1.99
Surface Density (g cm^{-2})	0.27	0.38	0.17	0.02	4.28
Clump Mass ($M_\odot$)	1.57×10^3	2.46×10^3	9.30×10^2	11.07	1.62×10^4
Column Density (cm^{-2})	1.68×10^{24}	2.29×10^{24}	1.15×10^{24}	7.95×10^{22}	2.50×10^{25}
FIR luminosity ($L_\odot$)	1.74×10^4	3.91×10^4	6.44×10^3	1.33×10^2	3.28×10^5

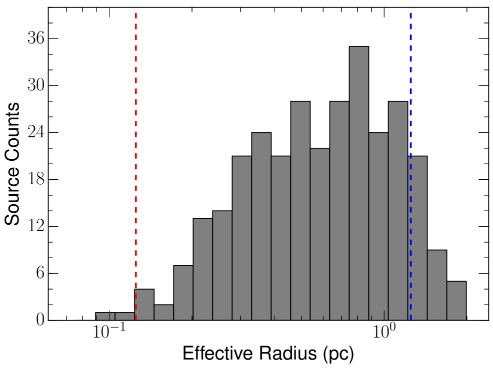

Figure 5.4: Distribution of source size. The dashed red and blue lines show nominal boundaries between cores and clumps, and clumps and clouds, respectively.

in clouds. However, all our data is from single dish telescopes, and it is likely that many sources may fragment into multiple objects when observed at higher angular resolution.

We find no correlation between the angular size of the source and its distance. This leads to a strong correlation between the source radius and distance to the source. Hence, the distinction between the identification of the source as a cloud, clump or core is primarily a result of the distance to the source. For instance, the sources that are classified as clouds are seen to have distances between 8.4 and 17.1 kpc with a mean value of 12.5 kpc, which is much larger than the mean distance to the entire sample (8.0 kpc). We will hence refer to all sources in our sample as clumps that will give rise to clusters rather than a single star. Our observation of lack of correlation between angular size of the source and the distance is similar to the findings of Tackenberg et al. (2013) for ATLASGAL candidate starless clumps and Urquhart et al. (2013a) for ATLASGAL sources associated with 6.7 GHz methanol masers. This is likely to be due to the hierarchical structure of molecular clouds from size scales of clouds to cores.

5.4.2 Dust temperature

The cold dust temperature is found to range from 10.9 K to 47.6 K, with mean and median values of 21.5 K and 20.9 K respectively. Figure 5.5 shows the distribution of dust temperature. The dust temperatures compare well with kinetic temperatures determined from ammonia measurements where a median temperature of 23.4 K was observed (Pandian et al., 2012). This further corroborates the more evolved nature of 6.7 GHz methanol masers compared to infrared dark clouds where lower temperatures are measured (e.g. Pillai et al. (2006)).

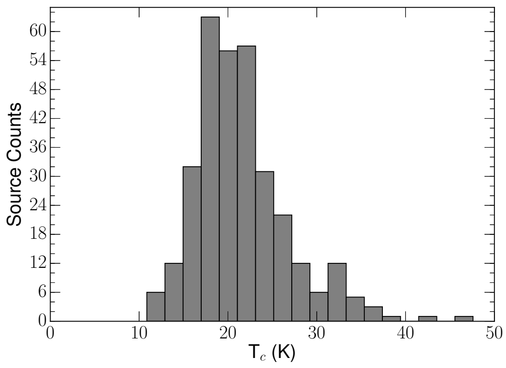

Figure 5.5: Distribution of cold dust temperature.

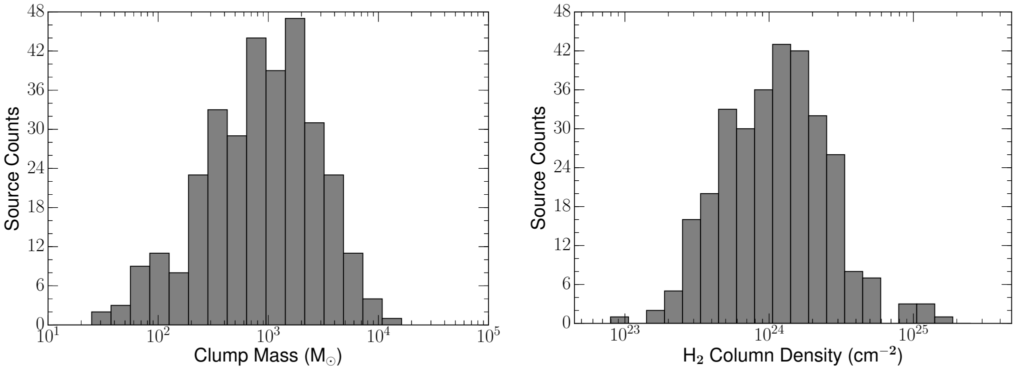

Figure 5.6: Distribution of mass (left panel) and H_2 column density (right panel).

5.4.3 Clump Masses, H_2 column densities and surface densities

The isothermal masses of the sources can be computed using the temperature values obtained from the best fit using the following equation:

$$M = \frac{D^2 S_\nu R}{B_\nu(T_D)\kappa_\nu} \tag{5.5}$$

where S_ν is the integrated 870 μm flux, D is the distance to the source, R is the gas-to-dust mass ratio (assumed to be 100), B_ν is the Planck function for the cold dust temperature T_D and κ_ν is the dust opacity which is taken as 1.85 cm^2 g^{-1} at 870 μm. The clump masses range from 11.07 $M_\odot$ to 1.62×10^4 $M_\odot$, the median mass being approximately 930 $M_\odot$. The mass distribution of the clumps is shown in Figure 5.6 (left panel). The shape of the mass distribution is similar to that observed by Urquhart et al. (2013a) although there are some key differences. While the peak of the distribution is similar, the maximum mass is well below that of Urquhart et al. (2013a). We also see a larger fraction of sources in the 100 to 1000 $M_\odot$

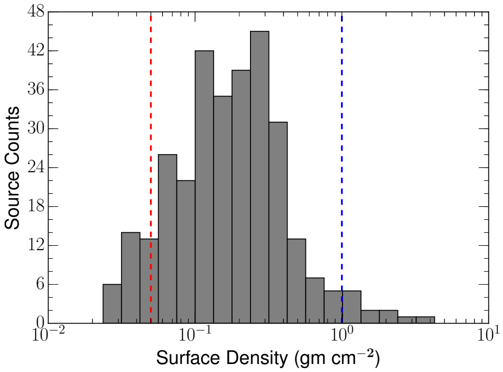

Figure 5.7: Distribution of the surface density. The *red* and *blue* dashed line show a threshold of 0.05 g cm^{-2} and 1.00 g cm^{-2} respectively.

range. These differences are most likely due to two reasons. First, the methodology of doing photometry is different – the HYPER software uses a Gaussian aperture to do photometry, while the fluxes of Urquhart et al. (2013a) are from the ATLASGAL compact source catalog where photometry has been done by SEXTRACTOR (Contreras et al., 2013). The former measures the flux of the compact source while the latter measures the flux of the entire clump including the diffuse emission around the compact source. To corroborate this, we have compared the fluxes determined by us with those of the GAUSSCLUMP catalog (Csengeri et al., 2014). We find our fluxes to be comparable though slightly larger than that of Csengeri et al. (2014). This is because the latter fit the entire clump including the outer diffuse structure with multiple Gaussians, while we only fit the central emission based on its morphology at 250 μm which is our reference wavelength. The larger fluxes in the ATLASGAL compact source catalog translate to larger masses in the work of Urquhart et al. (2013a).

An additional factor that contributes to the different mass distribution is the assumption of a uniform dust temperature of 20 K by Urquhart et al. (2013a) as opposed to our deriving the dust temperature by fitting the spectral energy distribution. As mentioned in the section 5.4.2, the dust temperature ranges from 10.9 K to 47.6 K, with 185 out of 320 sources having temperatures greater than 20 K. As is evident from Equation 5.5, assumption of a dust temperature of 20 K leads to the mass being overestimated when the true temperature is greater than 20 K. Since a majority of sources have temperatures greater than 20 K, our masses will be lower than that derived by Urquhart et al. (2013a) even without accounting for the difference in photometry. However, since the mean temperature is very close to 20 K, we see the peak in our mass distribution to be comparable to that of Urquhart et al. (2013a).

The molecular hydrogen column densities are estimated from the 870 μm flux density using the following equation:

$$N_{H_2} = \frac{S_\nu R}{B_\nu(T_D)\Omega\kappa_\nu\mu m_H} \tag{5.6}$$

where Ω is the deconvolved solid angle of the source, μ is the mean molecular weight and is assumed to be equal to 2.8 (the hydrogen mass fraction is assumed to be $\sim$ 0.7) and m_H is the mass of an hydrogen atom. It has to be noted that we have determined the column densities of only those sources that have sizes larger than the beam size (since we have used the deconvolved solid angle in Equation 5.6). The column densities of the maser associated clumps range from 7.95×10^{22} to 2.5×10^{25} cm^{-2} with a median value of 1.15×10^{24} cm^{-2}. The observed values are generally higher than those found in previous studies of high-mass star forming sources (e.g. Garay et al. 2004) due to the usage of deconvolved rather than observed solid angle of the source. The distribution of column densities of the sample are shown in the right panel of Figure 5.6.

Another parameter of high interest in star formation is the surface density (Σ) of the clump or core. The surface densities are obtained by dividing the mass of the clump by its physical area (πR_{eff}^2 where R_{eff} is the effective radius). The surface densities inferred for our sample (that are properly deconvolved) range from 0.02 to 4.28 g cm^{-2} with a mean and median value of 0.27 and 0.17 g cm^{-2} respectively. Figure 5.7 shows the distribution of surface density for our sample. Also shown in Figure 5.7 is the threshold of 0.05 g cm^{-2} that is suggested by Urquhart et al. (2013a) as the minimum surface density required for forming massive stars.

5.4.4 Clump and maser luminosities

The luminosity of the individual clumps have been calculated by integrating the SED:

$$L = 4\pi D^2 \int f_\nu d\nu \tag{5.7}$$

where D is the distance to the source and $\int f_\nu d\nu$ is the integrated flux. We have calculated the Far Infrared (FIR) luminosity using the modified blackbody fit of the cold dust. The FIR luminosity estimates range from 133 L$_\odot$ to 3.3×10^5 L$_\odot$ with mean and median values of 1.74×10^4 L$_\odot$ and 6.4×10^3 L$_\odot$ respectively. Figure 5.8 shows the distribution of the FIR luminosities of the sample.

Although the total IR luminosity is expected to be higher than the FIR luminosity,

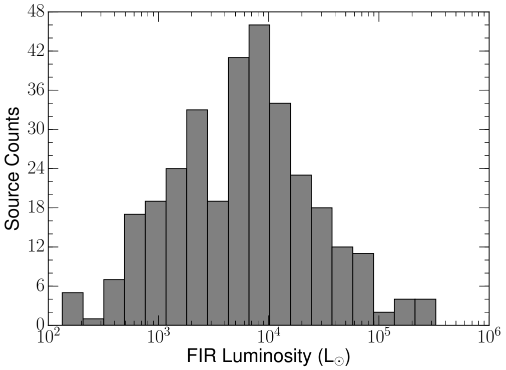

Figure 5.8: Distribution of the far infrared luminosity.

especially since the methanol maser sources are sufficiently evolved to have emission at 24 μm and shorter wavelengths covered by the GLIMPSE survey, it is interesting that we detect relatively low luminosity sources with luminosities lower than 10^3 L$_\odot$ hosting methanol masers. This suggests that there is a small population of methanol masers that are associated with intermediate-mass or low-mass stars.

One of the aims of this study is to explore the relation between methanol maser luminosity and the global properties of the maser hosts. We have hence computed the isotropic methanol maser luminosities using the following equation:

$$L_{MMB} = 4\pi D^2 S_\nu \tag{5.8}$$

where S_ν is the integrated flux across the maser line and is taken from Breen et al. (2015). The methanol maser luminosity values range from 3.31×10^{-10} to 1.81×10^{-5} L$_\odot$ with mean and median values of 5.05×10^{-7} L$_\odot$ and 6.3×10^{-8} L$_\odot$ respectively. The left panel of Figure 5.9 shows the clump mass as a function of the maser luminosity. A partial Spearman correlation test to remove the mutual dependence on the distance to the source gives a correlation coefficient of 0.27. The right panel of Figure 5.9 shows the FIR luminosity of the clumps as a function of the maser luminosity, the partial Spearman coefficient between these being 0.37. These results are similar to that observed by Urquhart et al. (2014a) wherein a weak correlation was seen between the clump mass and maser luminosity. It is to be noted that Urquhart et al. (2014a) computed the maser luminosity using the peak line flux (i.e. in Jy kpc^2) rather than integrated line flux. However, we verify that the values of correlation coefficients obtained using methanol maser luminosities computed from their peak line fluxes are very similar to those reported above using the integrated line flux.

One of the concerns with the work presented here is the limited resolution of the data,

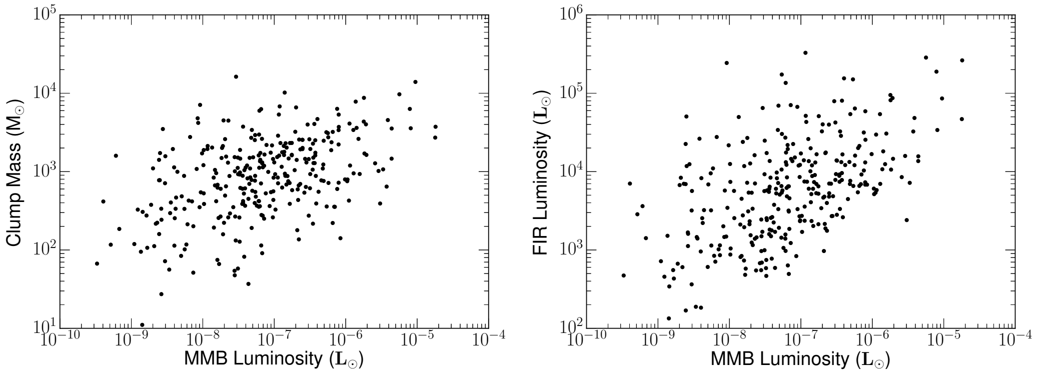

Figure 5.9: Relationship of 6.7 GHz methanol maser luminosity with (a) clump mass (left panel) and (b) FIR luminosity (right panel).

which when coupled with the large distances to the sources could result in more than one compact source (which may be in a different evolutionary state) being observed within the same telescope beam. However, as indicated in section 5.3, a large fraction of sources (~ 90%) are not observed to be resolved into multiple sources at the 10″ resolution of the Hi-GAL 70 μm data. An additional way to test whether multiplicity affects the results presented here is to divide the sample into two groups, based on a distance threshold. We computed the correlation coefficient based on the partial Spearman test for the two groups for different values of the distance threshold. We found that as long as the masers with maser luminosity greater than 10^{-6} L$_\odot$ were excluded from the sample, both groups had similar correlation coefficients that were less than 0.2 (irrespective of the value used for the distance threshold) which is consistent with no correlation. However, the correlation coefficient increased significantly when including the masers with maser luminosity greater than 10^{-6} L$_\odot$. This correlation was found to be driven by the relatively high FIR luminosity of the clumps hosting the masers with high maser luminosity. Since the number of such sources is relatively small, it is not possible to draw further conclusions on whether this is a systematic effect. However, if verified, this suggests that a high FIR luminosity is required to pump methanol masers with high maser luminosity, which is consistent with the radiative pumping mechanism for the masers (Sobolev et al., 2007). The weak to non-existent correlation between the FIR luminosity and maser luminosity for the rest of the sample suggests that other factors such as the density, methanol fractional abundance and the gas kinetic temperature in the masing spots are more important to determining the maser luminosity compared to the density of pumping photons.

5.5 Caveats in the study

At the outset, we remind the reader that the majority of sources in our sample are at large distances and almost all the clumps that are seen as isolated structures at 18″ resolution are likely to fragment into smaller structures at high spatial resolution. The clump properties derived from single dish observations will be representative of the most massive core within the clump. Thus, discussion of the clump properties in the context of their hosting a methanol maser makes the implicit assumption that the maser is excited by the most massive core, which is not necessarily true. However, Chibueze et al. (2017) has explored the association of 6.7 GHz methanol masers with massive dense cores (MDC) detected with the Atacama Compact Array (ACA) at 4″ resolution, and find a direct association between the MDC and the methanol maser in 91% of their sample. A targeted 1.05 mm ALMA observtion towards the deeply embedded high-mass protocluster G11.92−0.61 by Cyganowski et al. (2017) also reveals the association of 6.7 GHz methanol masers with the massive cores in this region. These studies suggest that the 6.7 GHz methanol maser emission is indeed mostly associated with the most massive core in the clump. However, a caveat must be borne in mind that there may be a small number of cases where the maser emission may arise from a source other than the most massive core in the clump.

5.6 Mass-radius relation

The mass-radius relationship of nearby molecular cloud complexes was investigated by Kauffmann et al. (2010a,b) who then compared the relation with those of known high-mass star forming regions. This led to a suggestion that clumps with the potential to form at least one massive star follow the following empirical relationship:

$$m(r) \geq 580\ M_{\odot} \left(\frac{R_{\text{eff}}}{1\ \text{pc}} \right)^{1.33} \tag{5.9}$$

where R_{eff} is the effective radius of the source. Figure 5.10 shows the mass-radius relationship for our sample. We find that 295 out of 320 sources (92%) satisfy the criterion in the equation above. The results are somewhat different from that of Urquhart et al. (2013a, 2014b) who found a much larger fraction ($\sim$ 97%) of the methanol masers satisfying the criterion above. This discrepancy is most likely to be due to two factors. First, the photometry is different as explained in section 5.4.2. The compact source catalog used by Urquhart et al. (2013a) is sensitive to the entire submillimeter clump including the diffuse emission,

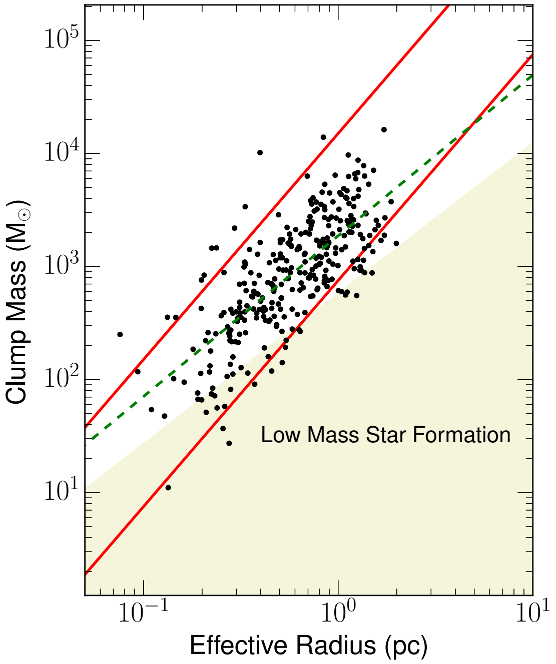

Figure 5.10: The clump mass as a function of source radius. The shaded region represents the area where the sources doesn't satisfy the Kauffman criteria. The *dashed green* line is the power law fit to the data. The upper and lower *solid red line* shows the surface densities of 1 g cm^{-2} and 0.05 g cm^{-2}, respectively.

while the photometry using HYPER is sensitive only to the compact emission, similar to the catalog of Csengeri et al. (2014). A second factor is that we have determined effective radii using the 250 μm Hi-GAL maps (which we have used as the reference wavelength for HYPER) rather than the 870 μm ATLASGAL maps. The former typically has much better signal to noise ratio leading to a better estimation of the source size. To further examine this matter, we looked at the sources in our sample that do not satisfy the Kauffmann criterion and compared the effective radius given in the compact source catalog with that of our work. We found that the effective radius is listed for only 5 out of 25 sources, the remaining being too compact for deconvolution. We found the effective radius and the enclosed flux to be larger in the compact source catalog compared to the HYPER results leading to the former satisfying the Kauffmann criterion. Although the number of sources examined here is small, it seems to confirm the hypothesis of the difference between our results and those of Urquhart et al. (2013a) as primarily arising from the differences in photometry.

Figure 5.10 also shows that the mass of the clump is correlated to its effective radius. A partial Spearman correlation test was done to remove any dependence of the correlation on distance yielding a correlation coefficient of 0.22, showing that the two quantities are weakly correlated. A least squares fit to the data gives the mass-radius relationship for our sample as

$$\log M_{\mathrm{clump}} = 3.27 + 1.42 \log R_{\mathrm{eff}} \tag{5.10}$$

This is somewhat different from the results of Urquhart et al. (2013a) who found a power law index of 1.67. The upper diagonal line in Figure 5.10 shows a line with a constant surface density of 1 g cm^{-2}, which is suggested to be the threshold for the formation of massive stars from turbulent cores (McKee & Tan, 2003). It can be seen that only a small fraction of the sources satisfy the threshold above. However, it must be borne in mind that the threshold of McKee & Tan (2003) applies to cores which will form one or two massive stars. As explained in section 5.4.1, the resolution of the Hi-GAL and ATLASGAL data is such that most of the structures seen in our images are clumps rather than cores. Using the mass-radius relation, Urquhart et al. (2013a) suggested that a surface density of 0.05 g cm^{-2} (lower red line in Figure 5.10) provided an empirical lower bound for the clump surface density required for massive star formation, although it differs from the Kauffmann criterion for low values of effective radius. A total of 293 sources in our sample have surface densities higher than 0.05 g cm^{-2} agreeing with the results of Urquhart et al. (2013a).

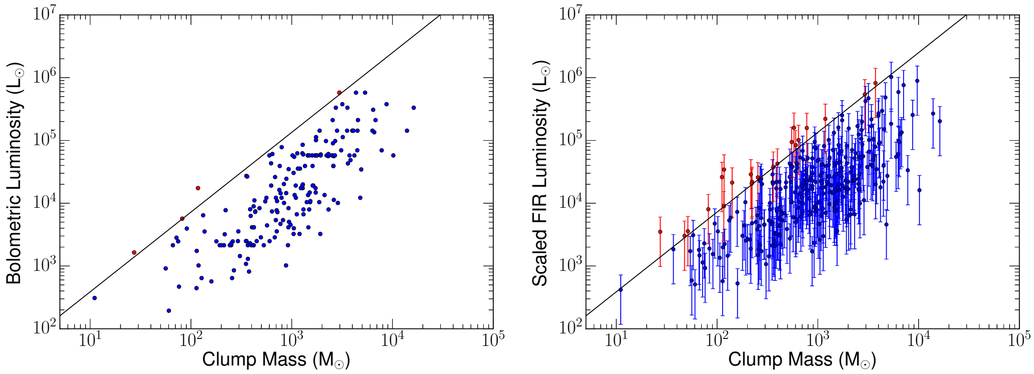

Figure 5.11: The left panel shows the bolometric luminosity of 198 sources that has MIPSGAL counterparts as a function of mass.The right panel illustrates the scaled FIR luminosities as a function of clump mass. The solid line represents the fit to the "IR-P" sources in Molinari et al. (2008). The methanol maser hosts that are in accretion phase and clearing phase are shown in *blue* and *red* points respectively.

5.7 Evolutionary stage of the source

The evolutionary state of the source can be inferred from a plot of the source luminosity as a function of mass. For a given clump mass, the luminosity is expected to increase as star formation progresses in the clump. Thus, larger values of the L/M ratio are indicative of more evolved sources. In order to construct a L-M diagram, one needs to compute the bolometric luminosity (L_{bol}) of the sources. Since 6.7 GHz methanol masers are pumped by warm dust, the maser hosts have significant emission at mid-infrared wavelengths, indicated by the presence of counterparts in the MIPSGAL survey at 24 μm and at shorter wavelengths in the GLIMPSE survey. Hence, the FIR luminosity estimated from the ATLASGAL and Hi-GAL data will be an underestimate of the bolometric luminosity.To address this issue, we constructed the full SED to near-infrared wavelengths for 198 sources using the fluxes in the MIPSGAL and GLIMPSE catalogues (the remaining sources had no counterpart in the MIPSGAL catalogue, presumably due to saturation effects). We then fit the SED from 870 μm to 3.6 μm using the models of Robitaille et al. (2007). The choice of models is not very important since the purpose of this exercise is not to determine the properties of the embedded young stellar object, but rather to obtain the bolometric luminosity by fitting the full SED from submillimeter to near infrared. We found the FIR to bolometric luminosity ratio to have a median value of 0.31 with a standard deviation of 0.23.

The left panel Figure 5.11 shows the bolometric luminosity as a function of mass for the 198 sources whose SED was fit using the Robitaille et al. (2007) models. The right panel shows the FIR luminosity that is scaled by the ratio of bolometric to FIR luminosity as a function of mass. A partial Spearman correlation test to remove the dependence on distance gives the correlation coefficient between bolometric luminosity and mass (Figure 5.11, left panel) to be 0.43. The same correlation test when performed on scaled FIR luminosities and clump mass for the entire sample (Figure 5.11, right panel) yielded a correlation coefficient of 0.42 with a p value $\ll 0.05$ showing that the bolometric luminosity is weakly correlated to the mass of the clump. The correlation is however smaller than that observed by Urquhart et al. (2013a) who observed a correlation coefficient of 0.78.

Molinari et al. (2008) constructed a model for the evolution of a source in the L-M diagram based on the turbulent core model of McKee & Tan (2003). This model shows the evolution to be in two stages – in the initial phase, the central star accretes matter from the envelope with the accretion rate being dependent on the instantaneous stellar mass. Thus, as the stellar mass increases with time, so does the accretion rate leading to this phase being referred to as the accelerating accretion phase. During this phase, the envelope mass is almost constant while the luminosity of the source increases leading to vertical tracks in the L-M diagram (see Figure 9 of Molinari et al. 2008). This is followed by the envelope clean-up phase wherein the envelope is expelled through outflows and accretion onto lower mass objects in the same clump. Since the luminosity is dominated by that of the massive star (which has reached its final mass), this phase corresponds to horizontal tracks to the left in the L-M diagram. One of the attractive features of this model is that it is a natural extension of the evolution in the low-mass regime (Saraceno et al., 1996).

Although we do not have the evolutionary tracks modelled by Molinari et al. (2008), a rough boundary between the accretion phase and envelope clearing phase is obtained by fitting the "IR-P" sources (the primary sources in the targeted fields whose SEDs can be fit with a model of an embedded zero age main sequence star) in Molinari et al. (2008). This is shown as a solid line in the left and right panels of Figure 5.11, with sources below and above this line being color coded as blue and red respectively. Comparing this figure with Figure 9 of Molinari et al. (2008) shows two prominent results: First, almost all sources including the lowest mass source lie in the high-mass regime spanned by the "IR-P" sources of Molinari et al. (2008). The other prominent result is that most of the sources ($\sim$ 93%) are in the accretion phase. It has to be noted that in the L_{bol}-M plot shown in the left panel of Figure 5.11, almost all the sources lie in accretion phase. However, this is most likely a selection effect due to SEDs being fit for only those sources that have a counterpart in the MIPSGAL catalogue. The lack of a counterpart in the MIPSGAL catalogue is most likely due to the source being saturated at 24 μm and thus in a later evolutionary phases.To verify this hypothesis, we constructed SEDs for 20 sources that had no counterpart in the MIPSGAL catalogue using fluxes from the MSX (Benjamin et al., 2003) and GLIMPSE (Egan & Price, 1996) catalogues. We found about 15% of the sources to be in the clearing phase which is consistent with the overall fraction of ~ 10% to be in the clearing phase based on scaled FIR luminosities.

The results above however must be treated with caution. First, it is based on the turbulent core model for massive star formation, and alternate theories exist for forming massive stars (e.g. competitive accretion model of Bonnell et al. 2001). Second, the L-M diagram does not give information about the surface density of a clump which is one of the factors that determine whether or not it will form a massive star. Thus, some sources which fail the Kauffmann et al. (2010a) criterion based on the clump masses and radii are located in the high-mass end of the L-M diagram. However, bearing these caveats in mind, the overall results including statistics are consistent with the findings of Pandian et al. (2010) wherein most 6.7 GHz methanol masers are associated with rapidly accreting massive stars, with ~ 80% being in phases earlier than ultracompact H II regions (i.e. in the accelerating accretion phase).

5.8 Are 6.7 GHz methanol masers exclusively associated with massive star formation?

According to Lada & Lada (2003) and Motte et al. (2003), stellar clusters form from clumps with masses more than 100−1000 $M_\odot$ and radii 0.5−1 pc. Assuming that the stars formed in clusters follow the initial mass function of Kroupa (2001), the total stellar mass in a cluster with at least one 8 $M_\odot$ star is around 110 $M_\odot$. Assuming a star formation efficiency of 30%, the minimum mass that a clump must have to form a cluster with at least one massive star is 360 $M_\odot$. In our sample, 187 sources have effective radii above 0.5 pc, and 179 out of 187 have masses more than 360 $M_\odot$. Examining sources with effective radii below 0.5 pc, the masses range from 11 to 1.02×10^4 $M_\odot$. One can thus conclude that most of the 6.7 GHz methanol hosts have masses sufficient to form at least one massive star.

However, there is a small population of 6.7 GHz methanol masers which may be associated with intermediate or low-mass stars. For example, the minimum mass in our sample is 11 $M_\odot$ which is likely to form a star < 8 $M_\odot$ depending on the fraction of mass that goes to the central star. A similar conclusion was inferred by Urquhart et al. (2013a) although their masses were obtained by assuming a constant dust temperature of 20 K. The survey Minier et al. (2003) towards 175 low-mass young stellar objects detected 6.7 GHz methanol maser emission towards the source NGC 2024: FIR 4. While the nature of this source has been debated (e.g. Choi et al. 2015 and references therein), Choi et al. (2015) conclude that the source is a low-mass protostar based on analysis of several archival data sets from the Very Large Array. The minimum luminosity of a source that is associated with 6.7 GHz maser emission also appears to be somewhat lower than the 10^3 $L_\odot$ that is estimated by Bourke et al. (2005).

The mechanism by which 6.7 GHz methanol masers are excited by low-mass protostars is however not clear. The dust temperatures required to pump the line are expected to be at distances where the H_2 number density is high enough to quench maser action in low-mass protostars (Pandian et al., 2008). Thus, 6.7 GHz maser action in low-mass protostars may be restricted to select geometries wherein the physical conditions for maser pumping are satisfied. This may also be the reason why the vast majority ($> 95\%$) of the methanol masers are associated with high-mass star formation.

5.9 A special note on distances

The most reliable way to estimate the distance to Galactic sources is trigonometric parallax. Due to difficulties in measuring the trigonometric parallax to distant sources, especially in the Galactic disk where extinction is severe, distances are commonly estimated kinematically by assuming that the observed radial velocity is a result of differential rotation of the Milky Way. However, the kinematic distance can be discrepant from the true distance when proper motions, such as from spiral density waves, are significant. The method of calculating distances from Galactic kinematics also suffers from an ambiguity between two distances in the inner Galaxy, requiring use of additional techniques such as H I Self Absorption (HISA) in order to distinguish between the two values.

As mentioned in section 5.2, the distances to the sources in our sample are taken from Urquhart et al. (2013b); Reid et al. (2014); Pandian et al. (2009) and Green et al. (2017). Green & McClure-Griffiths (2011) uses the technique of H I Self Absorption (HISA) assuming a flat rotation curve (Reid et al., 2009; McMillan & Binney, 2010) to determine the kinematic distances towards 442 6.7GHz methanol masers. The distances reported in Urquhart et al. (2013a) is a modified version of those presented in Green & McClure-Griffiths (2011) in that the Galactic rotation curve of Brand & Blitz (1993) is assumed to account for the significant variations between the model-derived tangent velocities and the empirically derived values from the H I termination velocities in the fourth quadrant.

We have made use of the distances of Urquhart et al. (2013a) instead of those in Green & McClure-Griffiths (2011) for our analysis. Green et al. (2017) presents the distance towards an additional 202 methanol maser sources using the HISA method.

Recently, the distances to a large number of high-mass star forming regions have been estimated using trigonometric parallax with Very Long Baseline Interferometry (e.g. Reid et al. 2014 and references therein). Since high-mass star forming regions are expected to be good tracers of spiral arms in galaxies, Reid et al. (2016) suggested use of a Bayesian approach to assign sources to spiral arms based on their location and radial velocities and comparing with spiral arm signatures as seen in CO and H I surveys. Reid et al. (2016) claim that the use of this method should significantly improve the accuracy and reliability of distance estimates to sources that are good tracers of spiral structure. Green et al. (2017) apply this technique to estimate distances to the entire 972 methanol maser sources that are catalogued to date with the consideration that 6.7 GHz methanol masers are mostly associated with high-mass star formation, which trace spiral structure.

We have used the new distances of Green et al. (2017) to test whether any of the results derived in the previous sections are significantly altered. We first test whether the distances adopted from earlier references are significantly different from that of Green et al. (2017) (methods 1 and 2 respectively hereafter). We compared the two sets of distances with a t-test, which yielded a t-value of 1.27 with a significance value of 0.20. Thus it can be inferred that the distance values calculated using these two methods are not significantly different. This is confirmed by examining the mean and median distances from the two methods – while method 1 gives a mean and median distance of 8.03 kpc and 8.55 kpc, the values from method 2 are 8.07 kpc and 8.25 kpc respectively. A histogram showing the distribution of distance values are shown in Figure 5.12.

We further analysed the differences in physical parameters computed using distances from methods 1 and 2. The left panel of Figure 5.13 shows a comparison of the mass distribution from method 1 (green hatched histogram) and method 2 (solid red histogram). As expected from the differences in the distance distribution, the mass distribution from the two methods are slightly different. However, the overall statistics are similar – while method 1 gives a mean and median mass of 1570 $M_\odot$ and 930 $M_\odot$, the respective values obtained by distances from method 2 are 1785 $M_\odot$ and 925 $M_\odot$. A t-test between the two mass distributions gives a t-value of 0.71 with a significance value of 0.48. Thus, there is no significant difference in the distribution of masses computed using distances from the two methods.

The right panel of Figure 5.13 shows the mass-radius relation computed using distances

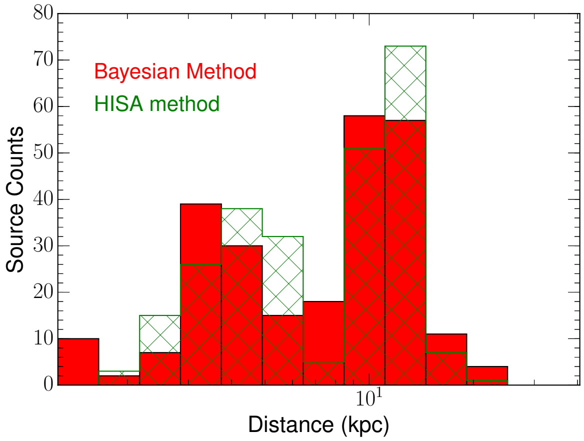

Figure 5.12: Distance distribution based on Method 1 and 2 described in section 5.9

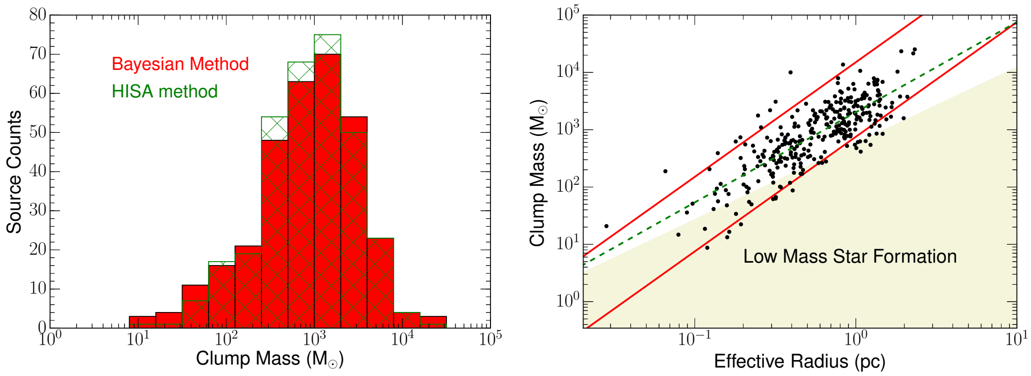

Figure 5.13: Mass distribution using two methods (left panel) and (b) MR plot obtained using the distances obtained with the approach presented by Reid et al. (2016)(right panel).The *dashed green line* represents the power law fit to the data. The upper and lower *solid red line* shows the surface densities of 1 g cm^{-2} and 0.05 g cm^{-2}, respectively.

from method 2. With method 2, 287 out of 320 sources satisfy the Kauffmann criterion for potential to form massive stars. This is comparable to method 1 wherein 295 out of 320 sources satisfy the Kauffmann criterion. Thus, although the distances from method 1 are different from that of method 2, the overall statistical properties of sources associated with 6.7 GHz methanol masers are similar between the two methods. We are thus unable to make any distinction regarding accuracy of distances when considering the entire sample statistically.

5.10 Summary

We have constructed SEDs from 870 μm to 70 μm for 320 6.7 GHz methanol masers using data from the ATLASGAL and Hi-GAL surveys. The SEDs from 870 μm to 160 μm were fit with single component grey body models. We observe a mean dust temperature of 22 K confirming the later evolutionary stage of the maser sources in comparison to infrared dark clouds, with some sources showing temperatures as high as 48 K. Almost 92% of the methanol maser sources satisfy the Kauffmann criterion for potential to form massive stars. A comparison of the mass-luminosity diagram of the sample with simple evolutionary tracks from the turbulent core model suggest that most methanol masers are associated with massive young stellar objects with over 90% in early evolutionary stages of accelerating accretion. However, there also appears to be a small population of sources that are likely to be associated with intermediate or low-mass stars suggesting that the association between high-mass star formation and methanol maser emission is not exclusive. We have also compared the physical parameters inferred from the use of the new Bayesian method of distance computation with that of the traditional kinematic distances and found no statistical differences in the same.

Chapter 6

Chemical environments of 6.7 GHz methanol maser hosts

6.1 Introduction*

In the previous chapter (hereafter Work I), we analysed the evolutionary stage of 320 sources associated with 6.7 GHz methanol masers using spectral energy distributions of dust continuum maps. We concluded that while a majority of our sources are more evolved as compared to infrared dark clouds, they are still in an early evolutionary stage. This result is also in agreement with several other previous studies (e.g., Minier et al., 2001; Ellingsen, 2006b; Pandian et al., 2010; Billington et al., 2019, and references therein). Since the chemical composition in star forming environments is highly sensitive to the physical conditions (Gerner et al., 2014), it is of interest to examine whether the chemical properties of the methanol maser hosts are in accordance with them tracing an early phase of massive star formation. Although there have been many studies that focus on the chemistry of high mass star forming regions (e.g. Sanhueza et al., 2012; Hoq et al., 2013; Miettinen, 2014; Zhang et al., 2016), chemical processes surrounding 6.7 GHz methanol maser hosts are not much discussed yet. For example, Saral et al. (2018) investigated the physical and chemical properties of 30 high mass star forming clumps, the chemistry of which was traced using four molecular species: N_2H^+, HCO^+, HCN and HNC. This was used to classify the clumps into protostellar candidates, young stellar objects (YSOs), and massive star forming regions (MSF), the latter containing H II regions, radio bright sources and methanol masers.

---

*This chapter is based on the published paper: Pauslon & Pandian 2022 [Sonu Tabitha Paulson, Jagadheep D Pandian, Chemical environments of 6.7 GHz methanol maser sources, Monthly Notices of the Royal Astronomical Society, Volume 509, Issue 3, January 2022, Pages 3677–3692]. The paper is reproduced here with minor changes.

The MALT90 survey (Jackson et al., 2013) carried out a comprehensive study of molecular emission towards 3246 high-mass clumps detected in the ATLASGAL survey. It was found that ratios of integrated line intensities of several molecules such as HCO^+/HNC and HCN/HNC showed systematic variation with the evolutionary stage of the source (Rathborne et al., 2016). A similar study targeting a much wider range of molecules towards ~600 high mass clumps, was performed by Urquhart et al. (2019). They also discovered that several line ratios were probes of the evolutionary state of the source. However, a direct comparison to chemical models is not possible since the studies of both Rathborne et al. (2016) and Urquhart et al. (2019) focused on integrated line intensities rather than column densities. Since the column density shows additional dependence on the excitation temperature and the optical depth, one needs to carry out radiative transfer modelling of the molecular spectra in order to compare the results with chemical models. Since all the studies focused on the evolutionary state in the context of massive star formation, there is a lack of proper knowledge on the chemistry of methanol maser sources alone.

In this chapter, we present the molecular study of 68 6.7 GHz methanol maser sources using the MALT90 data. We also discuss whether the evolutionary phase of methanol maser hosts inferred from chemical signatures aligns with results in Work I.

6.2 Source Selection And Data Analysis

6.2.1 MALT90 Data

The source sample of the present study was chosen among the sources studied in Work I, that have MALT90 data available. The MALT90 survey aims at characterizing the physical and chemical properties of massive star formation in our Galaxy. The survey is targeted towards 2014 compact sources detected in the ATLASGAL survey (Schuller et al., 2009) covering Galactic longitude ranges $300° < l < 357°$ and $3° < l < 20°$, with the Mopra Spectrometer (MOPS)* arrayed on the Mopra 22 m telescope. The survey obtained $3' \times 3'$ maps around each source covering a total of 3264 high-mass clumps. MALT90 has mapped 16 molecular lines simultaneously at frequencies near 90 GHz with a velocity resolution of 0.11 km s^{-1}. The 16 spectral lines and their rest frequencies are shown in Table 6.1 (Jackson et al., 2013). The beam size of Mopra is $38''$ at 86 GHz, with a main beam efficiency of 0.49 (Ladd et al., 2005). Among the 320 sources listed in Work I, 138 of them were found

---

*The University of New South Wales Digital Filter Bank used for the observations with the Mopra Telescope was provided with support from the Australian Research Council.

Table 6.1: Spectral lines in MALT90 survey

Transition	Frequency (MHz)	Tracer
HCO^+(1–0)	89188.526	Density; Kinematics
$H^{13}CO^+$(1–0)	86754.330	Optical depth, Column density, V_{LSR}
N_2H^+(1–0)	93173.772	Density, chemically robust
HCN (1–0)	88631.847	Density
HNC(1–0)	90663.572	Density; Cold chemistry
^{13}CS (2–1)	92494.303	Optical depth, Column density, V_{LSR}
CH_3CN 5(0)–4(0)	91987.086	Hot core
HC_3N (10–9)	90978.989	Hot core
$^{13}C^{3}4S$ (2–1)	90926.036	Optical depth, Column density, V_{LSR}
$HC^{13}CCN$ (10–9)	90593.059	Hot core
HNCO 4(1,3)–3(1,2)	88239.027	Hot core
HNCO 4(0,4)–3(0,3)	87925.238	Hot core
C_2H (1–0) 3/2–1/2	87316.925	Photodissociation region
$HN^{13}C$ (1–0)	87090.859	Optical depth, Column density, V_{LSR}
SiO (1–0)	86847.010	Shock/outflow

to be included in the MALT90 survey. We have further narrowed down our study to sources that have strong detections (S/N $\geq$ 3 in the moment zero map) in HCO^+(1-0), HCN(1-0), HNC(1-0) and N_2H^+(1-0). These molecular transitions are considered the brightest of the transitions covered by the MALT90 survey and have shown to be good tracers of density. In order to verify the association of the methanol masers with the MALT90 clump, we have compared the peak velocity of maser emission with that of molecular emission from the clump. We find that the velocity offsets are less than 10 km s^{-1}, with the mean offset being 3 km s^{-1}, which is similar to that observed in earlier studies (e.g. Billington et al., 2019). We investigated the spatial matching of methanol maser sites and MALT90 clumps by analysing the differences in their positions, obtained from their catalogues. If the angular offset was found to be less than half of the MALT90 beam size, the maser is considered to be physically associated with the clump. If more than one clump is found to be matched with a particular maser, we chose the clump having the least angular offset as the physically associated one. The angular offsets between maser sites and clumps for the 68 MM sources were typically less than 6 arcseconds. This suggests that all the methanol masers in this study are indeed physically associated with the MALT90 clumps.

The molecular line modelling was performed in CASSIS (Caux et al., 2011), under the assumption of local thermodynamic equilibrium (LTE). CASSIS gives the best fit estimates for molecular column density, excitation temperature, line width and local standard of rest (LSR) velocity based on the initial parameters provided for the same. The values of initial parameters are obtained by fitting the spectra using the CLASS program of the GILDAS[†] software package. Prior to the fitting, the spectrum of each pixel in the data cube is extracted and data were converted from antenna temperatures to main beam temperatures by dividing it by main beam efficiency ($\eta = 0.49$). For the molecules that exhibit hyperfine components (HCN and N_2H^+), fitting is performed using method HFS (hyperfine-structure fit). For the molecules that do not have hyperfine satellites (HCO^+ and HNC), method GAUSS[‡] (Gaussian fit) is employed. The fit performed using method HFS gives the optical depth in addition to the LSR velocity and FWHM of the spectral line, while the method GAUSS gives an estimate of only the latter two parameters. We estimate the excitation temperature of the line using the antenna equation

$$T_{mb} = f[J(T_{ex}) - J(T_{bg})](1 - e^{-\tau_\nu}) \tag{6.1}$$

where T_{mb} is the main beam temperature, f is the filling factor, τ_ν is the optical depth of the line, T_{bg} is the background temperature, and $J(T)$ is defined by

$$J(T) = \frac{h\nu}{k}\frac{1}{e^{h\nu/kT} - 1} \tag{6.2}$$

For lines whose optical depth is known through fitting of hyperfine structure, Equation (6.1) can be used to determine the excitation temperature. The excitation temperature can also be determined for lines that are known to be very optically thick by assuming τ to be infinity in Equation (6.1). For the molecules that do not possess hyperfine transitions, we followed the method described in Sanhueza et al. (2012) to estimate the optical depths. The process essentially involves computing the ratio of peak main beam temperatures of an optically thick and optically thin line and then equating it with the ratio of their optical depths. Once we obtain the optical depths, we estimate their excitation temperatures using Equation (6.1).

In order to study the chemical evolution within the maser host, we performed a pixel-by-pixel spectral energy distribution (SED) fitting of molecular data cubes. For this purpose, we chose sources where at least 30 pixels in the moment zero map of MALT90, have S/N ratio ≥ 5. This results in a sample of nine sources that are used for what we refer to as the

---

[†] http://www.iram.fr/IRAMFR/GILDAS

[‡] A detailed description of method HFS and method GAUSS can be found here, http://www.iram.fr/IRAMFR/GILDAS/doc/html/classhtml/class.html

"pixel-by-pixel analysis". We also aim to study properties of methanol maser hosts from a chemical perspective compared to sources belonging to different evolutionary stages. Since this cannot be accomplished with just 9 sources, we expanded our source sample to the ones where the brightest pixel in the moment zero map has S/N > 3. It is to be noted that the peak signal to noise ratio of individual spectra are much higher since the moment zero map is obtained from the total intensity of the full spectrum of the spectrometer sub-band, with most spectral channels being devoid of any signal. We call this as the statistical analysis of maser sources. 59 sources, apart from the nine sources listed above, were chosen for the latter approach. In total, our sample constitutes of 68 6.7 GHz methanol maser sources (hereafter MM sources), where we carry out a pixel-by-pixel analysis (approach I) for nine sources and a statistical analysis (approach II) for the entire source sample. A comparison of the distances and methanol maser luminosities of our sample with that of the 320 sources in Work I as well as the 972 sources in the entire MMB catalogue shows our sample to be representative of the methanol maser population in the Galaxy with no systematic biases being introduced by our sample selection procedure (see Appendix B.2). The MMB names and ATLASGAL names of the entire sample of sources are listed in Table 6.2. Among the 68 maser sources, we have 51 N_2H^+ detections, 59 HCO^+, 57 HNC and 52 HCN detections.

6.2.2 Dust continuum data

The molecular abundance is calculated by dividing the molecular column density by the H_2 column density. The H_2 column density is determined using the spectral energy distribution of the dust continuum emission. We made use of the 70, 160 μm (PACS) as well as 250, 350 and 500 μm (SPIRE) data, observed as a part of the Herschel infrared Galactic plane survey (Hi-GAL, Molinari et al. (2010)). The 870 μm data is obtained from the ATLASGAL survey (Schuller et al., 2009). The maps at different wave bands have different data units, resolution and plate scales. Moreover, in order to calculate the molecular abundances, it is important to ensure that the H_2 column densities are determined at the same world coordinates as that of the MALT90 data. We hence processed the data using the Herschel Interactive Processing Environment (HIPE)[§] using the following steps: First, the surface brightness unit of all the images were converted to Jy pixel^{-1} using the task 'Convert Image Unit'. The data were then projected onto a common grid, with the pixel size and resolution of the MALT90 data cube. This made sure that each coordinate of the dust continuum

---

[§] http://herschel.esac.esa.int/hipe/

MMB names	ATLASGAL names	MMB names	ATLASGAL names
G006.189-0.358	AGAL006.188-00.357	G338.497+0.207	AGAL338.497+00.207
G010.724-0.334	AGAL010.724-00.332	G338.566+0.110	AGAL338.567+00.109
G010.958+0.022	AGAL010.957+00.022	G338.850+0.409	AGAL338.851+00.409
G011.034+0.062	AGAL011.034+00.061	G339.282+0.136	AGAL339.283+00.134
G012.625-0.017	AGAL012.623-00.017	G339.476+0.185	AGAL339.476+00.184
G012.889+0.489	AGAL012.888+00.489	G339.582-0.127	AGAL339.584-00.127
G013.179+0.061	AGAL013.178+00.059	G339.622-0.121	AGAL339.623-00.122
G014.631-0.577	AGAL014.632-00.577	G340.249-0.046	AGAL340.249-00.046
G305.799-0.245	AGAL305.799-00.244	G340.785-0.096	AGAL340.784-00.097
G309.384-0.135	AGAL309.384-00.134	G341.218-0.212	AGAL341.217-00.212
G311.947+0.142	AGAL311.947+00.142	G341.276+0.062	AGAL341.274+00.061
G324.923-0.568	AGAL324.923-00.569	G346.480+0.221	AGAL346.481+00.221
G326.608+0.799	AGAL326.607+00.799	G346.481+0.132	AGAL346.481+00.131
G326.859-0.677	AGAL326.859-00.677	G347.628+0.149	AGAL347.627+00.149
G329.469+0.503	AGAL329.469+00.502	G348.884+0.096	AGAL348.886+00.097
G330.283+0.493	AGAL330.284+00.492	G349.092+0.105	AGAL349.091+00.106
G331.134+0.156	AGAL331.134+00.156	G350.015+0.433	AGAL350.016+00.432
G331.342-0.346	AGAL331.342-00.347	G350.520-0.350	AGAL350.521-00.349
G331.442-0.187	AGAL331.442-00.187	G350.686-0.491	AGAL350.687-00.491
G331.710+0.603	AGAL331.709+00.602	G351.688+0.171	AGAL351.689+00.172
G332.295-0.094	AGAL332.296-00.094	G352.604-0.225	AGAL352.604-00.226
G332.364+0.607	AGAL332.364+00.604	G352.855-0.201	AGAL352.856-00.202
G332.560-0.148	AGAL332.559-00.147	G354.615+0.472	AGAL354.616+00.472
G332.942-0.686	AGAL332.942-00.686	G354.724+0.300	AGAL354.724+00.301
G333.163-0.101	AGAL333.161-00.099	G355.538-0.105	AGAL355.538-00.104
G333.387+0.032	AGAL333.386+00.032	G013.657-0.599^a	AGAL013.658-00.599
G336.809+0.119	AGAL336.808+00.119	G318.948-0.196^b	AGAL318.948-00.197
G336.957-0.225	AGAL336.958-00.224	G326.474+0.703^c	AGAL326.474+00.702
G336.958-0.977	AGAL336.958-00.977	G327.393+0.199^d	AGAL327.393+00.199
G337.097-0.929	AGAL337.098-00.929	G330.876-0.384^e	AGAL330.876-00.384
G337.201+0.114	AGAL337.201+00.114	G333.314+0.105^f	AGAL333.314+00.106
G337.258-0.101	AGAL337.258-00.101	G335.586-0.289^g	AGAL335.586-00.291
G337.300-0.874	AGAL337.301-00.874	G338.281+0.541^h	AGAL338.281+00.542
G337.632-0.079	AGAL337.632-00.079	G353.463+0.563^i	AGAL353.464+00.562

Table 6.2: The MMB and ATLASGAL names of the 68 sources studied in this work. The nine sources considered for pixel-by-pixel study are indicated by alphabets a to i. These nine sources are referred to as G13, G318, G326, G327, G330, G333, G335, G338 and G353 respectively

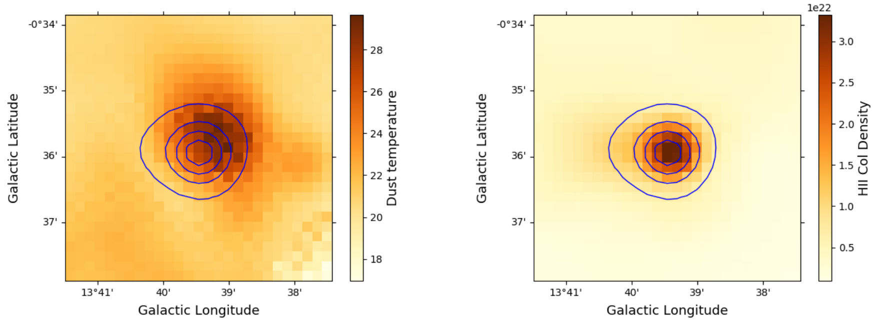

Figure 6.1: An example of temperature(left) and H_2 column density (right) maps obtained by pixel-by-pixel fitting of dust continuum data for the source G13. The SPIRE 250 μ m emission is overlaid as contours.

map corresponds to the same location in the MALT90 data cube. The plug-in 'Photometric Convolution' is used for this purpose. A constant background, estimated from the mean continuum in a region devoid of source emission, was then subtracted from the data. The pixels were then fit using the standard grey body model. We derive the hydrogen column density ($N(H_2)$) using the equations discussed in Work I. The maps obtained for source G13 is shown in Figure 6.1 as an example.

For the pixel-by-pixel analysis, we modelled the spectra corresponding to each pixel of the MALT90 data cube and then compared with the dust temperatures and H_2 column densities of same pixels obtained by pixel-by-pixel SED fitting of dust continuum maps. For the statistical study, we modelled the brightest pixel in the molecular data cube (brightest in the moment zero map) and compared with the H_2 column density corresponding to that pixel. The dust temperatures for the latter are taken from Work I.

6.3 Results

We present the results obtained from pixel-by-pixel study as well as the statistical study of the sources. We mainly focus on the column densities and abundances of molecules obtained after line modelling. We also briefly account for the integrated line intensities of the molecular emissions. The uncertainties in the column densities and abundances obtained are typically less than 20 per cent.

Table 6.3: Column densities and abundances.

Quantity	Min	Max	Mean	Std.	Median
N_I(HCN)	7.56(12)	9.77(13)	3.39(13)	1.97(13)	2.98(13)
X_I(HCN)	1.51(-10)	1.32(-8)	1.74(-9)	1.81(-9)	1.29(-9)
N_{II}(HCN)	1.20(13)	1.06(14)	3.21(13)	2.11(13)	2.66(13)
X_{II}(HCN)	1.68(-10)	1.06(-8)	2.27(-9)	2.05(-9)	1.56(-9)
N_I(HNC)	1.59(12)	1.57(14)	2.14(13)	1.95(13)	1.45(13)
X_I(HNC)	4.49(-11)	2.45(-8)	1.47(-9)	1.70(-9)	1.14(-9)
N_{II}(HNC)	5.25(12)	8.89(13)	2.12(13)	5.76(12)	1.83(13)
X_{II}(HNC)	2.24(-10)	4.64(-9)	1.28(-9)	8.27(-10)	9.47(-10)
N_I(HCO^+)	2.72(12)	9.69(13)	1.83(13)	1.81(13)	1.20(13)
X_I(HCO^+)	1.76(-10)	1.53(-8)	1.37(-9)	1.81(13)	1.06(-9)
N_{II}(HCO^+)	4.36(12)	4.82(13)	1.80(13)	1.16(13)	1.42(13)
X_{II}(HCO^+)	1.35(-10)	4.79(-9)	1.26(-9)	1.00(-9)	9.61(-10)
N_I(N_2H^+)	5.29(12)	9.25(13)	2.97(13)	1.72(13)	2.50(13)
X_I(N_2H^+)	1.33(-10)	7.84(-9)	1.85(-9)	1.41(-9)	1.42(-9)
N_{II}(N_2H^+)	2.31(11)	6.84(13)	2.97(13)	1.51(13)	2.48(13)
X_{II}(N_2H^+)	1.58(-11)	4.09(-9)	1.81(-9)	1.01(-9)	1.53(-9)

a(b) indicates a×10^b. N and X represents column density and abundance respectively. Subscripts I and II indicates pixel-by-pixel study and statistical study. The full table with best fit values, obtained after fitting the spectra towards the brightest pixel of sources, is given in Appendix B.1.

Table 6.4: Spearman correlation coefficients.

Molecules	Pix-by-pix	Stat
HCN	-0.62	-0.64
HNC	-0.53	-0.54
HCO^+	-0.61	-0.62
N_2H^+	-0.61	-0.55

Correlation coefficients between different molecular species and H_2 column densities for pixel-by-pixel study and statistical study.

6.3.1 Dust temperatures and H_2 column densities

The dust temperatures obtained after pixel-by-pixel SED fitting ranges from 13 to 49 K with a mean value 24 K. The H_2 column densities derived for each pixel lie in the range, $(0.16 - 10.4) \times 10^{22}$ cm^{-2} with an average value of 2.68×10^{22} cm^{-2}. For the statistical analysis, the dust temperature (taken from Paper I) ranges between 13 and 36 K with a mean value of 23 K and the H_2 column densities lie in the range $(0.25 - 6.98) \times 10^{22}$ cm^{-2} with an average value of 1.86×10^{22} cm^{-2}. These values are comparable to what are typically seen in massive star forming regions. For example, the dust temperature and H_2 column density values derived by Hoq et al. (2013) for 332 high mass clumps are 6.7−41.5 K (22 K on average) and $(0.2 - 93.99) \times 10^{22}$ cm^{-2} (4.89×10^{22} cm^{-2} on average) respectively. The dust temperature values are also consistent with what have been reported by Guzmán et al. (2015) for MALT90 clumps (See Appendix B.3).

6.3.2 Optical depths and excitation temperatures

The fits to the hyperfine structure of HCN (1−0) show the line to be optically thick with typical values of τ being greater than 5. In contrast, N_2H^+ (1−0) was found to be typically optically thin, with the optical depth ranging from 0.1 to 1.2 and a mean value of 0.3. We derived the optical depths for HCO^+ and HNC lines using the optically thin N_2H^+ line, as their optically thin isotopologues ($H^{13}CO^+$ and $HN^{13}C$) were undetected in our sources and found both lines to be optically thick. The excitation temperatures calculated for HCN, ranges from 4 to 10 K. We employed the same excitation temperatures for modelling HNC as well, as the HCN and HNC molecules show a tight correlation in their integrated intensity. The two molecules are also observed to have formed via similar chemical channels. The excitation temperatures of HCO^+ and N_2H^+ range from 6−12 K and 17−30 K respectively.

6.3.3 Anomalies in the HCN spectra

Most of the HCN spectra modelled in this work exhibit anomalous and asymmetric line profiles. The complex line profiles are mostly due to hyperfine anomalies observed in the $J = 1 - 0$ line, and also in part due to complex motions within the source. Anomalies in the hyperfine structure of HCN have been observed by several authors to date (Guilloteau & Baudry, 1981; Loughnane et al., 2012; Mullins et al., 2016). The $J = 1 - 0$ transition of HCN has three hyperfine lines ($F = 1 - 0, 1 - 1$ and $2 - 1$). Under LTE conditions, the ratios of the relative intensities of the two nearby hyperfine lines of HCN(1-0), are in the form 1:5:3.

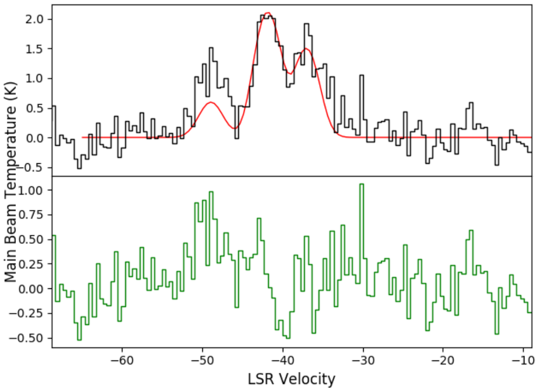

Figure 6.2: An anomalous HCN line profile. The fit obtained (assuming LTE) is shown in red. The fit residual is marked in green.

If the spectrum is anomalous, we observe a boosted $F = 0 - 1$ hyperfine line. This line can also be broader than the rest of the hyperfine components. Figure 6.2 shows an example of an anomalous HCN spectrum taken from our sample. While the anomalous spectra could in principle be modelled using non-LTE radiative transfer codes such as MOLFIT (Möller et al., 2017), such an analysis is beyond the scope of our present work. We have modelled the HCN spectra by fitting the $F = 1 - 1$ and $2 - 1$ components under assumption of LTE. The poor fit to the $F = 0 - 1$ hyperfine line is likely to lead to systematic uncertainties in the derived column densities. In order to account for this, we calculated the ratios of area under the hyperfine satellites of the spectrum and the fit. In almost all the cases, the area under the CASSIS fit is $\sim$ 20 per cent less than area under the actual spectrum. Hence, we infer that the column densities obtained for HCN are underestimated by 20 per cent.

6.3.4 Molecular column densities and abundances

Table 6.3 shows the minimum, maximum, mean and median values of molecular column densities and abundances for both the pixel-by-pixel and statistical methods (indicated by I and II respectively). We can see that the column densities and abundances obtained from two methods are very similar to each other. Miettinen (2014) reports a similar range for HCN, HNC, HCO^+ and N_2H^+ column densities and abundances for their sample of 35 massive clumps, though their mean HCN and N_2H^+ column density is an order of magnitude higher than our values. While the N_2H^+ column densities and abundances for all the 51 sources fall in a range similar to that reported by Hoq et al. (2013) and Saral et al. (2018), the HCO^+ column densities show some deviations. The HCO^+ column densities derived by Hoq et al. (2013) for their sample of 333 massive clumps, $(0.4 - 35.8) \times 10^{14}$ cm^{-2} $(3.57 \times 10^{14}$

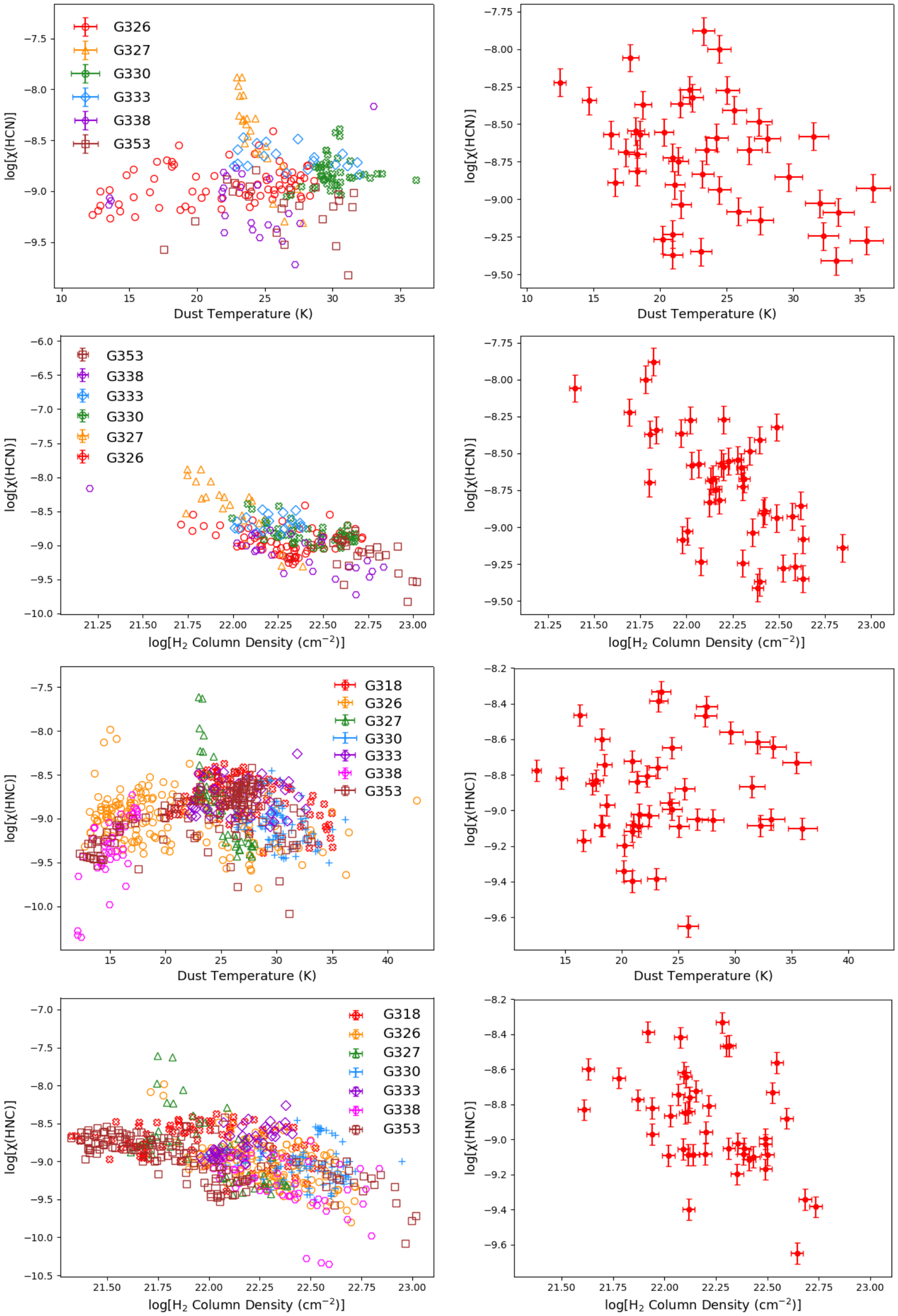

Figure 6.3: Variation of HCN and HNC abundance (X(HCN) and X(HNC)) with respect to dust temperature and H_2 column density. The panels in the left column show the plots for pixel-by-pixel study whereas those in the right column depict the results for statistical study. For the pixel-by-pixel case, only a characteristic error bar is shown in its top corner for the sake of clarity.

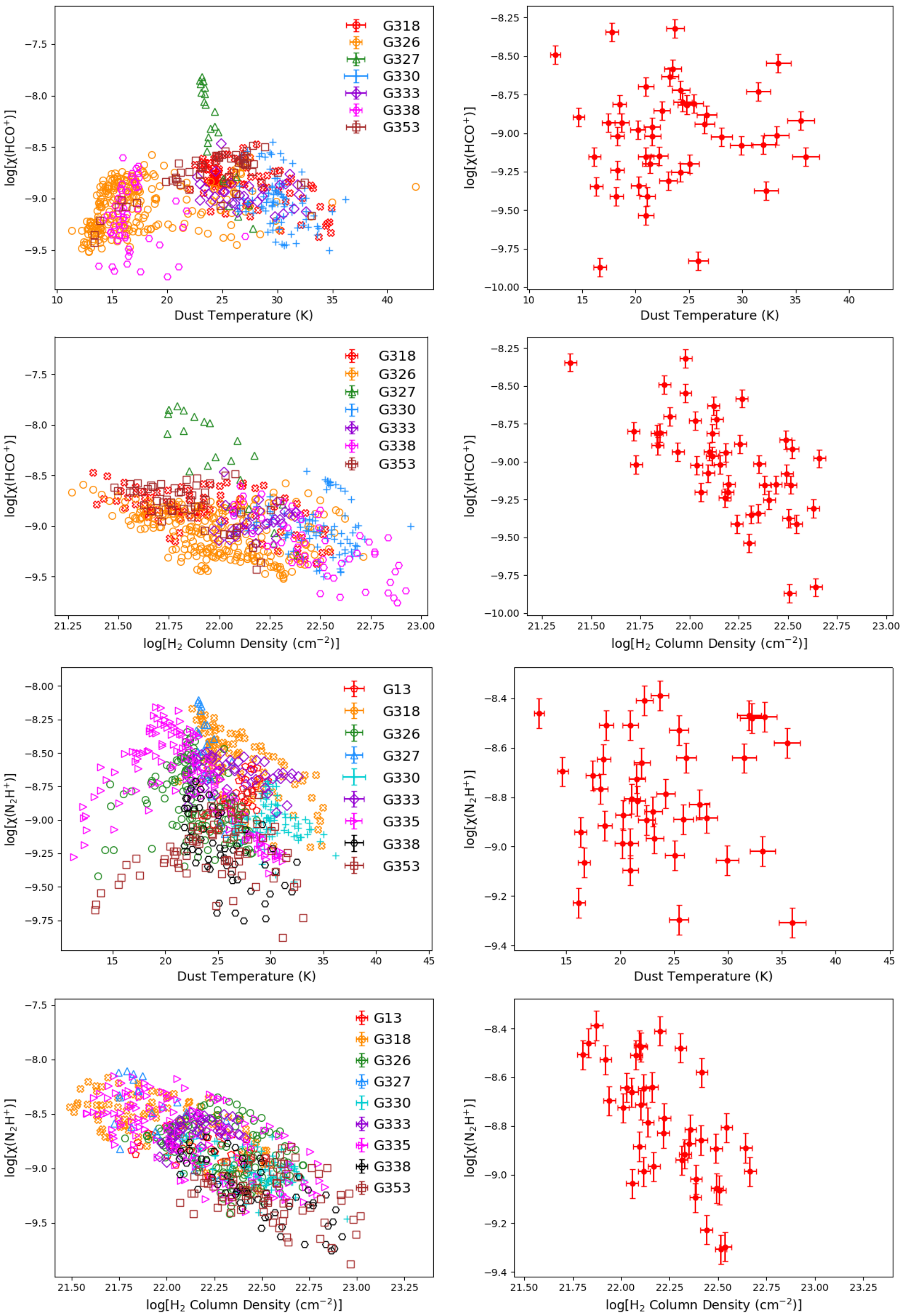

Figure 6.4: Variation of HCO^+ and N_2H^+ abundance ($X(HCO^+)$ and $X(N_2H^+)$) with respect to dust temperature and H_2 column density. The panels in the left column show the plots for pixel-by-pixel study whereas those in the right column depict the results for statistical study. For the pixel-by-pixel case, only a characteristic error bar is shown in its top-right corner for the sake of clarity.

cm^{-2} on average), are an order of magnitude higher than those derived for our sources. On the other hand, the median value of HCO^+ abundance of our sample (1.09×10^{-9}) is found to be higher than that observed by Zhang et al. (2016) for their sources categorised as H II regions/PDRs (3×10^{-10}). The mean HCO^+ column density value is also less than those derived by Saral et al. (2018) for their sample of YSOs and protostellar sources. This could be due to the differences in the methodology adopted for calculating the excitation temperature. Zhang et al. (2016) and Hoq et al. (2013) assume the excitation temperature to be equal to the dust temperature. Saral et al. (2018) on the other hand, derive excitation temperatures using the optical depth of N_2H^+ and use the same for the optically thick lines: HCO^+, HCN and HNC. In contrast, we find the excitation temperature of HCO^+, HCN and HNC to be significantly lower compared to that of N_2H^+, and much less than the dust temperature.

Figures 6.3 and 6.4 show HCN, HNC, HCO^+ and N_2H^+ abundances plotted as a function of dust temperature and H_2 column density. While there does not appear to be any trend of the molecular abundances with dust temperature, they appear to be negatively correlated with H_2 column density. The correlation coefficients obtained from the Spearman correlation test performed on molecular abundances, and H_2 column densities, are given in Table 6.4. We note that the trends shown by the abundances in the statistical study are also reflected in the pixel wise analysis. We also carried out Pearson correlation test on the sample of 68 MM sources for HCN and HNC abundances (with respect to H_2 column density) and the coefficients obtained are -0.52 and -0.35 respectively. The Pearson correlation coefficient found between HCN abundance and H_2 column density is very similar to that reported by Miettinen (2014), who found the correlation coefficient to be -0.55 for their sample. While Hoq et al. (2013) and Miettinen (2014) infer that HCO^+ abundances tend to increase with evolution, we do not see any such trend in our data. It is to be noted that the inference of HCO^+ abundance increasing with evolutionary stage was made by Miettinen (2014) assuming that the H_2 column density increases with source evolution. This is, however, unlikely to be true since the observation of high H_2 column density in single dish studies is more likely to be due to factors other than evolution, such as a larger physical source area being covered in a telescope beam for a more distant source. In contrast, the dust temperature is seen to be a much better probe of the evolutionary stage of the source, with temperatures seen in infrared dark clouds seen to be systematically lower than that in more evolved sources such as methanol masers and H II regions (Giannetti et al., 2013). The lack of any correlation between the dust temperature and HCO^+ abundance thus casts doubt on the interpretation of Miettinen (2014) on the increase of HCO^+ abundance with

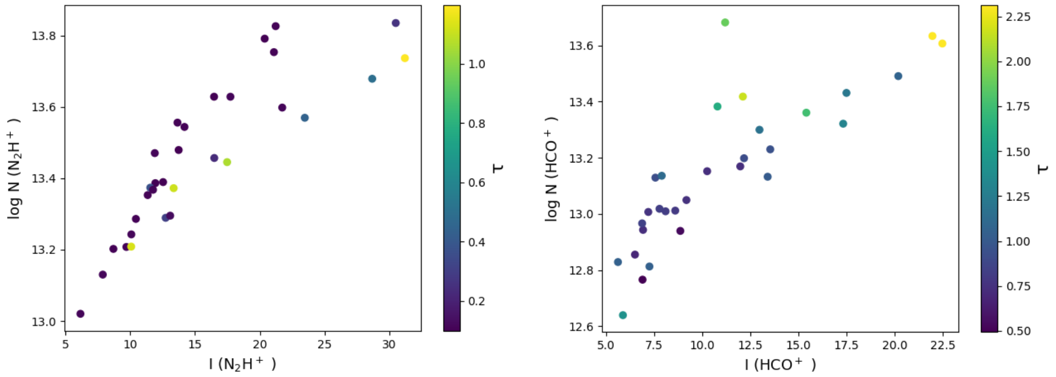

Figure 6.5: Column densities plotted against the integrated intensities of different molecules for MM sources. The colours indicate the variation in optical depth.

source evolution.

6.3.5 Integrated line intensities

Earlier studies (e.g., Rathborne et al., 2016; Urquhart et al., 2019) have studied the chemistry in high-mass clumps using integrated line intensities and their ratios. The integrated line intensities divided by H_2 column density have also been considered as a rough estimate of molecular abundance (Urquhart et al., 2019). However, this assumes that the physical conditions are similar for various transitions. In practice, different transitions have different excitation temperatures and optical depths, which result in a variation of the column density from a simple linear relation to the integrated intensity. To illustrate this, Figure 6.5 shows the plot of integrated line intensity as a function of column density for N_2H^+ and HCO^+ molecules corresponding to MM sources in our study. The data points are colour-coded by the variation in optical depth. Figure 6.5 shows that the sources exhibit a clear bifurcation between high and low optical depth values. The sources possessing lower τ values tend to show a stronger linear correlation with scatter among these points arising from variations in the excitation temperature. On the other hand, sources with larger optical depth tend to show more dispersion. This implies that integrated intensities are good proxies for column densities only for complex molecules with low optical depth, and studies that target optically thick molecules such as HCN, HNC and HCO^+ require radiative transfer modelling in order to obtain reliable column densities.

The HCN integrated intensities do not show any variation with the dust temperature. On the contrary, the integrated intensity of HNC shows a weak positive correlation (Spearman correlation coefficient, $r = 0.28$). This trend in HNC is in agreement with what is reported by Zhang et al. (2016) and Urquhart et al. (2019). The HNC line intensities divided by H_2 column densities, on the other hand, show no discernible trend. The HCO^+ line intensity displays a slight increasing trend with dust temperature ($r = 0.32$), much in agreement with Zhang et al. (2016) and Urquhart et al. (2019). The integrated intensity of HCO^+ divided by H_2 column density show no obvious trends with dust temperature. This is contrary to what is inferred by Urquhart et al. (2019), where they detect a weak positive correlation with dust temperature. The integrated intensity of N_2H^+ appears to be invariant with dust temperature. This result is in congruence with what is observed by Urquhart et al. (2019). Zhang et al. (2016) however, reports a slightly positive correlation. The ratio of integrated line intensity of N_2H^+ to the H_2 column density show no distinct trend with dust temperature, which is in good agreement with the results of Urquhart et al. (2019).

6.4 Discussion

In this section we discuss in detail the chemistry of different molecules based on the chemical models, followed by a brief discussion on the infall signatures observed in our sample. We also discuss the evolutionary status of methanol maser sources, gleaned from their molecular abundance and integrated line intensity ratios.

6.4.1 Chemistry of molecules

6.4.1.1 HCN,HNC (hydrogen (iso)-cyanide)

HCN and its metastable geometrical isomer HNC are ubiquitous in the dense star forming regions and are considered to be probing high-density gas. They are also good tracers of infall motions in star forming regions (Wu & Evans II, 2003). According to gas-phase chemical models, HCN and HNC are primarily produced through the following dissociative recombination reaction of $HCNH^+$ (Mendes et al., 2012):

$$\mathrm{HCNH^+ + e^-} \longrightarrow \begin{cases} \mathrm{HCN + H} \\ \mathrm{HNC + H} \end{cases} \tag{6.3}$$

Here both HCN and HNC are formed in equal measures causing HCN/HNC abundance ratio close to unity ($\simeq 0.9$). An additional channel where only HNC is produced, is through the dissociative recombination of H_2CN^+ and H_2NC^+ (Allen et al., 1980):

$$\left.\begin{array}{l} H_2CN^+ + e^- \\ H_2NC^+ + e^- \end{array}\right\} \longrightarrow HNC + H \tag{6.4}$$

This results HCN/HNC ratio to slightly rise above unity. These molecules are also formed through other channels say,

$$CH_2 + N \longrightarrow HCN + H \tag{6.5}$$

$$NH_2 + C \longrightarrow HNC + H \tag{6.6}$$

These are then followed by rapid isomerisation reactions, once again resulting in near unity HCN/HNC ratio. The destruction of HCN and HNC molecules in dense clouds, primarily happens via the following reaction channels,

$$HCN + H^+ \longrightarrow HCN^+ + H \tag{6.7}$$

$$HCN + HCO^+ \longrightarrow H_2CN^+ + CO \tag{6.8}$$

$$HNC + H \longrightarrow HCN + H \tag{6.9}$$

$$HNC + H^+ \longrightarrow HCN + H^+ \tag{6.10}$$

$$HNC + O \longrightarrow NH + CO \tag{6.11}$$

6.4.2 HCO^+

HCO^+ molecule, regarded as one of the excellent tracers of high-density gas, is mainly formed via the following two channels (Schlingman et al., 2011) :

$$H_3^+ + CO \longrightarrow HCO^+ + H_2 \tag{6.12}$$

$$N_2H^+ + CO \longrightarrow HCO^+ + N_2 \tag{6.13}$$

In the cold dense molecular clouds ($n > 10^4$ cm^{-3}, T$_{kin} < 24$ K), CO is frozen out on to the dust grains, resulting in the depletion of HCO^+. As the temperature increases, CO is liberated from the dust grains, enhancing the production of HCO^+. Hence, the column densities and abundances of HCO^+ molecule is expected to increase as the source evolves. The destruction of HCO^+ is primarily due to the dissociative recombination reaction:

$$HCO^+ + e^- \longrightarrow CO + H$$

6.4.2.1 N_2H^+

These molecules are primarily formed through the gas-phase reaction :

$$H_3^+ + N_2 \longrightarrow N_2H^+ + H_2 \tag{6.14}$$

and destroyed by the reaction with CO molecules in gas phase producing HCO^+ Bergin & Langer (1997)

$$N_2H^+ + CO \longrightarrow HCO^+ + N_2 \tag{6.15}$$

Free electrons can also destroy N_2H^+ molecules via the dissociative recombination reaction and it's the primary destruction mechanism when CO is depleted.

$$H_3^+ + N_2 \longrightarrow N_2H^+ + H_2 \tag{6.16}$$

$$N_2H^+ + e^- \longrightarrow N_2 + H/NH + H \tag{6.17}$$

6.4.3 Comparison to chemical models

According to gas-phase chemical models, HCN and its metastable geometrical isomer HNC are primarily produced through the dissociative recombination reaction of $HCNH^+$ as described in Equation 6.3. Figure 6.6 shows HCN abundance plotted as a function of HNC abundance. We can clearly see a strong positive correlation in the pixel-by-pixel case whereas there is more scatter in the statistical study. A Pearson correlation test carried out on the HNC and HCN abundances for the pixel-by-pixel analysis yields a correlation coefficient of 0.72 with 99.8% confidence level (p-value of 0.002)¶ For the statistical

---

¶Throughout this work we have adopted a threshold of $> 3\sigma$ confidence for claiming statistical significance, which corresponds to a p-value < 0.003 for the null hypothesis of the two samples not being correlated.

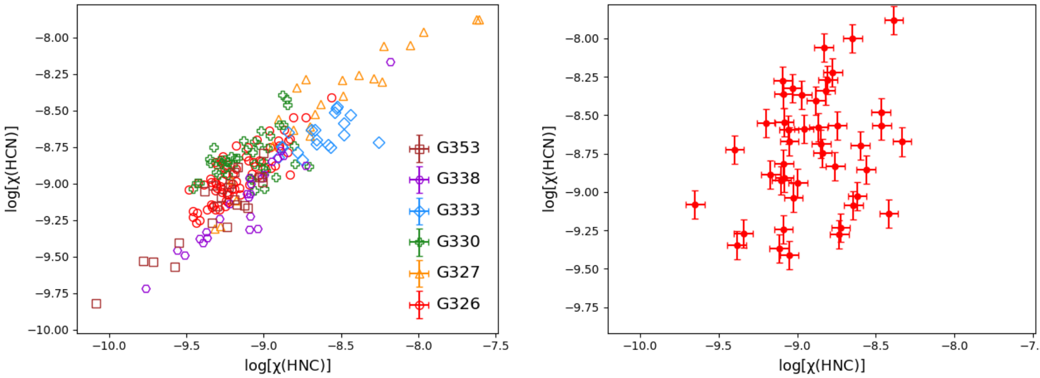

Figure 6.6: X(HNC) vs X(HCN). The left panel shows the plots for pixel-by-pixel study whereas the right panel depicts the results for statistical study. Pearson correlation coefficient for these two molecular species are 0.72 and 0.35, for pixel-by-pixel and statistical studies, respectively.

analysis, we obtained the Pearson correlation coefficient to be 0.35 (p-value of 0.0003). A similar positive correlation is observed by Miettinen (2014) (Pearson correlation coefficient being 0.45) for their statistical study of IRDCs. The abundance ratio between HCN and HNC is found to lie in the range 0.21 to 4.76 with a mean value of 1.64 (median is 1.49). The mean value is closer to unity as suggested by the chemical models. Miettinen (2014) reports their HCN/HNC ratio to be in the range 0.15 to 16.6, with a median value of 1.40. These values agree well with our results. The mean value of abundance ratio determined by Zhang et al. (2016) for their sample of high mass stars is seen to be greater than unity (3.91). However, the HCN/HNC abundance ratio is very sensitive to the adopted dust temperatures (Goldsmith et al., 1986; Schilke et al., 1992). While Zhang et al. (2016) have assumed the excitation temperature to be equal to the dust temperature, we find the excitation temperature to be much lower than the dust temperature. The very different abundance ratio of Zhang et al. (2016) may be due to this difference in the value of assumed excitation temperature.

This being said, the HCN/HNC abundance ratio has been shown to vary between regions (Schilke et al., 1992) and this has been attributed to conversion of HNC to HCN at temperatures above $T \sim 24$ K [see Equation (6.9)]. The abundance ratio appears to show a variation around 24 K for the pixel-by-pixel case (left panel, Figure 6.7). We investigate this further in Figure 6.8 which shows the probability distribution functions (PDFs) for the ratios of samples with dust temperatures above and below $T_{dust} = 24$ K shown in red and blue, respectively. The sample with $T_{dust} > 24$ K has a higher median ratio, which is in agreement with Schilke et al. (1992) who interpret this increase with source evolution.

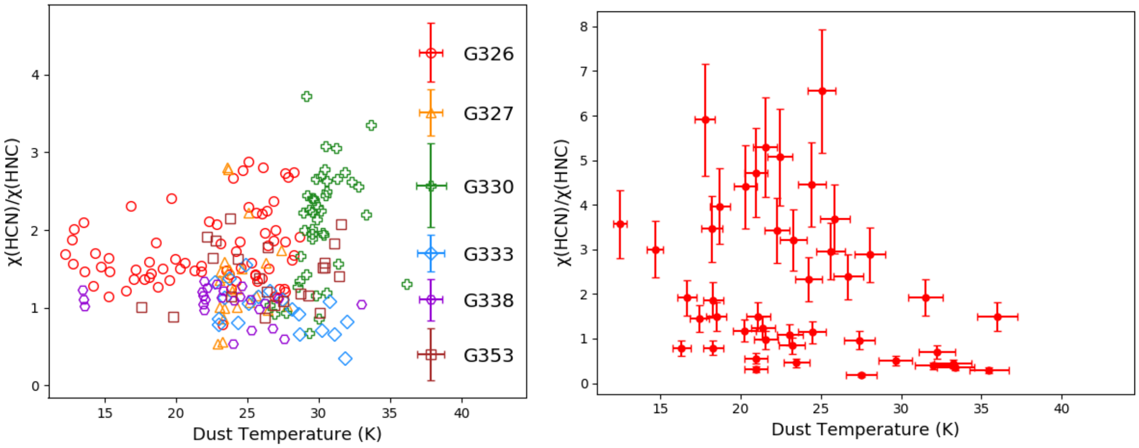

Figure 6.7: X(HNC)/X(HCN) vs dust temperature. The left panel (a) shows the plots for pixel-by-pixel study whereas the right panel (b) shows the results for statistical study.

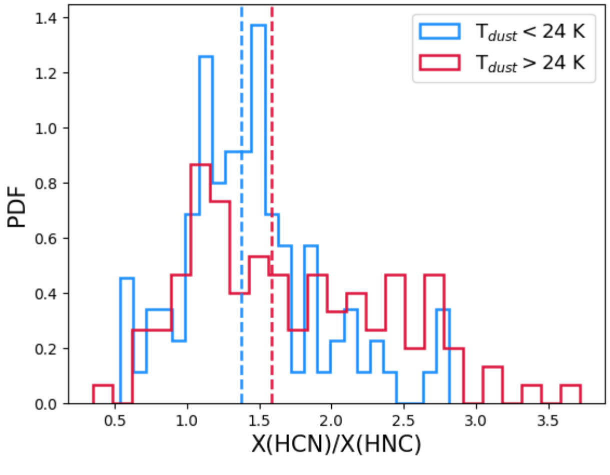

Figure 6.8: Probability density functions of HCN/HNC abundance ratios for $T_{dust} > 24$ K and $T_{dust} < 24$ K (marked in red and blue respectively). The median values are represented by dashed lines.

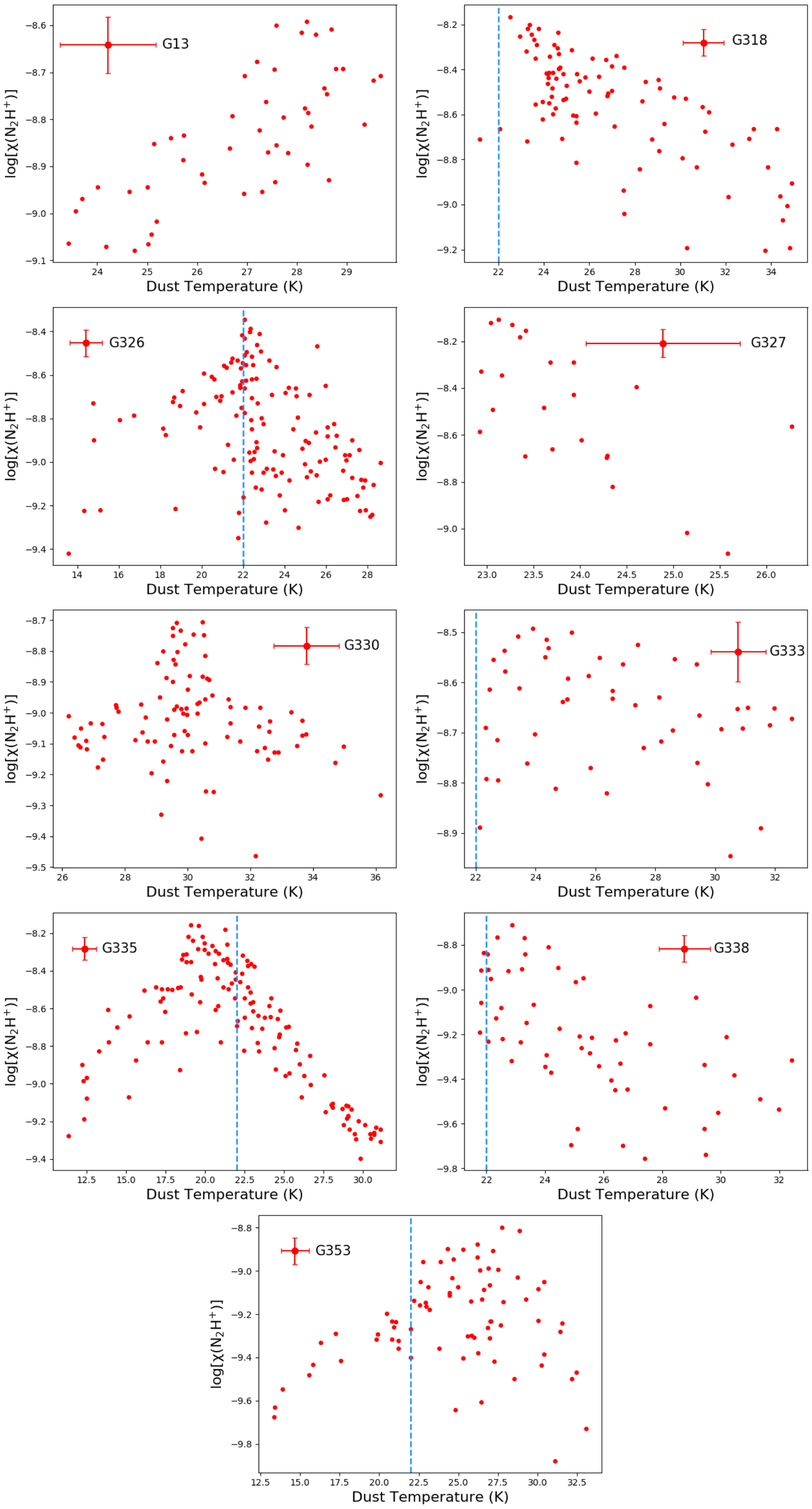

Figure 6.9: The abundance of N_2H^+ as a function of dust temperature. The vertical dashed blue line is at T_{dust} = 22 K. Characteristic error bar is shown in the top corner of the plot.

The right panel of Figure 6.7 shows a decreasing trend with increasing dust temperature, although at $< 3\sigma$ confidence level based on a Pearson test. We would therefore like to caution against over interpretation of this trend.

We also investigate the variation in N_2H^+ abundance with respect to dust temperature, for our sample of MM sources. Figure 6.9 shows the N_2H^+ abundance plotted as a function of dust temperature in each pixel of the 9 sources (S/N $\gtrsim$ 5). It is seen that for all the sources except G13, the abundances increase till $T_{dust} \simeq 22$ K and then decrease as the temperature increases. The increase in N_2H^+ abundances at lower temperatures ($T < 24$ K) is also observed by Sanhueza et al. (2012), Hoq et al. (2013), Miettinen (2014) and several other studies. This positive correlation is often associated with the enhanced N_2 evaporation from dust grains, resulting in the formation of more N_2H^+ molecules (Chen et al., 2013). As the temperature exceeds 22 K, we see a decline in the abundance of N_2H^+. This is in agreement with the chemical models, which suggest the liberation of CO molecules from the dust grains at $T_{dust} > 20$ K, causing the depletion of N_2H^+ molecules.

6.4.4 Detection of infall signatures

HCO^+ is one of the suitable candidates for investigating infall motions in both low mass and high mass star forming regions. To distinguish self-absorbed line from other double peaked line profiles, we generally make use of its optically thin isotopologue $H^{13}CO^+$ (Klaassen et al., 2012). Mardones et al. (1997) defined a dimensionless asymmetry parameter δV, to quantify the blue-skewed profiles,

$$\delta V = \frac{V_{thick} - V_{thin}}{\Delta V} \tag{6.18}$$

Here, V_{thick} and V_{thin} represent the LSR velocities of the optically thick and optically thin lines and ΔV is the FWHM of the optically thin line. Line profiles with blue asymmetry are characterized by negative values of the asymmetry parameter – i.e. $\delta V < 0$. As we do not have any strong ($> 3\sigma$) $H^{13}CO^+$ detections, we use optically thin N_2H^+ for the calculations. We obtained blue-asymmetries for 21 sources in our sample. In addition, two sources, G13 and G335, displayed a blue asymmetric self-absorbed line profile. The line profiles of these sources were modelled using the radiative transfer model "Hill5" (De Vries & Myers, 2005) in order to determine the infall velocity. Figure 6.10 illustrates HCO^+ fitted by "Hill5" model for a single pixel of G13 and G335. For sources that exhibited blue-asymmetry, but not self-absorption, we used $V_{in} = V_{thin} - V_{thick}$ as an estimate of the infall velocity. The mass infall rate is then computed from the infall velocity as

$$\dot{M}_{inf} = 3\frac{M_{cl}}{R_{cl}}V_{in} \tag{6.19}$$

where M_{cl} and R_{cl} are the mass and radius of the clumps respectively. These values are taken from table 3 of Work I. The mass infall rates calculated, fall in the range 8.0×10^{-5} $\mathrm{M_{\odot}yr^{-1}} - 1.24\times10^{-2}$ $\mathrm{M_{\odot}yr^{-1}}$ with median value being 2.3×10^{-3} $\mathrm{M_{\odot}yr^{-1}}$. The uncertainties in these values are typically less than 15 per cent. The calculated infall rates are in good agreement with values that are typically found towards massive star forming regions (Young et al., 1998; Fontani et al., 2002; López-Sepulcre et al., 2010; Saral et al., 2018). Figure 6.11 shows $\dot{M}_{inf}$ as a function of luminosity to mass (L/M) ratio. The L/M ratio serves as a diagnostic tool to infer the evolutionary state of the source. In Figure 6.11, the x-axis is $(L/M)^{1.42}$, since this represents the fit to the 'IR-P' sources in Molinari et al. (2008) and delineates sources in accretion phase from those in clearing phase (refer Figure 11 of Work I). The sources belonging to the accretion phase and clearing phase are marked in red and green respectively. Although the mass infall rates appear to show a weak positive correlation with L/M ratios ($r = 0.3$), this is inconclusive due to p-value>0.003. A larger sample of sources in clearing phase can elucidate the evolutionary effects of infall rates. Wyrowski et al. (2016) report a similar result for their sample of high mass clumps, where 3 of their 8 sources showed higher infall rates towards higher L/M. He et al. (2016) obtained median mass infall rates of $(7 - 8) \times 10^{-3}$ $\mathrm{M_{\odot}yr^{-1}}$ for pre-stellar, protostellar and ultra-compact H II regions for their sample of 732 massive clumps and concluded that the infall rates are independent of the evolutionary stage. We also found no significant trends in the mass infall rate when plotted against methanol maser luminosities.

6.4.5 Implications about the evolutionary stage

As indicated earlier in §1, a number of studies (e.g., Ellingsen, 2006b; Pandian et al., 2010; Billington et al., 2019, and references therein) using continuum emission from radio to infrared wavelengths strongly suggest that 6.7 GHz methanol masers trace an early evolutionary stage of massive star formation, mostly prior to the formation of a H II region. In particular, the mass to luminosity ratio of methanol maser sources are consistent with ~93 per cent of them being in accretion phase (Paper I). A similar study by Jones et al. (2020) compares the physical properties of clumps associated with maser emission with that of the protostellar sources without maser emission and find the L/M ratio for maser associated clumps to be slightly higher than that of the latter, suggesting that the maser

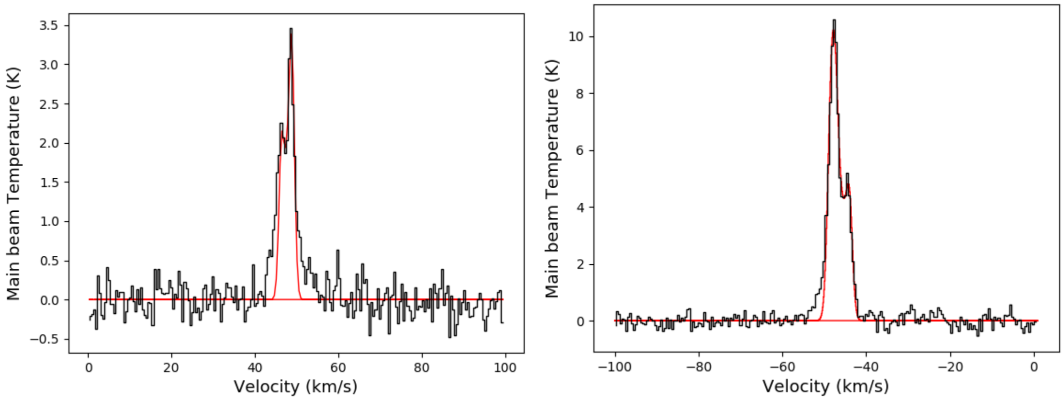

Figure 6.10: HCO^+ spectrum of a single pixel fitted by "Hill5" model for G13 and G335 (left and right panels respectively).

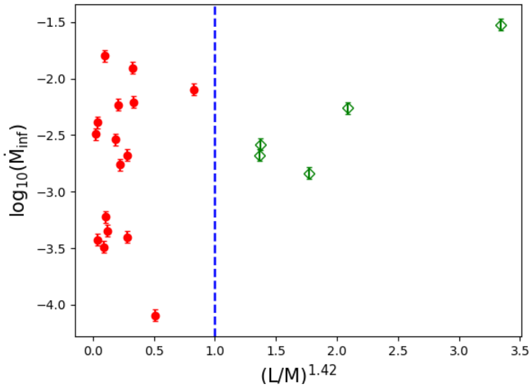

Figure 6.11: Mass infall rates plotted against $(L/M)^{1.42}$. The methanol maser hosts that are in accretion phase and clearing phase are shown in red (filled circles) and green (unfilled diamonds) points, respectively. The blue dashed line represents the fit to the 'IR-P' sources in Molinari et al. (2008).

sources are more evolved. In this context, it is of interest to see whether the chemical properties of these clumps, examined based on the chemical model, is in agreement with the conclusions derived from their physical properties. Since different molecular species form in specific chemical environments, the ratio of their abundances and intensities can act as a tracer for the evolutionary stage of the high-mass clump. For example, Rathborne et al. (2016) and Urquhart et al. (2019) have observed several line ratios to show systematic trends with source evolution.

We focus on four molecular abundance (intensity) ratios: HCN/HNC, HNC/HCO^+, N_2H^+/HCO^+ and N_2H^+/HNC. Here we compare these abundance ratios of our sources with those that are classified to be in different evolutionary stages by earlier studies. We also compare the line intensity ratios of the methanol maser sources with the overall sample of Rathborne et al. (2016) and Urquhart et al. (2019). In this regard, it should be noted that although our data is from the MALT90 survey, our integrated line intensities are in general higher than that of Rathborne et al. (2016). This is primarily due to the differences in spectrum extraction from the data cubes. While we have extracted our spectra from the brightest pixel as discussed in Section 2, Rathborne et al. (2016) use an averaged spectrum, obtained by averaging over 9 pixels around the dust peak. This has the effect of reducing the intensity of the spectrum although the signal to noise ratio can be higher. Our integrated line intensities are also found to be frequently different from those of Urquhart et al. (2019) for the same sources, with the discrepancy most likely arising from differences in the pointing location and velocity resolution (~ 0.9 km s^{-1}, which is worse than that of MALT90). We hence do not compare the line ratios determined in our work with that of Rathborne et al. (2016) and Urquhart et al. (2019). Rather, we extract the molecular line intensities of methanol maser detections in the MMB from Rathborne et al. (2016) and Urquhart et al. (2019) and compare their ratios with that of sources in other evolutionary states. This is done separately for the sample of Rathborne et al. (2016) and Urquhart et al. (2019). We will refer to the maser sample separated out from Rathborne et al. (2016) and Urquhart et al. (2019) as MM_R and MM_U respectively, for the sake of clarity. The minimum, maximum and median values of column density and abundance ratios between different molecules for 68 MM sources are given in Table 6.5.

We begin by comparing the HCN/HNC abundance ratios with the results of Jin et al. (2015) and Saral et al. (2018). The former estimate the abundance ratio for Infrared dark clouds (IRDCs, quiscent or active, depending on star formation activity), High-mass protostellar objects (HMPOs) and Ultra-compact H II regions (UCHIIs). The latter classify their sources into three evolutionary stages: massive star forming regions (MSF), young

Table 6.5: Molecular ratios

Molecular ratios	Min	Max	Median
N(HCN)/N(HNC)	0.21	4.76	1.49
X(HCN)/X(HNC)	0.21	4.76	1.50
N(HNC)/N(HCO^+)	0.37	7.68	1.17
X(HNC)/X(HCO^+)	0.29	7.68	1.16
N(N_2H^+)/N(HCO^+)	0.03	8.71	1.66
X(N_2H^+)/X(HCO^+)	0.03	8.71	1.58
N(N_2H^+)/N(HNC)	0.02	5.73	1.40
X(N_2H^+)/X(HNC)	0.02	5.73	1.47

Minimum, maximum and median values of different molecular ratios for 68 MM sources. N and X represents column density and abundance respectively.

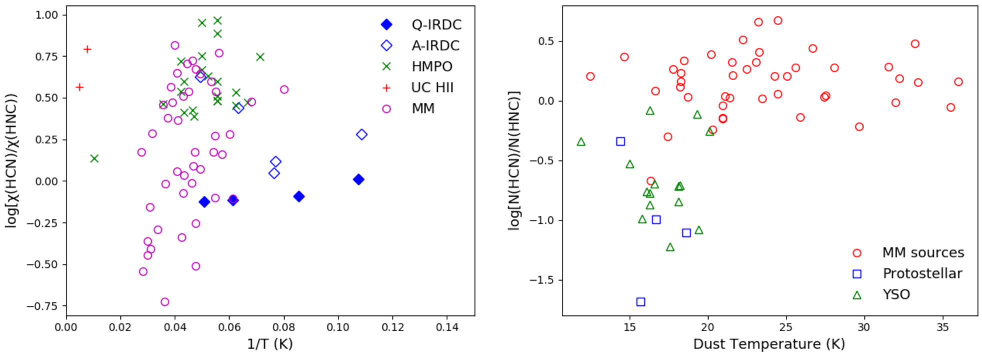

Figure 6.12: MM sources over plotted on results obtained by previous studies. The left panel shows the HCN/HNC ratios derived by Jin et al. (2015) and the right panel shows that of Saral et al. (2018).

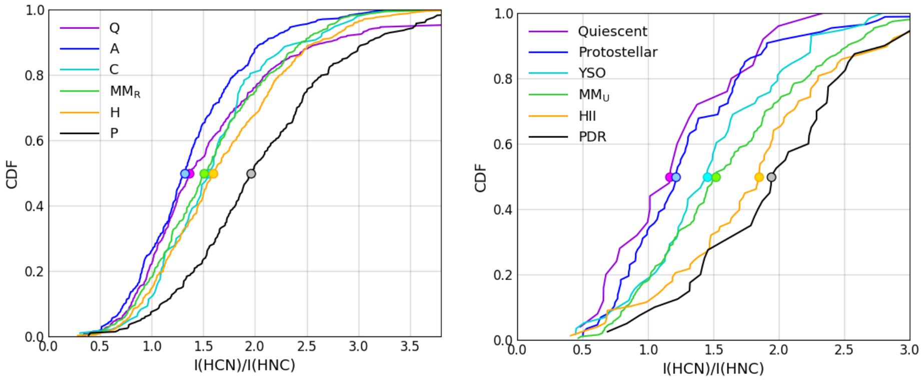

Figure 6.13: MM sources compared with the HCN/HNC integrated intensity ratios of Rathborne et al. (2016) and Urquhart et al. (2019) shown in left and right panels respectively. The filled circles on the CDFs represent the median line intensity ratios. Letters ‘Q’, ’A’, ’C’, ’H’ and ’P’ denotes quiescent, protostellar, compact H II regions, extended H II regions and photo-dominated regions respectively.

stellar objects (YSO) and protostellar. The left panel of Figure 6.12 shows that MM sources have similar temperatures as HMPOs but their abundance ratios partially span the IRDC region as well. In contrast, the right panel of Figure 6.12 shows the abundance ratio to be larger than YSOs and protostellar sources. Figure 6.12 also shows that the abundance ratio inferred by Jin et al. (2015) differs systematically from that of sources in similar evolutionary stage (e.g. HMPO vs Protostellar or YSO) in Saral et al. (2018). This may be due to the abundance ratio being determined by comparing the column densities of $H^{13}CN$ and $HN^{13}C$ by Jin et al. (2015). Considering that the methodology that we have used in our work is similar to that of Saral et al. (2018), the methanol masers appear to be tracing sources that are more evolved than the protostellar phase. However, due to the small sample size, this result is not statistically significant as inferred by a Kolmogorov-Smirnov (KS) test[‖]. In Figure 6.13 we compare the cumulative distribution functions (CDFs) of HCN/HNC line intensity ratios of MM_R and MM_U sources with quiescent, protostellar, H II regions and photo-dominated regions (PDRs) in Rathborne et al. (2016) (left panel) and Urquhart et al. (2019) (right panel), respectively. The median value of the ratio for methanol maser sources is seen to be greater than that of protostellar sources, but smaller than that of H II regions/PDRs. Since the HCN/HNC line ratio is seen to increase with source evolution, this suggests that the methanol maser sources are on average more evolved than protostellar

---

[‖] The null hypothesis considered for KS tests and Student’s T tests in this work is of the two samples being drawn from the same population. We infer two samples to be disparate only if the p-value<0.003, which corresponds to a $> 3\sigma$ confidence level.

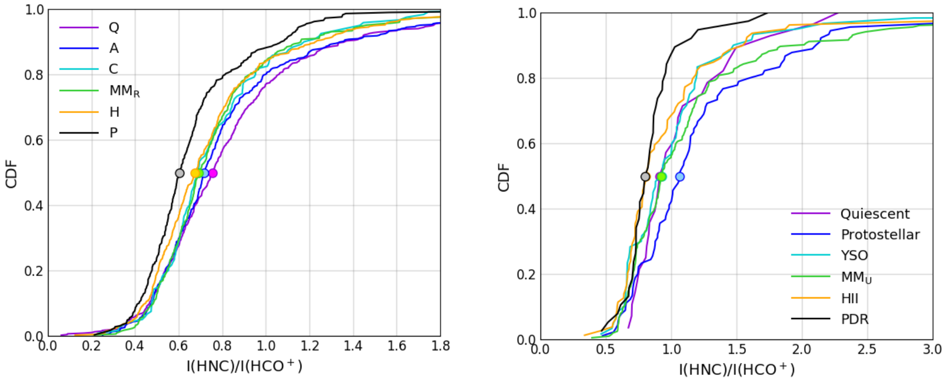

Figure 6.14: Methanol maser sources compared with the HNC/HCO$^+$ integrated intensity ratios of Rathborne et al. (2016) and Urquhart et al. (2019) shown in left and right panels respectively. The filled circles on the CDFs represent the median line intensity ratios. Letters ‘Q’, ’A’, ’C’, ’H’ and ’P’ denotes quiescent, protostellar, compact H II regions, extended H II regions and photo-dominated regions respectively.

sources but less evolved than H II regions/PDRs. The KS test shows the maser sample to be distinct from protostellar sources but not H II regions, showing the former to be a stasistically significant result.

Miettinen (2014) compute HNC/HCO$^+$ column density ratios for IR-dark sources and IR-bright sources, whereas Zhang et al. (2016) obtain HNC/HCO$^+$ abundance ratios of prestellar, protostellar and H II/PDR clumps. Both of these studies imply that the HNC/HCO$^+$ ratios decrease as the source evolves. On comparing the values for MM sources with these datasets, we find a higher median column density ratio than IR-dark sources and a lower median abundance ratio than H II/PDR sources. Figure 6.14 shows the line intensity ratio of HNC/HCO$^+$ for the classifications of Rathborne et al. (2016) and Urquhart et al. (2019). The line intensity ratio is seen to decline with source evolution, similar to the observation with ratios of column densities. This may be due to enhanced abundance of HNC in colder clumps (Hoq et al., 2013). Figure 6.14 shows that the MM$_R$ and MM$_U$ sources have a larger median I(HNC)/I(HCO)$^+$ than both PDRs and H II regions, and a smaller median ratio than protostellar sources. However, the KS test identifies only methanol maser sources and PDRs to be drawn from seperate populations. Hence, we can ascertain than that the maser sources are less evolved than PDRs. Comparing with Figure 6.13, we can also say that the HNC/HCO$^+$ ratio is not as sensitive as the HCN/HNC ratio in distinguishing between evolutionary states.

It has been reported that N_2H^+/HCO$^+$ abundance decreases as a high mass clump evolves (Sanhueza et al., 2012; Lee et al., 2003; Bergin & Tafalla, 2007). A comparison with the

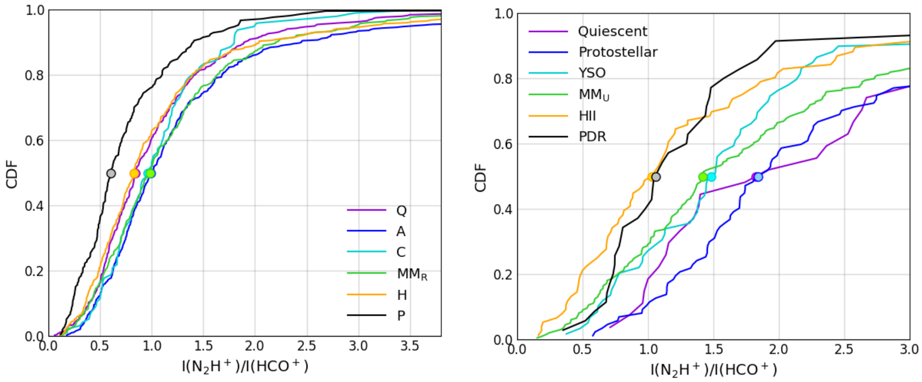

Figure 6.15: MM sources compared with the N_2H^+/HCO^+ integrated intensity ratios of Rathborne et al. (2016) and Urquhart et al. (2019) shown in left and right panels respectively. The filled circles on the CDFs represent the median line intensity ratios. Letters 'Q', 'A', 'C', 'H' and 'P' denotes quiescent, protostellar, compact H II regions, extended H II regions and photo-dominated regions respectively.

sources in Zhang et al. (2016) shows that MM sources have a larger median abundance ratio than H II/PDR but lesser than protostellar. We also find that the median abundance ratio of MM sources is higher than that of IR-bright souces in Miettinen (2014). As shown in Figure 6.15, we find a higher median ratio for MM_R and MM_U sources compared to H II regions and PDRs in Rathborne et al. (2016) and Urquhart et al. (2019). Given that the N_2H^+/HCO^+ intensity ratio declines as the source evolves, this is indicative of MM sources being less evolved than H II regions and PDRs. While, a KS test performed on Urquhart et al. (2019) identifies maser sources, protostellar sources and H II regions as distinct samples, the same test performed on Rathborne et al. (2016) identifies maser sources and PDRs as distinct. Hence, Rathborne et al. (2016) suggests maser sources to be less evolved than PDRs and the N_2H^+/HCO^+ line intensity ratios of Urquhart et al. (2019) is consistent with methanol maser sources being at a later evolutionary stage than protostellar phase and less evolved than H II regions.

Finally, we investigate how the N_2H^+/HNC ratio of MM sources compare with clumps in different evolutionary stages. The median column density and abundance ratios for MM sources are similar to IRDCs in Liu et al. (2013). Figure 6.16 shows the N_2H^+/HNC intensity ratio for sources in different evolutionary stages as per Rathborne et al. (2016) and Urquhart et al. (2019). It can be seen that the N_2H^+/HNC ratio declines as the source evolves, which is contrary to what was observed by Sanhueza et al. (2012). We also see that the median line ratio of MM_R and MM_U sources is higher than that of H II regions and PDRs (these are supported by the KS tests), which again is consistent with methanol maser

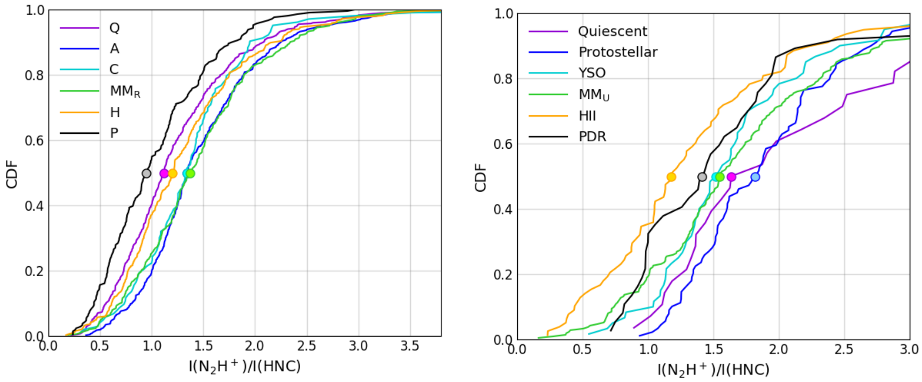

Figure 6.16: MM sources compared with the N_2H^+/HNC integrated intensity ratios of Rathborne et al. (2016) and Urquhart et al. (2019) shown in left and right panels respectively. The filled circles on the CDFs represent the median line intensity ratios. Letters ‘Q’, ’A’, ’C’, ’H’ and ’P’ denotes quiescent, protostellar, compact H II regions, extended H II regions and photo-dominated regions respectively.

sources tracing an earlier evolutionary stage than H II regions.

In short, the chemical properties are in agreement with the picture of methanol masers tracing an early evolutionary stage prior to the formation of PDRs and possibly H II regions (clearing phase). While the median line ratios of the sources with methanol masers are generally in between that of sources in the protostellar phase and sources identified as H II regions and PDRs, there is considerable overlap in the CDFs. This may be either due to the methanol maser phase overlapping with that of massive young stellar objects and H II regions, or due to chemical properties having lower sensitivity (compared to continuum studies) with respect to discriminating between different evolutionary phases.

6.5 Summary

We have investigated the chemical environments of 6.7 GHz methanol maser hosts using N_2H^+(1-0), HCO^+(1-0), HCN(1-0) and HNC(1-0) molecular lines from the MALT90 survey, where the sources were selected to be representative of the full sample in Work I. The abundances of these molecular species is in congruence to the typical values observed in massive star forming regions. We do not find any correlation between molecular abundance and dust temperature, which suggest that the molecular abundances do not evolve much during the evolutionary stage traced by methanol masers. The HNC and HCO^+ integrated intensities, on the other hand, showed a weak positive correlation with source evolution. The HCN/HNC, HNC/HCO^+, N_2H^+/HCO^+ and N_2H^+/HNC ratios are in agreement with the picture of the methanol maser phase occurring prior to the formation of H II regions/PDRs. The analysis of HCN/HNC ratios hint methanol maser sources being more evolved than protostellar sources.These results are consistent with earlier studies including the SED studies of Work I wherein a majority of the methanol masers had mass to luminosity ratios suggestive of them being in accretion phase, with the masers turning off in the clearing phase.

Chapter 7

Conclusions and future work

7.1 Conclusions

This thesis presented an investigation into the early stages of massive stars using 6.7 GHz methanol masers as tracers. Astrophysical masers are one of the effective tracers of high mass star forming regions. The population inversion in astrophysical masers can be achieved via collisional excitation or radiational pumping. Many species and transitions of astrophysical masers have been detected towards massive star forming regions, but the most common and strong transitions are from OH, methanol and water molecules. As far as the early stages of star formation is concerned, methanol masers hold a special place as most of them are associated with sources that have not developed an H II region. There are more than 50 different methanol transitions that have been observed to show maser emission, and these are divided into two classes - Class I and Class II. Class I methanol masers are collisionally pumped and are generally found slightly offset from star-forming regions. Class II methanol masers, on the other hand, are dominated by radiative processes and are observed in the close vicinity of massive star forming regions. The 6.7 GHz transition of the Class II methanol maser is the brightest, and the second brightest maser transition ever observed. These masers are pumped by the infrared emission from local warm dust of temperatures exceeding 150 K. Furthermore, gas densities $3 \times 10^3 < n_{H_2} < \times 10^9$ cm^{-3} with methanol column densities $> 2 \times 10^{15}$ cm^{-2} are also required for the 6.7 GHz masers to occur. Such physical conditions are commonly found in massive star forming regions–making 6.7 GHz methanol masers closely associated with high-mass star formation, based on theoretical models. This has also been bolstered observationally via numerous surveys targeted towards ultracompact H II regions (selected through their IRAS colors) and OH masers. A majority of these masers have also been found to lack the presence of any associated radio continuum, suggesting that they are associated with early stages of massive star formation.

We have carried out a comprehensive study of the physical environments of 6.7 GHz methanol maser sources. We conducted this study by taking 320 methanol maser sources from the MMB survey and constructing their SEDs from 70 to 870 μm, with flux values derived from Hi-GAL and ATLASGAL maps. An average dust temperature of 22 K was observed, confirming the later evolutionary stage of the maser sources in comparison to infrared dark clouds, with some sources showing temperatures as high as 48 K. We estimated the clump properties such as mass, far-infrared luminosity, and column density using the best-fitting parameters of the SED fits. The values of these parameters suggest that the vast majority of these clumps are in the process of forming high-mass stars. Considering the Kauffman criteria for massive star formation, we found that all but a few maser hosts have the potential to harbour at least one high-mass star. The evolutionary stages of 6.7 GHz maser sources, explored using the mass luminosity diagram, suggest that they are predominantly associated with high-mass stars, with the majority being in the accretion phase. However, we observed a small number of sources that could possibly be related to intermediate- or low-mass stars.

We also investigated the chemistry of 6.7 GHz methanol maser hosts. This study was intended to compliment our work on the physical environments of the maser sources. We embarked on this project by choosing 68 6.7 GHz methanol maser sources, from the 320 sources we had already studied, with the selection based on data availability and the signal-to-noise ratio of the molecular lines. We performed (1) pixel-by-pixel study of 9 methanol maser sources that have high signal-to-noise ratio and (2) statistical study taking into account the entire 68 sources. We estimated the molecular column densities, integrated line intensities and abundances of N_2H^+(1-0), HCO^+(1-0), HCN(1-0) and HNC(1-0) lines. The derived abundances were found to be in good agreement with the typical values found towards high mass star forming regions. We found the column density and abundance ratio of HCN to HNC to increase and that of N_2H^+ to HCO^+ to decline with source evolution, as suggested by the chemical models. The HCN/HNC, N_2H^+ /HCO^+, HNC/HCO^+ and N_2H^+/HNC ratios of the methanol maser sources bolster the idea that they are at a later evolutionary state than quiescent phase and possibly protostellar phase, but at an earlier stage than H II regions and PDRs–much in agreement with previous dust continuum studies.

This thesis work thus provides a strong evidence that along a timeline for massive star formation, the 6.7 GHz methanol maser phase originates at high-mass young stellar objects that are more evolved than infrared dark clouds, and disappears before the onset of UC-H II regions. We also obtained hints regarding the likely association of 6.7 GHz methanol maser emission with intermediate- or low-mass stars, although the mechanisms by which it happens is not clear. A possible explanation is that the 6.7 GHz maser action in low-mass protostars may be restricted to select geometries wherein the physical conditions for maser pumping are satisfied.

7.2 Future work

The majority of the sources studied in our sample are at large distances and consequently, many of them, which are ostensibly isolated structures at 18 arcscec resolution, could fragment to smaller substructures at high spatial resolution. This is an inherent limitation of any study carried out using data from single dish telescopes. We have assumed a one-to-one correspondence between the massive clump and observed maser, and several high resolution studies have indeed buttressed this assumption. However, if we need to address whether 6.7 GHz methanol masers are exclusively associated with massive star formation in a more robust fashion, it is of paramount importance to conduct the study at higher resolution. It is also worth noting that there has been various studies where maser luminosity is deemed as a useful diagnostic of embedded source evolution. However, as already discussed in Chapter 5, we observe no significant trends between maser luminosity and source evolution (indicated by the luminosity of the source). Resolving these inconsistencies warrants a more detailed study that could be undertaken in the future.

Our molecular line studies have made use of MALT90 archival data to study the chemical environments of the methanol maser hosts. A better estimate of excitation temperatures and number density of the molecular gas can be obtained using spectroscopic data of multiple transitions of the same molecule. It is therefore instructive to perform follow-up high resolution spectral line observations, taking into account various higher order molecular transitions, to unveil the true chemistry of massive star forming regions. Furthermore, the analysis can be made more robust by incorporating non-LTE radiative transfer modelling, especially to shed light on the hyperfine anomalies in HCN.

Bibliography

Allamandola L. J., Sandford S. A., Tielens A. G. G. M., Herbst T. M., 1992, ApJ, 399, 134

Allen T. L., Goddard J. D., Schaefer III H. F., 1980, The Journal of chemical physics, 73, 3255

Anderson L., et al., 2014, Monthly Notices of the Royal Astronomical Society, 441, 24

André P., 2011, Spectral Classification of Embedded Stars. Springer Berlin Heidelberg, Berlin, Heidelberg, pp 1549–1553, doi:10.1007/978-3-642-11274-4_504, `https://doi.org/10.1007/978-3-642-11274-4_504`

Arce H. G., Sargent A. I., 2006, ApJ, 646, 1070

Bains I., Yates J., Gledhill T., Richards A., 2003, Monthly Notices of the Royal Astronomical Society, 346, L46

Bartkiewicz A., Szymczak M., Van Langevelde H., Richards A., Pihlström Y., 2009, Astronomy & Astrophysics, 502, 155

Batrla W., Matthews H. E., Menten K. M., Walmsley C. M., 1987, Nature, 326, 49

Battersby C., et al., 2011, Astronomy & Astrophysics, 535, A128

Baumgardt H., Klessen R., 2011, Monthly Notices of the Royal Astronomical Society, 413, 1810

Beltrán M. T., Rivilla V. M., 2018, arXiv preprint arXiv:1806.08137

Benjamin R. A., et al., 2003, Publications of the Astronomical Society of the Pacific, 115, 953

Bergin E. A., Langer W. D., 1997, The Astrophysical Journal, 486, 316

Bergin E. A., Tafalla M., 2007, Annu. Rev. Astron. Astrophys., 45, 339

Bergman P., Parise B., Liseau R., Larsson B., 2011, A&A, 527, A39

Bertoldi F., McKee C. F., 1992, The Astrophysical Journal, 395, 140

Beuther H., Walsh A., Schilke P., Sridharan T., Menten K., Wyrowski F., 2002, Astronomy & Astrophysics, 390, 289

Beuther H., Churchwell E. B., McKee C. F., Tan J. C., 2006a, arXiv preprint astro-ph/0602012

Beuther H., Zhang Q., Sridharan T., Lee C.-F., Zapata L., 2006b, Astronomy & Astrophysics, 454, 221

Beuther H., Leurini S., Schilke P., Wyrowski F., Menten K., Zhang Q., 2007, Astronomy & Astrophysics, 466, 1065

Billington S., et al., 2019, Monthly Notices of the Royal Astronomical Society, 490, 2779

Blaszkiewicz L., Kus A. J., 2003, VizieR Online Data Catalog, pp J/A+A/413/233

Blitz L., 2000, Interstellar Molecular Clouds. p. 1711, doi:10.1888/0333750888/1711

Bolatto A. D., Leroy A. K., Rosolowsky E., Walter F., Blitz L., 2008, The Astrophysical Journal, 686, 948

Bonnell I. A., 2002, in Crowther P., ed., Astronomical Society of the Pacific Conference Series Vol. 267, Hot Star Workshop III: The Earliest Phases of Massive Star Birth. p. 193 (`arXiv:astro-ph/0111275`)

Bonnell I. A., Bate M. R., 2006, Monthly Notices of the Royal Astronomical Society, 370, 488

Bonnell I. A., Bate M. R., Zinnecker H., 1998, Monthly Notices of the Royal Astronomical Society, 298, 93

Bonnell I., Bate M., Clarke C., Pringle J., 2001, Monthly Notices of the Royal Astronomical Society, 323, 785

Boogert A. C. A., et al., 2008, ApJ, 678, 985

Boogert A. C. A., Gerakines P. A., Whittet D. C. B., 2015, ARA&A, 53, 541

Bottinelli S., et al., 2010, ApJ, 718, 1100

Bourke T. L., Hyland A., Robinson G., 2005, The Astrophysical Journal, 625, 883

Bouton E., Verschuur G. L., Kellermann K. I., 2012, Galactic and extragalactic radio astronomy. Springer Science & Business Media

Brand J., Blitz L., 1993, Astronomy and Astrophysics, 275, 67

Brand J., Wouterloot J. G. A., 1995, A&A, 303, 851

Breen S. L., Ellingsen S. P., Caswell J. L., Lewis B. E., 2010, MNRAS, 401, 2219

Breen S., et al., 2015, Monthly Notices of the Royal Astronomical Society, 450, 4109

Carpenter J. M., Snell R. L., Schloerb F. P., 1990, The Astrophysical Journal, 362, 147

Caswell J. L., 1996, MNRAS, 279, 79

Caswell J., 1997, Monthly Notices of the Royal Astronomical Society, 289, 203

Caswell J. L., Vaile R. A., Forster J. R., 1995, MNRAS, 277, 210

Caswell J., et al., 2010, Monthly Notices of the Royal Astronomical Society, 404, 1029

Caswell J., et al., 2011, Monthly Notices of the Royal Astronomical Society, 417, 1964

Caux E., Bottinelli S., Vastel C., Glorian J., 2011, The Molecular Universe, 280, 120

Cesaroni R., 2005, Proceedings of the International Astronomical Union, 1, 59

Chen X., Ellingsen S. P., Shen Z. Q., 2009, MNRAS, 396, 1603

Chen X., Gan C.-G., Ellingsen S. P., He J.-H., Shen Z.-Q., Titmarsh A., 2013, The Astrophysical Journal Supplement Series, 206, 22

Chiar J. E., Adamson A. J., Whittet D. C. B., 1996, ApJ, 472, 665

Chibueze J. O., et al., 2017, The Astrophysical Journal, 836, 59

Choi M., Kang M., Lee J.-E., 2015, The Astronomical Journal, 150, 29

Churchwell E., 2002, Annual Review of Astronomy and Astrophysics, 40, 27

Compiègne M., Flagey N., Noriega-Crespo A., Martin P., Bernard J.-P., Paladini R., Molinari S., 2010, The Astrophysical Journal Letters, 724, L44

Contreras Y., et al., 2013, Astronomy & Astrophysics, 549, A45

Cragg D. M., Johns K. P., Godfrey P. D., Brown R. D., 1992, MNRAS, 259, 203

Cragg D. M., Sobolev A. M., Godfrey P. D., 2005, MNRAS, 360, 533

Crowther P. A., Schnurr O., Hirschi R., Yusof N., Parker R. J., Goodwin S. P., Kassim H. A., 2010, Monthly Notices of the Royal Astronomical Society, 408, 731

Csengeri T., et al., 2014, Astronomy & Astrophysics, 565, A75

Cuppen H. M., Penteado E. M., Isokoski K., van der Marel N., Linnartz H., 2011, MNRAS, 417, 2809

Cyganowski C. J., et al., 2008, AJ, 136, 2391

Cyganowski C., Brogan C. L., Hunter T. R., Churchwell E., 2009, in American Astronomical Society Meeting Abstracts #213. p. 439.13

Cyganowski C. J., Brogan C. L., Hunter T. R., Smith R., Kruijssen J. M. D., Bonnell I. A., Zhang Q., 2017, Monthly Notices of the Royal Astronomical Society, 468, 3694–3708

Dartois E., Schutte W., Geballe T. R., Demyk K., Ehrenfreund P., D'Hendecourt L., 1999, A&A, 342, L32

De Villiers H. M., et al., 2015, Monthly Notices of the Royal Astronomical Society, 449, 119

De Vries C. H., Myers P. C., 2005, The Astrophysical Journal, 620, 800

Dib S., Schmeja S., Hony S., 2017, Monthly Notices of the Royal Astronomical Society, 464, 1738

Dobbs C. L., et al., 2014, Protostars and Planets VI, 1312, 3

Edgar R., Clarke C., 2004, Monthly Notices of the Royal Astronomical Society, 349, 678

Egan M. P., Price S. D., 1996, AJ, 112, 2862

Egan M., Shipman R., Price S., Carey S., Clark F., Cohen M., 1998, The Astrophysical Journal Letters, 494, L199

Elia D., et al., 2017, Monthly Notices of the Royal Astronomical Society, 471, 100

Elitzur M., 1992, Astronomical masers. Vol. 170, doi:10.1007/978-94-011-2394-5,

Ellingsen S., 2004, in Symposium-International Astronomical Union. pp 133–140

Ellingsen S. P., 2005, MNRAS, 359, 1498

Ellingsen S. P., 2006a, ApJ, 638, 241

Ellingsen S., 2006b, The Astrophysical Journal, 638, 241

Ellingsen S. P., 2007, VizieR Online Data Catalog, p. J/MNRAS/377/571

Ellingsen S. P., von Bibra M. L., McCulloch P. M., Norris R. P., Deshpande A. A., Phillips C. J., 1996, MNRAS, 280, 378

Elmegreen B., 1994, The Astrophysical Journal, 433, 39

Elmegreen B. G., 1998, in Woodward C. E., Shull J. M., Thronson Harley A. J., eds, Astronomical Society of the Pacific Conference Series Vol. 148, Origins. p. 150 (`arXiv:astro-ph/9712352`)

Figer D. F., Najarro F., Geballe T., Blum R., Kudritzki R. P., 2005, The Astrophysical Journal Letters, 622, L49

Fontani F., Cesaroni R., Caselli P., Olmi L., 2002, Astronomy & Astrophysics, 389, 603

Friberg P., Madden S. C., Hjalmarson A., Irvine W. M., 1988, A&A, 195, 281

Fuchs G. W., Cuppen H. M., Ioppolo S., Romanzin C., Bisschop S. E., Andersson S., van Dishoeck E. F., Linnartz H., 2009, A&A, 505, 629

Fukui Y., Kawamura A., 2010, Annual Review of Astronomy and Astrophysics, 48, 547

Garay G., Faúndez S., Mardones D., Bronfman L., Chini R., Nyman L.-Å., 2004, The Astrophysical Journal, 610, 313

Garrod R., Park I. H., Caselli P., Herbst E., 2006, Faraday Discussions, 133, 51

Gaume R. A., Claussen M. J., de Pree C. G., Goss W. M., Mehringer D. M., 1995, ApJ, 449, 663

Gentry E. S., 2013, arXiv preprint arXiv:1312.2105

Geppert W. D., et al., 2006, Faraday Discussions, 133, 177

Gerner T., Beuther H., Semenov D., Linz H., Vasyunina T., Bihr S., Shirley Y. L., Henning T., 2014, Astronomy & Astrophysics, 563, A97

Giannetti A., et al., 2013, Astronomy & Astrophysics, 556, A16

Giannetti A., Wyrowski F., Leurini S., Urquhart J., Csengeri T., Menten K., Bronfman L., Van der Tak F., 2015, Astronomy & Astrophysics, 580, L7

Gibb E. L., et al., 2000, ApJ, 536, 347

Goddi C., Moscadelli L., Sanna A., 2011, Astronomy & Astrophysics, 535, L8

Goldsmith P., Langer W., Wilson R., 1986, The Astrophysical Journal, 303, L11

Gray M., 1999, Philosophical Transactions of the Royal Society of London Series A, 357, 3277

Green J., McClure-Griffiths N., 2011, Monthly Notices of the Royal Astronomical Society, 417, 2500

Green J., et al., 2009, Monthly Notices of the Royal Astronomical Society, 392, 783

Green J., et al., 2010, Monthly Notices of the Royal Astronomical Society, 409, 913

Green J., et al., 2012, Monthly Notices of the Royal Astronomical Society, 420, 3108

Green J., et al., 2017, Monthly Notices of the Royal Astronomical Society, 469, 1383

Grim R. J. A., Baas F., Geballe T. R., Greenberg J. M., Schutte W. A., 1991, A&A, 243, 473

Guilloteau S., Baudry A., 1981, Astronomy and Astrophysics, 97, 213

Gutermuth R. A., Heyer M., 2014, in American Astronomical Society Meeting Abstracts# 223.

Guzmán V. V., et al., 2013, A&A, 560, A73

Guzmán A. E., Sanhueza P., Contreras Y., Smith H. A., Jackson J. M., Hoq S., Rathborne J. M., 2015, The Astrophysical Journal, 815, 130

Hartmann L., Calvet N., Gullbring E., D'Alessio P., 1998, The Astrophysical Journal, 495, 385

Haschick A. D., Baan W. A., 1989, ApJ, 339, 949

Haschick A. D., Menten K. M., Baan W. A., 1990, ApJ, 354, 556

He Y.-X., et al., 2016, Monthly Notices of the Royal Astronomical Society, 461, 2288

Hennebelle P., Pérault M., Teyssier D., Ganesh S., 2001, Astronomy & Astrophysics, 365, 598

Heyer M. H., Carpenter J. M., Snell R. L., 2001, The Astrophysical Journal, 551, 852

Hill T., Burton M., Minier V., Thompson M., Walsh A., Hunt-Cunningham M., Garay G., 2005, Monthly Notices of the Royal Astronomical Society, 363, 405

Hiraoka K., Ohashi N., Kihara Y., Yamamoto K., Sato T., Yamashita A., 1994, Chemical Physics Letters, 229, 408

Hoare M., Kurtz S., Lizano S., Keto E., Hofner P., 2007, B. Reipurth, D. Jewitt & K. Keil, pp 181–196

Hoq S., et al., 2013, The Astrophysical Journal, 777, 157

Jackson J., et al., 2013, Publications of the Astronomical Society of Australia, 30

Jin M., Lee J.-E., Kim K.-T., 2015, The Astrophysical Journal Supplement Series, 219, 2

Jones B., et al., 2020, Monthly Notices of the Royal Astronomical Society, 493, 2015

Kalenskii S. V., Kurtz S., Slysh V. I., Hofner P., Walmsley C. M., Johansson L. E. B., Bergman P., 2010, Astronomy Reports, 54, 932

Kalenskiĭ S. V., Slysh V. I., Val'tts I. E., Winnberg A., Johansson L. E., 2001, Astronomy Reports, 45, 26

Kauffmann J., Pillai T., Shetty R., Myers P. C., Goodman A. A., 2010a, The Astrophysical Journal, 712, 1137

Kauffmann J., Pillai T., Shetty R., Myers P. C., Goodman A. A., 2010b, The Astrophysical Journal, 716, 433

Kemball A. J., Gaylard M. J., Nicolson G. D., 1988, ApJ, 331, L37

Kennicutt R. C., 2005, Proceedings of the International Astronomical Union, 1, 3

Kennicutt Jr R. C., 1998, Annual Review of Astronomy and Astrophysics, 36, 189

Kessler M., et al., 1996, Astronomy and Astrophysics, 315, L27

Klaassen P., Testi L., Beuther H., 2012, Astronomy & Astrophysics, 538, A140

Koo B.-C., Williams D. R. D., Heiles C., Backer D. C., 1988, ApJ, 326, 931

Kroupa P., 2001, Monthly Notices of the Royal Astronomical Society, 322, 231

Kroupa P., 2002, Science, 295, 82

Kurtz S., 2005a, Proceedings of the International Astronomical Union, 1, 111

Kurtz S., 2005b, in Lis D. C., Blake G. A., Herbst E., eds, Vol. 231, Astrochemistry: Recent Successes and Current Challenges. pp 47–56, doi:10.1017/S1743921306007034

Kurtz S., Cesaroni R., Churchwell E., Hofner P., Walmsley C., 2000, Protostars and Planets IV (The University of Arizona Press), 299

Lada C. J., Lada E. A., 2003, Annual Review of Astronomy and Astrophysics, 41, 57

Ladd N., Purcell C., Wong T., Robertson S., 2005, Publications of the Astronomical Society of Australia, 22, 62

Lamb J., Oey M., Graus A., Adams F., Segura-Cox D., 2013, The Astrophysical Journal, 763, 101

Larson R. B., 2003, Reports on Progress in Physics, 66, 1651

Lee J.-E., Evans II N. J., Shirley Y. L., Tatematsu K., 2003, the Astrophysical Journal, 583, 789

Lees R. M., Baker J. G., 1968, J. Chem. Phys., 48, 5299

Leurini S., Menten K. M., Walmsley C. M., 2016, A&A, 592, A31

Liu X.-L., Wang J.-J., Xu J.-L., 2013, Monthly Notices of the Royal Astronomical Society, 431, 27

Liu T., et al., 2018, The Astrophysical Journal, 859, 151

López-Sepulcre A., Cesaroni R., Walmsley C., 2010, Astronomy & Astrophysics, 517, A66

Loughnane R., Redman M., Thompson M., Lo N., O'Dwyer B., Cunningham M., 2012, Monthly Notices of the Royal Astronomical Society, 420, 1367

Luna A., Bronfman L., Carrasco L., May J., 2006, The Astrophysical Journal, 641, 938

Mac Low M.-M., Klessen R. S., 2004, Reviews of modern physics, 76, 125

MacLeod G. C., Gaylard M. J., 1992, MNRAS, 256, 519

Magnani L., Blitz L., Mundy L., 1985, The Astrophysical Journal, 295, 402

Mardones D., Myers P., Tafalla M., Wilner D., Bachiller R., Garay G., 1997, The Astrophysical Journal, 489, 719

Massi F., et al., 2019, Astronomy & Astrophysics, 628, A110

McKee C. F., Ostriker E. C., 2007, Annu. Rev. Astron. Astrophys., 45, 565

McKee C. F., Tan J. C., 2003, The Astrophysical Journal, 585, 850

McMillan P. J., Binney J. J., 2010, Monthly Notices of the Royal Astronomical Society, 402, 934

Mendes M. B., et al., 2012, The Astrophysical Journal Letters, 746, L8

Menten K. M., 1991, ApJ, 380, L75

Menten K. M., Walmsley C. M., Henkel C., Wilson T. L., Snyder L. E., Hollis J. M., Lovas F. J., 1986, A&A, 169, 271

Menten K. M., Reid M. J., Moran J. M., Wilson T. L., Johnston K. J., Batrla W., 1988, ApJ, 333, L83

Menten K., Reid M., Pratap P., Moran J., Wilson T., 1992, The Astrophysical Journal, 401, L39

Mezger P., Altenhoff W., Schraml J., Burke B., Reifenstein III E., Wilson T., 1967, The Astrophysical Journal, 150, L157

Miettinen O., 2014, Astronomy & Astrophysics, 562, A3

Millar T. J., 1993, The Chemistry of Hot Molecular Cores. p. 249

Minier V., Booth R., Conway J., 1998, Astronomy and Astrophysics, 336, L5

Minier V., Booth R., Conway J., 2000, Astronomy and Astrophysics, 362, 1093

Minier V., Conway J., Booth R., 2001, Astronomy & Astrophysics, 369, 278

Minier V., Booth R., Conway J., 2002, Astronomy & Astrophysics, 383, 614

Minier V., Ellingsen S., Norris R., Booth R., 2003, Astronomy & Astrophysics, 403, 1095

Molinari S., Pezzuto S., Cesaroni R., Brand J., Faustini F., Testi L., 2008, Astronomy & Astrophysics, 481, 345

Molinari S., et al., 2010, Publications of the Astronomical Society of the Pacific, 122, 314

Möller T., Endres C., Schilke P., 2017, Astronomy & Astrophysics, 598, A7

Moscadelli L., Menten K. M., Walmsley C. M., Reid M. J., 2002, ApJ, 564, 813

Motte F., Schilke P., Lis D. C., 2003, The Astrophysical Journal, 582, 277

Motte F., et al., 2018, Nature Astronomy, 2, 478

Müller H. S. P., Menten K. M., Mäder H., 2004, A&A, 428, 1019

Mullins A., Loughnane R., Redman M., Wiles B., Guegan N., Barrett J., Keto E., 2016, Monthly Notices of the Royal Astronomical Society, 459, 2882

Myers P., Dame T., Thaddeus P., Cohen R., Silverberg R., Dwek E., Hauser M., 1986, The Astrophysical Journal, 301, 398

Nanda Kumar M., Kamath U., Davis C., 2004, Monthly Notices of the Royal Astronomical Society, 353, 1025

Nomura H., Millar T., 2004, Astronomy & Astrophysics, 414, 409

Norris R. P., Caswell J. L., Gardner F. F., Wellington K. J., 1987, ApJ, 321, L159

Norris R. P., McCutcheon W. H., Caswell J. L., Wellington K. J., Reynolds J. E., Peng R. S., Kesteven M. J., 1988, Nature, 335, 149

Öberg K. I., Garrod R. T., van Dishoeck E. F., Linnartz H., 2009, A&A, 504, 891

Öberg K. I., Lauck T., Graninger D., 2014, ApJ, 788, 68

Offner S. S. R., Hansen C. E., Krumholz M. R., 2009, The Astrophysical Journal, 704, L124

Oka T., Hasegawa T., Sato F., Tsuboi M., Miyazaki A., Sugimoto M., 2001, The Astrophysical Journal, 562, 348

Padoan P., 1995, Monthly Notices of the Royal Astronomical Society, 277, 377

Palla F., Stahler S. W., 1993, The Astrophysical Journal, 418, 414

Pandian J. D., Goldsmith P. F., Deshpande A. A., 2007, The Astrophysical Journal, 656, 255

Pandian J., Leurini S., Menten K., Belloche A., Goldsmith P., 2008, Astronomy & Astrophysics, 489, 1175

Pandian J., Menten K., Goldsmith P., 2009, The Astrophysical Journal, 706, 1609

Pandian J., Momjian E., Xu Y., Menten K., Goldsmith P., 2010, Astronomy & Astrophysics, 522, A8

Pandian J., Momjian E., Xu Y., Menten K., Goldsmith P., 2011, The Astrophysical Journal, 730, 55

Pandian J., Wyrowski F., Menten K., 2012, The Astrophysical Journal, 753, 50

Parise B., et al., 2002, A&A, 393, L49

Peng R. S., Whiteoak J. B., 1993, MNRAS, 260, 529

Penteado E. M., Boogert A. C. A., Pontoppidan K. M., Ioppolo S., Blake G. A., Cuppen H. M., 2015, MNRAS, 454, 531

Perault M., et al., 1996, Astronomy and astrophysics, 315, L165

Pestalozzi M., Elitzur M., Conway J., 2009, Astronomy & Astrophysics, 501, 999

Phillips C., Norris R., Ellingsen S., McCulloch P., 1998, Monthly Notices of the Royal Astronomical Society, 300, 1131

Pihlström Y. M., Sjouwerman L. O., Fish V. L., 2011, ApJ, 739, L21

Pillai T., Wyrowski F., Carey S. J., Menten K. M., 2006, Astronomy & Astrophysics, 450, 569

Pontoppidan K. M., Dartois E., van Dishoeck E. F., Thi W. F., d'Hendecourt L., 2003, A&A, 404, L17

Pratap P., Shute P. A., Keane T. C., Battersby C., Sterling S., 2008, AJ, 135, 1718

Price S. D., Egan M. P., Carey S. J., Mizuno D. R., Kuchar T. A., 2001, The Astronomical Journal, 121, 2819

Qasim D., Chuang K. J., Fedoseev G., Ioppolo S., Boogert A. C. A., Linnartz H., 2018, A&A, 612, A83

Rabli D., Flower D., 2010, Monthly Notices of the Royal Astronomical Society, 403, 2033

Rathborne J. M., Jackson J., Simon R., 2006, The Astrophysical Journal, 641, 389

Rathborne J., et al., 2016, Publications of the Astronomical Society of Australia, 33

Reid M. J., Moran J. M., 1988, Astronomical masers.. pp 255–294

Reid M., et al., 2009, The Astrophysical Journal, 700, 137

Reid M., et al., 2014, The Astrophysical Journal, 783, 130

Reid M., Dame T., Menten K., Brunthaler A., 2016, The Astrophysical Journal, 823, 77

Rivilla V. M., Fontani F., Beltrán M., Vasyunin A., Caselli P., Martín-Pintado J., Cesaroni R., 2017, Proceedings of the International Astronomical Union, 13, 409

Robitaille T. P., Whitney B. A., Indebetouw R., Wood K., 2007, The Astrophysical Journal Supplement Series, 169, 328

Rosen A. L., Li P. S., Zhang Q., Burkhart B., 2019, The Astrophysical Journal, 887, 108

Rosolowsky E., et al., 2010, The Astrophysical Journal Supplement Series, 188, 123

Rybicki G. B., Lightman A. P., 1985, Radiative processes in astrophysics.

Salpeter E. E., 1955, ApJ, 121, 161

Sanhueza P., Jackson J. M., Foster J. B., Garay G., Silva A., Finn S. C., 2012, The Astrophysical Journal, 756, 60

Saraceno P., André P., Ceccarelli C., Griffin M., Molinari S., 1996, Astronomy and Astrophysics, 309, 827

Saral G., Audard M., Wang Y., 2018, Astronomy & Astrophysics, 620, A158

Schilke P., 2015, EAS Publications Series, 75, 227

Schilke P., Walmsley C. M., Pineau Des Forets G., Roueff E., Flower D. R., Guilloteau S., 1992, A&A, 256, 595

Schlingman W. M., et al., 2011, The Astrophysical Journal Supplement Series, 195, 14

Schuller F., et al., 2009, Astronomy & Astrophysics, 504, 415

Scoville N., Good J., 1989, The Astrophysical Journal, 339, 149

Shima K., Tasker E. J., Habe A., 2017, MNRAS, 467, 512

Shu F. H., Adams F. C., Lizano S., 1987a, ARA&A, 25, 23

Shu F. H., Adams F. C., Lizano S., 1987b, Annual review of astronomy and astrophysics, 25, 23

Simon R., Jackson J. M., Rathborne J. M., Chambers E. T., 2006, The Astrophysical Journal, 639, 227

Skinner C. J., Tielens A. G. G. M., Barlow M. J., Justtanont K., 1992, ApJ, 399, L79

Slysh V. I., Kalenskii S. V., Valtts I. E., Otrupcek R., 1994, MNRAS, 268, 464

Sobolev A. M., 1992, Soviet Astronomy, 36, 590

Sobolev A. M., Deguchi S., 1994, A&A, 291, 569

Sobolev A. M., Cragg D. M., Godfrey P. D., 1997, A&A, 324, 211

Sobolev A. M., Ostrovskii A. B., Kirsanova M. S., Shelemei O. V., Voronkov M. A., Malyshev A. V., 2005, in Cesaroni R., Felli M., Churchwell E., Walmsley M., eds, Vol. 227, Massive Star Birth: A Crossroads of Astrophysics. pp 174–179, doi:10.1017/S1743921305004503

Sobolev A., et al., 2007, Proceedings of the International Astronomical Union, 3, 81

Solomon P., Rivolo A., Barrett J., Yahil A., 1987, The Astrophysical Journal, 319, 730

Sridharan T., Beuther H., Schilke P., Menten K., Wyrowski F., 2002, The Astrophysical Journal, 566, 931

Stark A. A., Lee Y., 2005, The Astrophysical Journal Letters, 619, L159

Szczepanski J. C., Ho P. T. P., Haschick A. D., Baan W. A., 1989, in Morris M., ed., Vol. 136, The Center of the Galaxy. p. 383

Szymczak M., Kus A., Hrynek G., Kępa A., Pazderski E., 2002, Astronomy & Astrophysics, 392, 277

Taban I. M., Schutte W. A., Pontoppidan K. M., van Dishoeck E. F., 2003, A&A, 399, 169

Tackenberg J., Beuther H., Plume R., Henning T., Stil J., Walmsley M., Schuller F., Schmiedeke A., 2013, Astronomy & Astrophysics, 550, A116

Takahira K., Tasker E. J., Habe A., 2014, The Astrophysical Journal, 792, 63

Tan J. C., 2007, in Elmegreen B. G., Palous J., eds, Vol. 237, Triggered Star Formation in a Turbulent ISM. pp 258–264 (`arXiv:astro-ph/0610490`), doi:10.1017/S1743921307001573

Tan J. C., Kong S., Butler M. J., Caselli P., Fontani F., 2013, The Astrophysical Journal, 779, 96

Tan J., Beltrán M., Caselli P., et al., 2014

Taquet V., López-Sepulcre A., Ceccarelli C., Neri R., Kahane C., Charnley S. B., 2015, ApJ, 804, 81

Townsley L. K., Broos P. S., Garmire G. P., Bouwman J., Povich M. S., Feigelson E. D., Getman K. V., Kuhn M. A., 2014, The Astrophysical Journal Supplement Series, 213, 1

Traficante A., Fuller G., Pineda J., Pezzuto S., 2015, Astronomy & Astrophysics, 574, A119

Turner B. E., 1998, ApJ, 501, 731

Urquhart J., et al., 2013a, Monthly Notices of the Royal Astronomical Society, 431, 1752

Urquhart J., et al., 2013b, Monthly Notices of the Royal Astronomical Society, 431, 1752

Urquhart J., et al., 2014a, Monthly Notices of the Royal Astronomical Society, 443, 1555

Urquhart J., et al., 2014b, Monthly Notices of the Royal Astronomical Society, 446, 3461

Urquhart J., et al., 2015, Monthly Notices of the Royal Astronomical Society, 446, 3461

Urquhart J., et al., 2019, Monthly Notices of the Royal Astronomical Society, 484, 4444

Val'tts I. E., Ellingsen S. P., Slysh V. I., Kalenskii S. V., Otrupcek R., Larionov G. M., 2000, MNRAS, 317, 315

Voronkov M. A., Caswell J. L., Britton T. R., Green J. A., Sobolev A. M., Ellingsen S. P., 2010, MNRAS, 408, 133

Voronkov M. A., Caswell J. L., Ellingsen S. P., Green J. A., Breen S. L., 2014, MNRAS, 439, 2584

Walsh A., Burton M., Hyland A., Robinson G., 1998, Monthly Notices of the Royal Astronomical Society, 301, 640

Walsh A., Macdonald G., Alvey N., Burton M., Lee J.-K., 2003, Astronomy & Astrophysics, 410, 597

Wang K., Zhang Q., Wu Y., Zhang H., 2011, The Astrophysical Journal, 735, 64

Watanabe N., Kouchi A., 2002, ApJ, 571, L173

Weaver H., Williams D. R. W., Dieter N. H., Lum W. T., 1965, Nature, 208, 29

Weinreb S., Barrett A. H., Meeks M. L., Henry J. C., 1963, Nature, 200, 829

Williams J. P., Blitz L., Mckee C. F., 2000, in University of Arizona.

Wirström E. S., et al., 2011, A&A, 533, A24

Wright N. J., 2015, arXiv preprint arXiv:1512.06854

Wright M., Gray M., Diamond P., 2004, Monthly Notices of the Royal Astronomical Society, 350, 1272

Wu J., Evans II N. J., 2003, The Astrophysical Journal Letters, 592, L79

Wyrowski F., et al., 2016, Astronomy & Astrophysics, 585, A149

Xu Y., Li J., Hachisuka K., Pandian J., Menten K., Henkel C., 2008, Astronomy & Astrophysics, 485, 729

Yorke H. W., 1986, Annual review of astronomy and astrophysics, 24, 49

Yorke H. W., Sonnhalter C., 2002, The Astrophysical Journal, 569, 846

Young L. M., Keto E., Ho P. T., 1998, The Astrophysical Journal, 507, 270

Yu N.-P., Wang J.-J., 2013, Research in Astronomy and Astrophysics, 13, 28

Zeng Q., 1992, in Singh P. D., ed., Vol. 150, Astrochemistry of Cosmic Phenomena. p. 341

Zhang Y., Tan J. C., 2015, ApJ, 802, L15

Zhang Y.-J., et al., 2016, Astrophysics and Space Science, 361, 191

Zhou C., Zhu M., Yuan J., Wu Y., Yuan L., Moore T., Eden D., 2019, Monthly Notices of the Royal Astronomical Society, 485, 3334

Zinnecker H., 2002, in , The Evolution of Galaxies. Springer, pp 147–158

Zinnecker H., Yorke H. W., 2007, Annual Review of Astronomy and Astrophysics, 45

Zinnecker H., McCaughrean M., Rayner J., Wilking B., Moneti A., 1993, in Reviews in Modern Astronomy. pp 191–208

van Dishoeck E. F., Hogerheijde M. R., 1999, in Lada C. J., Kylafis N. D., eds, NATO Advanced Study Institute (ASI) Series C Vol. 540, The Origin of Stars and Planetary Systems. p. 97 (`arXiv:astro-ph/9906119`)

van der Walt J., 2005, MNRAS, 360, 153

List of Publications

Refereed Journals

1. Sonu Tabitha Paulson, Jagadheep D Pandian, Probing the early phases of high-mass star formation with 6.7 GHz methanol masers, Monthly Notices of the Royal Astronomical Society, Volume 492, Issue 1, February 2020, Pages 1335–1347, https://doi.org/10.1093/mnras/stz3558
2. Sonu Tabitha Paulson, Jagadheep D Pandian, Chemical environments of 6.7 GHz methanol maser sources, Monthly Notices of the Royal Astronomical Society, Volume 509, Issue 3, January 2022, Pages 3677–3692, https://doi.org/10.1093/mnras/stab3227

Refereed Conferences

1. Paulson, S., & Pandian, J. (2017). Probing Early Phases of High Mass Stars with 6.7 GHz Methanol Masers. Proceedings of the International Astronomical Union, 13(S336), 323-324. doi:10.1017/S1743921318000376

Appendix A

SED fits and Data Tables

A.1 Data tables

Table A.1: Flux densities of sources hosting 6.7 GHz methanol masers from 870 to 160 μms. The uncertainties in the measured flux densities are given in parentheses.

Source name	Flux density (Jy)				
	870 μm	500 μm	350 μm	250 μm	160 μm
G345.131−0.174	4.15 (0.11)	17.52 (0.77)	49.45 (1.56)	97.06 (2.64)	125.80 (4.46)
G345.576−0.225	1.90 (0.06)	6.71 (0.40)	19.95 (0.79)	29.80 (1.03)	33.28 (0.90)
G345.807−0.044	0.84 (0.05)	3.92 (0.33)	8.03 (0.48)	11.69 (0.65)	9.75 (0.48)
G345.824+0.044	2.85 (0.09)	5.40 (0.82)	21.25 (2.15)	44.66 (2.92)	61.33 (3.30)
G345.985−0.020	2.29 (0.07)	18.31 (0.46)	46.04 (1.02)	91.47 (2.08)	175.43 (5.99)
G346.036+0.048	1.47 (0.05)	7.62 (0.33)	21.18 (0.68)	48.29 (1.21)	99.01 (3.40)
G346.231+0.119	1.28 (0.05)	12.67 (1.90)	27.89 (0.89)	47.01 (1.24)	85.72 (2.82)
G346.480+0.221	5.17 (0.14)	19.14 (0.45)	57.10 (1.23)	87.11 (2.12)	79.99 (2.91)
G346.481+0.132	2.66 (0.07)	15.28 (0.61)	39.76 (0.59)	78.84 (1.58)	161.35 (5.33)
G346.517+0.117	1.14 (0.11)	18.50 (1.27)	32.55 (3.99)	23.53 (5.04)	32.99 (1.67)
G347.230+0.016	1.59 (0.10)	15.67 (0.92)	30.97 (1.61)	26.66 (2.48)	36.01 (1.91)
G347.628+0.149	13.82 (0.41)	83.03 (2.32)	290.12 (6.93)	710.10 (17.80)	1239.24 (46.40)
G348.884+0.096	2.42 (0.10)	11.29 (0.74)	31.39 (1.31)	57.09 (1.67)	71.19 (2.32)
G349.067−0.017	1.53 (0.05)	7.83 (0.43)	23.27 (0.58)	50.16 (1.29)	110.16 (3.13)
G349.092+0.105	9.88 (0.24)	83.42 (1.74)	225.93 (6.06)	394.96 (10.31)	815.80 (21.63)
G349.151+0.021	2.35 (0.16)	12.49 (1.05)	35.12 (2.19)	64.03 (3.45)	96.63 (4.66)
G349.884+0.231	0.63 (0.03)	4.07 (0.19)	11.10 (0.35)	28.04 (0.92)	58.46 (2.75)
G350.015+0.433	7.75 (0.14)	57.07 (0.32)	170.45 (1.42)	396.75 (7.66)	1018.96 (28.11)
G350.116+0.220	1.23 (0.06)	6.67 (0.22)	15.67 (0.61)	19.08 (0.92)	33.49 (1.07)
G350.299+0.122	3.59 (0.11)	24.31 (1.00)	58.49 (2.61)	103.84 (2.25)	157.14 (4.73)

Continued on next page

Table A.1 – continued from previous page

Source name	Flux density (Jy)				
	870 μm	500 μm	350 μm	250 μm	160 μm
G350.340+0.141	5.08 (0.25)	31.30 (4.26)	69.43 (13.61)	155.54 (9.29)	293.56 (9.56)
G350.344+0.116	3.70 (0.31)	40.64 (2.83)	87.18 (9.04)	118.74 (19.97)	194.80 (5.09)
G350.356−0.068	1.16 (0.04)	6.78 (0.42)	18.65 (0.61)	37.16 (0.94)	65.36 (1.78)
G350.520−0.350	5.02 (0.13)	27.04 (0.94)	70.53 (1.70)	129.59 (3.25)	172.16 (5.90)
G350.686−0.491	7.49 (0.24)	39.35 (0.84)	118.05 (2.72)	235.02 (5.93)	365.90 (14.61)
G351.382−0.181	1.66 (0.05)	9.66 (0.16)	26.11 (0.38)	49.57 (0.99)	77.27 (2.42)
G351.688+0.171	1.38 (0.07)	11.69 (0.76)	29.38 (2.25)	58.71 (2.19)	94.91 (4.65)
G352.083+0.167	1.40 (0.07)	9.91 (0.73)	27.54 (1.39)	50.15 (2.48)	79.69 (3.93)
G352.111+0.176	3.18 (0.13)	23.29 (0.91)	54.33 (2.01)	86.06 (3.12)	121.42 (3.36)
G352.133−0.944	3.85 (0.15)	27.74 (0.67)	68.65 (2.28)	132.26 (4.31)	279.58 (13.65)
G352.525−0.158	2.41 (0.09)	6.57 (0.90)	32.38 (1.40)	79.71 (3.66)	107.81 (17.76)
G352.604−0.225	2.85 (0.12)	13.55 (1.61)	32.24 (3.14)	47.42 (1.95)	30.66 (1.39)
G352.855−0.201	8.60 (0.22)	42.45 (0.98)	140.61 (2.81)	348.08 (8.35)	773.24 (28.67)
G353.216−0.249	2.95 (0.10)	17.59 (0.43)	58.82 (1.37)	118.38 (3.20)	160.02 (7.45)
G353.378+0.438	1.13 (0.04)	5.38 (0.20)	12.29 (0.45)	25.52 (0.74)	32.92 (1.92)
G353.429−0.090	4.22 (0.15)	32.80 (2.60)	80.58 (3.89)	131.59 (3.11)	179.77 (5.25)
G353.464+0.562	6.48 (0.15)	43.97 (0.50)	113.18 (1.49)	221.35 (3.65)	386.89 (12.22)
G353.537−0.091	1.12 (0.07)	5.49 (0.56)	12.63 (0.92)	26.58 (1.16)	31.21 (1.71)
G354.496+0.083	1.57 (0.09)	5.99 (0.44)	18.87 (1.25)	28.57 (2.49)	29.78 (2.51)
G354.615+0.472	16.20 (0.36)	112.07 (1.96)	288.81 (4.91)	529.51 (12.98)	992.39 (26.83)
G354.701+0.299	7.48 (0.25)	41.06 (1.20)	136.43 (3.77)	196.20 (9.57)	261.80 (11.24)
G354.724+0.300	10.43 (0.28)	85.11 (1.34)	230.51 (4.68)	478.57 (11.41)	932.11 (27.30)
G355.538−0.105	2.37 (0.08)	17.27 (0.40)	49.43 (1.14)	105.75 (2.49)	235.57 (6.14)
G355.642+0.398	1.16 (0.05)	7.19 (0.35)	17.47 (0.72)	27.28 (0.96)	39.87 (1.32)
G005.618−0.082	4.69 (0.15)	33.64 (0.48)	65.57 (1.19)	101.33 (2.18)	102.29 (3.26)
G005.630−0.294	1.86 (0.06)	11.47 (0.35)	27.96 (0.75)	59.00 (1.27)	129.81 (3.34)
G006.189−0.358	11.21 (0.27)	50.42 (0.71)	188.97 (3.07)	419.85 (9.85)	867.27 (23.64)
G006.368−0.052	3.14 (0.10)	15.61 (0.40)	52.17 (1.08)	110.69 (2.92)	185.00 (6.66)
G008.317−0.096	1.45 (0.09)	7.31 (0.86)	21.22 (1.75)	21.25 (1.95)	21.21 (1.25)
G008.683−0.368	5.65 (0.17)	34.08 (0.77)	108.23 (2.07)	227.30 (5.32)	389.40 (10.69)
G008.832−0.028	2.26 (0.16)	19.03 (0.88)	41.34 (1.42)	93.42 (2.96)	138.04 (4.30)
G010.444−0.018	4.75 (0.14)	33.22 (3.32)	70.83 (2.13)	130.08 (4.11)	157.45 (4.52)
G010.629−0.333	14.41 (0.38)	70.58 (13.10)	210.41 (17.42)	487.07 (14.54)	682.15 (24.32)
G010.724−0.334	4.05 (0.16)	18.46 (0.99)	55.75 (2.00)	81.11 (2.97)	112.08 (3.71)
G010.886+0.123	1.73 (0.07)	12.01 (0.44)	35.92 (1.28)	80.35 (2.51)	175.80 (9.20)
G010.958+0.022	5.75 (0.14)	33.00 (0.44)	105.02 (1.06)	254.29 (4.22)	608.26 (16.79)
G011.034+0.062	3.63 (0.11)	25.41 (0.52)	71.34 (1.32)	157.02 (3.28)	363.28 (9.80)
G011.109−0.114	3.73 (0.16)	26.90 (1.27)	51.13 (2.05)	90.67 (2.39)	144.25 (4.56)

Continued on next page

Table A.1 – continued from previous page

Source name	Flux density (Jy)				
	870 μm	500 μm	350 μm	250 μm	160 μm
G011.903−0.102	1.69 (0.07)	11.85 (2.37)	30.74 (4.52)	54.48 (1.74)	84.86 (2.04)
G011.992−0.272	1.91 (0.08)	12.12 (0.77)	29.87 (0.91)	62.06 (1.67)	117.38 (3.58)
G012.025−0.031	2.41 (0.08)	16.00 (0.38)	39.82 (0.96)	76.46 (2.09)	147.67 (4.32)
G012.265−0.051	1.58 (0.05)	10.67 (0.43)	24.16 (0.83)	46.93 (1.38)	61.10 (2.19)
G012.526+0.016	1.42 (0.06)	8.97 (0.39)	25.58 (0.61)	44.71 (1.07)	59.14 (2.23)
G012.625−0.017	7.76 (0.27)	55.04 (1.46)	149.77 (3.16)	267.98 (7.11)	335.37 (12.25)
G012.889+0.489	19.14 (0.54)	111.22 (2.67)	364.60 (6.62)	592.89 (21.91)	1815.19 (104.41)
G013.179+0.061	14.17 (0.38)	67.43 (3.85)	198.70 (8.38)	347.91 (12.45)	456.45 (16.42)
G013.657−0.599	7.60 (0.21)	43.31 (0.68)	156.49 (2.08)	366.71 (7.59)	742.11 (25.43)
G013.713−0.083	2.87 (0.12)	13.54 (0.66)	45.37 (1.78)	95.25 (3.11)	187.45 (6.10)
G014.101+0.087	5.96 (0.14)	40.89 (0.72)	107.82 (1.95)	235.22 (5.05)	371.14 (14.03)
G014.390−0.020	1.06 (0.05)	5.32 (0.61)	15.63 (1.56)	41.30 (1.91)	72.98 (3.51)
G014.631−0.577	16.07 (0.47)	70.09 (2.01)	209.46 (6.58)	408.52 (12.38)	500.24 (16.05)
G014.991−0.121	2.97 (0.09)	15.04 (0.64)	43.18 (1.18)	90.46 (2.34)	142.97 (4.65)
G015.665−0.499	6.07 (0.17)	49.28 (1.09)	108.64 (2.28)	231.63 (4.44)	421.94 (12.21)
G016.112−0.303	0.69 (0.04)	3.99 (0.26)	11.60 (0.57)	21.67 (0.88)	28.01 (1.61)
G016.302−0.196	0.78 (0.04)	9.27 (1.07)	13.84 (1.24)	27.80 (0.81)	42.27 (1.65)
G016.403−0.181	1.33 (0.04)	11.79 (1.15)	27.92 (1.48)	59.17 (1.56)	107.38 (2.91)
G016.585−0.051	9.81 (0.24)	74.89 (0.96)	184.69 (2.04)	340.37 (5.90)	727.68 (23.29)
G016.831+0.079	2.70 (0.07)	16.39 (0.38)	41.06 (0.83)	79.64 (1.74)	137.98 (3.92)
G016.855+0.641	1.96 (0.06)	12.50 (0.37)	27.61 (0.78)	43.78 (1.05)	57.54 (1.68)
G017.029−0.071	2.34 (0.07)	15.46 (0.41)	38.47 (1.16)	76.52 (2.02)	125.35 (4.01)
G017.862+0.074	1.58 (0.05)	7.28 (0.39)	23.75 (0.66)	57.43 (1.24)	112.47 (3.36)
G018.159+0.094	0.68 (0.03)	5.08 (0.30)	10.85 (0.52)	20.81 (0.89)	31.07 (1.65)
G018.262−0.244	5.47 (0.20)	48.09 (1.73)	83.58 (4.23)	102.35 (6.74)	190.16 (6.61)
G018.460−0.004	2.49 (0.13)	22.76 (0.97)	50.30 (2.61)	62.72 (4.85)	140.39 (6.84)
G018.661+0.034	4.97 (0.12)	20.42 (0.65)	62.66 (1.17)	127.09 (2.91)	180.80 (7.82)
G018.733−0.224	6.81 (0.24)	47.86 (1.46)	150.65 (3.28)	300.26 (6.66)	449.93 (16.54)
G018.735−0.227	6.81 (0.24)	47.86 (1.46)	150.65 (3.28)	300.26 (6.66)	449.93 (16.54)
G018.874+0.053	2.11 (0.07)	15.20 (0.69)	29.03 (1.43)	49.28 (2.17)	73.74 (3.19)
G018.888−0.475	8.66 (0.39)	59.50 (2.27)	200.83 (6.58)	257.10 (8.58)	249.07 (9.18)
G018.999−0.239	1.19 (0.05)	7.22 (0.45)	18.11 (0.72)	29.77 (0.90)	24.27 (0.77)
G019.009−0.029	6.48 (0.16)	29.16 (1.29)	91.29 (2.53)	194.64 (5.12)	367.12 (11.39)
G019.249+0.267	1.58 (0.04)	11.30 (0.24)	24.92 (0.26)	43.00 (0.82)	46.66 (1.46)
G019.365−0.030	6.44 (0.25)	50.26 (1.38)	134.43 (3.46)	270.33 (7.20)	406.01 (14.60)
G019.486+0.151	2.68 (0.18)	30.07 (3.49)	58.51 (9.80)	93.81 (8.72)	133.25 (5.31)
G019.496+0.115	1.02 (0.06)	8.07 (0.74)	20.33 (1.54)	35.88 (1.47)	59.21 (3.27)
G019.612−0.120	1.81 (0.09)	12.00 (0.39)	33.13 (1.05)	78.05 (3.50)	141.17 (6.56)

Continued on next page

Table A.1 – continued from previous page

Source name	Flux density (Jy)				
	870 μm	500 μm	350 μm	250 μm	160 μm
G019.612−0.134	5.56 (0.15)	26.42 (0.71)	97.45 (1.44)	239.03 (4.93)	443.87 (16.23)
G019.667+0.117	0.70 (0.03)	5.27 (0.16)	12.07 (0.36)	18.08 (0.46)	27.09 (0.79)
G019.701−0.267	3.13 (0.11)	15.57 (0.89)	50.82 (2.22)	94.90 (3.25)	164.13 (4.81)
G330.226+0.290	1.18 (0.05)	4.46 (0.19)	13.81 (0.39)	26.25 (0.84)	35.07 (1.46)
G330.283+0.493	5.35 (0.13)	34.56 (0.41)	92.35 (1.53)	178.79 (3.89)	359.40 (13.22)
G330.875−0.383	11.23 (0.64)	79.61 (3.40)	214.05 (13.12)	318.26 (27.96)	332.89 (38.91)
G331.059+0.375	0.82 (0.04)	4.24 (0.33)	10.49 (0.54)	19.68 (0.82)	26.82 (1.88)
G331.134+0.156	2.93 (0.11)	20.63 (0.97)	39.25 (2.16)	59.88 (2.15)	82.13 (3.42)
G331.342−0.346	4.60 (0.21)	39.35 (1.40)	100.47 (3.33)	225.95 (6.84)	494.34 (16.66)
G331.425+0.264	1.51 (0.05)	7.04 (0.22)	21.82 (0.43)	45.03 (0.97)	64.66 (2.65)
G331.442−0.187	11.38 (0.28)	71.95 (1.76)	178.71 (3.01)	372.33 (7.58)	682.91 (21.92)
G331.710+0.603	7.82 (0.41)	45.59 (1.91)	149.79 (5.66)	294.84 (12.52)	510.23 (16.09)
G332.094−0.421	12.96 (0.35)	80.31 (1.49)	284.90 (4.95)	678.53 (17.08)	1480.67 (60.81)
G332.295−0.094	15.39 (0.36)	69.00 (1.50)	236.35 (4.62)	514.99 (11.74)	1060.61 (37.93)
G332.351−0.436	4.65 (0.14)	15.09 (0.59)	41.54 (1.33)	79.01 (2.43)	72.37 (3.30)
G332.352−0.117	3.68 (0.12)	21.58 (0.76)	62.10 (1.63)	142.47 (3.77)	268.38 (9.36)
G332.364+0.607	4.32 (0.13)	15.88 (0.39)	44.74 (1.24)	64.74 (2.33)	59.22 (3.49)
G332.560−0.148	3.51 (0.12)	14.41 (2.16)	43.99 (5.10)	96.26 (3.84)	85.79 (4.08)
G332.604−0.168	2.38 (0.08)	16.43 (0.74)	42.87 (1.63)	69.92 (2.06)	93.11 (4.96)
G332.701−0.588	3.58 (0.16)	25.58 (4.00)	70.57 (11.62)	127.18 (3.94)	245.37 (8.54)
G332.813−0.701	3.76 (0.10)	12.87 (0.46)	48.90 (1.04)	101.92 (2.52)	204.90 (6.48)
G332.942−0.686	7.22 (0.33)	50.73 (4.81)	132.98 (14.73)	258.11 (9.20)	506.64 (17.02)
G332.987−0.487	8.37 (0.29)	52.39 (3.96)	171.59 (9.04)	378.82 (12.94)	744.60 (26.93)
G333.029−0.063	4.68 (0.13)	23.45 (0.91)	87.29 (1.90)	237.79 (5.17)	561.24 (18.11)
G333.109−0.500	6.19 (0.28)	32.32 (2.57)	79.75 (4.65)	188.93 (10.23)	398.81 (19.73)
G333.128−0.440	18.87 (0.53)	88.18 (2.66)	282.49 (5.83)	527.04 (13.99)	666.83 (24.37)
G333.130−0.560	18.87 (0.53)	88.18 (2.66)	280.84 (5.82)	520.05 (13.66)	666.83 (24.37)
G333.163−0.101	6.17 (0.23)	27.28 (1.47)	94.60 (4.10)	244.15 (8.45)	531.31 (18.18)
G333.184−0.091	4.48 (0.18)	16.71 (1.42)	65.11 (5.14)	145.22 (4.87)	244.99 (9.45)
G333.234−0.060	13.80 (0.31)	86.88 (1.10)	223.28 (3.20)	407.62 (8.20)	699.81 (21.84)
G333.315+0.105	7.42 (0.25)	33.96 (0.91)	119.48 (2.63)	279.13 (6.12)	536.58 (19.14)
G333.387+0.032	3.05 (0.08)	21.47 (0.35)	51.56 (0.82)	100.01 (1.60)	169.26 (8.05)
G333.646+0.058	5.48 (0.17)	17.37 (1.27)	50.88 (2.67)	96.21 (3.68)	119.52 (5.04)
G333.851+0.527	1.84 (0.06)	6.07 (0.18)	15.82 (0.45)	23.81 (0.66)	19.81 (0.98)
G333.900−0.099	0.95 (0.04)	5.78 (0.38)	12.79 (0.61)	15.50 (0.92)	19.75 (0.97)
G334.138−0.023	0.94 (0.04)	6.92 (0.30)	17.15 (0.63)	33.73 (0.88)	67.84 (2.55)
G335.556−0.307	0.65 (0.04)	2.86 (5.25)	8.59 (7.52)	22.21 (0.69)	52.54 (2.06)
G335.585−0.285	26.92 (0.54)	128.22 (1.65)	434.56 (7.18)	872.34 (23.42)	2006.64 (63.93)

Continued on next page

Table A.1 – continued from previous page

Source name	Flux density (Jy)				
	870 μm	500 μm	350 μm	250 μm	160 μm
G335.726+0.191	2.26 (0.10)	15.39 (1.48)	27.34 (3.23)	60.15 (2.20)	95.33 (3.14)
G336.018−0.827	15.43 (0.35)	58.26 (0.88)	222.02 (3.82)	537.60 (12.13)	884.63 (29.88)
G336.809+0.119	3.66 (0.10)	15.55 (0.99)	47.59 (1.99)	95.33 (2.95)	108.84 (4.53)
G336.825+0.139	1.90 (0.12)	9.76 (1.17)	22.56 (2.85)	40.29 (3.74)	30.22 (1.81)
G336.916−0.024	3.52 (0.14)	23.31 (1.97)	56.62 (2.66)	120.15 (4.44)	209.58 (11.12)
G336.957−0.225	2.58 (0.06)	15.36 (0.58)	32.59 (1.21)	46.91 (1.36)	47.28 (1.44)
G336.958−0.977	3.95 (0.11)	24.33 (0.41)	50.61 (1.11)	75.88 (1.72)	83.98 (2.49)
G337.052−0.226	0.72 (0.03)	3.77 (0.25)	12.42 (0.55)	28.98 (0.56)	57.93 (1.95)
G337.097−0.929	4.03 (0.13)	17.83 (0.67)	61.01 (1.50)	138.48 (3.31)	241.26 (11.93)
G337.153−0.395	4.41 (0.21)	26.90 (1.62)	69.81 (2.81)	103.06 (3.45)	127.74 (5.49)
G337.176−0.032	8.41 (0.29)	35.62 (2.56)	120.54 (6.31)	227.41 (9.73)	192.38 (7.44)
G337.201+0.114	1.38 (0.06)	12.10 (0.68)	24.94 (1.13)	62.97 (2.31)	132.86 (7.05)
G337.202−0.094	1.34 (0.10)	7.15 (1.82)	15.25 (3.13)	20.61 (1.79)	26.98 (1.35)
G337.258−0.101	4.81 (0.14)	23.77 (1.03)	77.00 (2.09)	156.90 (3.95)	240.43 (7.61)
G337.263−0.070	4.75 (0.14)	23.50 (0.96)	76.79 (1.98)	156.90 (3.95)	240.44 (7.61)
G337.300−0.874	3.54 (0.08)	20.94 (0.24)	48.36 (0.61)	91.44 (1.67)	131.07 (4.20)
G337.388−0.210	1.91 (0.08)	13.03 (0.39)	32.67 (0.96)	60.21 (2.19)	109.01 (7.63)
G337.632−0.079	3.24 (0.12)	25.74 (2.57)	65.82 (5.71)	128.96 (3.30)	231.82 (9.20)
G337.686+0.137	2.59 (0.10)	10.56 (0.77)	30.48 (1.16)	62.03 (2.04)	67.87 (3.18)
G337.966−0.169	2.54 (0.11)	11.98 (1.38)	37.66 (2.07)	84.73 (3.82)	79.90 (3.78)
G337.997+0.136	5.06 (0.17)	28.15 (1.71)	47.30 (2.90)	72.73 (2.90)	38.14 (5.82)
G338.140+0.178	1.69 (0.07)	6.80 (0.50)	22.13 (0.94)	35.63 (1.29)	43.84 (1.59)
G338.160−0.064	1.42 (0.07)	24.94 (0.54)	20.09 (1.35)	29.46 (1.60)	28.28 (1.26)
G338.280+0.542	5.20 (0.15)	29.79 (0.84)	72.68 (2.33)	140.75 (3.15)	231.28 (6.97)
G338.287+0.120	8.62 (0.21)	33.42 (1.10)	101.22 (2.45)	191.67 (4.82)	237.07 (7.77)
G338.325−0.409	2.04 (0.09)	15.24 (0.50)	48.60 (1.33)	90.68 (2.36)	134.27 (6.67)
G338.392−0.403	3.49 (0.12)	15.10 (0.83)	39.42 (1.72)	93.43 (3.16)	187.13 (7.77)
G338.461−0.245	4.12 (0.12)	20.46 (0.81)	75.94 (2.15)	184.10 (4.54)	386.62 (11.30)
G338.472+0.289	3.24 (0.08)	24.94 (0.32)	71.57 (0.56)	155.65 (2.65)	338.49 (8.83)
G338.497+0.207	2.50 (0.08)	11.06 (0.84)	30.21 (1.44)	51.20 (1.26)	50.56 (1.99)
G338.561+0.218	3.52 (0.11)	25.35 (0.73)	56.64 (1.40)	98.90 (2.27)	158.93 (5.25)
G338.566+0.110	5.26 (0.18)	28.15 (1.01)	88.62 (1.91)	176.35 (3.98)	277.69 (13.35)
G338.850+0.409	7.19 (0.20)	34.07 (0.85)	121.61 (1.99)	295.86 (7.36)	652.28 (21.63)
G338.875−0.084	0.72 (0.03)	4.76 (0.26)	14.00 (0.37)	32.03 (0.78)	63.97 (2.56)
G338.902+0.394	3.60 (0.16)	46.59 (1.34)	109.03 (3.17)	209.74 (3.98)	423.52 (17.21)
G338.925+0.634	14.64 (0.39)	76.66 (1.60)	248.22 (3.76)	556.50 (13.13)	659.97 (29.41)
G339.053−0.315	2.15 (0.06)	13.36 (0.26)	34.69 (0.55)	67.58 (1.54)	115.85 (3.92)
G339.064+0.152	1.85 (0.07)	11.80 (1.24)	27.52 (1.10)	49.36 (0.96)	68.53 (2.42)

Continued on next page

Table A.1 – continued from previous page

Source name	Flux density (Jy)				
	870 μm	500 μm	350 μm	250 μm	160 μm
G339.282+0.136	3.79 (0.13)	23.27 (0.42)	58.27 (1.10)	105.73 (2.72)	142.62 (4.69)
G339.294+0.139	2.10 (0.10)	8.25 (0.43)	30.34 (1.01)	64.06 (2.29)	67.41 (3.23)
G339.476+0.185	5.67 (0.14)	42.37 (0.43)	120.68 (1.39)	258.22 (4.67)	476.29 (16.39)
G339.477+0.043	1.47 (0.07)	4.99 (0.87)	14.83 (0.96)	26.93 (1.05)	38.02 (1.39)
G339.582−0.127	8.89 (0.22)	33.62 (2.04)	100.33 (2.98)	191.06 (4.36)	269.18 (10.99)
G339.622−0.121	9.46 (0.25)	44.35 (2.29)	144.62 (4.70)	347.86 (7.89)	764.67 (28.95)
G339.762+0.054	1.06 (0.05)	5.38 (0.65)	16.55 (1.14)	33.93 (1.35)	72.03 (2.54)
G339.909+0.240	1.83 (0.06)	8.60 (0.45)	19.29 (0.59)	30.47 (1.13)	37.81 (1.61)
G339.980−0.538	3.41 (0.12)	25.05 (2.06)	70.05 (6.91)	168.94 (3.88)	433.21 (13.88)
G339.986−0.425	1.61 (0.06)	13.92 (0.32)	39.43 (0.65)	92.91 (1.92)	254.06 (6.41)
G340.118−0.021	2.08 (0.07)	9.79 (0.54)	17.08 (0.96)	24.66 (1.05)	20.88 (1.33)
G340.249−0.046	6.84 (0.20)	59.46 (1.69)	175.83 (4.34)	384.79 (8.03)	878.08 (26.00)
G340.249−0.372	17.68 (0.53)	70.50 (1.45)	247.51 (4.34)	586.52 (15.40)	1134.01 (39.70)
G340.543−0.162	1.72 (0.10)	1.17 (0.54)	9.24 (1.35)	22.66 (1.72)	14.26 (1.47)
G340.655−0.235	1.21 (0.04)	5.34 (0.24)	12.48 (0.33)	19.82 (0.51)	24.45 (1.08)
G340.785−0.096	7.46 (0.15)	59.87 (0.86)	142.61 (1.74)	285.28 (5.03)	575.47 (16.81)
G341.124−0.361	6.72 (0.17)	38.72 (0.83)	99.88 (1.65)	216.07 (4.84)	332.19 (15.17)
G341.218−0.212	8.65 (0.25)	68.13 (2.23)	183.22 (6.48)	342.35 (9.40)	715.70 (22.36)
G341.238−0.270	5.45 (0.20)	39.63 (2.85)	86.67 (2.39)	147.98 (3.51)	171.53 (6.54)
G341.276+0.062	1.81 (0.05)	13.18 (0.27)	37.50 (0.51)	79.60 (1.75)	152.72 (5.21)
G341.367+0.336	0.80 (0.04)	4.32 (0.32)	10.06 (0.45)	13.50 (0.79)	11.08 (0.54)
G341.990−0.103	1.61 (0.05)	10.06 (0.28)	23.38 (0.58)	41.49 (0.93)	63.29 (2.13)
G305.799−0.245	19.46 (0.72)	89.76 (1.19)	304.70 (3.24)	575.93 (15.54)	2067.37 (115.31)
G308.754+0.549	2.42 (0.09)	21.34 (0.90)	50.82 (1.97)	104.65 (2.73)	214.17 (7.50)
G309.384−0.135	7.22 (0.29)	34.35 (1.04)	104.22 (2.65)	210.16 (5.34)	376.29 (11.26)
G311.947+0.142	3.18 (0.13)	17.92 (0.60)	52.83 (1.30)	99.72 (2.38)	157.10 (4.66)
G317.466−0.402	2.58 (0.09)	10.19 (0.69)	36.16 (0.85)	88.31 (2.10)	156.15 (4.81)
G317.701+0.110	5.70 (0.26)	38.87 (1.43)	113.04 (2.80)	212.16 (5.71)	354.03 (13.24)
G318.948−0.196	13.38 (0.40)	65.02 (1.34)	227.45 (4.36)	506.08 (11.94)	1252.81 (53.69)
G320.231−0.284	12.16 (0.29)	87.21 (0.82)	256.51 (2.96)	507.33 (11.77)	1277.08 (43.58)
G321.148−0.529	0.88 (0.10)	16.63 (0.56)	42.71 (1.33)	91.48 (3.25)	177.77 (10.02)
G324.923−0.568	6.77 (0.24)	43.28 (1.03)	154.39 (2.86)	337.13 (8.94)	904.91 (29.68)
G326.475+0.703	26.52 (0.72)	113.88 (1.57)	377.17 (6.17)	611.29 (19.30)	1530.54 (47.26)
G326.608+0.799	5.17 (0.20)	39.47 (1.04)	87.45 (2.06)	126.38 (3.30)	182.78 (5.65)
G326.859−0.677	4.25 (0.10)	27.37 (0.35)	63.76 (0.81)	117.29 (2.37)	168.29 (4.89)
G327.402+0.445	8.00 (0.16)	52.44 (0.56)	125.43 (1.42)	233.45 (4.40)	365.30 (11.08)
G327.392+0.199	22.29 (0.52)	111.44 (1.48)	379.78 (5.02)	714.52 (17.45)	1827.52 (65.60)
G327.590−0.094	1.79 (0.07)	8.94 (0.84)	25.96 (0.89)	47.35 (1.19)	70.41 (3.01)

Continued on next page

Table A.1 – continued from previous page

Source name	Flux density (Jy)				
	870 μm	500 μm	350 μm	250 μm	160 μm
G329.029−0.205	17.70 (0.37)	128.26 (1.67)	340.55 (4.50)	601.41 (16.89)	1045.51 (31.09)
G329.066−0.308	11.48 (0.34)	51.97 (1.22)	138.26 (2.65)	235.71 (5.90)	325.87 (9.98)
G329.183−0.314	13.02 (0.33)	99.07 (1.09)	255.02 (3.14)	446.20 (8.26)	1001.37 (37.01)
G329.469+0.503	7.06 (0.23)	48.98 (1.07)	121.34 (3.15)	228.40 (6.50)	403.30 (16.71)
G329.622+0.138	2.15 (0.09)	12.54 (0.69)	26.74 (1.50)	40.32 (1.62)	47.00 (3.15)
G023.706−0.198	5.46 (0.15)	25.11 (0.90)	82.05 (2.39)	187.89 (5.63)	358.80 (11.61)
G023.885+0.060	1.42 (0.06)	11.89 (0.44)	25.89 (1.28)	42.13 (2.04)	35.24 (2.11)
G023.966−0.109	8.47 (0.20)	57.15 (1.65)	139.95 (3.71)	261.75 (4.97)	381.07 (11.89)
G024.541+0.312	1.69 (0.07)	11.64 (1.11)	27.36 (1.21)	45.88 (1.52)	58.05 (2.54)
G024.634−0.324	3.39 (0.11)	16.10 (0.81)	45.83 (1.61)	91.91 (2.25)	144.38 (4.56)
G024.943+0.074	3.00 (0.09)	21.82 (1.21)	55.28 (4.16)	110.22 (2.74)	202.84 (6.56)
G025.270−0.434	2.60 (0.08)	12.65 (0.54)	37.31 (1.18)	70.77 (1.70)	86.05 (3.28)
G025.710+0.044	5.52 (0.13)	46.57 (0.66)	126.00 (2.06)	289.22 (6.76)	626.96 (16.53)
G025.826−0.178	3.13 (0.12)	34.00 (3.96)	84.35 (11.90)	201.81 (4.44)	445.51 (10.92)
G026.601−0.221	1.69 (0.05)	10.67 (0.29)	28.37 (0.54)	59.43 (1.04)	108.57 (3.04)
G027.286+0.151	4.93 (0.13)	26.46 (0.94)	78.65 (1.87)	163.84 (3.98)	250.40 (10.48)
G027.783−0.259	2.78 (0.09)	16.23 (0.56)	42.75 (1.79)	78.61 (1.95)	125.98 (3.11)
G027.784+0.057	4.25 (0.14)	21.49 (1.06)	65.56 (3.07)	130.80 (3.57)	222.30 (8.22)
G028.146−0.005	4.53 (0.11)	26.80 (0.49)	66.46 (1.33)	133.68 (3.22)	206.22 (5.87)
G028.397+0.081	10.19 (0.36)	63.38 (1.59)	185.66 (4.02)	352.45 (9.18)	456.83 (15.04)
G028.817+0.365	3.72 (0.10)	14.42 (0.31)	57.62 (0.88)	137.64 (2.36)	263.23 (8.47)
G028.842+0.493	3.21 (0.09)	21.67 (0.42)	46.24 (0.87)	79.47 (1.67)	101.02 (2.89)
G029.320−0.162	0.98 (0.05)	6.85 (0.45)	16.16 (0.77)	27.40 (1.08)	52.24 (2.78)
G033.133−0.092	7.66 (0.25)	43.88 (0.79)	152.80 (2.65)	361.79 (8.47)	769.25 (27.69)
G033.634−0.021	1.25 (0.08)	8.92 (0.72)	15.85 (1.43)	20.61 (1.13)	35.80 (2.27)
G033.852+0.018	1.58 (0.06)	9.22 (0.31)	21.35 (0.50)	31.24 (0.81)	41.45 (1.53)
G033.980−0.019	2.80 (0.07)	16.74 (0.29)	37.63 (0.68)	65.19 (1.71)	70.01 (2.25)
G034.757+0.025	2.91 (0.08)	20.52 (0.48)	53.93 (0.92)	109.95 (2.53)	206.42 (5.96)
G034.820+0.350	8.77 (0.23)	39.29 (0.84)	125.82 (2.04)	290.46 (6.71)	509.91 (16.97)
G035.132−0.744	13.90 (0.50)	118.75 (2.17)	255.66 (7.37)	437.98 (13.02)	660.28 (22.60)
G035.197−0.743	1.39 (0.52)	16.33 (5.63)	36.37 (17.06)	47.11 (18.49)	60.55 (6.35)
G035.397+0.025	1.56 (0.06)	7.15 (0.36)	19.00 (0.58)	37.19 (0.84)	53.52 (2.02)
G035.793−0.175	5.28 (0.13)	31.35 (0.56)	76.18 (1.02)	138.83 (2.62)	230.02 (6.41)
G036.115+0.552	2.57 (0.07)	15.33 (0.20)	41.98 (0.50)	84.84 (1.67)	177.77 (5.12)
G036.839−0.022	2.65 (0.11)	19.99 (0.57)	40.80 (1.12)	51.81 (1.60)	78.39 (2.73)
G036.918+0.483	1.21 (0.04)	4.43 (0.11)	14.56 (0.26)	33.34 (0.70)	64.27 (2.62)
G037.030−0.038	1.78 (0.08)	9.54 (0.33)	26.22 (0.76)	44.04 (1.90)	49.44 (2.48)
G037.043−0.035	4.47 (0.14)	17.91 (0.37)	54.36 (0.98)	113.68 (2.83)	177.40 (5.84)

Continued on next page

Table A.1 – continued from previous page

Source name	Flux density (Jy)				
	870 μm	500 μm	350 μm	250 μm	160 μm
G037.479−0.105	2.08 (0.07)	8.38 (0.41)	27.76 (0.78)	65.32 (1.54)	111.56 (3.50)
G037.554+0.201	7.19 (0.28)	56.69 (1.41)	140.35 (4.06)	315.83 (10.52)	684.06 (38.91)
G037.598+0.425	1.89 (0.07)	11.74 (0.18)	29.24 (0.41)	54.53 (1.04)	86.91 (2.86)
G037.735−0.112	5.45 (0.15)	34.75 (0.47)	97.83 (1.67)	195.14 (3.84)	364.55 (10.47)
G037.753−0.189	2.39 (0.08)	13.63 (1.95)	40.18 (3.51)	75.14 (2.12)	96.30 (3.23)
G037.767−0.214	5.89 (0.24)	35.53 (0.84)	93.70 (3.22)	194.34 (8.89)	226.68 (14.62)
G038.037−0.300	1.27 (0.06)	8.43 (0.26)	20.41 (0.54)	38.47 (1.03)	62.20 (2.13)
G038.119−0.229	2.35 (0.07)	12.45 (0.25)	40.59 (0.64)	94.30 (2.29)	193.42 (6.63)
G038.203−0.067	3.61 (0.10)	21.09 (0.42)	48.60 (0.81)	79.68 (1.54)	97.42 (3.52)
G038.255−0.200	0.93 (0.05)	4.73 (0.50)	15.19 (0.72)	34.04 (0.82)	74.45 (2.59)
G038.598−0.212	1.63 (0.06)	6.62 (0.49)	16.60 (0.66)	29.36 (1.06)	47.51 (1.94)
G038.653+0.088	2.12 (0.08)	7.62 (0.33)	21.47 (0.64)	32.70 (1.09)	65.79 (2.83)
G038.916−0.353	9.70 (0.29)	37.74 (1.04)	112.47 (2.46)	219.99 (5.71)	247.91 (9.00)
G039.388−0.141	3.88 (0.12)	25.07 (0.38)	70.37 (0.85)	162.72 (2.41)	387.32 (13.45)
G040.282−0.219	11.36 (0.27)	71.02 (0.52)	195.20 (1.75)	386.00 (5.79)	830.34 (31.84)
G041.075−0.125	2.90 (0.11)	9.65 (0.51)	29.43 (1.06)	43.16 (1.72)	60.80 (2.41)
G041.121−0.107	1.05 (0.05)	7.19 (0.35)	16.86 (0.61)	26.89 (0.75)	50.72 (2.34)
G041.123−0.220	3.52 (0.12)	12.86 (1.11)	32.52 (2.66)	62.99 (3.71)	87.91 (4.60)
G041.226−0.197	1.92 (0.07)	4.85 (0.66)	19.33 (1.06)	44.25 (1.25)	65.98 (3.04)
G041.348−0.136	1.14 (0.06)	6.79 (0.27)	16.06 (0.51)	30.87 (1.07)	53.11 (3.23)
G042.034+0.190	1.51 (0.08)	7.45 (0.32)	16.32 (0.64)	32.60 (0.89)	55.02 (2.09)
G042.304−0.299	2.43 (0.08)	13.33 (0.29)	29.06 (0.72)	45.57 (1.03)	62.72 (2.62)
G042.435−0.260	1.93 (0.08)	5.63 (0.60)	23.46 (1.51)	48.55 (2.81)	35.24 (4.26)
G043.074−0.077	2.10 (0.08)	9.02 (0.41)	30.27 (0.96)	62.01 (1.86)	73.52 (2.29)
G043.890−0.784	8.66 (0.30)	37.73 (0.57)	132.25 (2.55)	308.38 (7.57)	692.89 (22.06)
G044.310+0.041	5.74 (0.18)	48.47 (0.97)	113.86 (2.02)	223.69 (4.81)	484.96 (12.83)
G045.467+0.053	12.24 (0.38)	104.54 (1.56)	301.71 (5.27)	707.29 (17.47)	1406.78 (44.36)
G045.493+0.126	3.74 (0.22)	16.22 (1.22)	56.01 (5.27)	98.06 (11.52)	94.45 (7.00)
G045.804−0.356	3.29 (0.08)	20.28 (0.31)	55.13 (0.78)	127.27 (2.59)	267.82 (7.43)
G048.902−0.273	6.53 (0.41)	25.14 (3.11)	109.57 (7.34)	187.84 (12.08)	329.31 (21.38)
G048.990−0.299	14.59 (0.49)	73.46 (2.85)	219.75 (6.65)	475.54 (14.05)	892.44 (41.13)
G049.265+0.311	2.06 (0.07)	11.52 (0.14)	29.23 (0.33)	55.53 (1.04)	89.84 (2.90)
G049.617−0.360	1.48 (0.07)	5.49 (0.66)	14.49 (1.26)	31.73 (1.27)	32.26 (1.52)
G052.922+0.414	2.66 (0.08)	12.49 (0.38)	38.15 (0.77)	73.97 (1.76)	101.14 (3.42)
G053.142+0.071	10.49 (0.23)	64.42 (0.82)	159.39 (1.89)	306.50 (6.41)	559.24 (15.66)
G053.618+0.035	4.11 (0.12)	17.61 (0.56)	56.01 (1.49)	107.75 (3.29)	168.02 (5.96)
G020.239+0.065	2.98 (0.09)	14.59 (0.51)	46.97 (1.19)	98.02 (1.88)	158.36 (5.41)
G020.364−0.013	3.09 (0.12)	22.21 (0.51)	60.50 (1.63)	111.77 (3.85)	179.77 (9.33)

Continued on next page

Table A.1 – continued from previous page

Source name	Flux density (Jy)				
	870 μm	500 μm	350 μm	250 μm	160 μm
G020.733−0.059	6.40 (0.18)	29.69 (2.12)	90.30 (4.43)	167.00 (5.24)	196.45 (8.27)
G020.963−0.075	0.85 (0.04)	7.04 (0.18)	18.61 (0.41)	41.82 (0.93)	85.31 (3.46)
G023.003+0.124	1.28 (0.06)	6.86 (0.57)	18.05 (1.40)	25.92 (1.28)	34.05 (0.92)
G023.365−0.291	6.18 (0.19)	23.85 (3.20)	59.78 (3.09)	82.99 (2.86)	69.13 (3.01)
G023.389+0.185	4.19 (0.11)	25.70 (0.34)	64.68 (0.92)	120.07 (2.02)	210.30 (5.74)
G023.986−0.089	4.68 (0.14)	31.63 (2.31)	58.48 (5.95)	105.07 (3.60)	109.92 (4.51)
G023.996−0.100	3.98 (0.13)	17.73 (2.24)	55.14 (2.71)	117.39 (3.46)	178.21 (6.43)
G024.461+0.198	3.15 (0.12)	29.87 (1.57)	67.67 (2.52)	109.68 (2.53)	149.57 (6.80)
G025.226+0.288	4.49 (0.15)	24.36 (0.75)	69.77 (1.98)	115.08 (3.44)	94.63 (3.81)
G025.613+0.226	3.46 (0.12)	14.80 (0.78)	43.47 (1.63)	38.42 (1.62)	18.55 (0.96)
G025.838−0.378	2.57 (0.09)	8.99 (0.52)	23.63 (0.93)	37.33 (1.93)	40.15 (1.68)
G026.545+0.423	2.55 (0.11)	13.65 (1.81)	35.04 (3.96)	78.76 (2.63)	104.67 (4.23)
G027.011−0.039	1.18 (0.05)	4.49 (0.23)	14.52 (0.60)	35.97 (1.19)	51.81 (2.08)
G027.757+0.050	3.11 (0.11)	11.39 (1.17)	40.13 (3.12)	81.21 (2.04)	114.55 (3.47)
G028.321−0.011	4.54 (0.15)	18.19 (1.26)	55.69 (2.66)	112.77 (4.35)	156.89 (6.14)
G028.687−0.283	2.16 (0.08)	16.81 (0.79)	41.63 (1.82)	75.60 (1.82)	105.12 (3.16)
G029.603−0.625	2.74 (0.16)	17.53 (0.67)	49.09 (1.27)	87.69 (2.88)	76.89 (3.13)
G029.993−0.282	6.16 (0.17)	24.88 (0.49)	57.07 (1.40)	88.53 (2.72)	101.77 (3.72)
G030.010−0.273	1.56 (0.10)	10.09 (1.39)	33.34 (4.12)	58.39 (2.82)	160.03 (9.46)
G030.370+0.482	2.05 (0.09)	10.84 (0.54)	27.14 (1.14)	57.11 (2.25)	96.35 (5.21)
G030.400−0.296	8.36 (0.28)	52.65 (1.01)	132.83 (3.15)	179.38 (4.46)	314.75 (11.97)
G030.423+0.466	9.55 (0.32)	49.19 (1.60)	177.33 (4.15)	430.05 (10.78)	1049.34 (34.90)
G030.960+0.086	3.72 (0.14)	17.96 (1.00)	62.44 (1.73)	155.86 (3.95)	314.90 (9.82)
G030.973+0.562	0.76 (0.04)	4.94 (0.33)	14.27 (0.44)	39.34 (0.75)	76.38 (2.06)
G030.980+0.216	3.94 (0.13)	16.70 (1.06)	42.40 (1.91)	74.98 (3.27)	89.61 (3.81)
G031.122+0.063	1.20 (0.06)	5.31 (1.26)	15.81 (1.50)	35.22 (1.26)	79.91 (2.53)
G031.182−0.148	1.85 (0.09)	6.82 (0.61)	16.60 (1.59)	36.63 (2.29)	55.88 (2.25)
G032.825−0.328	5.11 (0.10)	38.43 (0.38)	104.93 (1.14)	218.80 (3.98)	483.77 (11.86)
G033.317−0.360	0.89 (0.04)	4.76 (0.21)	10.98 (0.25)	22.93 (0.55)	42.08 (0.95)
G034.267−0.210	1.73 (0.06)	11.10 (0.28)	27.51 (0.77)	55.36 (1.41)	104.68 (3.38)
G045.380−0.594	1.97 (0.07)	13.57 (0.27)	27.19 (0.57)	46.69 (0.85)	66.01 (2.60)
G052.199+0.723	3.30 (0.10)	12.61 (0.99)	42.40 (2.12)	104.15 (2.73)	198.64 (7.52)
G056.963−0.235	2.47 (0.07)	15.69 (0.31)	38.07 (0.80)	69.09 (1.45)	126.69 (3.53)
G057.610+0.025	1.82 (0.06)	8.02 (0.16)	25.37 (0.42)	55.59 (1.26)	106.37 (3.27)

Table A.2: The best fit parameters of sources. The columns show the source name, distance, temperature of the cold dust component, the solid angle of cold dust as seen in aperture photometry, optical depth of dust at 500 μm and the dust spectral index, β.

Source name	d (kpc)	T_c (K)	Ω_c (sr)	τ	β
G345.131-0.174	3.05	19.97	8.54×10^9	0.024	1.60
G345.576-0.225	5.50	17.80	1.05×10^8	0.010	1.45
G345.807-0.044	10.80	14.29	1.13×10^8	0.007	1.71
G345.824+0.044	10.90	25.04	1.36×10^8	0.005	1.00
G345.985-0.020	10.75	19.91	6.54×10^9	0.025	2.06
G346.036+0.048	10.90	27.56	7.90×10^9	0.006	1.53
G346.231+0.119	10.39	18.08	5.04×10^9	0.023	2.14
G346.480+0.221	14.18	16.32	8.23×10^9	0.042	1.73
G346.481+0.132	10.90	24.43	7.89×10^9	0.013	1.59
G346.517+0.117	10.90	13.14	3.74×10^9	0.072	2.79
G347.230+0.016	11.18	13.21	7.79×10^9	0.035	2.33
G347.628+0.149	5.30	24.40	9.06×10^9	0.075	2.13
G348.884+0.096	10.86	17.78	8.47×10^9	0.019	1.79
G349.067-0.017	11.30	28.26	6.90×10^9	0.007	1.53
G349.092+0.105	10.77	22.46	6.61×10^9	0.094	2.09
G349.151+0.021	11.30	19.40	7.32×10^9	0.019	1.79
G349.884+0.231	11.30	28.22	3.92×10^{10}	0.058	1.80
G350.015+0.433	12.83	26.69	8.51×10^9	0.041	1.98
G350.116+0.220	18.05	19.86	7.23×10^9	0.009	1.40
G350.299+0.122	11.13	19.11	6.37×10^9	0.038	1.87
G350.340+0.141	11.26	24.22	1.61×10^8	0.013	1.61
G350.344+0.116	11.00	16.26	7.23×10^9	0.068	2.51
G350.356-0.068	10.92	21.24	6.41×10^9	0.010	1.79
G350.520-0.350	3.56	18.20	1.09×10^8	0.031	1.84
G350.686-0.491	2.40	20.94	1.05×10^8	0.038	1.85
G351.382-0.181	5.76	19.00	5.99×10^9	0.018	1.90
G351.688+0.171	12.13	18.29	4.15×10^9	0.029	2.24
G352.083+0.167	10.73	23.96	3.92×10^{10}	0.191	2.03
G352.111+0.176	5.73	17.39	5.49×10^9	0.050	2.01
G352.133-0.944	1.72	22.09	4.74×10^9	0.046	1.85
G352.525-0.158	11.11	29.51	1.02×10^8	0.006	1.42
G352.604-0.225	5.10	12.47	1.28×10^8	0.034	2.19
G352.855-0.201	11.10	33.22	1.19×10^8	0.017	1.57
G353.216-0.249	4.09	17.38	9.66×10^9	0.027	2.31
G353.378+0.438	13.58	20.10	9.36×10^9	0.006	1.53
G353.429-0.090	10.61	17.86	6.65×10^9	0.052	2.06

Continued on next page

Table A.2 – continued from previous page

Source name	d (kpc)	T_c (K)	Ω_c (sr)	τ	β
G353.464+0.562	11.01	20.90	5.50×10^9	0.074	1.93
G353.537-0.091	10.76	18.01	2.86×10^9	0.025	1.74
G354.496+0.083	11.70	17.44	2.90×10^9	0.033	1.62
G354.615+0.472	4.74	23.06	7.30×10^9	0.118	1.90
G354.701+0.299	6.10	17.11	9.47×10^9	0.068	2.14
G354.724+0.300	5.80	22.55	7.63×10^9	0.088	2.13
G355.538-0.105	19.76	23.72	5.19×10^9	0.024	1.95
G355.642+0.398	14.22	17.90	5.07×10^9	0.016	1.80
G005.618-0.082	5.10	15.06	6.15×10^9	0.092	2.03
G005.630-0.294	2.80	27.55	6.49×10^9	0.009	1.51
G006.189-0.358	5.10	29.64	9.87×10^9	0.030	1.71
G006.368-0.052	7.40	21.66	8.21×10^9	0.019	1.89
G008.317-0.096	11.50	13.73	1.06×10^8	0.016	1.97
G008.683-0.368	5.02	21.18	7.08×10^9	0.048	2.06
G008.832-0.028	5.20	18.07	1.23×10^8	0.016	2.13
G010.444-0.018	10.83	17.25	7.22×10^9	0.054	2.00
G010.629-0.333	5.20	19.90	1.37×10^8	0.068	1.97
G010.724-0.334	5.20	18.48	7.25×10^9	0.034	1.67
G010.886+0.123	2.53	23.75	3.63×10^9	0.024	1.99
G010.958+0.022	13.43	30.59	5.08×10^9	0.034	1.77
G011.034+0.062	2.87	25.52	6.09×10^9	0.026	1.85
G011.109-0.114	13.49	20.48	7.11×10^9	0.028	1.61
G011.903-0.102	12.81	19.32	6.88×10^9	0.016	1.91
G011.992-0.272	11.46	23.11	6.58×10^9	0.013	1.70
G012.025-0.031	11.10	21.58	7.36×10^9	0.018	1.78
G012.265-0.051	11.15	16.79	8.28×10^9	0.017	2.05
G012.526+0.016	12.33	16.24	5.98×10^9	0.024	2.19
G012.625-0.017	2.73	16.64	1.31×10^8	0.062	2.29
G012.889+0.489	2.30	25.87	1.33×10^8	0.058	1.78
G013.179+0.061	4.37	19.30	1.24×10^8	0.069	1.76
G013.657-0.599	11.97	25.11	6.94×10^9	0.047	2.09
G013.713-0.083	4.14	25.62	8.70×10^9	0.012	1.64
G014.101+0.087	5.40	20.07	7.89×10^9	0.052	2.07
G014.390-0.020	13.51	22.79	8.64×10^9	0.006	1.82
G014.631-0.577	13.66	20.22	1.20×10^8	0.068	1.70
G014.991-0.121	12.31	20.95	1.26×10^8	0.012	1.75
G015.665-0.499	16.97	21.38	7.42×10^9	0.051	1.94
G016.112-0.303	3.29	16.36	8.58×10^9	0.008	2.14
G016.302-0.196	4.25	17.94	5.88×10^9	0.011	2.09

Continued on next page

Table A.2 – continued from previous page

Source name	d (kpc)	T_c (K)	Ω_c (sr)	τ	β
G016.403-0.181	12.75	19.83	7.38×10^9	0.013	2.14
G016.585-0.051	4.70	21.72	6.97×10^9	0.088	1.91
G016.831+0.079	11.75	20.79	1.03×10^8	0.014	1.75
G016.855+0.641	13.79	17.41	3.04×10^9	0.049	1.83
G017.029-0.071	10.50	19.23	9.66×10^9	0.017	1.94
G017.862+0.074	9.85	26.73	2.96×10^9	0.018	1.65
G018.159+0.094	11.77	17.48	9.96×10^9	0.006	2.00
G018.262-0.244	5.05	17.61	8.51×10^9	0.052	1.87
G018.460-0.004	3.92	17.82	8.51×10^9	0.026	2.06
G018.661+0.034	10.91	22.09	8.07×10^9	0.026	1.57
G018.733-0.224	12.39	18.26	1.23×10^8	0.050	2.33
G018.735-0.227	12.84	18.77	9.48×10^9	0.061	2.32
G018.874+0.053	12.79	17.74	8.86×10^9	0.017	1.82
G018.888-0.475	4.23	16.69	5.75×10^9	0.170	2.43
G018.999-0.239	4.79	12.88	1.12×10^8	0.018	2.42
G019.009-0.029	11.90	26.53	9.14×10^9	0.023	1.51
G019.249+0.267	14.11	15.63	3.04×10^9	0.057	2.14
G019.365-0.030	2.35	38.37	3.92×10^{10}	0.574	2.29
G019.486+0.151	1.97	16.61	7.08×10^9	0.040	2.31
G019.496+0.115	9.33	18.59	4.94×10^9	0.016	2.04
G019.612-0.120	12.00	21.37	8.26×10^9	0.013	1.99
G019.612-0.134	11.84	27.57	2.85×10^9	0.067	1.87
G019.667+0.117	14.59	17.00	4.78×10^9	0.013	1.90
G019.701-0.267	12.48	21.81	7.87×10^9	0.019	1.74
G330.226+0.290	5.53	20.41	8.01×10^9	0.007	1.55
G330.283+0.493	5.44	21.54	8.36×10^9	0.036	1.85
G330.875-0.383	4.41	16.62	7.74×10^9	0.160	2.38
G331.059+0.375	5.06	18.75	5.85×10^9	0.008	1.70
G331.134+0.156	4.53	17.19	1.08×10^8	0.020	1.75
G331.342-0.346	4.17	23.20	8.87×10^9	0.030	2.04
G331.425+0.264	9.55	19.72	9.96×10^9	0.008	1.85
G331.442-0.187	9.60	23.65	8.21×10^9	0.063	1.74
G331.710+0.603	4.59	21.10	9.97×10^9	0.046	2.02
G332.094-0.421	3.86	26.76	1.17×10^8	0.046	2.04
G332.295-0.094	3.00	32.24	6.55×10^9	0.056	1.51
G332.351-0.436	3.57	19.00	5.17×10^9	0.041	1.37
G332.352-0.117	3.12	23.29	1.11×10^8	0.015	1.83
G332.364+0.607	11.74	17.01	6.89×10^9	0.037	1.53
G332.560-0.148	3.68	14.64	1.33×10^8	0.031	2.21

Continued on next page

Table A.2 – continued from previous page

Source name	d (kpc)	T_c (K)	Ω_c (sr)	τ	β
G332.604-0.168	3.42	15.96	8.84×10^9	0.028	2.18
G332.701-0.588	11.03	23.20	1.61×10^8	0.010	1.77
G332.813-0.701	11.53	32.05	1.16×10^8	0.007	1.31
G332.942-0.686	3.54	23.88	1.16×10^8	0.028	1.77
G332.987-0.487	3.74	23.09	1.26×10^8	0.035	2.01
G333.029-0.063	2.89	32.29	7.49×10^9	0.017	1.77
G333.109-0.500	3.50	31.65	8.77×10^9	0.017	1.35
G333.128-0.440	2.70	20.89	7.45×10^9	0.138	1.89
G333.130-0.560	3.80	22.38	4.86×10^9	0.191	1.86
G333.163-0.101	5.67	33.10	1.14×10^8	0.013	1.52
G333.184-0.091	5.02	24.00	1.19×10^8	0.014	1.65
G333.234-0.060	5.18	22.47	5.42×10^9	0.136	1.83
G333.315+0.105	12.24	27.05	5.73×10^9	0.042	1.78
G333.387+0.032	10.56	18.37	6.34×10^9	0.038	2.00
G333.646+0.058	9.96	22.13	1.02×10^8	0.019	1.21
G333.851+0.527	12.34	16.24	1.32×10^8	0.008	1.46
G333.900-0.099	11.32	15.36	5.88×10^9	0.015	1.85
G334.138-0.023	12.93	22.00	6.78×10^9	0.008	1.82
G335.556-0.307	8.78	32.77	1.03×10^8	0.002	1.43
G335.585-0.285	3.48	47.59	1.66×10^9	0.244	1.46
G335.726+0.191	12.25	21.33	4.08×10^9	0.027	1.64
G336.018-0.827	11.81	31.70	6.41×10^9	0.051	1.57
G336.809+0.119	10.44	18.29	4.97×10^9	0.048	1.82
G336.825+0.139	10.28	13.69	7.15×10^9	0.033	2.13
G336.916-0.024	7.82	21.08	1.39×10^8	0.014	1.85
G336.957-0.225	11.16	14.67	1.07×10^8	0.025	1.94
G336.958-0.977	12.07	15.97	4.56×10^9	0.081	1.87
G337.052-0.226	10.75	23.76	7.32×10^9	0.004	1.85
G337.097-0.929	12.57	25.05	7.57×10^9	0.019	1.69
G337.153-0.395	3.61	16.61	7.57×10^9	0.051	1.95
G337.176-0.032	4.36	16.37	7.41×10^9	0.101	2.10
G337.201+0.114	11.66	24.02	4.37×10^9	0.016	1.91
G337.202-0.094	11.19	19.71	5.30×10^9	0.011	1.31
G337.258-0.101	11.13	20.29	9.45×10^9	0.029	1.89
G337.263-0.070	3.06	20.11	1.06×10^8	0.026	1.91
G337.300-0.874	10.34	18.71	7.23×10^9	0.032	1.77
G337.388-0.210	3.95	18.90	4.50×10^9	0.031	1.97
G337.632-0.079	4.01	21.38	5.48×10^9	0.035	1.99
G337.686+0.137	10.90	17.85	5.52×10^9	0.030	1.77

Continued on next page

Table A.2 – continued from previous page

Source name	d (kpc)	T_c (K)	Ω_c (sr)	τ	β
G337.966-0.169	4.15	15.32	1.01×10^8	0.027	2.25
G337.997+0.136	13.11	12.54	9.26×10^9	0.081	2.10
G338.140+0.178	12.98	17.39	1.58×10^8	0.007	1.74
G338.160-0.064	11.32	11.97	5.20×10^9	0.082	2.61
G338.280+0.542	4.05	21.63	6.31×10^9	0.040	1.66
G338.287+0.120	3.15	20.65	6.43×10^9	0.062	1.56
G338.325-0.409	2.23	16.92	5.90×10^9	0.038	2.44
G338.392-0.403	13.05	33.85	8.34×10^9	0.008	1.18
G338.461-0.245	3.81	26.56	1.09×10^8	0.014	1.83
G338.472+0.289	2.49	22.25	6.17×10^9	0.033	2.09
G338.497+0.207	2.41	15.94	4.83×10^9	0.044	1.87
G338.561+0.218	12.71	18.41	1.11×10^8	0.023	1.89
G338.566+0.110	4.86	20.35	7.20×10^9	0.043	1.95
G338.850+0.409	11.83	31.52	5.38×10^9	0.035	1.68
G338.875-0.084	3.27	22.02	6.94×10^9	0.006	2.00
G338.902+0.394	2.29	20.27	4.85×10^9	0.070	2.35
G338.925+0.634	4.28	21.96	5.77×10^9	0.136	2.09
G339.053-0.315	9.55	20.14	5.48×10^9	0.024	1.86
G339.064+0.152	10.49	18.02	8.93×10^9	0.015	1.86
G339.282+0.136	4.71	17.44	9.22×10^9	0.033	1.97
G339.294+0.139	4.90	16.63	8.96×10^9	0.018	2.14
G339.476+0.185	10.51	20.94	6.92×10^9	0.057	2.15
G339.477+0.043	15.00	21.68	6.70×10^9	0.008	1.30
G339.582-0.127	2.64	22.24	6.54×10^9	0.055	1.44
G339.622-0.121	2.81	31.99	8.71×10^9	0.028	1.52
G339.762+0.054	12.10	27.32	6.56×10^9	0.005	1.53
G339.909+0.240	14.78	17.93	1.19×10^8	0.009	1.50
G339.980-0.538	10.48	29.84	1.03×10^8	0.011	1.81
G339.986-0.425	10.47	26.81	6.38×10^9	0.012	1.99
G340.118-0.021	9.21	14.80	7.06×10^9	0.024	1.54
G340.249-0.046	9.10	23.49	9.58×10^9	0.043	2.19
G340.249-0.372	12.10	33.39	4.73×10^9	0.078	1.56
G340.543-0.162	3.96	19.08	8.08×10^9	0.007	1.00
G340.655-0.235	13.97	18.21	6.58×10^9	0.010	1.46
G340.785-0.096	9.85	21.57	7.23×10^9	0.065	1.98
G341.124-0.361	3.20	21.74	6.87×10^9	0.050	1.78
G341.218-0.212	3.25	22.43	1.07×10^8	0.046	1.98
G341.238-0.270	4.00	17.20	5.28×10^9	0.090	2.06
G341.276+0.062	11.24	19.70	9.83×10^9	0.014	2.16

Continued on next page

Table A.2 – continued from previous page

Source name	d (kpc)	T_c (K)	Ω_c (sr)	τ	β
G341.367+0.336	10.86	12.94	6.74×10^9	0.017	2.14
G341.990-0.103	3.27	18.52	8.61×10^9	0.013	1.79
G305.799-0.245	4.00	35.99	8.13×10^9	0.047	1.59
G308.754+0.549	6.67	21.34	7.53×10^9	0.020	2.04
G309.384-0.135	5.40	24.24	6.90×10^9	0.040	1.64
G311.947+0.142	8.02	20.32	3.59×10^9	0.053	1.91
G317.466-0.402	9.95	25.14	7.78×10^9	0.012	1.65
G317.701+0.110	2.91	19.60	8.31×10^9	0.050	2.08
G318.948-0.196	10.48	35.48	8.38×10^9	0.034	1.57
G320.231-0.284	4.27	25.18	8.03×10^9	0.074	1.96
G321.148-0.529	4.48	16.34	9.35×10^9	0.021	2.85
G324.923-0.568	5.09	28.05	9.42×10^9	0.028	1.96
G326.475+0.703	11.56	33.44	8.06×10^9	0.068	1.34
G326.608+0.799	11.18	17.12	7.79×10^9	0.060	1.93
G326.859-0.677	3.77	17.78	1.08×10^8	0.031	1.91
G327.402+0.445	5.21	20.01	5.51×10^9	0.095	1.88
G327.392+0.199	5.34	33.38	5.94×10^9	0.091	1.60
G327.590-0.094	8.91	19.39	4.68×10^9	0.023	1.77
G329.029-0.205	12.00	20.09	1.33×10^8	0.096	2.10
G329.066-0.308	11.61	24.68	1.52×10^9	0.292	1.57
G329.183-0.314	3.64	20.99	7.83×10^9	0.116	2.00
G329.469+0.503	10.12	20.95	5.66×10^9	0.077	1.91
G329.622+0.138	9.44	15.70	1.18×10^8	0.016	1.82
G023.706-0.198	6.21	28.29	4.65×10^9	0.035	1.56
G023.885+0.060	12.40	12.39	1.02×10^8	0.031	2.70
G023.966-0.109	11.40	19.22	8.34×10^9	0.071	1.97
G024.541+0.312	5.50	16.26	7.23×10^9	0.022	2.06
G024.634-0.324	12.60	22.11	3.68×10^9	0.042	1.63
G024.943+0.074	12.10	21.42	8.41×10^9	0.020	1.90
G025.270-0.434	11.60	17.72	5.29×10^9	0.035	1.93
G025.710+0.044	10.20	22.22	1.01×10^8	0.036	2.16
G025.826-0.178	5.00	22.86	8.63×10^9	0.023	2.29
G026.601-0.221	9.50	21.44	8.35×10^9	0.011	1.84
G027.286+0.151	12.90	21.37	4.38×10^9	0.061	1.87
G027.783-0.259	9.80	20.20	7.49×10^9	0.021	1.77
G027.784+0.057	5.70	23.09	3.99×10^9	0.047	1.70
G028.146-0.005	5.30	20.10	8.11×10^9	0.033	1.80
G028.397+0.081	4.20	42.93	3.67×10^{10}	0.805	2.26
G028.817+0.365	9.80	27.11	6.77×10^9	0.016	1.80

Continued on next page

Table A.2 – continued from previous page

Source name	d (kpc)	T_c (K)	Ω_c (sr)	τ	β
G028.842+0.493	4.60	16.65	7.35×10^{9}	0.039	1.93
G029.320-0.162	11.90	20.87	8.48×10^{9}	0.006	1.73
G033.133-0.092	4.20	25.50	1.10×10^{8}	0.029	2.01
G033.634-0.021	5.80	22.04	5.00×10^{9}	0.010	1.25
G033.852+0.018	10.50	20.45	3.92×10^{10}	0.238	1.71
G033.980-0.019	3.40	15.79	6.23×10^{9}	0.043	1.98
G034.757+0.025	4.70	20.80	7.04×10^{9}	0.026	1.97
G034.820+0.350	3.60	26.79	6.56×10^{9}	0.042	1.63
G035.132-0.744	2.10	19.29	8.10×10^{9}	0.147	2.08
G035.197-0.743	2.19	14.52	6.47×10^{9}	0.035	2.55
G035.397+0.025	6.10	21.08	1.83×10^{9}	0.040	1.59
G035.793-0.175	3.90	20.21	9.59×10^{9}	0.031	1.72
G036.115+0.552	3.50	23.64	1.01×10^{8}	0.011	1.71
G036.839-0.022	3.70	16.84	4.56×10^{9}	0.051	1.79
G036.918+0.483	15.80	30.66	5.75×10^{9}	0.004	1.42
G037.030-0.038	5.10	15.77	5.63×10^{9}	0.030	2.08
G037.043-0.035	1.88	24.23	5.20×10^{9}	0.028	1.53
G037.479-0.105	9.60	30.07	3.67×10^{10}	0.156	1.59
G037.554+0.201	5.60	23.40	7.46×10^{9}	0.053	1.97
G037.598+0.425	6.20	18.88	9.39×10^{9}	0.014	1.83
G037.735-0.112	10.30	22.08	6.23×10^{9}	0.048	1.89
G037.753-0.189	9.50	17.17	5.99×10^{9}	0.034	2.09
G037.767-0.214	9.40	17.54	9.84×10^{9}	0.049	2.09
G038.037-0.300	3.90	19.10	9.42×10^{9}	0.009	1.85
G038.119-0.229	5.50	25.41	1.01×10^{8}	0.009	1.82
G038.203-0.067	7.70	17.00	4.50×10^{9}	0.064	1.86
G038.255-0.200	9.00	27.31	5.44×10^{9}	0.006	1.64
G038.598-0.212	4.20	24.47	1.61×10^{8}	0.003	1.17
G038.653+0.088	16.30	28.55	5.93×10^{9}	0.008	1.00
G038.916-0.353	10.50	19.17	1.34×10^{8}	0.037	1.67
G039.388-0.141	4.30	27.42	1.22×10^{8}	0.012	1.72
G040.282-0.219	4.90	25.01	4.57×10^{9}	0.111	1.79
G041.075-0.125	8.40	21.78	7.24×10^{9}	0.014	1.19
G041.121-0.107	10.00	20.85	6.94×10^{9}	0.008	1.63
G041.123-0.220	8.70	24.27	4.70×10^{9}	0.022	1.12
G041.226-0.197	8.70	24.69	1.13×10^{8}	0.005	1.33
G041.348-0.136	11.60	20.86	8.61×10^{9}	0.007	1.66
G042.034+0.190	11.10	24.79	9.26×10^{9}	0.005	1.27
G042.304-0.299	10.50	17.58	9.43×10^{9}	0.017	1.61

Continued on next page

Table A.2 – continued from previous page

Source name	d (kpc)	T_c (K)	Ω_c (sr)	τ	β
G042.435-0.260	7.90	21.12	3.92×10^{10}	0.239	1.68
G043.074-0.077	11.20	17.53	8.33×10^{9}	0.018	1.99
G043.890-0.784	8.26	31.61	1.54×10^{8}	0.012	1.66
G044.310+0.041	7.90	22.08	1.11×10^{8}	0.031	1.91
G045.467+0.053	8.40	25.35	6.42×10^{9}	0.108	2.20
G045.493+0.126	7.10	17.16	1.17×10^{8}	0.022	1.81
G045.804-0.356	7.00	25.65	1.02×10^{8}	0.013	1.72
G048.902-0.273	5.10	22.79	9.02×10^{9}	0.031	1.69
G048.990-0.299	5.10	26.44	9.52×10^{9}	0.053	1.62
G049.265+0.311	10.50	20.19	8.54×10^{9}	0.013	1.71
G049.617-0.360	5.10	16.88	1.05×10^{8}	0.010	1.72
G052.922+0.414	5.10	18.72	1.13×10^{8}	0.015	1.87
G053.142+0.071	1.90	21.68	1.36×10^{8}	0.040	1.73
G053.618+0.035	2.10	22.52	6.54×10^{9}	0.026	1.59
G020.239+0.065	4.10	21.31	5.91×10^{9}	0.026	1.85
G020.364-0.013	3.70	18.57	4.45×10^{9}	0.058	2.16
G020.733-0.059	11.90	17.73	9.12×10^{9}	0.051	1.90
G020.963-0.075	13.10	20.64	5.08×10^{9}	0.012	2.13
G023.003+0.124	5.60	17.63	7.56×10^{9}	0.011	1.70
G023.365-0.291	4.60	14.95	9.61×10^{9}	0.054	1.66
G023.389+0.185	4.30	21.21	4.79×10^{9}	0.048	1.73
G023.986-0.089	11.50	15.80	8.90×10^{9}	0.049	1.98
G023.996-0.100	11.40	20.82	7.07×10^{9}	0.030	1.75
G024.461+0.198	9.40	16.77	5.65×10^{9}	0.058	2.26
G025.226+0.288	2.80	14.33	9.43×10^{9}	0.059	2.32
G025.613+0.226	9.50	10.87	1.31×10^{8}	0.057	2.35
G025.838-0.378	15.30	18.41	1.16×10^{8}	0.011	1.32
G026.545+0.423	10.50	17.55	1.36×10^{8}	0.015	2.00
G027.011-0.039	17.10	23.17	6.83×10^{9}	0.006	1.61
G027.757+0.050	5.20	19.91	8.61×10^{9}	0.019	1.70
G028.321-0.011	5.30	21.11	1.18×10^{8}	0.018	1.56
G028.687-0.283	4.90	17.42	4.84×10^{9}	0.041	2.17
G029.603-0.625	4.40	13.77	1.09×10^{8}	0.038	2.56
G029.993-0.282	5.40	18.83	8.28×10^{9}	0.036	1.33
G030.010-0.273	5.60	37.22	2.36×10^{9}	0.014	1.45
G030.370+0.482	13.40	23.10	4.46×10^{9}	0.019	1.57
G030.400-0.296	5.40	19.30	5.40×10^{9}	0.103	1.72
G030.423+0.466	14.00	32.35	8.81×10^{9}	0.029	1.73
G030.960+0.086	12.00	26.10	8.08×10^{9}	0.017	1.80

Continued on next page

Table A.2 – continued from previous page

Source name	d (kpc)	T_c (K)	Ω_c (sr)	τ	β
G030.973+0.562	13.10	22.10	5.73×10^9	0.008	2.12
G030.980+0.216	5.90	18.66	1.21×10^8	0.018	1.52
G031.122+0.063	2.90	33.68	7.93×10^9	0.003	1.29
G031.182-0.148	11.50	27.11	1.25×10^8	0.004	1.08
G032.825-0.328	4.50	22.39	7.77×10^9	0.039	2.01
G033.317-0.360	1.80	25.75	6.04×10^9	0.005	1.38
G034.267-0.210	3.00	21.97	6.50×10^9	0.014	1.75
G045.380-0.594	8.40	17.06	5.29×10^9	0.031	1.81
G052.199+0.723	10.20	28.59	1.17×10^8	0.008	1.45
G056.963-0.235	2.30	21.04	6.96×10^9	0.019	1.70
G057.610+0.025	2.90	26.11	7.87×10^9	0.007	1.61

Table A.3: The physical properties derived from best fit parameters of sources. The columns show the source name, clump Mass, Hydrogen column density, effective radius, surface density and FIR Luminosity.

Source name	Clump Mass ($M_\odot$)	N_{H_2} (cm^{-2})	$R_{\rm eff}$ (pc)	Σ (g cm^{-2})	$L_{\rm FIR}$ ($L_\odot$)
G345.131−0.174	2.13×10^2	1.20×10^{24}	0.307	0.150	8.42×10^2
G345.576−0.225	3.77×10^2	5.30×10^{23}	0.618	0.065	6.68×10^2
G345.807−0.044	9.18×10^2	3.11×10^{23}	1.321	0.035	7.45×10^2
G345.824+0.044	1.35×10^3	3.75×10^{23}	1.508	0.039	6.19×10^3
G345.985−0.020	1.47×10^3	8.69×10^{23}	0.873	0.127	1.31×10^4
G346.036+0.048	6.13×10^2	2.92×10^{23}	1.003	0.040	1.39×10^4
G346.231+0.119	8.83×10^2	7.25×10^{23}	0.636	0.144	5.39×10^3
G346.480+0.221	7.81×10^3	2.11×10^{24}	1.352	0.283	1.07×10^4
G346.481+0.132	1.31×10^3	6.25×10^{23}	0.969	0.092	1.71×10^4
G346.517+0.117	1.46×10^3	1.47×10^{24}	0.237	1.723	2.41×10^3
G347.230+0.016	2.12×10^3	9.74×10^{23}	1.018	0.136	2.55×10^3
G347.628+0.149	1.61×10^3	2.83×10^{24}	0.553	0.348	2.71×10^4
G348.884+0.096	1.88×10^3	8.39×10^{23}	1.075	0.107	5.45×10^3
G349.067−0.017	6.65×10^2	3.37×10^{23}	0.877	0.057	1.72×10^4
G349.092+0.105	5.34×10^3	3.11×10^{24}	0.853	0.485	5.89×10^4
G349.151+0.021	1.73×10^3	8.27×10^{23}	0.518	0.426	8.44×10^3
G349.884+0.231	2.74×10^2	2.44×10^{24}	0.067	4.034	7.83×10^3
G350.015+0.433	4.68×10^3	1.49×10^{24}	1.110	0.252	1.55×10^5
G350.116+0.220	2.22×10^3	4.21×10^{23}	0.546	0.492	7.30×10^3
G350.299+0.122	2.61×10^3	1.48×10^{24}	0.891	0.218	1.24×10^4
G350.340+0.141	2.70×10^3	5.91×10^{23}	1.739	0.059	3.40×10^4

Continued on next page

Table A.3 – continued from previous page

Source name	Clump Mass ($M_\odot$)	N_{H_2} (cm^{-2})	$R_{\rm eff}$ (pc)	Σ (g cm^{-2})	$L_{\rm FIR}$ ($L_\odot$)
G350.344+0.116	3.38×10^{3}	1.73×10^{24}	0.333	2.021	1.31×10^{4}
G350.356−0.068	6.97×10^{2}	4.08×10^{23}	0.311	0.477	6.04×10^{3}
G350.520−0.350	4.03×10^{2}	1.31×10^{24}	0.413	0.157	1.40×10^{3}
G350.686−0.491	2.22×10^{2}	1.64×10^{24}	0.278	0.191	1.54×10^{3}
G351.382−0.181	3.27×10^{2}	7.36×10^{23}	0.441	0.112	1.70×10^{3}
G351.688+0.171	1.28×10^{3}	9.34×10^{23}	0.671	0.188	8.50×10^{3}
G352.083+0.167	6.84×10^{2}	6.77×10^{24}	...	...	6.03×10^{3}
G352.111+0.176	7.09×10^{2}	1.76×10^{24}	0.371	0.341	2.36×10^{3}
G352.133−0.944	5.42×10^{1}	1.73×10^{24}	0.110	0.298	5.52×10^{2}
G352.525−0.158	9.56×10^{2}	3.39×10^{23}	1.209	0.043	2.39×10^{4}
G352.604−0.225	8.78×10^{2}	1.18×10^{24}	0.675	0.127	5.48×10^{2}
G352.855−0.201	2.93×10^{3}	8.92×10^{23}	1.390	0.100	1.73×10^{5}
G353.216−0.249	3.36×10^{2}	9.29×10^{23}	0.446	0.112	1.67×10^{3}
G353.378+0.438	1.14×10^{3}	2.94×10^{23}	1.349	0.041	4.57×10^{3}
G353.429−0.090	3.10×10^{3}	1.85×10^{24}	0.753	0.361	1.21×10^{4}
G353.464+0.562	4.05×10^{3}	2.72×10^{24}	0.743	0.486	2.86×10^{4}
G353.537−0.091	8.36×10^{2}	1.13×10^{24}	0.393	0.359	2.38×10^{3}
G354.496+0.083	1.45×10^{3}	1.64×10^{24}	0.224	1.918	2.70×10^{3}
G354.615+0.472	1.63×10^{3}	4.45×10^{24}	0.397	0.684	1.46×10^{4}
G354.701+0.299	1.94×10^{3}	2.46×10^{24}	0.644	0.310	5.67×10^{3}
G354.724+0.300	1.63×10^{3}	2.83×10^{24}	0.505	0.422	1.99×10^{4}
G355.538−0.105	3.99×10^{3}	8.79×10^{23}	1.199	0.184	7.91×10^{4}
G355.642+0.398	1.52×10^{3}	6.64×10^{23}	0.804	0.156	5.09×10^{3}
G005.618−0.082	1.04×10^{3}	2.91×10^{24}	0.333	0.622	1.50×10^{3}
G005.630−0.294	5.13×10^{1}	4.51×10^{23}	0.210	0.077	1.15×10^{3}
G006.189−0.358	9.32×10^{2}	1.62×10^{24}	0.539	0.212	3.06×10^{4}
G006.368−0.052	8.44×10^{2}	8.39×10^{23}	0.720	0.108	8.22×10^{3}
G008.317−0.096	1.92×10^{3}	6.13×10^{23}	1.300	0.075	1.76×10^{3}
G008.683−0.368	7.21×10^{2}	1.81×10^{24}	0.435	0.252	6.82×10^{3}
G008.832−0.028	3.92×10^{2}	5.26×10^{23}	0.675	0.057	2.40×10^{3}
G010.444−0.018	3.83×10^{3}	2.02×10^{24}	0.721	0.488	1.11×10^{4}
G010.629−0.333	2.16×10^{3}	2.61×10^{24}	0.721	0.275	1.19×10^{4}
G010.724−0.334	6.79×10^{2}	1.55×10^{24}	0.462	0.210	1.95×10^{3}
G010.886+0.123	4.75×10^{1}	9.14×10^{23}	0.128	0.191	9.68×10^{2}
G010.958+0.022	3.18×10^{3}	1.55×10^{24}	0.854	0.289	1.50×10^{5}
G011.034+0.062	1.17×10^{2}	1.04×10^{24}	0.218	0.162	2.86×10^{3}
G011.109−0.114	3.61×10^{3}	1.25×10^{24}	1.137	0.185	1.81×10^{4}
G011.903−0.102	1.61×10^{3}	6.37×10^{23}	0.894	0.133	9.58×10^{3}

Continued on next page

Table A.3 – continued from previous page

Source name	Clump Mass ($M_\odot$)	N_{H_2} (cm^{-2})	$R_{\rm eff}$ (pc)	Σ (g cm^{-2})	$L_{\rm FIR}$ ($L_\odot$)
G011.992−0.272	1.12×10^3	5.79×10^{23}	0.896	0.092	1.32×10^4
G012.025−0.031	1.46×10^3	7.21×10^{23}	0.971	0.103	1.36×10^4
G012.265−0.051	1.41×10^3	6.12×10^{23}	1.043	0.086	4.66×10^3
G012.526+0.016	1.64×10^3	8.05×10^{23}	0.894	0.136	5.22×10^3
G012.625−0.017	4.21×10^2	1.93×10^{24}	0.367	0.207	1.39×10^3
G012.889+0.489	3.88×10^2	2.46×10^{24}	0.313	0.262	6.95×10^3
G013.179+0.061	1.57×10^3	2.96×10^{24}	0.563	0.328	5.66×10^3
G013.657−0.599	4.35×10^3	1.95×10^{24}	1.035	0.269	9.48×10^4
G013.713−0.083	1.91×10^2	5.72×10^{23}	0.418	0.072	3.32×10^3
G014.101+0.087	9.51×10^2	1.85×10^{24}	0.496	0.256	6.97×10^3
G014.390−0.020	8.83×10^2	2.50×10^{23}	1.367	0.031	1.20×10^4
G014.631−0.577	1.62×10^4	3.24×10^{24}	1.720	0.364	6.48×10^4
G014.991−0.121	2.32×10^3	5.42×10^{23}	1.607	0.059	1.66×10^4
G015.665−0.499	8.73×10^3	1.83×10^{24}	1.265	0.361	8.14×10^4
G016.112−0.303	5.61×10^1	2.70×10^{23}	0.239	0.065	1.88×10^2
G016.302−0.196	9.10×10^1	3.83×10^{23}	0.372	0.043	4.94×10^2
G016.403−0.181	1.21×10^3	4.50×10^{23}	0.821	0.119	1.25×10^4
G016.585−0.051	1.06×10^3	3.07×10^{24}	0.334	0.627	8.83×10^3
G016.831+0.079	1.94×10^3	6.10×10^{23}	0.937	0.146	1.38×10^4
G016.855+0.641	2.53×10^3	1.95×10^{24}	1.149	0.127	6.53×10^3
G017.029−0.071	1.51×10^3	6.33×10^{23}	0.879	0.129	9.26×10^3
G017.862+0.074	5.61×10^2	8.72×10^{23}	1.091	0.031	1.22×10^4
G018.159+0.094	6.37×10^2	2.06×10^{23}	0.469	0.192	2.71×10^3
G018.262−0.244	9.29×10^2	1.91×10^{24}	0.521	0.227	2.81×10^3
G018.460−0.004	2.51×10^2	8.57×10^{23}	0.076	2.894	1.23×10^3
G018.661+0.034	2.82×10^3	1.31×10^{24}	1.163	0.138	1.79×10^4
G018.733−0.224	6.59×10^3	1.56×10^{24}	1.217	0.295	4.01×10^4
G018.735−0.227	6.79×10^3	1.94×10^{24}	1.261	0.283	4.30×10^4
G018.874+0.053	2.27×10^3	7.01×10^{23}	1.184	0.107	7.42×10^3
G018.888−0.475	1.12×10^3	4.88×10^{24}	0.544	0.252	2.63×10^3
G018.999−0.239	3.06×10^2	5.32×10^{23}	0.483	0.087	3.42×10^2
G019.009−0.029	3.40×10^3	1.17×10^{24}	1.203	0.156	5.41×10^4
G019.249+0.267	2.54×10^3	1.87×10^{24}	1.026	0.160	5.29×10^3
G019.365−0.030	8.19×10^1	1.69×10^{25}	0.280	0.069	2.57×10^3
G019.486+0.151	7.61×10^1	1.24×10^{24}	0.190	0.140	2.96×10^2
G019.496+0.115	5.46×10^2	5.68×10^{23}	0.359	0.281	3.32×10^3
G019.612−0.120	1.30×10^3	4.88×10^{23}	...	...	1.62×10^4
G019.612−0.134	2.74×10^3	3.07×10^{24}	0.923	0.213	6.39×10^4

Continued on next page

Table A.3 – continued from previous page

Source name	Clump Mass (M$_\odot$)	N_{H_2} (cm^{-2})	R$_{\rm eff}$ (pc)	Σ (g cm^{-2})	L$_{\rm FIR}$ (L$_\odot$)
G019.667+0.117	1.04×10^{3}	4.58×10^{23}	0.799	0.108	3.41×10^{3}
G019.701−0.267	2.37×10^{3}	8.64×10^{23}	1.129	0.123	2.00×10^{4}
G330.226+0.290	1.93×10^{2}	3.52×10^{23}	0.536	0.044	8.13×10^{2}
G330.283+0.493	7.82×10^{2}	1.41×10^{24}	0.554	0.169	7.15×10^{3}
G330.875−0.383	1.59×10^{3}	4.73×10^{24}	...	...	3.62×10^{3}
G331.059+0.375	1.28×10^{2}	3.81×10^{23}	0.317	0.084	4.67×10^{2}
G331.134+0.156	4.17×10^{2}	8.40×10^{23}	0.393	0.178	1.02×10^{3}
G331.342−0.346	3.56×10^{2}	1.03×10^{24}	0.317	0.235	6.91×10^{3}
G331.425+0.264	7.73×10^{2}	3.80×10^{23}	0.930	0.059	4.46×10^{3}
G331.442−0.187	4.55×10^{3}	2.68×10^{24}	0.827	0.440	4.83×10^{4}
G331.710+0.603	8.39×10^{2}	1.78×10^{24}	0.205	1.323	7.47×10^{3}
G332.094−0.421	7.06×10^{2}	1.81×10^{24}	0.453	0.228	2.18×10^{4}
G332.295−0.094	3.97×10^{2}	3.01×10^{24}	0.299	0.294	1.37×10^{4}
G332.351−0.436	3.52×10^{2}	2.39×10^{24}	0.380	0.161	6.78×10^{2}
G332.352−0.117	1.59×10^{2}	6.56×10^{23}	0.288	0.127	2.32×10^{3}
G332.364+0.607	4.19×10^{3}	1.97×10^{24}	1.265	0.173	5.73×10^{3}
G332.560−0.148	4.26×10^{2}	1.06×10^{24}	0.455	0.136	7.09×10^{2}
G332.604−0.168	2.16×10^{2}	9.35×10^{23}	0.283	0.178	6.03×10^{2}
G332.701−0.588	1.94×10^{3}	4.43×10^{23}	0.711	0.254	2.63×10^{4}
G332.813−0.701	1.44×10^{3}	4.19×10^{23}	1.364	0.051	4.23×10^{4}
G332.942−0.686	3.87×10^{2}	1.19×10^{24}	0.288	0.309	5.52×10^{3}
G332.987−0.487	5.24×10^{2}	1.33×10^{24}	0.510	0.134	8.37×10^{3}
G333.029−0.063	1.12×10^{2}	7.99×10^{23}	0.288	0.089	8.35×10^{3}
G333.109−0.500	2.23×10^{2}	9.26×10^{23}	0.541	0.050	6.99×10^{3}
G333.128−0.440	7.10×10^{2}	5.85×10^{24}	0.330	0.433	3.19×10^{3}
G333.130−0.560	1.28×10^{3}	8.12×10^{24}	0.464	0.392	6.49×10^{3}
G333.163−0.101	5.50×10^{2}	6.71×10^{23}	0.741	0.066	3.02×10^{4}
G333.184−0.091	4.79×10^{2}	7.14×10^{23}	0.457	0.152	5.75×10^{3}
G333.234−0.060	1.72×10^{3}	5.30×10^{24}	0.504	0.448	1.18×10^{4}
G333.315+0.105	4.01×10^{3}	2.09×10^{24}	1.109	0.216	8.67×10^{4}
G333.387+0.032	2.12×10^{3}	1.34×10^{24}	0.605	0.384	1.01×10^{4}
G333.646+0.058	2.59×10^{3}	1.14×10^{24}	1.201	0.119	9.29×10^{3}
G333.851+0.527	2.12×10^{3}	4.71×10^{23}	1.546	0.059	2.13×10^{3}
G333.900−0.099	1.01×10^{3}	5.99×10^{23}	0.770	0.113	1.50×10^{3}
G334.138−0.023	7.54×10^{2}	2.97×10^{23}	0.849	0.069	9.04×10^{3}
G335.556−0.307	1.41×10^{2}	7.95×10^{22}	0.516	0.035	6.81×10^{3}
G335.585−0.285	5.79×10^{2}	1.29×10^{25}	0.380	0.265	5.10×10^{4}
G335.726+0.191	1.70×10^{3}	1.24×10^{24}	1.660	0.041	1.06×10^{4}

Continued on next page

Table A.3 – continued from previous page

Source name	Clump Mass ($M_\odot$)	N_{H_2} (cm^{-2})	R$_{\rm eff}$ (pc)	Σ (g cm^{-2})	L$_{\rm FIR}$ (L$_\odot$)
G336.018−0.827	6.31×10^3	3.15×10^{24}	0.694	0.866	1.89×10^5
G336.809+0.119	2.51×10^3	2.07×10^{24}	0.704	0.336	7.81×10^3
G336.825+0.139	2.02×10^3	1.20×10^{24}	1.137	0.104	2.02×10^3
G336.916−0.024	1.10×10^3	5.76×10^{23}	. . .	. . .	9.73×10^3
G336.957−0.225	2.87×10^3	9.63×10^{23}	0.494	0.780	3.58×10^3
G336.958−0.977	4.47×10^3	3.01×10^{24}	0.904	0.362	7.06×10^3
G337.052−0.226	3.59×10^2	1.89×10^{23}	0.528	0.085	6.56×10^3
G337.097−0.929	2.55×10^3	9.52×10^{23}	1.113	0.136	3.98×10^4
G337.153−0.395	4.19×10^2	1.90×10^{24}	0.506	0.108	9.72×10^2
G337.176−0.032	1.20×10^3	3.79×10^{24}	0.504	0.312	2.24×10^3
G337.201+0.114	7.95×10^2	5.98×10^{23}	0.703	0.106	1.67×10^4
G337.202−0.094	9.40×10^2	6.33×10^{23}	0.736	0.115	2.34×10^3
G337.258−0.101	3.21×10^3	1.23×10^{24}	1.009	0.209	2.12×10^4
G337.263−0.070	2.43×10^2	1.09×10^{24}	0.277	0.209	1.61×10^3
G337.300−0.874	2.30×10^3	1.33×10^{24}	0.894	0.191	8.77×10^3
G337.388−0.210	1.79×10^2	1.14×10^{24}	0.221	0.242	9.69×10^2
G337.632−0.079	2.61×10^2	1.32×10^{24}	0.275	0.227	2.69×10^3
G337.686+0.137	2.01×10^3	1.37×10^{24}	1.176	0.096	5.39×10^3
G337.966−0.169	3.63×10^2	9.33×10^{23}	0.469	0.109	8.35×10^2
G337.997+0.136	1.02×10^4	2.86×10^{24}	0.397	4.285	5.16×10^3
G338.140+0.178	1.94×10^3	3.25×10^{23}	0.563	0.404	4.79×10^3
G338.160−0.064	2.32×10^3	1.56×10^{24}	0.727	0.291	2.13×10^3
G338.280+0.542	4.19×10^2	1.81×10^{24}	0.281	0.352	2.76×10^3
G338.287+0.120	4.49×10^2	3.15×10^{24}	0.340	0.257	1.70×10^3
G338.325−0.409	7.19×10^1	1.09×10^{24}	0.232	0.088	3.64×10^2
G338.392−0.403	1.60×10^3	5.03×10^{23}	1.990	0.027	5.15×10^4
G338.461−0.245	2.21×10^2	6.24×10^{23}	0.208	0.337	6.57×10^3
G338.472+0.289	9.49×10^1	1.11×10^{24}	0.162	0.240	1.52×10^3
G338.497+0.207	1.13×10^2	1.81×10^{24}	0.197	0.194	1.83×10^2
G338.561+0.218	3.55×10^3	8.84×10^{23}	0.817	0.352	1.57×10^4
G338.566+0.110	6.67×10^2	1.75×10^{24}	0.464	0.205	4.50×10^3
G338.850+0.409	2.97×10^3	1.76×10^{24}	1.381	0.103	1.35×10^5
G338.875−0.084	3.69×10^1	2.22×10^{23}	0.256	0.037	5.90×10^2
G338.902+0.394	1.02×10^2	1.79×10^{24}	0.143	0.331	1.14×10^3
G338.925+0.634	1.29×10^3	5.45×10^{24}	0.505	0.335	8.51×10^3
G339.053−0.315	1.07×10^3	9.55×10^{23}	0.810	0.108	7.19×10^3
G339.064+0.152	1.31×10^3	5.95×10^{23}	0.676	0.190	4.85×10^3
G339.282+0.136	5.69×10^2	1.24×10^{24}	0.387	0.251	1.92×10^3

Continued on next page

Table A.3 – continued from previous page

Source name	Clump Mass ($M_\odot$)	N_{H_2} (cm^{-2})	R_{eff} (pc)	Σ (g cm^{-2})	L_{FIR} ($L_\odot$)
G339.294+0.139	3.67×10^2	7.63×10^{23}	0.251	0.387	1.06×10^3
G339.476+0.185	3.22×10^3	1.88×10^{24}	0.779	0.352	3.26×10^4
G339.477+0.043	1.62×10^3	4.79×10^{23}	0.842	0.151	6.49×10^3
G339.582−0.127	2.93×10^2	2.87×10^{24}	0.270	0.265	1.45×10^3
G339.622−0.121	2.16×10^2	1.41×10^{24}	0.296	0.163	9.20×10^3
G339.762+0.054	5.53×10^2	2.57×10^{23}	1.245	0.024	1.21×10^4
G339.909+0.240	2.60×10^3	4.46×10^{23}	1.186	0.122	5.37×10^3
G339.980−0.538	1.19×10^3	4.69×10^{23}	0.771	0.132	7.05×10^4
G339.986−0.425	6.43×10^2	4.11×10^{23}	0.786	0.069	3.25×10^4
G340.118−0.021	1.55×10^3	1.16×10^{24}	0.882	0.132	1.15×10^3
G340.249−0.046	2.48×10^3	1.40×10^{24}	0.736	0.303	5.41×10^4
G340.249−0.372	7.10×10^3	4.58×10^{24}	1.520	0.203	2.43×10^5
G340.543−0.162	1.60×10^2	5.63×10^{23}	0.437	0.055	1.69×10^2
G340.655−0.235	1.49×10^3	5.19×10^{23}	1.090	0.083	3.11×10^3
G340.785−0.096	3.57×10^3	2.28×10^{24}	0.732	0.442	3.39×10^4
G341.124−0.361	3.36×10^2	2.13×10^{24}	0.330	0.204	2.54×10^3
G341.218−0.212	4.26×10^2	1.69×10^{24}	0.198	0.721	5.38×10^3
G341.238−0.270	6.03×10^2	3.19×10^{24}	0.368	0.295	1.59×10^3
G341.276+0.062	1.28×10^3	4.62×10^{23}	0.869	0.112	1.32×10^4
G341.367+0.336	1.05×10^3	5.90×10^{23}	0.940	0.079	8.38×10^2
G341.990−0.103	1.07×10^2	5.17×10^{23}	0.269	0.098	4.32×10^2
G305.799−0.245	7.77×10^2	2.67×10^{24}	0.472	0.231	5.05×10^4
G308.754+0.549	5.38×10^2	7.18×10^{23}	0.363	0.270	7.00×10^3
G309.384−0.135	8.82×10^2	1.96×10^{24}	0.568	0.181	9.51×10^3
G311.947+0.142	1.10×10^3	2.13×10^{24}	0.676	0.159	6.73×10^3
G317.466−0.402	1.02×10^3	5.91×10^{23}	0.997	0.068	1.58×10^4
G317.701+0.110	2.74×10^2	1.74×10^{24}	0.281	0.230	1.86×10^3
G318.948−0.196	3.73×10^3	1.81×10^{24}	0.940	0.280	2.63×10^5
G320.231−0.284	8.81×10^2	2.69×10^{24}	0.356	0.460	1.66×10^4
G321.148−0.529	1.32×10^2	3.15×10^{23}	0.220	0.181	1.71×10^3
G324.923−0.568	6.03×10^2	1.10×10^{24}	0.467	0.183	2.69×10^4
G326.475+0.703	9.70×10^3	4.02×10^{24}	1.127	0.506	2.85×10^5
G326.608+0.799	4.50×10^3	2.06×10^{24}	1.019	0.287	1.27×10^4
G326.859−0.677	3.97×10^2	1.16×10^{24}	0.331	0.240	1.43×10^3
G327.402+0.445	1.19×10^3	3.57×10^{24}	0.517	0.296	5.80×10^3
G327.392+0.199	1.74×10^3	4.60×10^{24}	0.570	0.356	6.70×10^4
G327.590−0.094	8.20×10^2	9.86×10^{23}	0.853	0.075	3.77×10^3
G329.029−0.205	1.39×10^4	3.25×10^{24}	0.840	1.308	8.58×10^4

Continued on next page

Table A.3 – continued from previous page

Source name	Clump Mass ($M_\odot$)	N_{H_2} (cm^{-2})	$R_{\rm eff}$ (pc)	Σ (g cm^{-2})	$L_{\rm FIR}$ ($L_\odot$)
G329.066−0.308	6.32×10^3	1.38×10^{25}	1.366	0.224	3.15×10^4
G329.183−0.314	8.85×10^2	3.81×10^{24}	0.259	0.872	6.03×10^3
G329.469+0.503	3.72×10^3	2.87×10^{24}	0.771	0.414	2.55×10^4
G329.622+0.138	1.53×10^3	6.50×10^{23}	0.574	0.308	2.45×10^3
G023.706−0.198	7.16×10^2	1.78×10^{24}	0.849	0.066	1.60×10^4
G023.885+0.060	2.62×10^3	7.46×10^{23}	...	...	3.18×10^3
G023.966−0.109	6.43×10^3	2.65×10^{24}	0.965	0.457	3.00×10^4
G024.541+0.312	3.86×10^2	7.90×10^{23}	0.382	0.176	1.04×10^3
G024.634−0.324	2.56×10^3	1.96×10^{24}	1.570	0.069	1.75×10^4
G024.943+0.074	2.19×10^3	7.94×10^{23}	0.294	1.680	2.25×10^4
G025.270−0.434	2.31×10^3	1.45×10^{24}	1.264	0.096	7.43×10^3
G025.710+0.044	2.71×10^3	1.15×10^{24}	0.850	0.249	4.68×10^4
G025.826−0.178	3.55×10^2	7.35×10^{23}	0.146	1.095	9.19×10^3
G026.601−0.221	7.60×10^2	4.51×10^{23}	0.198	1.278	7.63×10^3
G027.286+0.151	4.10×10^3	2.51×10^{24}	1.091	0.228	2.97×10^4
G027.783−0.259	1.45×10^3	9.00×10^{23}	0.632	0.240	8.52×10^3
G027.784+0.057	6.19×10^2	2.13×10^{24}	0.636	0.101	5.75×10^3
G028.146−0.005	6.96×10^2	1.36×10^{24}	0.511	0.177	3.98×10^3
G028.397+0.081	3.61×10^2	2.50×10^{25}	0.414	0.140	1.22×10^4
G028.817+0.365	1.28×10^3	8.83×10^{23}	0.386	0.572	3.25×10^4
G028.842+0.493	4.94×10^2	1.42×10^{24}	0.400	0.205	1.24×10^3
G029.320−0.162	7.15×10^2	2.66×10^{23}	0.646	0.114	5.30×10^3
G033.133−0.092	5.28×10^2	1.22×10^{24}	0.408	0.210	1.36×10^4
G033.634−0.021	2.01×10^2	5.34×10^{23}	...	...	8.58×10^2
G033.852+0.018	9.26×10^2	9.58×10^{24}	0.864	0.082	2.72×10^3
G033.980−0.019	2.56×10^2	1.59×10^{24}	0.274	0.225	4.82×10^2
G034.757+0.025	3.34×10^2	9.61×10^{23}	0.422	0.124	3.20×10^3
G034.820+0.350	4.15×10^2	2.18×10^{24}	0.423	0.154	7.03×10^3
G035.132−0.744	3.56×10^2	4.45×10^{24}	0.133	1.339	1.58×10^3
G035.197−0.743	6.04×10^1	8.69×10^{23}	...	...	1.63×10^2
G035.397+0.025	2.95×10^2	1.94×10^{24}	0.482	0.084	1.46×10^3
G035.793−0.175	4.35×10^2	1.33×10^{24}	0.312	0.296	2.33×10^3
G036.115+0.552	1.36×10^2	4.93×10^{23}	0.279	0.116	1.88×10^3
G036.839−0.022	2.60×10^2	1.86×10^{24}	0.334	0.154	5.86×10^2
G036.918+0.483	9.27×10^2	2.89×10^{23}	1.294	0.037	2.48×10^4
G037.030−0.038	3.67×10^2	1.12×10^{24}	...	...	7.74×10^2
G037.043−0.035	6.62×10^1	1.61×10^{24}	0.199	0.111	5.78×10^2
G037.479−0.105	6.00×10^2	7.93×10^{24}	1.041	0.037	1.03×10^4

Continued on next page

Table A.3 – continued from previous page

Source name	Clump Mass (M$_\odot$)	N_{H_2} (cm^{-2})	R$_{\rm eff}$ (pc)	Σ (g cm^{-2})	L$_{\rm FIR}$ (L$_\odot$)
G037.554+0.201	9.91×10^{2}	1.89×10^{24}	0.328	0.609	1.52×10^{4}
G037.598+0.425	4.35×10^{2}	5.38×10^{23}	0.415	0.167	2.15×10^{3}
G037.735−0.112	2.76×10^{3}	1.87×10^{24}	0.717	0.356	2.76×10^{4}
G037.753−0.189	1.50×10^{3}	1.24×10^{24}	0.630	0.250	5.27×10^{3}
G037.767−0.214	3.49×10^{3}	1.79×10^{24}	...	...	1.24×10^{4}
G038.037−0.300	1.14×10^{2}	3.56×10^{23}	0.343	0.064	6.35×10^{2}
G038.119−0.229	2.79×10^{2}	4.09×10^{23}	0.581	0.055	6.47×10^{3}
G038.203−0.067	1.51×10^{3}	2.52×10^{24}	0.575	0.302	3.34×10^{3}
G038.255−0.200	2.67×10^{2}	2.71×10^{23}	0.638	0.043	7.20×10^{3}
G038.598−0.212	1.19×10^{2}	1.87×10^{23}	0.455	0.038	7.18×10^{2}
G038.653+0.088	1.89×10^{3}	5.36×10^{23}	1.728	0.042	1.73×10^{4}
G038.916−0.353	6.27×10^{3}	1.90×10^{24}	1.131	0.324	1.94×10^{4}
G039.388−0.141	2.54×10^{2}	5.04×10^{23}	0.235	0.304	8.25×10^{3}
G040.282−0.219	1.09×10^{3}	4.46×10^{24}	0.331	0.661	1.33×10^{4}
G041.075−0.125	9.94×10^{2}	8.70×10^{23}	1.297	0.039	3.22×10^{3}
G041.121−0.107	5.44×10^{2}	3.50×10^{23}	0.721	0.069	3.45×10^{3}
G041.123−0.220	1.11×10^{3}	1.40×10^{24}	1.191	0.052	5.64×10^{3}
G041.226−0.197	5.93×10^{2}	3.10×10^{23}	1.112	0.032	4.79×10^{3}
G041.348−0.136	7.93×10^{2}	3.06×10^{23}	0.711	0.104	5.16×10^{3}
G042.034+0.190	7.54×10^{2}	2.95×10^{23}	0.890	0.063	6.06×10^{3}
G042.304−0.299	1.79×10^{3}	7.68×10^{23}	0.879	0.153	4.07×10^{3}
G042.435−0.260	6.11×10^{2}	1.12×10^{25}	0.337	0.357	1.78×10^{3}
G043.074−0.077	1.77×10^{3}	7.55×10^{23}	1.339	0.065	6.04×10^{3}
G043.890−0.784	1.74×10^{3}	7.39×10^{23}	0.838	0.164	8.03×10^{4}
G044.310+0.041	1.71×10^{3}	1.10×10^{24}	0.774	0.189	2.17×10^{4}
G045.467+0.053	3.40×10^{3}	3.35×10^{24}	0.849	0.312	6.94×10^{4}
G045.493+0.126	1.31×10^{3}	9.91×10^{23}	...	...	3.09×10^{3}
G045.804−0.356	6.25×10^{2}	5.59×10^{23}	0.581	0.123	1.36×10^{4}
G048.902−0.273	7.76×10^{2}	1.48×10^{24}	0.766	0.087	6.93×10^{3}
G048.990−0.299	1.41×10^{3}	2.55×10^{24}	0.616	0.246	2.25×10^{4}
G049.265+0.311	1.23×10^{3}	5.85×10^{23}	0.799	0.128	6.94×10^{3}
G049.617−0.360	2.75×10^{2}	4.50×10^{23}	0.630	0.046	5.53×10^{2}
G052.922+0.414	4.20×10^{2}	6.39×10^{23}	0.580	0.083	1.82×10^{3}
G053.142+0.071	1.85×10^{2}	1.69×10^{24}	0.180	0.380	1.41×10^{3}
G053.618+0.035	8.40×10^{1}	1.30×10^{24}	0.227	0.108	6.07×10^{2}
G020.239+0.065	2.52×10^{2}	1.13×10^{24}	0.312	0.172	2.05×10^{3}
G020.364−0.013	2.60×10^{2}	1.91×10^{24}	0.214	0.375	1.39×10^{3}
G020.733−0.059	5.98×10^{3}	2.07×10^{24}	1.231	0.261	1.75×10^{4}

Continued on next page

Table A.3 – continued from previous page

Source name	Clump Mass ($M_\odot$)	N_{H_2} (cm^{-2})	$R_{\rm eff}$ (pc)	Σ (g cm^{-2})	$L_{\rm FIR}$ ($L_\odot$)
G020.963−0.075	7.66×10^{2}	3.93×10^{23}	0.868	0.067	1.06×10^{4}
G023.003+0.124	2.67×10^{2}	5.03×10^{23}	0.514	0.067	6.90×10^{2}
G023.365−0.291	1.13×10^{3}	2.49×10^{24}	0.477	0.329	9.56×10^{2}
G023.389+0.185	3.92×10^{2}	1.98×10^{24}	0.259	0.387	2.62×10^{3}
G023.986−0.089	4.89×10^{3}	1.86×10^{24}	1.069	0.284	8.72×10^{3}
G023.996−0.100	2.68×10^{3}	1.31×10^{24}	0.977	0.186	1.69×10^{4}
G024.461+0.198	2.00×10^{3}	1.79×10^{24}	0.681	0.286	7.03×10^{3}
G025.226+0.288	3.27×10^{2}	1.98×10^{24}	0.303	0.236	4.55×10^{2}
G025.613+0.226	4.79×10^{3}	1.81×10^{24}	1.277	0.195	1.46×10^{3}
G025.838−0.378	3.75×10^{3}	6.16×10^{23}	1.871	0.071	6.42×10^{3}
G026.545+0.423	1.88×10^{3}	5.61×10^{23}	1.453	0.059	7.39×10^{3}
G027.011−0.039	1.53×10^{3}	3.43×10^{23}	1.436	0.049	1.39×10^{4}
G027.757+0.050	4.66×10^{2}	8.95×10^{23}	0.493	0.127	2.21×10^{3}
G028.321−0.011	6.49×10^{2}	8.75×10^{23}	0.662	0.098	3.36×10^{3}
G028.687−0.283	3.51×10^{2}	1.35×10^{24}	0.305	0.249	1.48×10^{3}
G029.603−0.625	5.28×10^{2}	1.12×10^{24}	0.511	0.134	8.73×10^{2}
G029.993−0.282	1.08×10^{3}	2.00×10^{24}	0.443	0.364	2.01×10^{3}
G030.010−0.273	1.17×10^{2}	7.09×10^{23}	0.093	0.891	1.10×10^{4}
G030.370+0.482	1.65×10^{3}	9.21×10^{23}	0.800	0.171	1.45×10^{4}
G030.400−0.296	1.42×10^{3}	4.02×10^{24}	0.350	0.763	4.83×10^{3}
G030.423+0.466	5.35×10^{3}	1.38×10^{24}	1.435	0.172	3.28×10^{5}
G030.960+0.086	2.03×10^{3}	7.78×10^{23}	1.153	0.101	4.97×10^{4}
G030.973+0.562	6.24×10^{2}	2.84×10^{23}	0.779	0.068	1.18×10^{4}
G030.980+0.216	8.38×10^{2}	8.89×10^{23}	0.747	0.099	2.11×10^{3}
G031.122+0.063	2.73×10^{1}	1.83×10^{23}	0.275	0.024	1.12×10^{3}
G031.182−0.148	8.78×10^{2}	2.37×10^{23}	1.494	0.026	7.34×10^{3}
G032.825−0.328	4.84×10^{2}	1.37×10^{24}	0.312	0.330	6.86×10^{3}
G033.317−0.360	1.11×10^{1}	2.53×10^{23}	0.134	0.041	1.34×10^{2}
G034.267−0.210	7.47×10^{1}	5.70×10^{23}	0.223	0.099	7.33×10^{2}
G045.380−0.594	9.75×10^{2}	1.17×10^{24}	0.575	0.195	2.54×10^{3}
G052.199+0.723	1.15×10^{3}	4.23×10^{23}	1.262	0.048	2.60×10^{4}
G056.963−0.235	6.69×10^{1}	8.12×10^{23}	0.190	0.122	4.72×10^{2}
G057.610+0.025	5.79×10^{1}	3.91×10^{23}	0.261	0.056	9.93×10^{2}

A.2 SED fits of 320 methanol maser sources

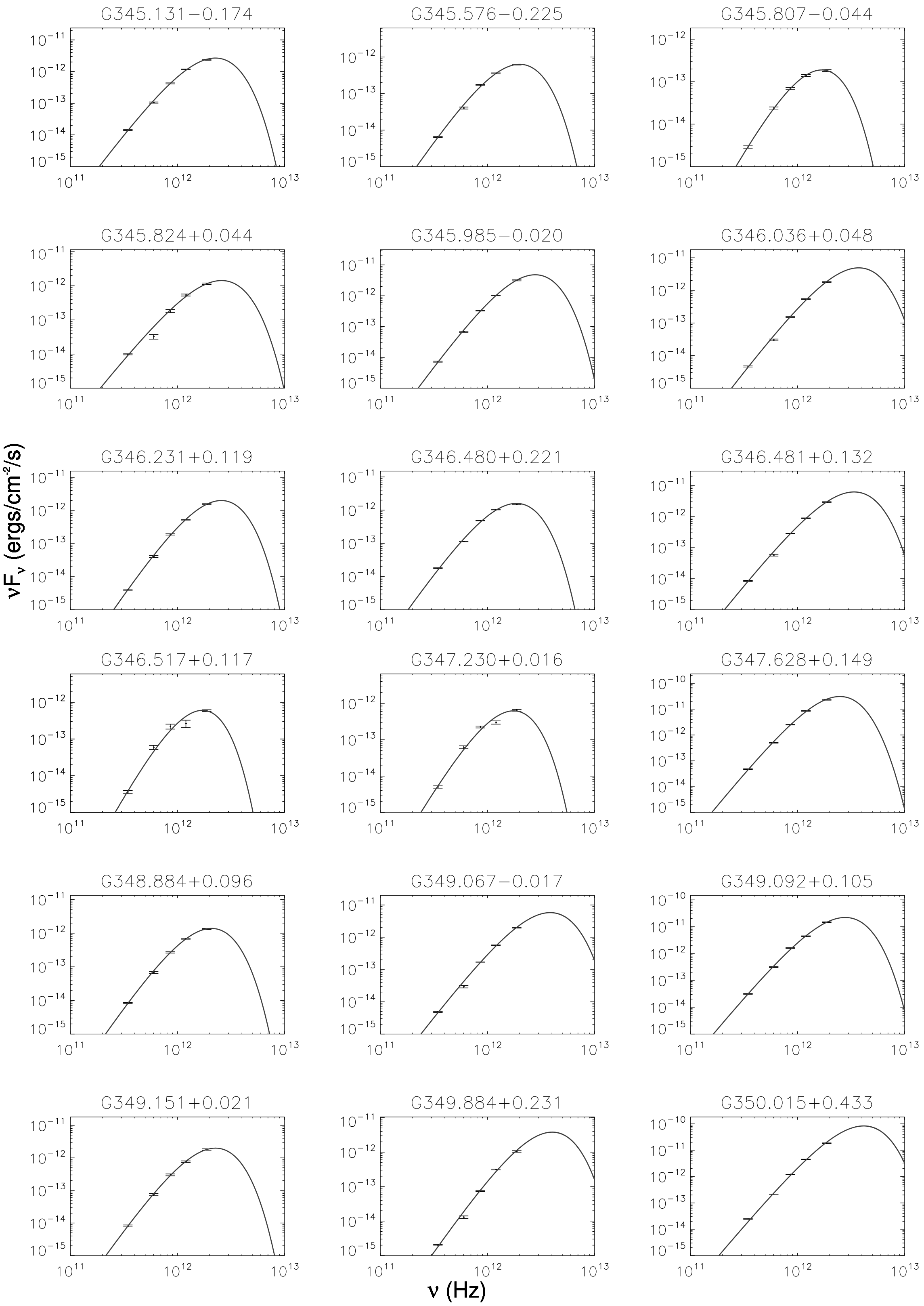

Figure A.1: SED fits at different wavelength ranges.

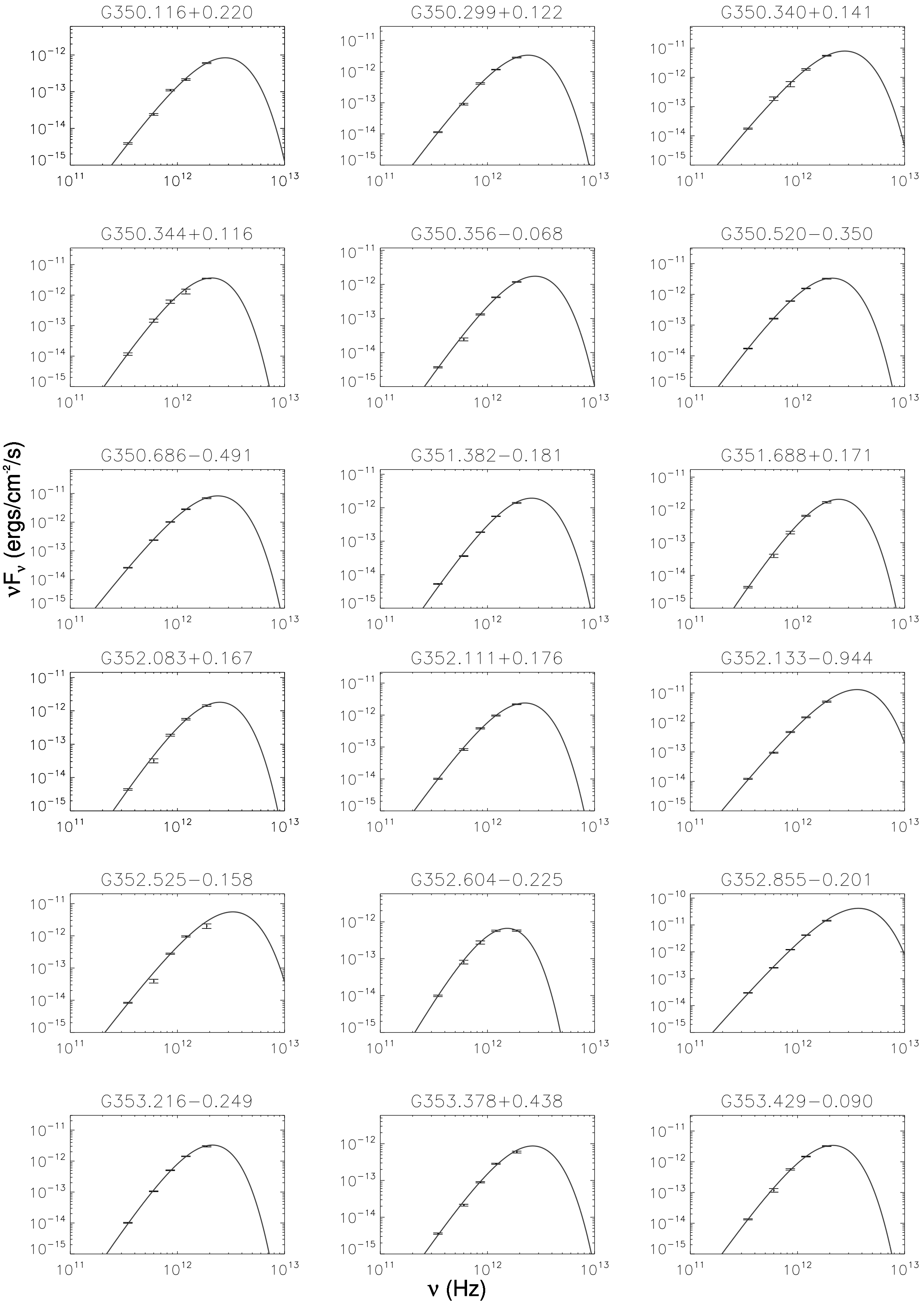

Continued from previous page.

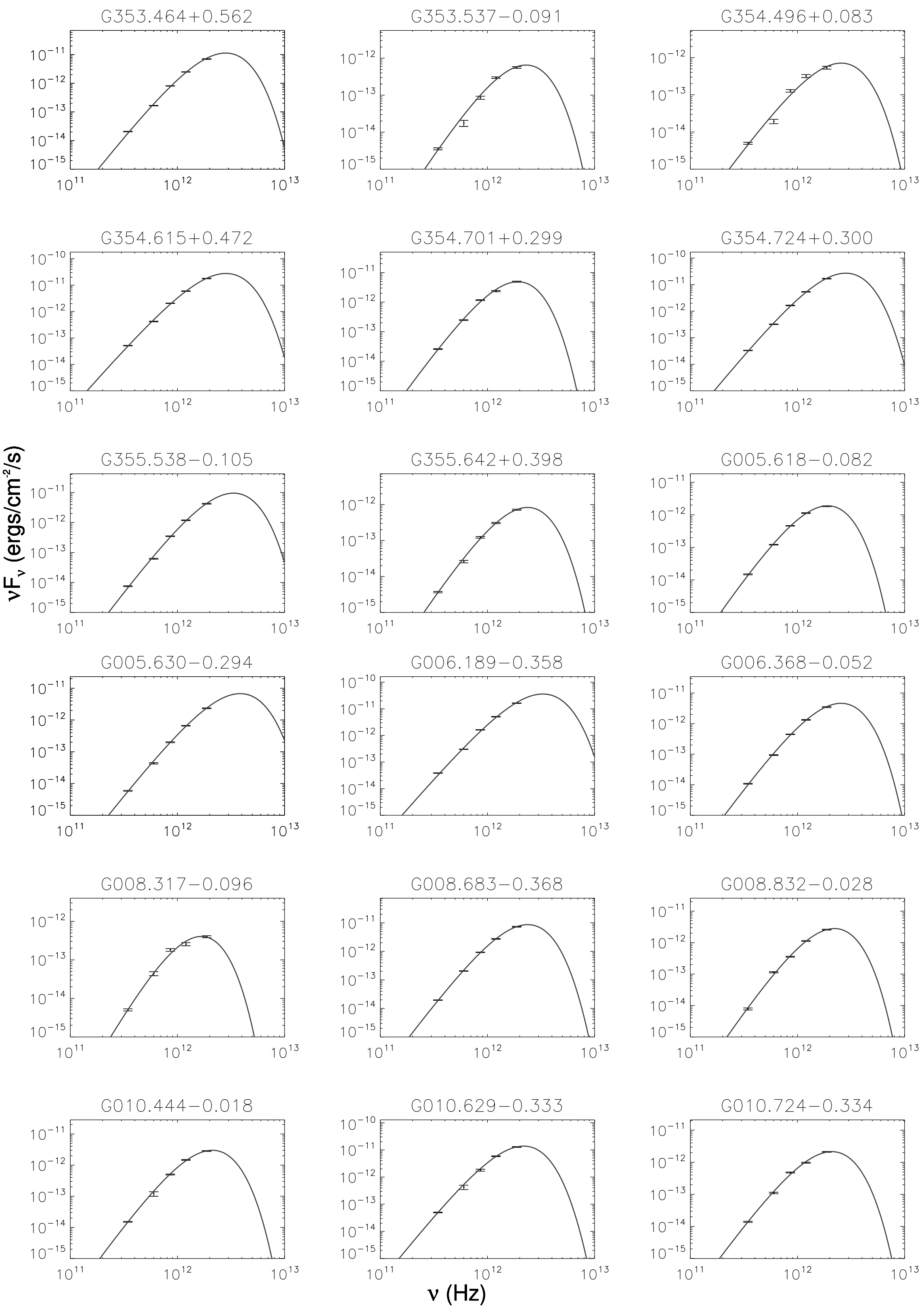

Continued from previous page.

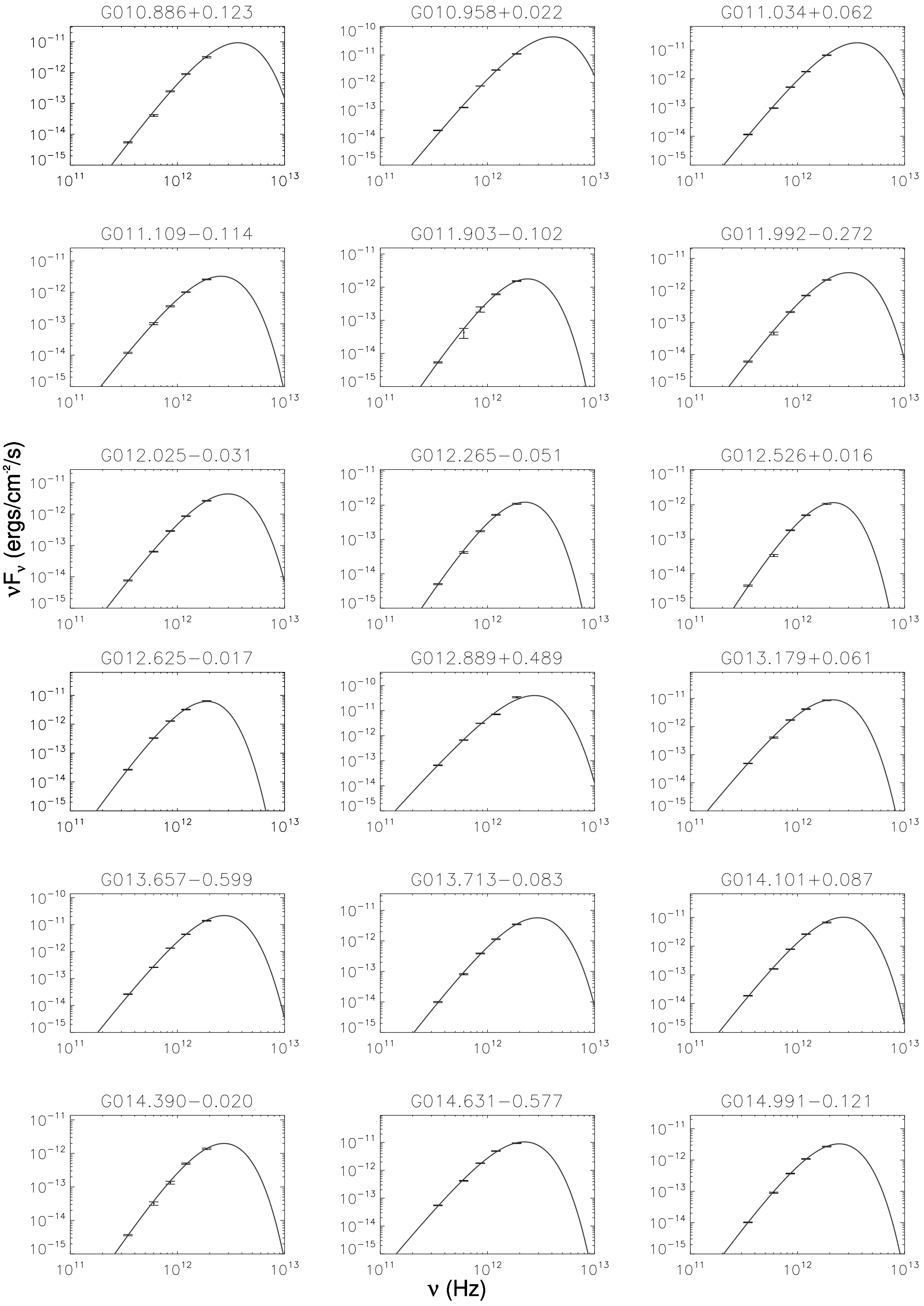

Continued from previous page.

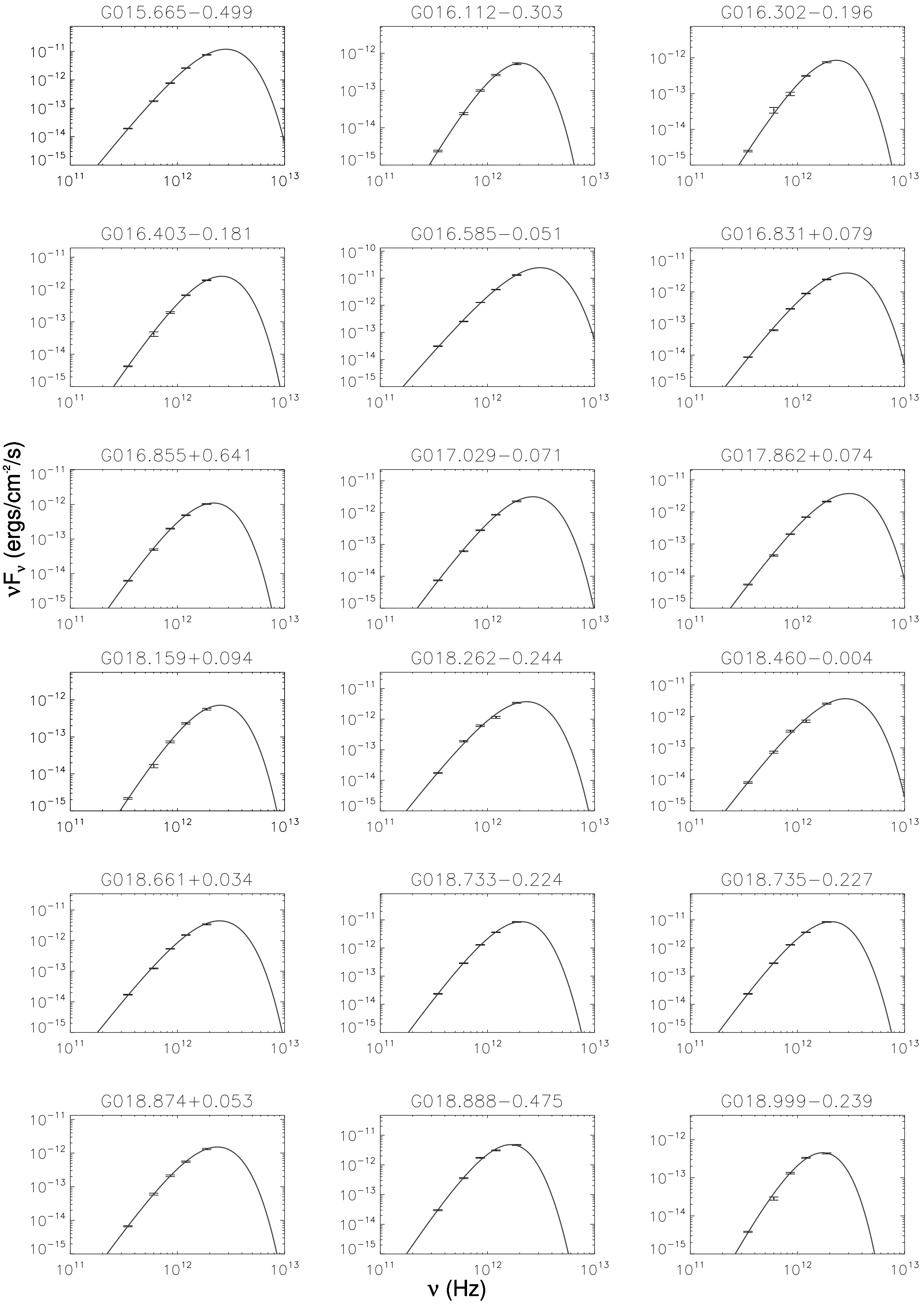

Continued from previous page.

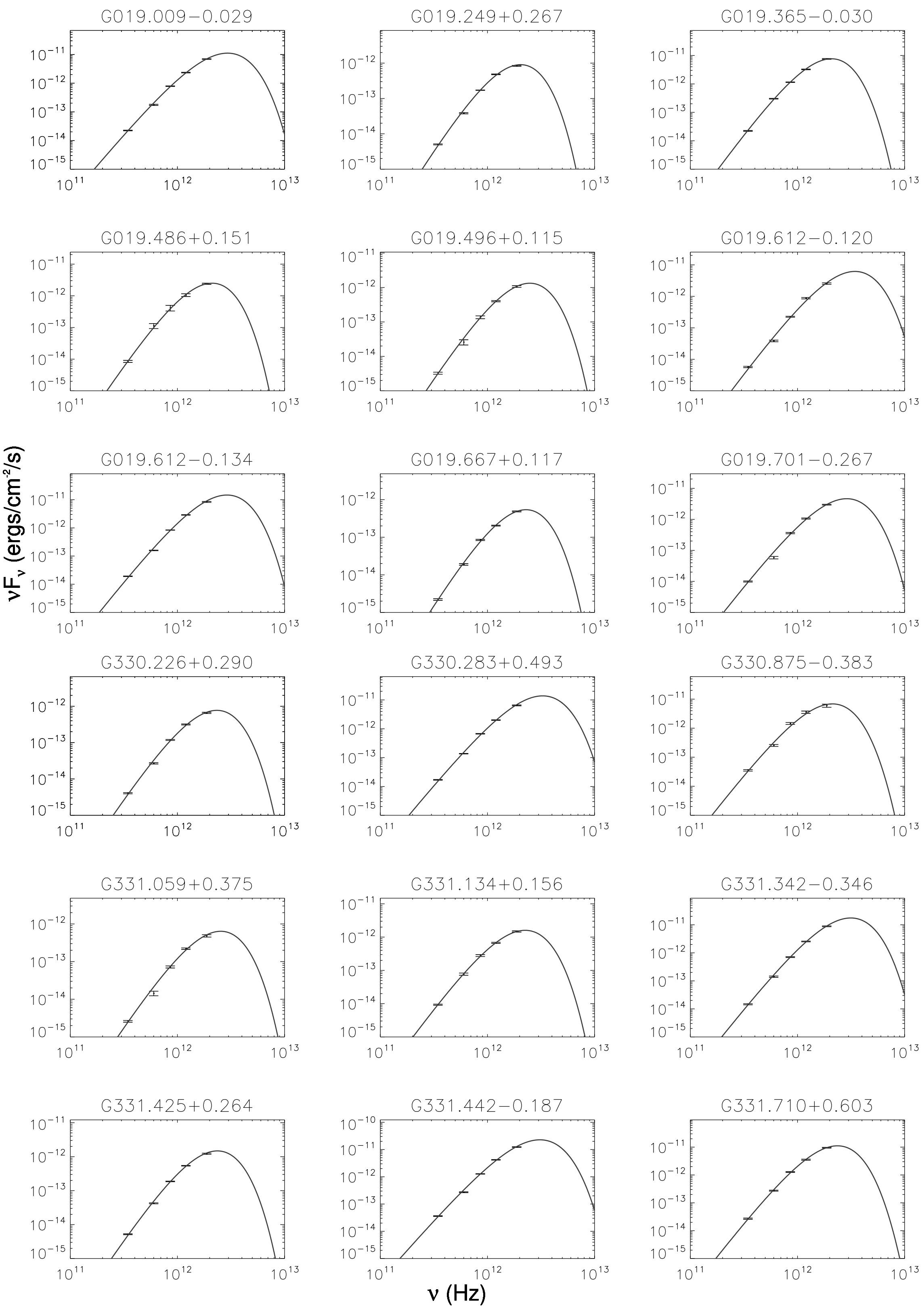

Continued from previous page.

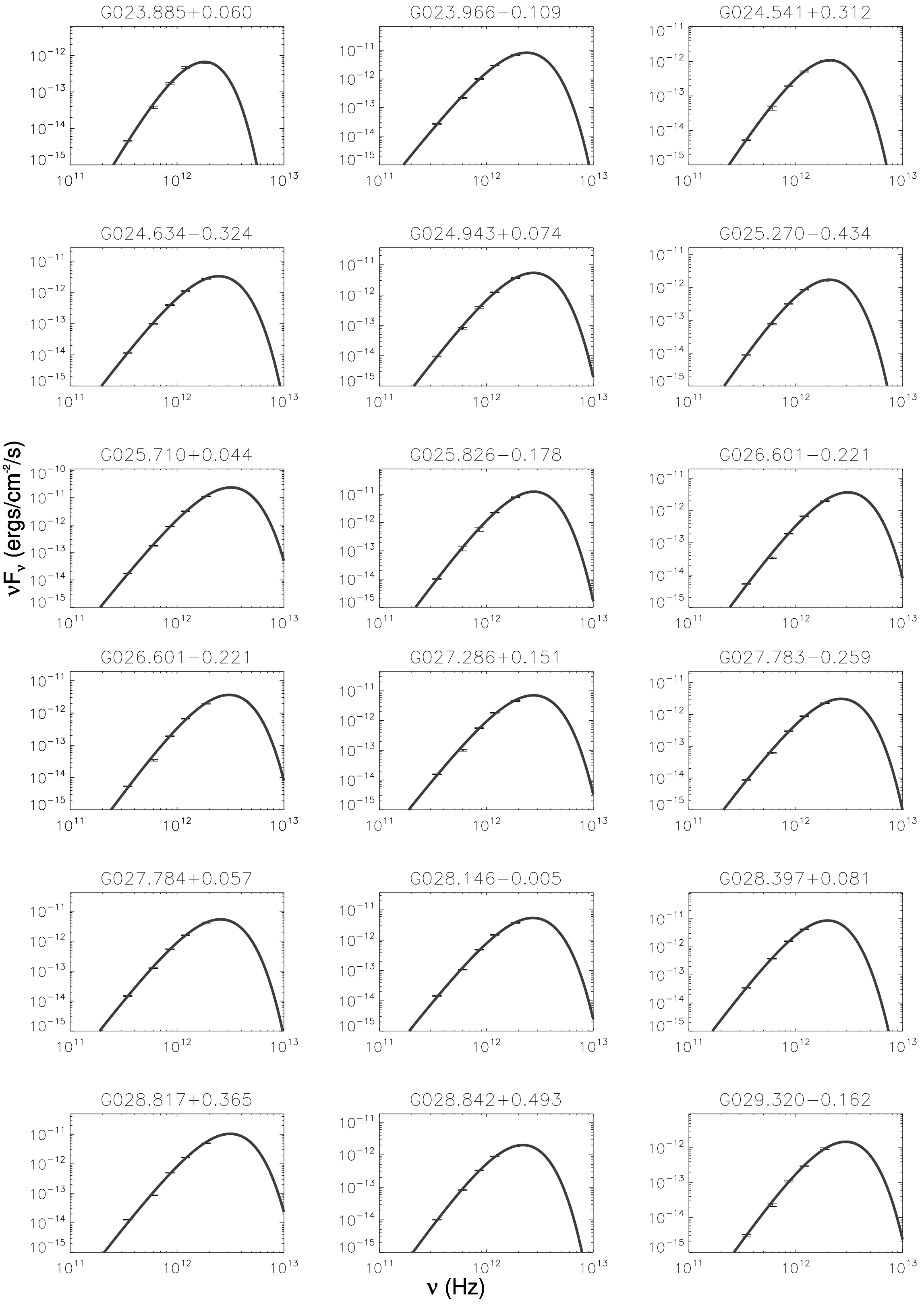

Continued from previous page.

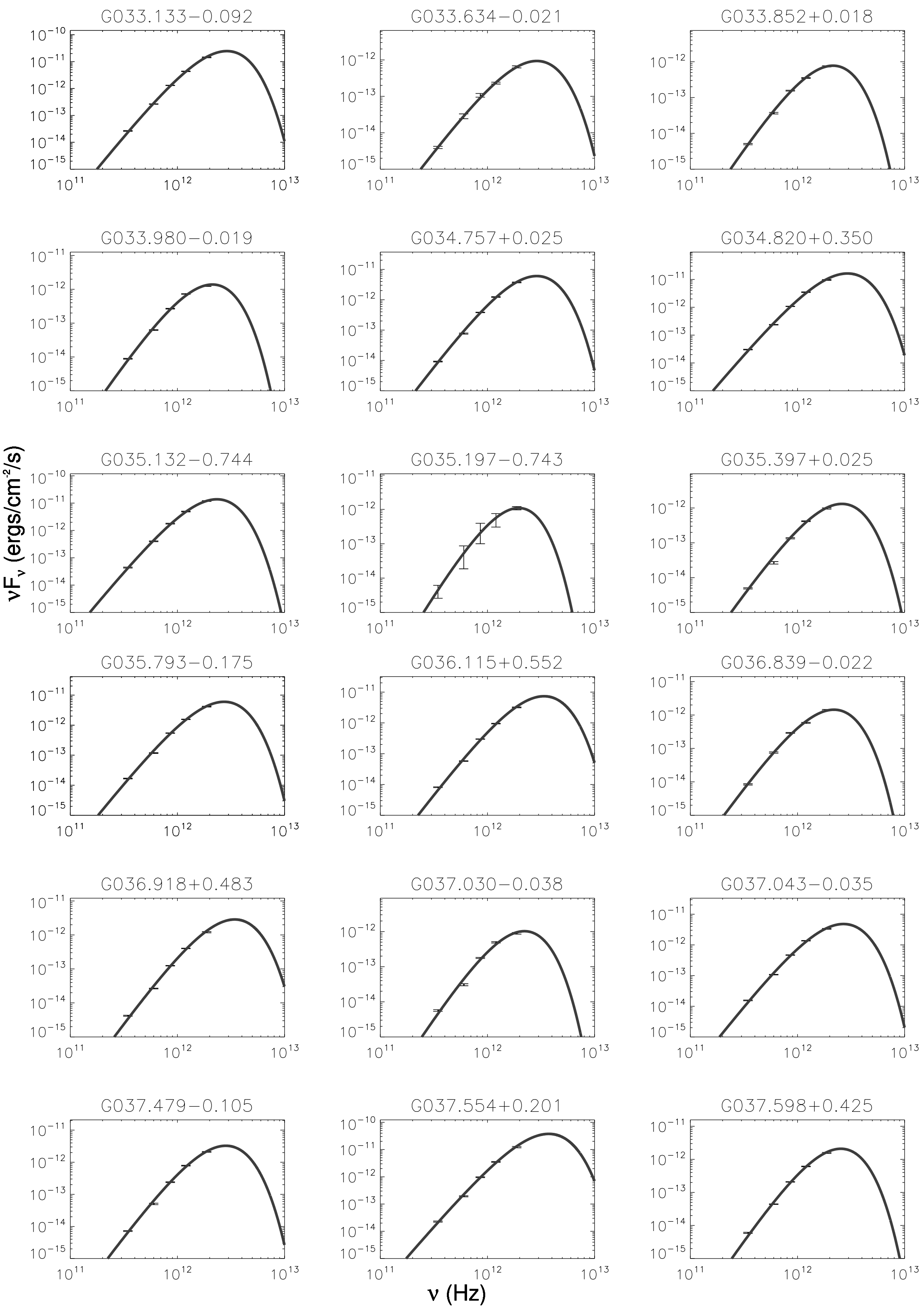

Continued from previous page.

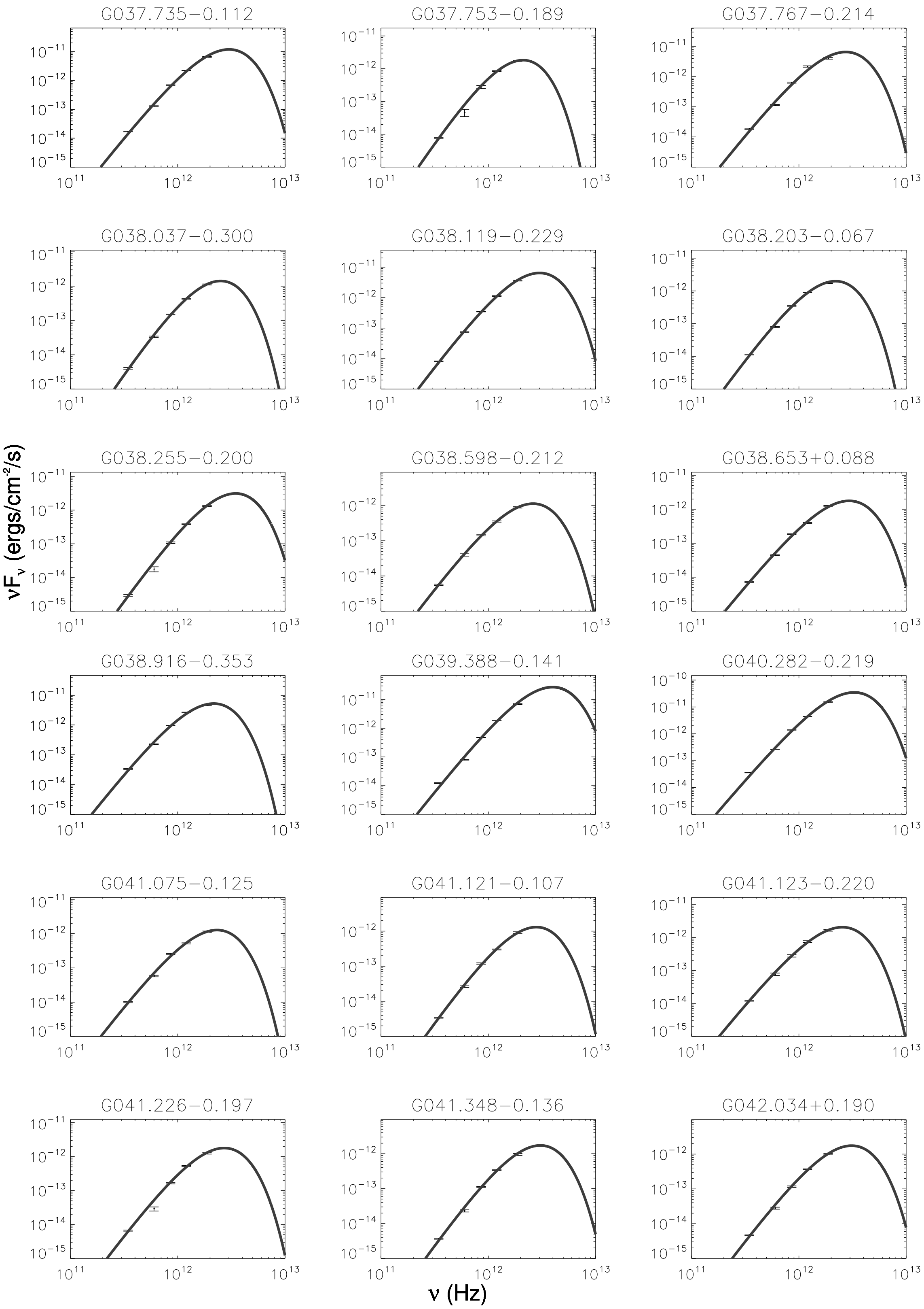

Continued from previous page.

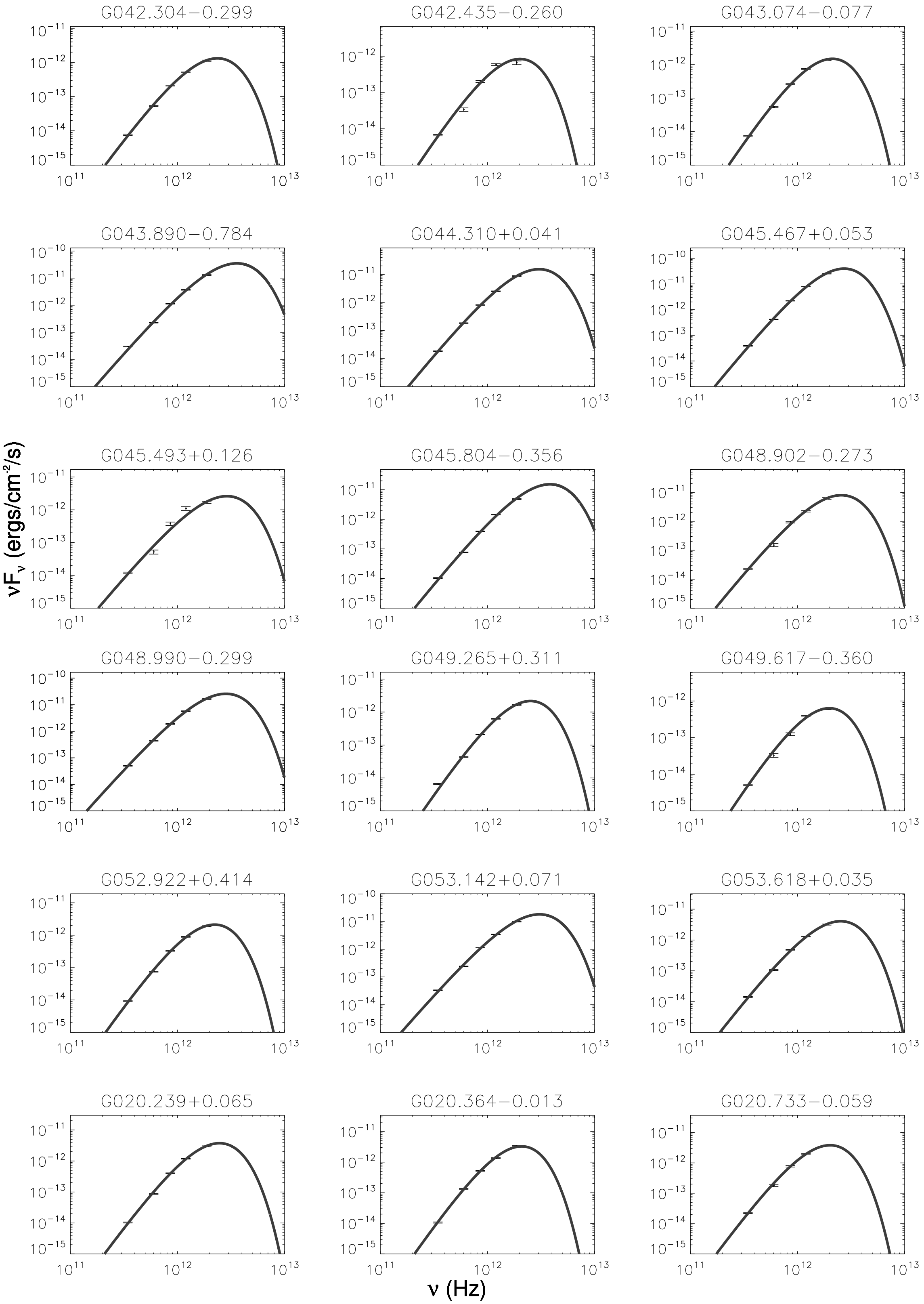

Continued from previous page.

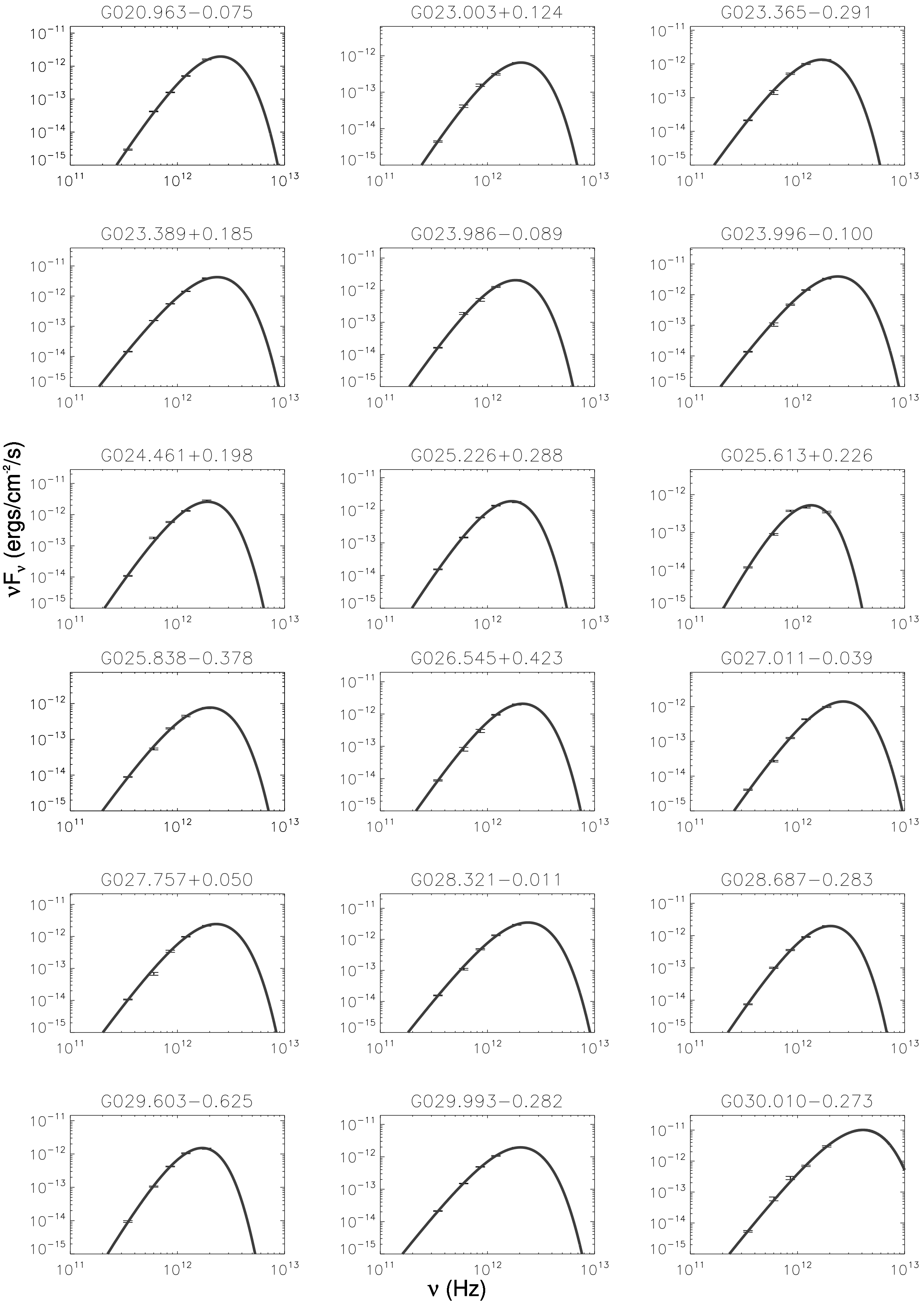

Continued from previous page.

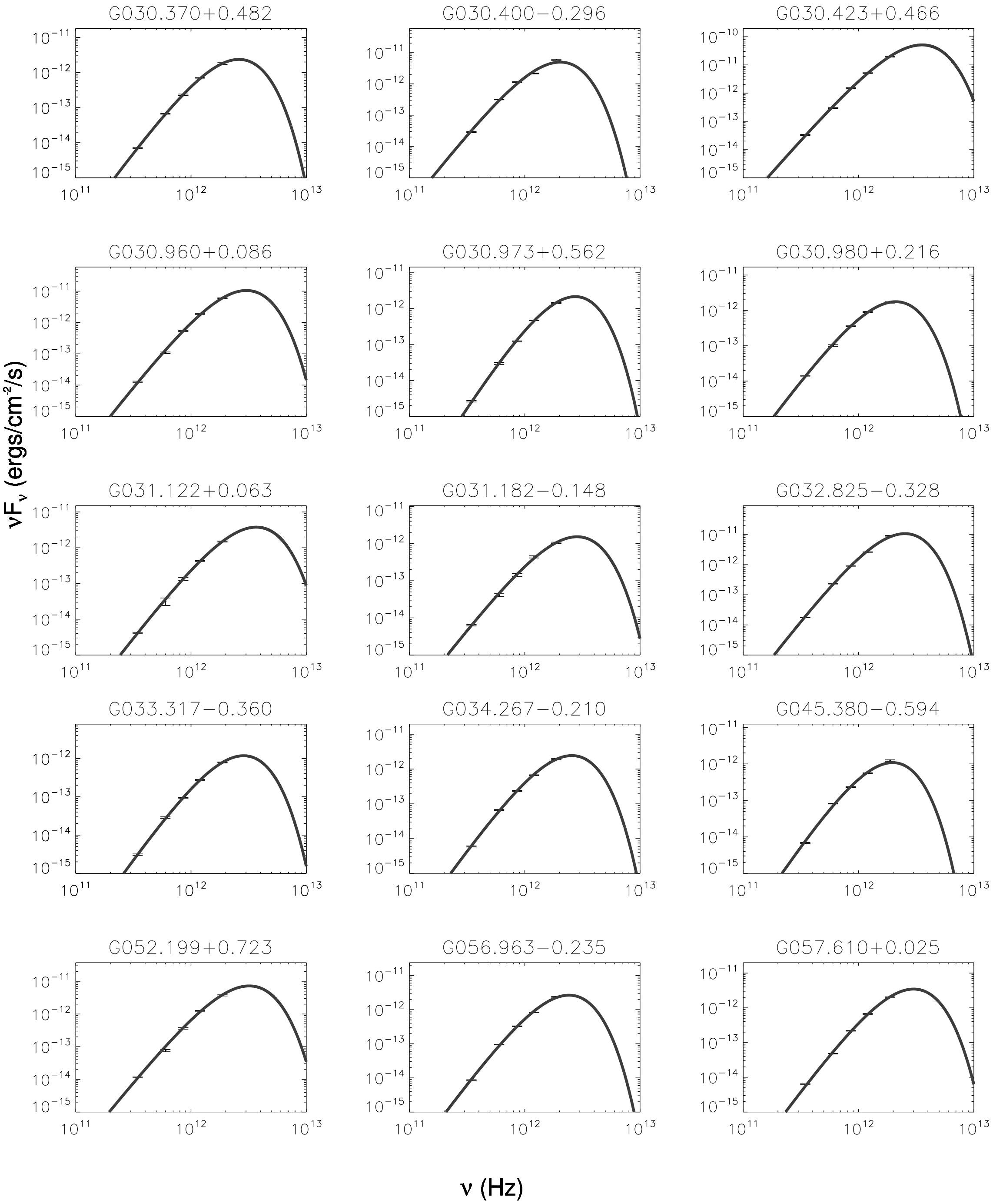

Continued from previous page.

Appendix B

Source chemistry : Statistical Analysis

B.1 Data Tables

Table B.1: Excitation temperatures (T_{ex}), LSR velocities (V_{LSR}) and molecular column densities ($N_{N_2H^+}$) obtained after fitting the brightest pixel of N_2H^+ spectrum towards each source are given below. The dust temperature (T_{dust}) and H_2 column density (N_{H_2}) estimates towards the same bright pixel of the dust continuum map of each source are also provided.

Source Name	T_{dust} (K)	N_{H_2} (cm^{-2})	T_{ex} (K)	V_{LSR} (km s^{-1})	$N_{N_2H^+}$(cm^{-2})
G006.189−0.358	29.64	1.62×10^{22}	25.14	−33.05	3.60×10^{13}
G010.724−0.334	18.48	1.31×10^{22}	28.30	−1.60	2.95×10^{13}
G012.625−0.017	16.64	3.23×10^{22}	6.31	21.76	2.79×10^{13}
G012.889+0.489	25.87	4.41×10^{22}	34.56	32.53	5.66×10^{13}
G013.179+0.061	19.30	2.96×10^{22}	14.52	49.32	5.64×10^{13}
G014.631−0.577	20.22	4.63×10^{22}	13.67	18.82	4.77×10^{13}
G305.799−0.245	35.99	3.27×10^{22}	18.63	−31.99	1.61×10^{13}
G309.384−0.135	24.24	1.38×10^{22}	20.45	−50.44	2.25×10^{13}
G311.947+0.142	20.32	2.13×10^{22}	13.41	−42.23	1.82×10^{13}
G324.923−0.568	28.05	1.24×10^{22}	5.82	−73.23	1.62×10^{13}
G326.608+0.799	17.12	2.06×10^{22}	31.04	−37.20	4.32×10^{13}
G329.469+0.503	20.95	2.42×10^{22}	12.26	−68.13	1.95×10^{13}
G330.283+0.493	21.54	1.03×10^{22}	22.44	−93.92	1.93×10^{13}
G331.134+0.156	0.00	0.00×10^{00}	12.25	−76.85	8.19×10^{12}
G331.342−0.346	23.20	1.47×10^{22}	20.14	−66.08	1.59×10^{13}
G331.442−0.187	23.65	2.68×10^{22}	2.97	−88.68	6.15×10^{12}
G331.710+0.603	21.10	3.50×10^{22}	7.88	−67.37	5.45×10^{13}
G332.295−0.094	32.24	2.02×10^{22}	40.33	−49.16	6.70×10^{13}
G332.364+0.607	17.01	1.97×10^{22}	28.77	−42.99	3.30×10^{13}
G332.560−0.148	14.64	1.06×10^{22}	13.63	−46.81	1.92×10^{13}

Continued on next page

Table B.1 – continued from previous page

Source Name	T_{dust} (K)	N_{H_2} (cm^{-2})	T_{ex} (K)	V_{LSR} (km s^{-1})	$N_{N_2H^+}$ (cm^{-2})
G336.809+0.119	18.29	1.46×10^{22}	4.06	−84.09	2.32×10^{13}
G336.957−0.225	14.67	8.70×10^{21}	17.90	−71.82	1.75×10^{13}
G336.958−0.977	15.97	3.01×10^{22}	24.82	−44.25	2.85×10^{13}
G337.097−0.929	25.05	1.14×10^{22}	14.07	−41.53	1.05×10^{13}
G337.201+0.114	24.02	5.98×10^{21}	8.12	−62.61	5.69×10^{12}
G337.258−0.101	20.29	2.25×10^{22}	28.26	−68.36	3.01×10^{13}
G337.300−0.874	18.71	6.36×10^{21}	11.60	−93.28	1.97×10^{13}
G338.850+0.409	31.52	1.07×10^{22}	26.08	−57.17	2.43×10^{13}
G339.282+0.136	17.44	1.27×10^{22}	21.02	−72.64	2.45×10^{13}
G339.476+0.185	20.94	1.31×10^{22}	15.27	−91.80	1.35×10^{13}
G339.582−0.127	22.24	1.59×10^{22}	37.77	−34.23	6.18×10^{13}
G339.622−0.121	31.99	1.25×10^{22}	32.17	−34.81	4.25×10^{13}
G340.785−0.096	21.57	2.28×10^{22}	28.33	−101.42	3.50×10^{13}
G346.480+0.221	16.32	2.06×10^{22}	5.28	−16.34	2.36×10^{13}
G347.628+0.149	24.40	2.83×10^{22}	18.31	−94.33	4.71×10^{13}
G349.092+0.105	22.46	3.09×10^{22}	23.48	−77.64	3.96×10^{13}
G350.520−0.350	18.20	1.68×10^{22}	16.81	−22.61	2.86×10^{13}
G350.686−0.491	20.94	1.20×10^{22}	13.42	−18.10	3.71×10^{13}
G352.604−0.225	12.47	6.82×10^{21}	7.89	−84.58	1.48×10^{13}
G352.855−0.201	33.22	2.44×10^{22}	21.88	−56.73	2.36×10^{13}
G354.615+0.472	23.06	2.60×10^{22}	25.97	−20.91	2.33×10^{13}
G013.657−0.599	29.35	2.89×10^{22}	20.70	47.95	4.46×10^{13}
G318.948−0.196	35.48	2.60×10^{22}	23.52	−34.54	6.84×10^{13}
G326.474+0.703	20.62	3.15×10^{22}	21.56	−41.14	9.25×10^{13}
G327.393+0.199	33.38	1.27×10^{22}	28.80	−89.18	4.25×10^{13}
G330.876−0.384	29.20	2.98×10^{22}	18.67	−63.95	4.73×10^{13}
G333.314+0.105	27.42	2.22×10^{22}	18.91	−46.43	6.62×10^{13}
G335.586−0.289	23.12	2.06×10^{22}	18.90	−46.68	8.67×10^{13}
G338.281+0.541	17.40	3.09×10^{22}	21.38	−60.83	3.87×10^{13}
G353.463+0.563	27.51	6.99×10^{22}	21.92	−46.00	7.09×10^{13}

Table B.2: Excitation temperatures (T_{ex}), LSR velocities (V_{LSR}) and molecular column densities (N_{HCN}) obtained after fitting the brightest pixel of HCN spectrum towards each source are given below. The dust temperature (T_{dust}) and H_2 column density (N_{H_2}) estimates towards the same bright pixel of the dust continuum map of each source are also provided.

Source Name	T_{dust} (K)	N_{H_2} (cm^{-2})	T_{ex} (K)	V_{LSR} (km s^{-1})	N_{HCN} (cm^{-2})
G006.189−0.358	29.64	1.59×10^{22}	5.15	−34.57	3.57×10^{13}
G010.724−0.334	18.48	1.17×10^{22}	5.38	−1.35	4.57×10^{13}

Continued on next page

Table B.2 – continued from previous page

Source Name	T_{dust} (K)	N_{H_2} (cm^{-2})	T_{ex} (K)	V_{LSR} (km s^{-1})	N_{HCN} (cm^{-2})
G012.625−0.017	16.64	2.66×10^{22}	4.66	18.45	2.54×10^{13}
G012.889+0.489	25.87	4.29×10^{22}	5.63	30.65	7.22×10^{12}
G014.631−0.577	20.22	3.90×10^{22}	5.92	20.20	5.39×10^{13}
G305.799−0.245	35.99	3.74×10^{22}	7.01	−32.67	3.08×10^{13}
G309.384−0.135	24.24	1.59×10^{22}	4.86	−52.30	2.79×10^{13}
G324.923−0.568	28.05	1.99×10^{22}	4.37	−75.13	2.06×10^{13}
G326.608+0.799	17.12	2.06×10^{22}	6.98	−36.15	2.38×10^{13}
G326.859−0.677	17.78	2.48×10^{21}	5.96	−67.50	1.10×10^{13}
G329.469+0.503	20.95	2.49×10^{22}	4.37	−67.67	1.81×10^{13}
G330.283+0.493	21.54	9.40×10^{21}	4.57	−94.05	2.37×10^{13}
G331.342−0.346	23.20	1.33×10^{22}	8.26	−66.24	1.06×10^{14}
G331.710+0.603	21.10	2.62×10^{22}	4.40	−69.33	2.19×10^{13}
G332.295−0.094	32.24	2.02×10^{22}	10.08	−50.25	4.00×10^{13}
G332.364+0.607	17.01	1.97×10^{22}	12.86	−42.54	3.83×10^{13}
G332.560−0.148	14.64	1.06×10^{22}	4.85	−47.31	5.77×10^{13}
G336.809+0.119	18.29	1.51×10^{22}	4.10	−83.58	1.56×10^{13}
G336.957−0.225	14.67	6.90×10^{21}	4.43	−73.00	3.08×10^{13}
G336.958−0.977	15.97	3.01×10^{22}	6.56	−43.78	1.44×10^{13}
G337.097−0.929	25.05	1.05×10^{22}	4.88	−42.52	1.37×10^{13}
G337.258−0.101	20.29	1.70×10^{22}	4.99	−69.81	8.09×10^{12}
G337.300−0.874	18.71	6.36×10^{21}	5.62	−93.09	1.01×10^{13}
G337.632−0.079	21.38	1.44×10^{22}	4.52	−56.15	1.99×10^{13}
G338.850+0.409	31.52	1.07×10^{22}	7.19	−56.87	2.80×10^{13}
G339.282+0.136	17.44	1.36×10^{22}	3.98	−71.95	1.27×10^{13}
G339.476+0.185	20.94	2.01×10^{22}	5.31	−93.73	1.70×10^{13}
G339.582−0.127	22.24	1.59×10^{22}	6.23	−35.94	1.29×10^{13}
G339.622−0.121	31.99	1.01×10^{22}	5.27	−32.86	2.90×10^{13}
G340.249−0.046	23.49	1.40×10^{22}	5.20	−121.95	9.20×10^{13}
G340.785−0.096	21.57	2.28×10^{22}	4.85	−102.26	3.51×10^{13}
G346.480+0.221	16.32	1.55×10^{22}	4.78	−15.35	1.51×10^{13}
G346.481+0.132	24.43	6.01×10^{21}	6.20	−8.31	6.39×10^{13}
G347.628+0.149	24.40	2.83×10^{22}	7.13	−94.05	8.33×10^{13}
G349.092+0.105	22.46	3.09×10^{22}	5.91	−76.54	5.34×10^{13}
G350.015+0.433	26.69	2.06×10^{22}	5.21	−31.01	5.02×10^{13}
G350.520−0.350	18.20	1.90×10^{22}	6.01	−23.15	1.69×10^{13}
G350.686−0.491	20.94	1.64×10^{22}	4.42	−17.85	1.94×10^{13}
G351.688+0.171	18.29	6.34×10^{21}	3.85	−40.08	1.83×10^{13}
G352.604−0.225	12.47	4.95×10^{21}	4.26	−83.94	2.00×10^{13}
G352.855−0.201	33.22	2.44×10^{22}	5.23	−56.10	6.53×10^{13}

Continued on next page

Table B.2 – continued from previous page

Source Name	$T_{\rm dust}$ (K)	$N_{\rm H_2}$ ($\rm cm^{-2}$)	$T_{\rm ex}$ (K)	$V_{\rm LSR}$ ($\rm km\ s^{-1}$)	$N_{\rm HCN}$ ($\rm cm^{-2}$)
G354.615+0.472	23.06	4.27×10^{22}	5.49	−21.76	4.71×10^{13}
G318.948−0.196	35.48	3.34×10^{22}	5.92	−32.70	5.49×10^{13}
G326.474+0.703	25.58	2.50×10^{22}	7.04	−41.183	9.77×10^{13}
G327.393+0.199	33.38	9.54×10^{21}	5.45	−89.57	4.14×10^{13}
G330.876−0.384	29.65	4.17×10^{22}	7.26	−64.22	5.82×10^{13}
G333.314+0.105	27.42	2.22×10^{22}	5.54	−46.39	7.26×10^{13}
G338.281+0.541	24.45	3.09×10^{22}	8.38	−60.86	3.56×10^{13}
G353.463+0.563	27.51	6.99×10^{22}	6.17	−45.93	5.05×10^{13}

Table B.3: Excitation temperatures ($T_{\rm ex}$), LSR velocities ($V_{\rm LSR}$) and molecular column densities ($N_{\rm HNC}$) obtained after fitting the brightest pixel of HNC spectrum towards each source are given below. The dust temperature ($T_{\rm dust}$) and H_2 column density ($N_{\rm H_2}$) estimates towards the same bright pixel of the dust continuum map of each source are also provided.

Source Name	$T_{\rm dust}$ (K)	$N_{\rm H_2}$ ($\rm cm^{-2}$)	$T_{\rm ex}$ (K)	$V_{\rm LSR}$ ($\rm km\ s^{-1}$)	$N_{\rm HNC}$ ($\rm cm^{-2}$)
G010.724−0.334	18.48	1.17×10^{22}	5.38	−1.22	2.10×10^{13}
G012.625−0.017	16.64	3.10×10^{22}	4.66	21.96	2.10×10^{13}
G012.889+0.489	25.87	4.41×10^{22}	5.63	34.29	9.88×10^{12}
G014.631−0.577	20.22	4.82×10^{22}	5.92	18.44	2.20×10^{13}
G305.799−0.245	35.99	2.70×10^{22}	5.20	−32.52	2.14×10^{13}
G309.384−0.135	24.24	1.59×10^{22}	4.86	−49.83	1.75×10^{13}
G324.923−0.568	28.05	1.24×10^{22}	4.39	−74.85	1.09×10^{13}
G326.859−0.677	17.78	4.06×10^{21}	5.96	−66.10	6.01×10^{12}
G329.469+0.503	20.95	2.59×10^{22}	4.37	−67.47	1.98×10^{13}
G330.283+0.493	21.54	1.38×10^{22}	4.57	−93.49	1.13×10^{13}
G331.342−0.346	23.20	1.33×10^{22}	8.26	−65.91	2.32×10^{13}
G331.710+0.603	21.10	2.41×10^{22}	4.40	−68.13	2.00×10^{13}
G332.295−0.094	32.24	3.17×10^{22}	10.08	−49.34	2.59×10^{13}
G336.809+0.119	18.29	1.31×10^{22}	4.10	−82.17	1.07×10^{13}
G336.957−0.225	14.67	8.70×10^{21}	4.28	−71.63	1.31×10^{13}
G337.097−0.929	25.05	1.05×10^{22}	4.88	−42.09	8.49×10^{12}
G337.258−0.101	20.29	2.25×10^{22}	4.99	−68.32	1.42×10^{13}
G337.300−0.874	18.71	8.74×10^{21}	5.62	−92.74	9.38×10^{12}
G337.632−0.079	21.38	1.30×10^{22}	4.52	−56.37	1.89×10^{13}
G338.850+0.409	31.52	1.07×10^{22}	7.19	−56.96	1.46×10^{13}
G339.282+0.136	17.44	1.27×10^{22}	3.98	−72.67	1.79×10^{13}
G339.476+0.185	20.94	1.31×10^{22}	5.31	−93.56	5.25×10^{12}
G339.582−0.127	22.24	1.64×10^{22}	6.23	−34.59	2.56×10^{13}
G339.622−0.121	31.99	1.25×10^{22}	5.17	−34.31	3.01×10^{13}

Continued on next page

Table B.3 – continued from previous page

Source Name	T_{dust} (K)	N_{H_2} (cm^{-2})	T_{ex} (K)	V_{LSR} (km s^{-1})	N_{HNC} (cm^{-2})
G340.249−0.046	23.49	1.91×10^{22}	5.20	−121.87	8.89×10^{13}
G340.785−0.096	21.57	2.28×10^{22}	4.85	−101.56	2.16×10^{13}
G346.480+0.221	16.32	2.07×10^{22}	3.89	−16.28	7.11×10^{13}
G346.481+0.132	24.43	6.01×10^{21}	6.20	−7.19	1.35×10^{13}
G349.092+0.105	22.46	3.09×10^{22}	5.91	−76.74	2.90×10^{13}
G350.015+0.433	26.69	2.06×10^{22}	5.75	−31.30	1.83×10^{13}
G350.520−0.350	18.20	1.58×10^{22}	6.01	−23.39	1.30×10^{13}
G350.686−0.491	20.94	1.42×10^{22}	5.00	−17.98	2.69×10^{13}
G351.688+0.171	18.29	4.26×10^{21}	4.41	−40.61	1.07×10^{13}
G352.604−0.225	12.47	7.41×10^{21}	4.26	−84.66	1.25×10^{13}
G352.855−0.201	33.22	2.44×10^{22}	5.58	−56.15	2.17×10^{13}
G354.615+0.472	23.06	5.43×10^{22}	5.72	−20.75	2.24×10^{13}
G318.948−0.196	35.48	3.34×10^{22}	5.94	−34.26	6.18×10^{13}
G326.474+0.703	24.92	3.94×10^{22}	7.14	−41.17	5.18×10^{13}
G327.393+0.199	33.38	1.27×10^{22}	5.27	−89.34	2.89×10^{13}
G330.876−0.384	28.56	3.52×10^{22}	8.89	−64.23	9.66×10^{13}
G333.314+0.105	25.20	2.00×10^{22}	6.61	−46.18	6.81×10^{13}
G338.281+0.541	17.40	3.09×10^{22}	8.44	−60.86	3.12×10^{13}
G353.463+0.563	27.75	1.20×10^{22}	7.00	−45.91	4.58×10^{13}

Table B.4: Excitation temperatures (T_{ex}), LSR velocities (V_{LSR}) and molecular column densities (N_{HCO^+}) obtained after fitting the brightest pixel of HCO^+ spectrum towards each source are given below. The dust temperature (T_{dust}) and H_2 column density (N_{H_2}) estimates towards the same bright pixel of the dust continuum map of each source are also provided.

Source Name	T_{dust} (K)	N_{H_2} (cm^{-2})	T_{ex} (K)	V_{LSR} (km s^{-1})	N_{HCO^+} (cm^{-2})
G006.189−0.358	29.64	1.62×10^{22}	5.58	−33.21	2.91×10^{13}
G010.724−0.334	18.48	1.31×10^{22}	8.45	−1.53	2.02×10^{13}
G010.958+0.022	30.59	1.55×10^{22}	5.35	21.17	1.48×10^{13}
G012.625−0.017	16.64	3.23×10^{22}	4.72	19.89	4.36×10^{12}
G012.889+0.489	25.87	4.39×10^{22}	6.02	35.01	6.50×10^{12}
G013.179+0.061	19.30	2.96×10^{22}	9.69	48.31	1.62×10^{13}
G014.631−0.577	20.22	4.58×10^{22}	5.93	18.52	4.81×10^{13}
G305.799−0.245	35.99	3.27×10^{22}	7.66	−33.02	2.29×10^{13}
G309.384−0.135	24.24	1.38×10^{22}	5.64	−49.14	2.62×10^{13}
G311.947+0.142	20.32	2.13×10^{22}	5.83	−41.65	7.75×10^{12}
G324.923−0.568	28.05	1.09×10^{22}	6.50	−75.12	1.03×10^{13}
G326.608+0.799	17.12	2.06×10^{22}	6.85	−37.43	1.84×10^{13}
G326.859−0.677	17.78	2.48×10^{21}	5.83	−66.51	1.12×10^{13}

Continued on next page

Table B.4 – continued from previous page

Source Name	T_{dust} (K)	N_{H_2}(cm^{-2})	T_{ex} (K)	V_{LSR} (km s^{-1})	N_{HCO^+} (cm^{-2})
G329.469+0.503	20.95	2.42×10^{22}	6.62	−67.74	1.70×10^{13}
G330.283+0.493	21.54	1.30×10^{22}	8.34	−93.83	1.42×10^{13}
G331.342−0.346	23.20	1.33×10^{22}	10.40	−66.10	3.10×10^{13}
G331.710+0.603	21.10	3.50×10^{22}	6.59	−69.35	1.36×10^{13}
G332.295−0.094	32.24	3.19×10^{22}	6.11	−50.73	1.35×10^{13}
G332.364+0.607	17.01	1.97×10^{22}	8.18	−42.59	1.68×10^{13}
G332.560−0.148	14.64	1.06×10^{22}	8.93	−47.20	2.22×10^{13}
G332.942−0.686	23.88	1.19×10^{22}	7.06	−48.78	1.89×10^{13}
G336.809+0.119	18.29	1.51×10^{22}	7.36	−82.65	8.70×10^{12}
G336.957−0.225	14.67	6.90×10^{21}	5.46	−71.80	8.78×10^{12}
G336.958−0.977	15.97	3.01×10^{22}	7.16	−45.01	9.35×10^{12}
G337.097−0.929	25.05	1.14×10^{22}	5.58	−41.79	7.17×10^{12}
G337.201+0.114	24.02	5.98×10^{21}	5.08	−63.64	7.10×10^{12}
G337.258−0.101	20.29	2.25×10^{22}	5.91	−68.85	1.02×10^{13}
G337.300−0.874	18.71	8.74×10^{21}	5.68	−93.23	1.02×10^{13}
G337.632−0.079	21.38	1.57×10^{22}	5.31	−56.10	9.88×10^{12}
G338.850+0.409	31.52	1.07×10^{22}	8.32	−56.85	1.99×10^{13}
G339.282+0.136	17.44	1.27×10^{22}	8.16	−72.51	1.48×10^{13}
G339.476+0.185	20.94	2.01×10^{22}	6.31	−94.45	5.84×10^{12}
G339.582−0.127	22.24	1.59×10^{22}	5.91	−35.99	1.12×10^{13}
G339.622−0.121	31.99	1.25×10^{22}	5.80	−33.63	1.04×10^{13}
G340.249−0.046	23.49	1.84×10^{22}	6.92	−121.58	4.82×10^{13}
G340.785−0.096	21.57	1.43×10^{22}	5.39	−101.28	1.37×10^{13}
G341.276+0.062	19.70	4.62×10^{21}	5.63	−70.27	6.29×10^{12}
G346.480+0.221	16.32	2.07×10^{22}	5.72	−16.72	9.26×10^{12}
G346.481+0.132	24.43	5.21×10^{21}	5.06	−8.18	8.28×10^{12}
G347.628+0.149	24.40	2.83×10^{22}	8.12	−94.32	8.31×10^{13}
G349.092+0.105	22.46	3.09×10^{22}	6.72	−76.99	4.30×10^{13}
G350.015+0.433	26.69	1.81×10^{22}	5.37	−31.16	2.37×10^{13}
G350.520−0.350	18.20	1.75×10^{22}	5.87	−23.93	6.74×10^{12}
G350.686−0.491	20.94	7.93×10^{21}	7.08	−17.39	1.58×10^{13}
G351.688+0.171	18.29	5.35×10^{21}	5.59	−40.96	5.10×10^{12}
G352.604−0.225	12.47	7.47×10^{21}	4.62	−83.77	2.41×10^{13}
G352.855−0.201	33.22	2.26×10^{22}	5.99	−56.50	2.18×10^{13}
G354.615+0.472	23.06	4.27×10^{22}	7.15	−20.97	2.10×10^{13}
G318.948−0.196	35.48	3.34×10^{22}	7.95	−34.09	4.04×10^{13}
G326.474+0.703	20.62	3.15×10^{22}	12.02	−41.39	5.69×10^{13}
G327.393+0.199	33.38	9.54×10^{21}	7.49	−89.44	2.70×10^{13}
G330.876−0.384	28.56	3.52×10^{22}	8.65	−64.04	9.66×10^{13}

Continued on next page

Table B.4 – continued from previous page

Source Name	T_{dust} (K)	$N_{H_2}(cm^{-2})$	T_{ex} (K)	V_{LSR} (km s^{-1})	N_{HCO^+} (cm^{-2})
G333.314+0.105	25.20	2.00×10^{22}	8.70	−46.84	2.34×10^{13}
G338.281+0.541	17.40	3.09×10^{22}	10.24	−60.96	4.03×10^{13}
G353.463+0.563	27.75	1.20×10^{22}	7.62	−46.41	3.95×10^{13}

B.2 Comparison of properties of 68 MM sources with that of larger MMB sample

Since the goal of our work is to examine the chemical properties of sources that host 6.7 GHz methanol masers, it is important to ensure that our sample is representative of the Galactic population. To this effect, we have examined the distances, methanol maser luminosities and the FIR luminosity of the host sources of our sample and compared them with that of the full MMB catalogue/sources in Work I (Figure B.1).

While the distribution of distances of our sample is similar to that of the full MMB catalogue and the sample studied in Work I, there appears to be a slight bias towards larger maser luminosities and FIR luminosities in this study. In order to check for any bias quantitatively, the Student's T-test was performed on the samples. The *p*-value obtained was 0.92 for the methanol maser distribution and 0.2 for the FIR luminosity distribution. These are significantly higher than 0.05, which suggests that the differences between the maser populations are not statistically significant.

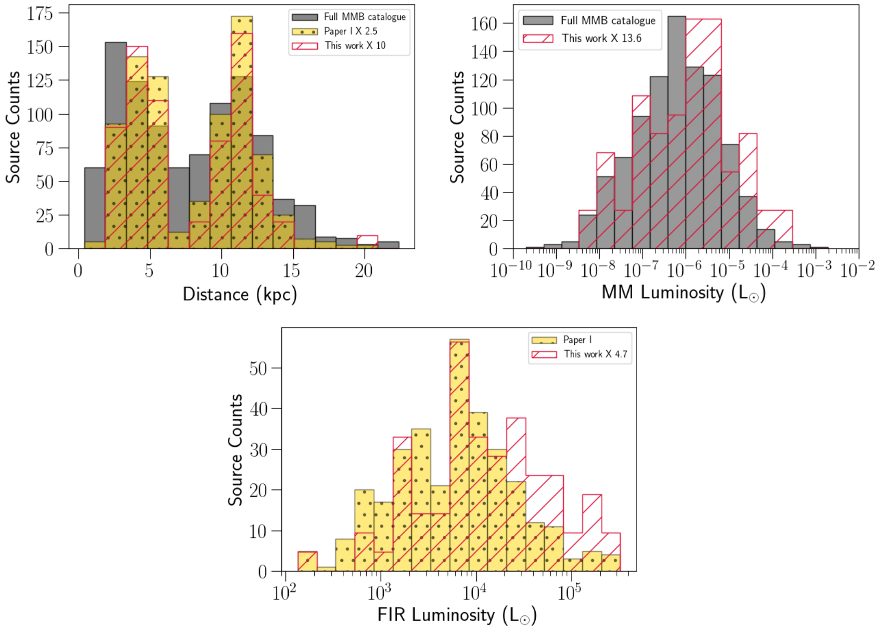

Figure B.1: The top-left, top-right and bottom panels show the histogram for distances, methanol maser luminosities and FIR luminosities towards the 68 sources of this paper (red with hatches), 321 sources of Paper I (yellow with dots) and the full MMB catalogue (grey). The histograms have been scaled for ease of comparison, with the scale factors being indicated in the legend of each panel.

B.3 Comparison of dust temperatures of 68 MM sources with that of previous works

The left panel of Figure B.2 illustrates the average dust temperature calculated for all the bright pixels (S/N ≥ 5) of each of the nine source (chosen for pixel-by-pixel study) and average dust temperature calculated for the same sources by (Guzmán et al., 2015). Except for two sources, the dust temperature values of the nine sources agree well with what is reported by Guzmán et al. (2015). The right panel of Figure B.2 shows the PDFs of dust temperatures of 68 MM sources (taken from Paper I) with that of Guzmán et al. (2015). The distributions can be seen comparable with each other.

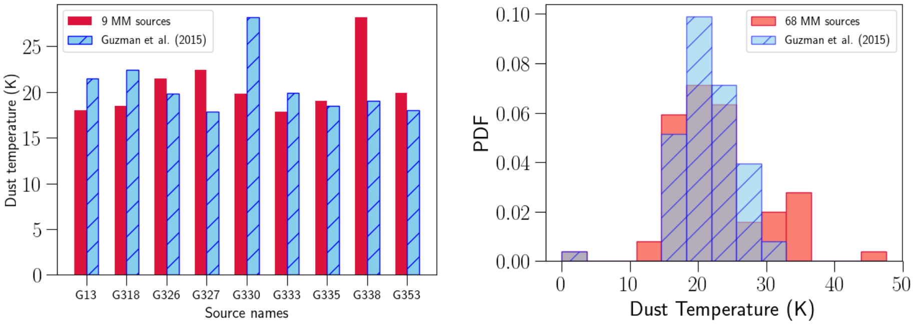

Figure B.2: Average dust temperatures of sources obtained from pixel-by-pixel fitting of the brightest pixels, compared with the average dust temperatures reported by Guzmán et al. (2015), is shown in the left panel. The right panel shows the PDFs of dust temperatures of 68 sources (taken from Work I) and the average dust temperatures given in Guzmán et al. (2015).

B.4 Fits to molecular spectra: Statistical Analysis

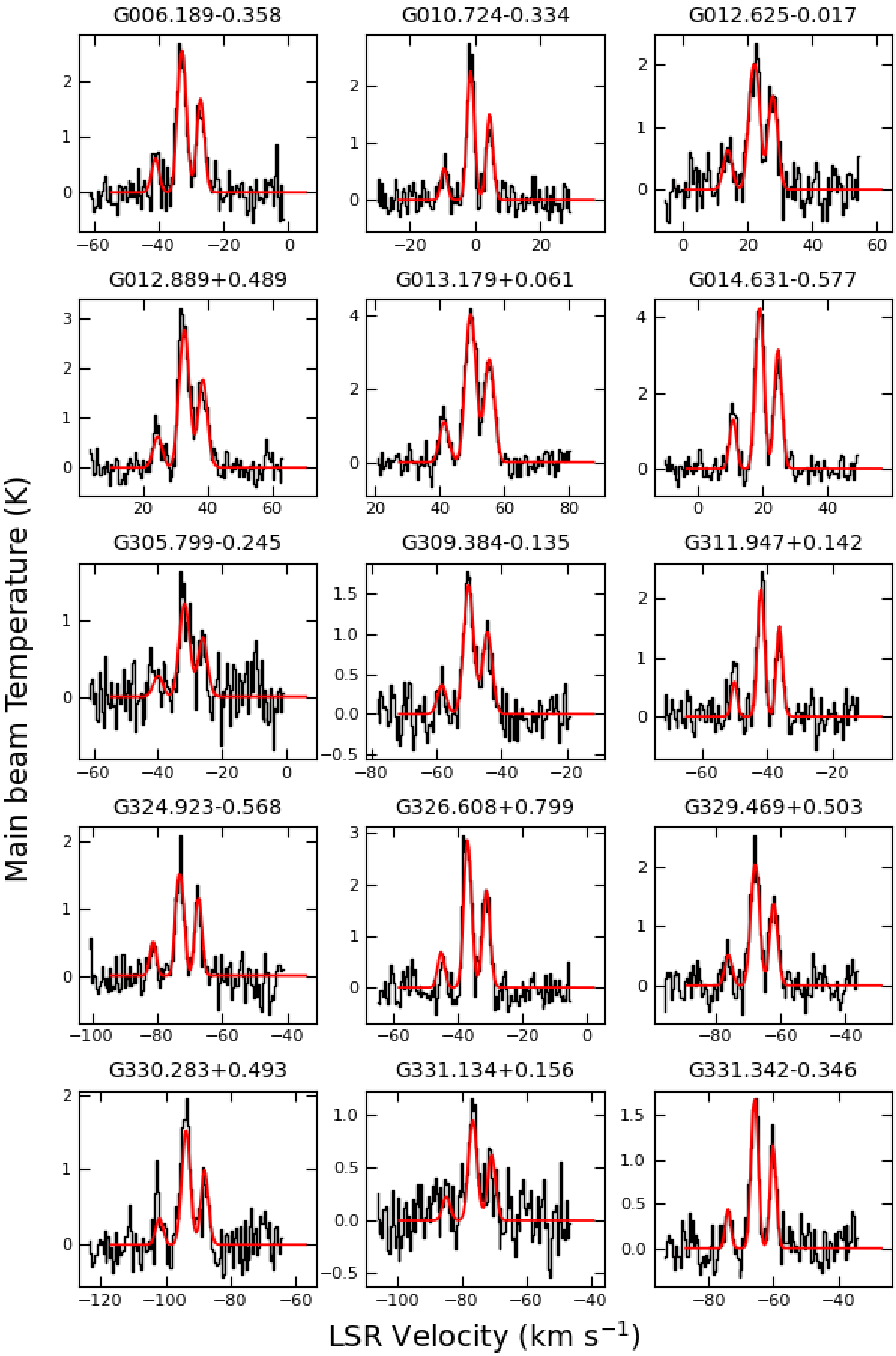

Figure B.3: Fits to N_2H^+ spectra towards the brightest pixel of each source.

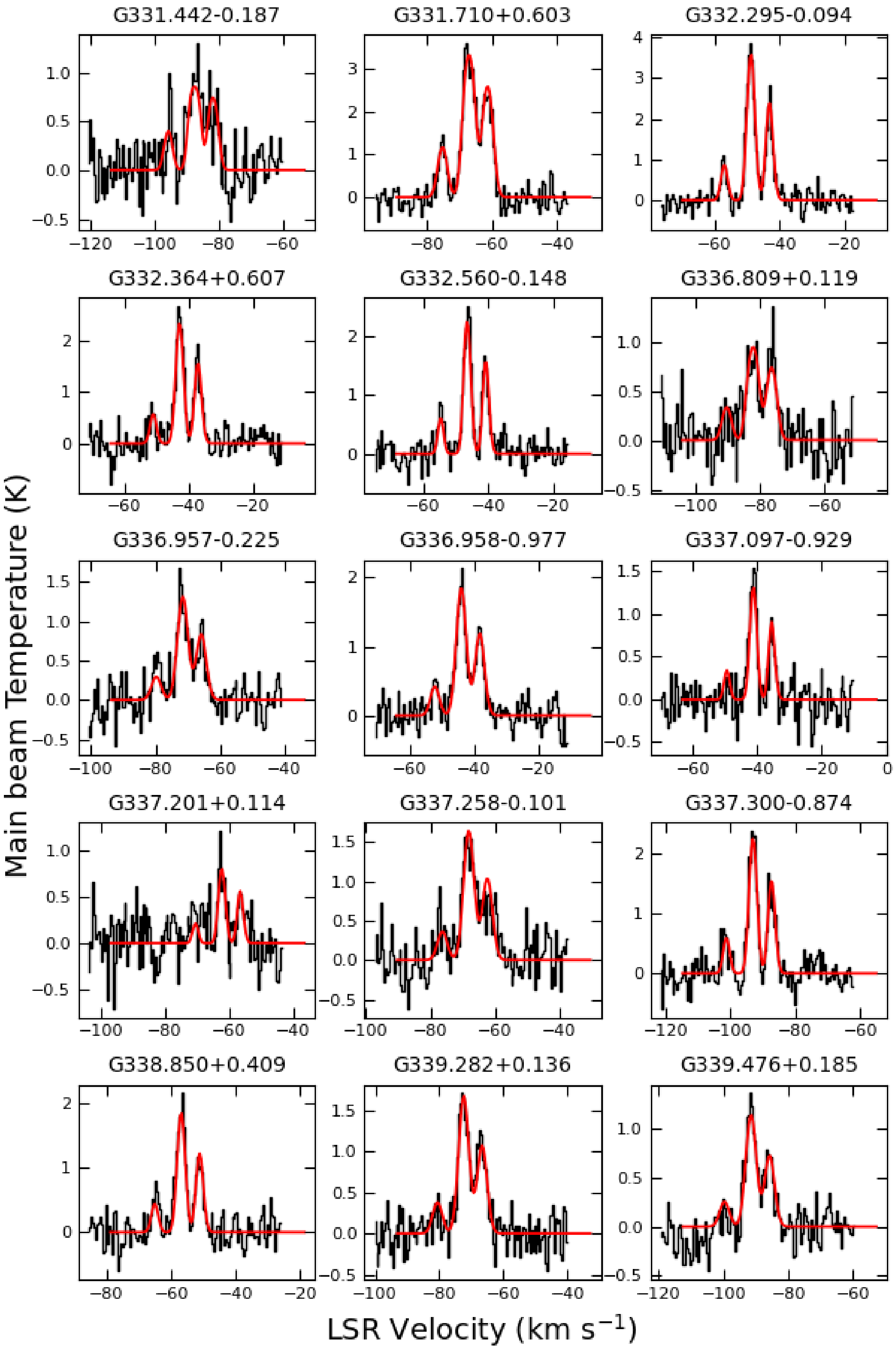

Continued from previous page.

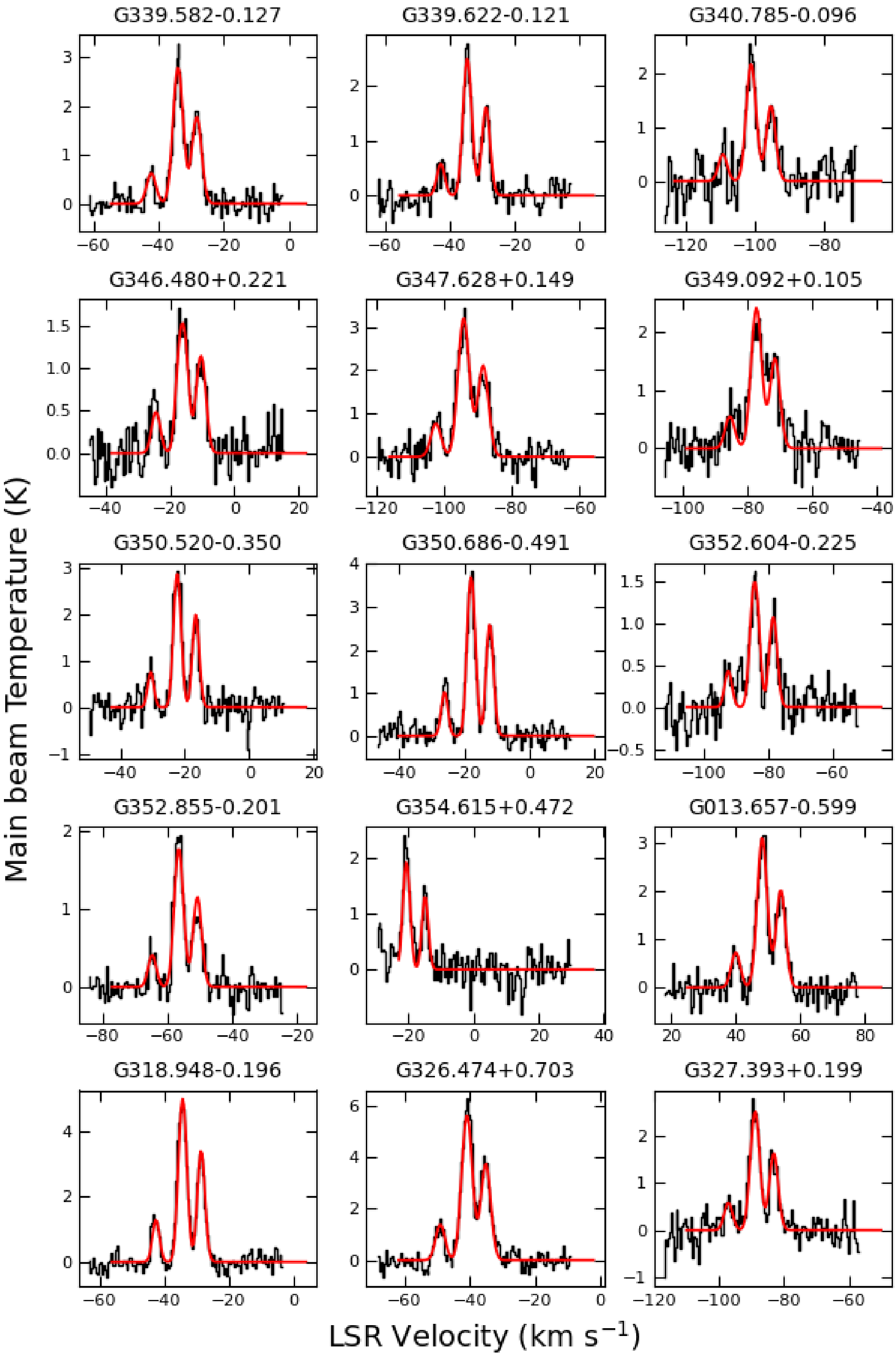

Continued from previous page.

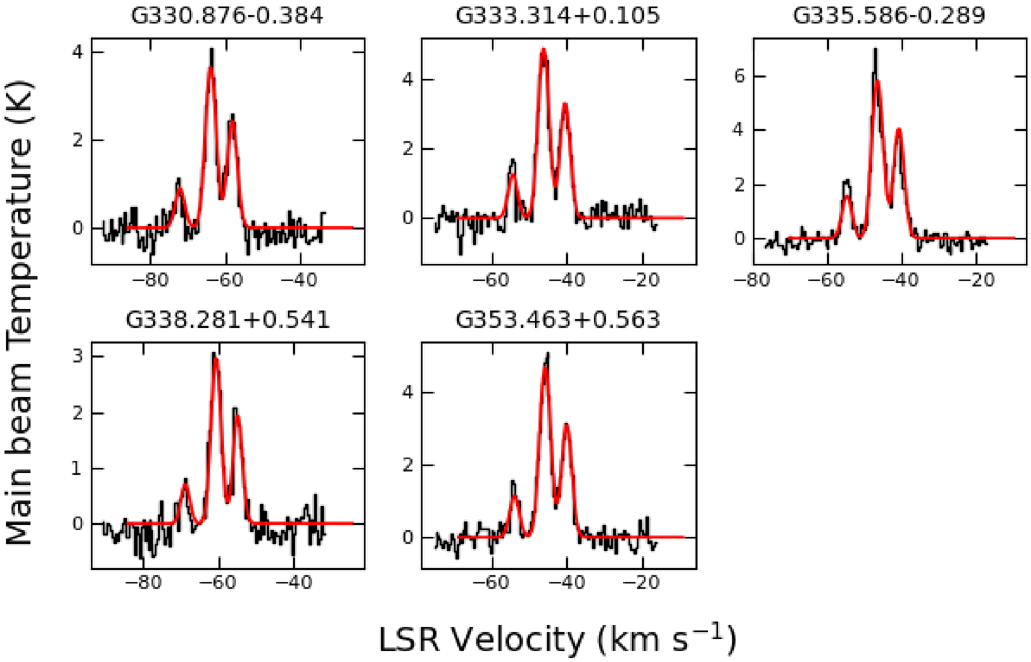

Continued from previous page.

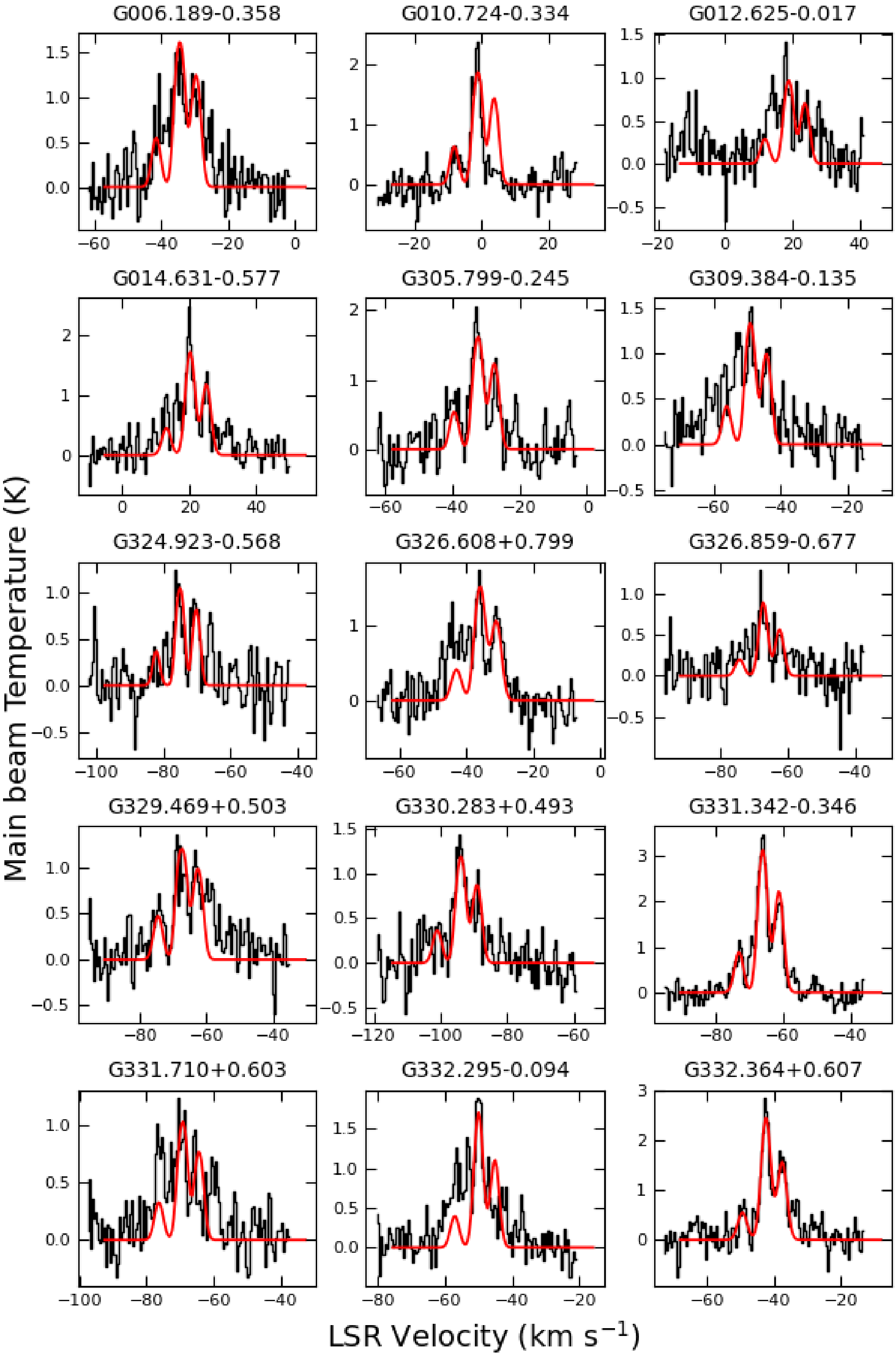

Figure B.7: Fits to HCN spectra towards the brightest pixel of each source.

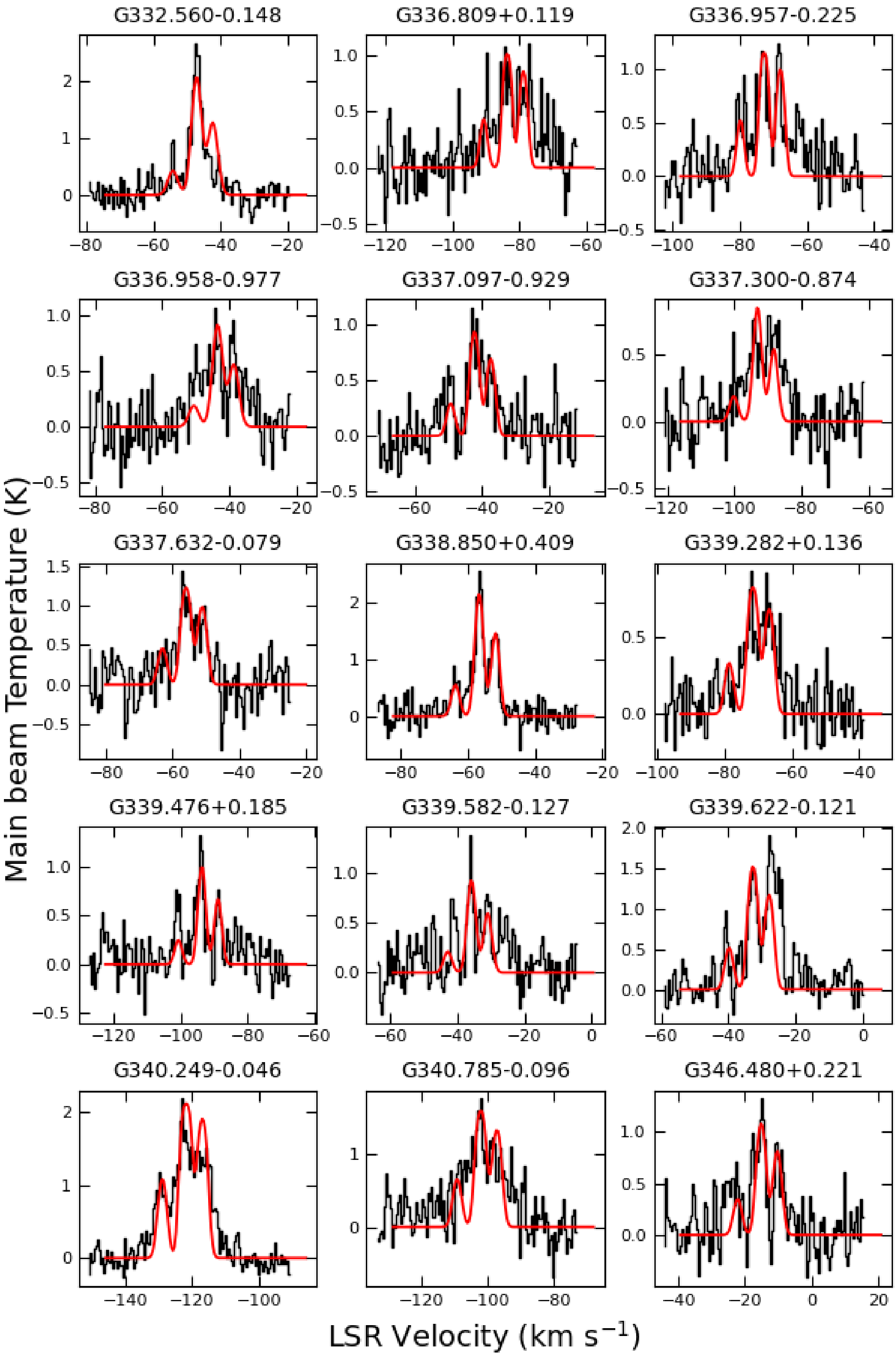

Continued from previous page.

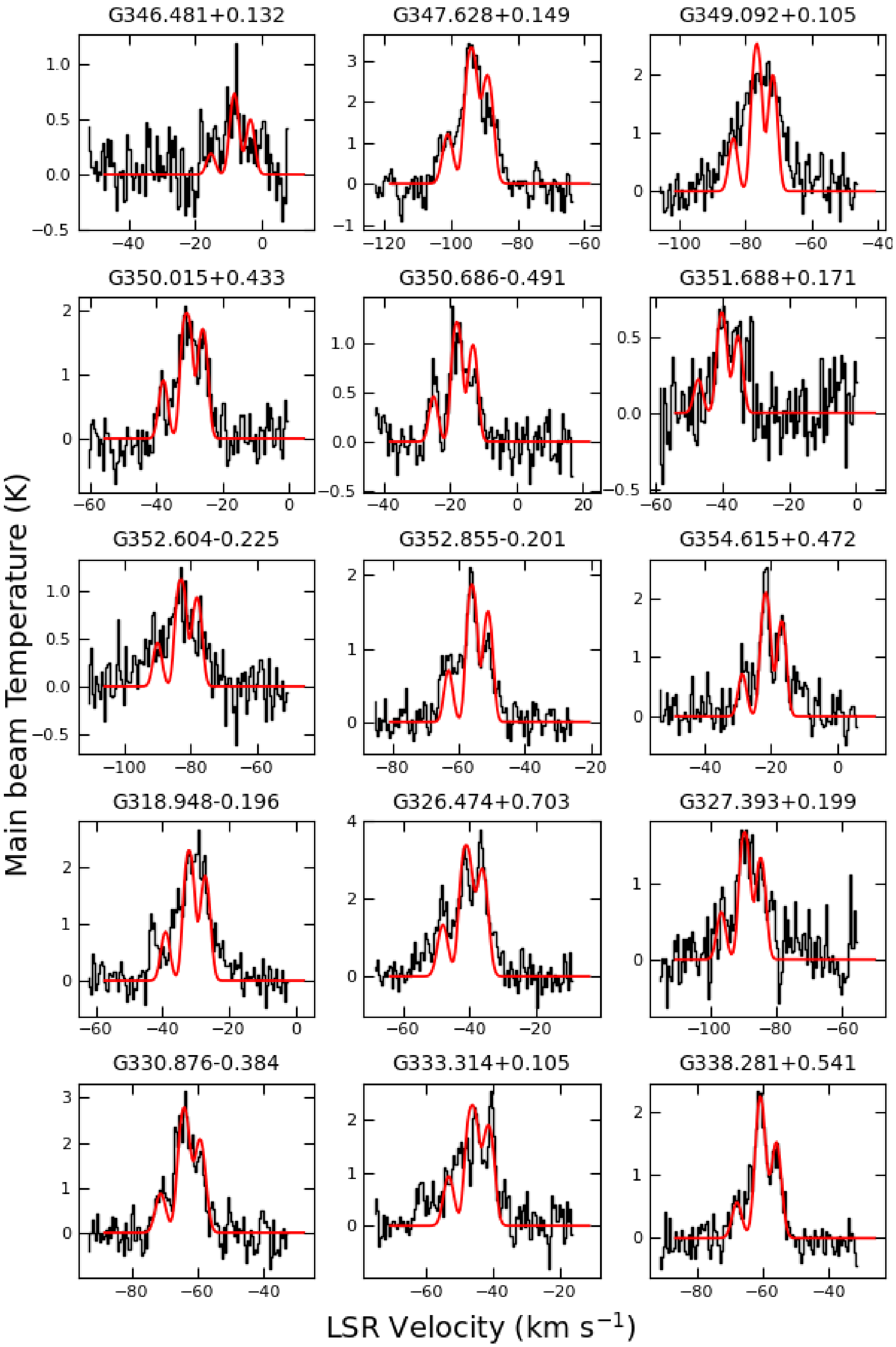

Continued from previous page.

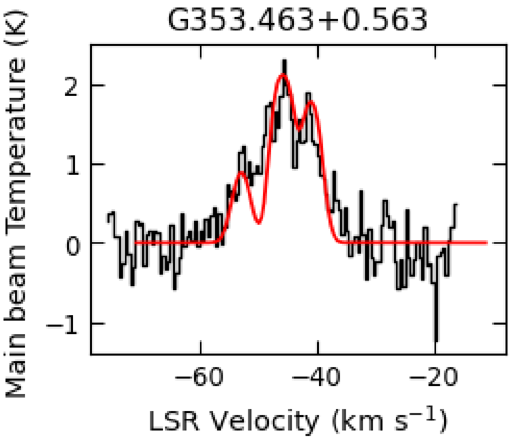

Continued from previous page.

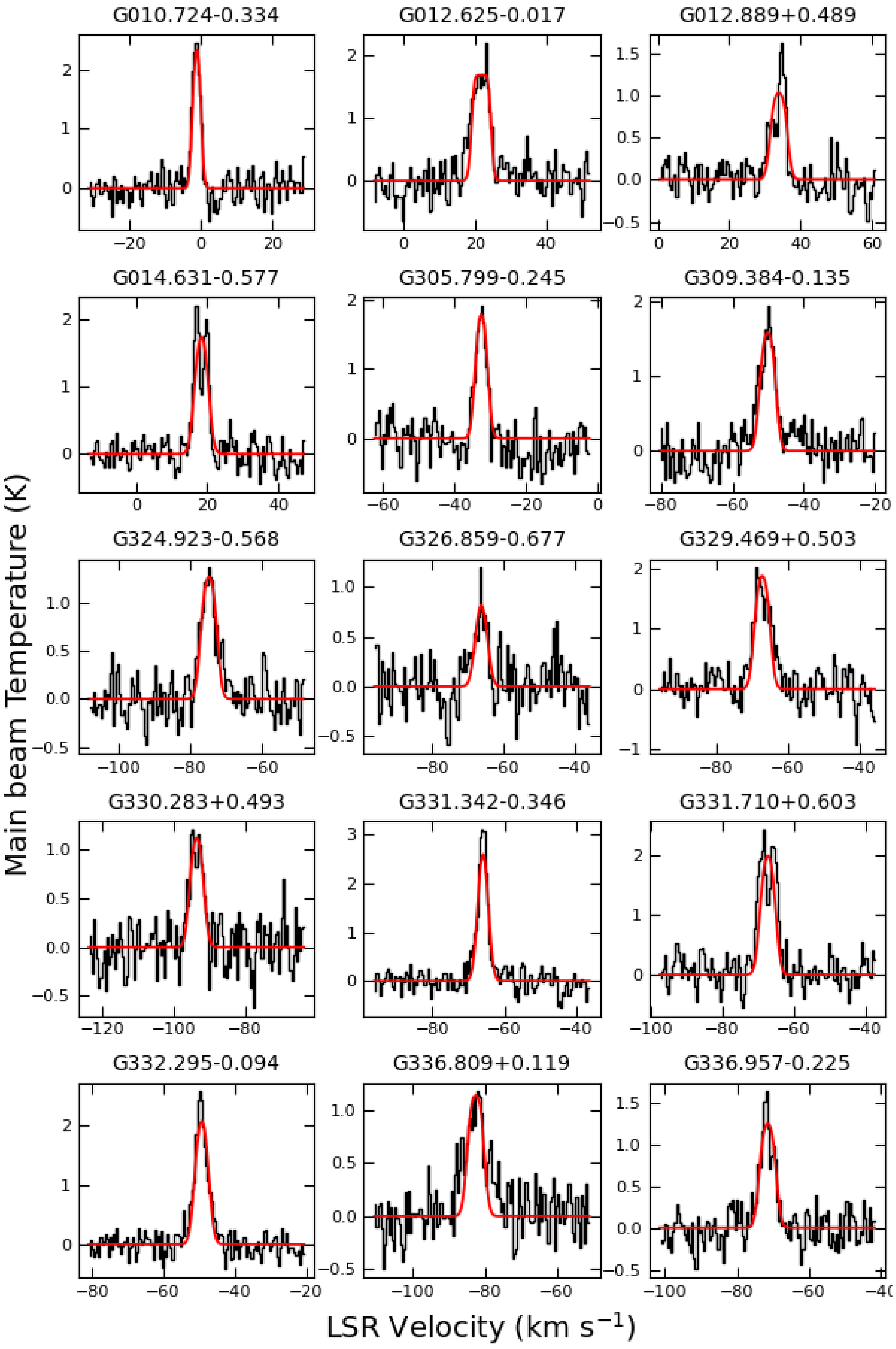

Figure B.11: Fits to HNC spectra towards the brightest pixel of each source.

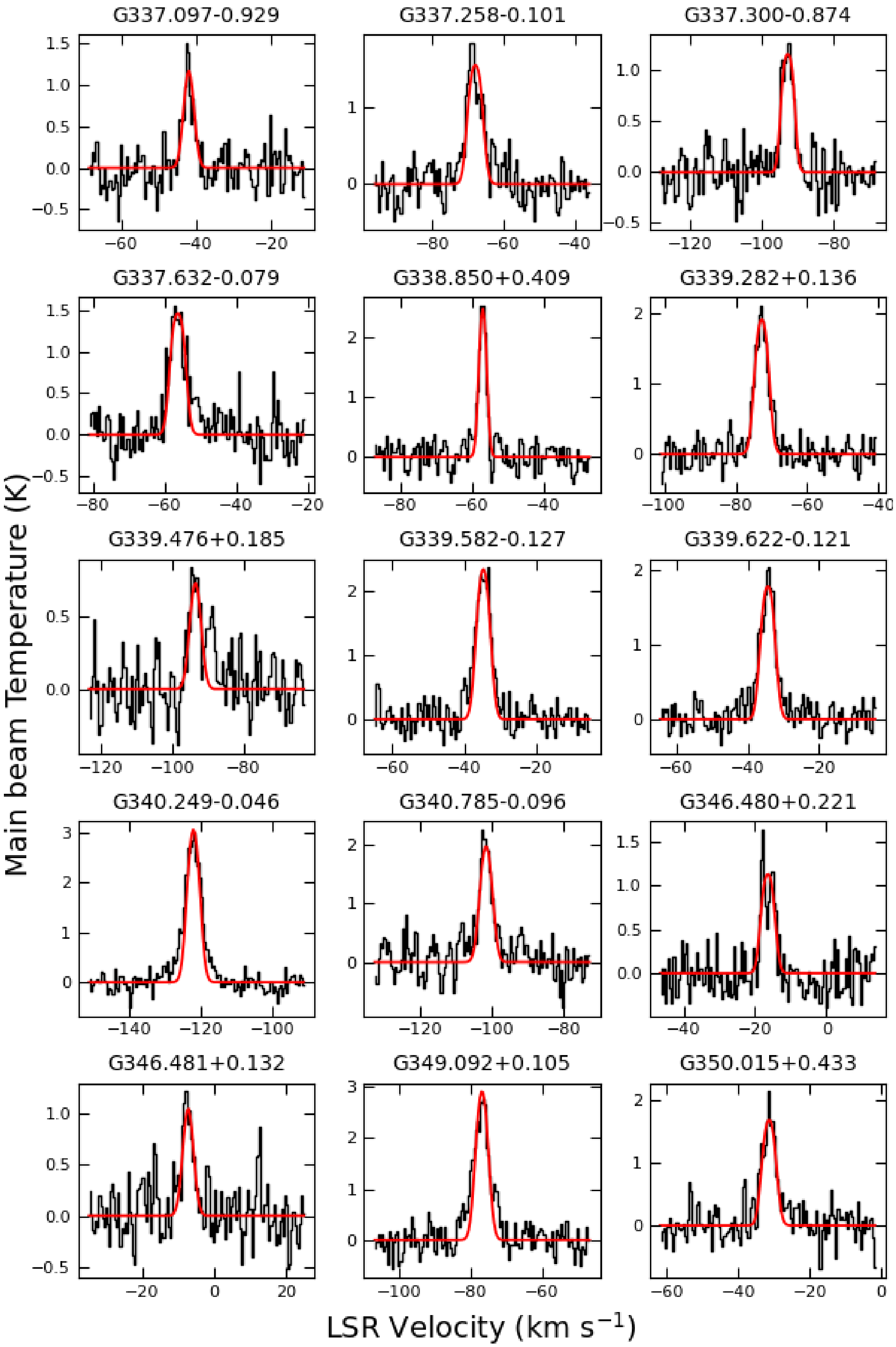

Continued from previous page.

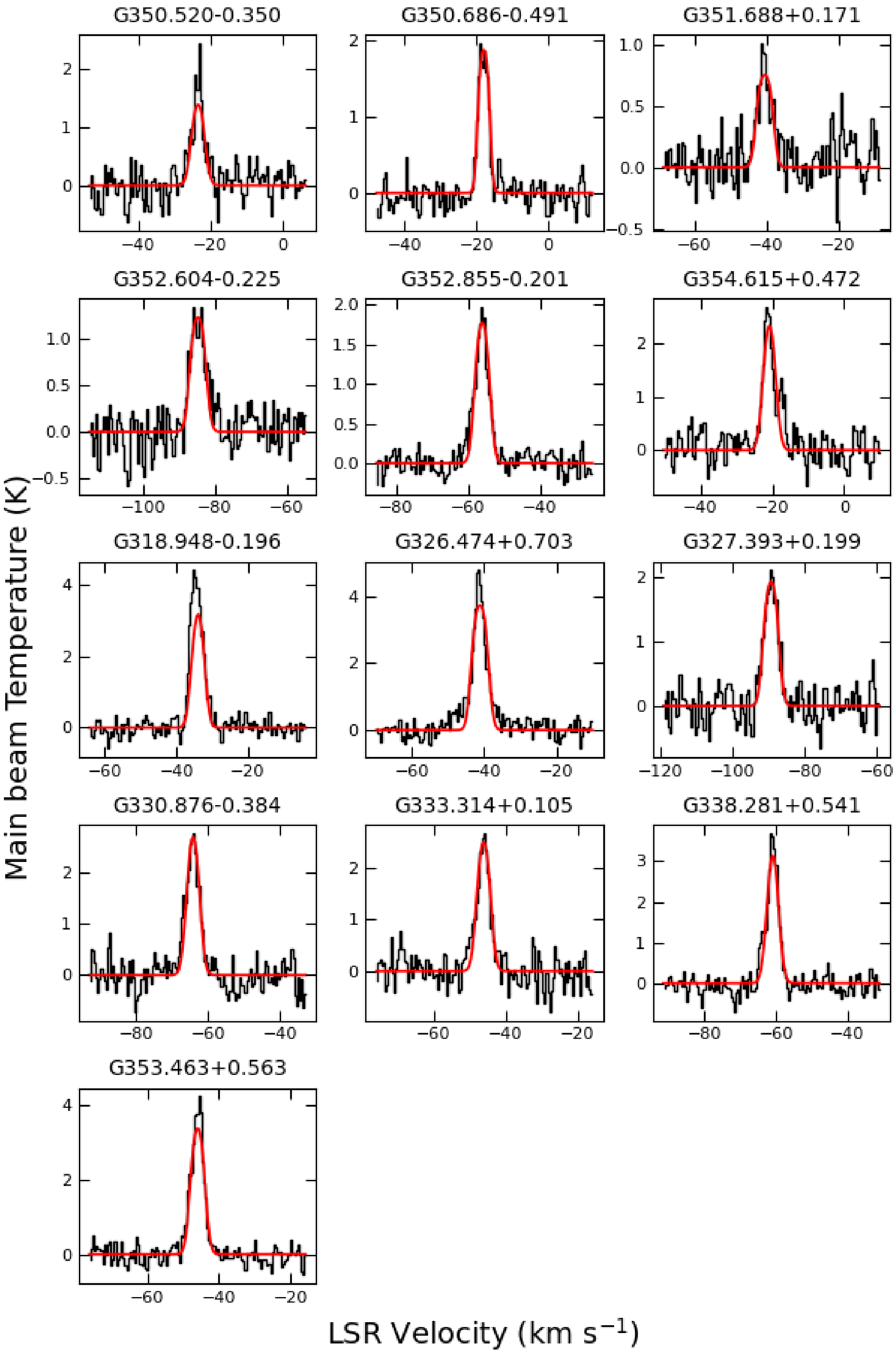

Continued from previous page.

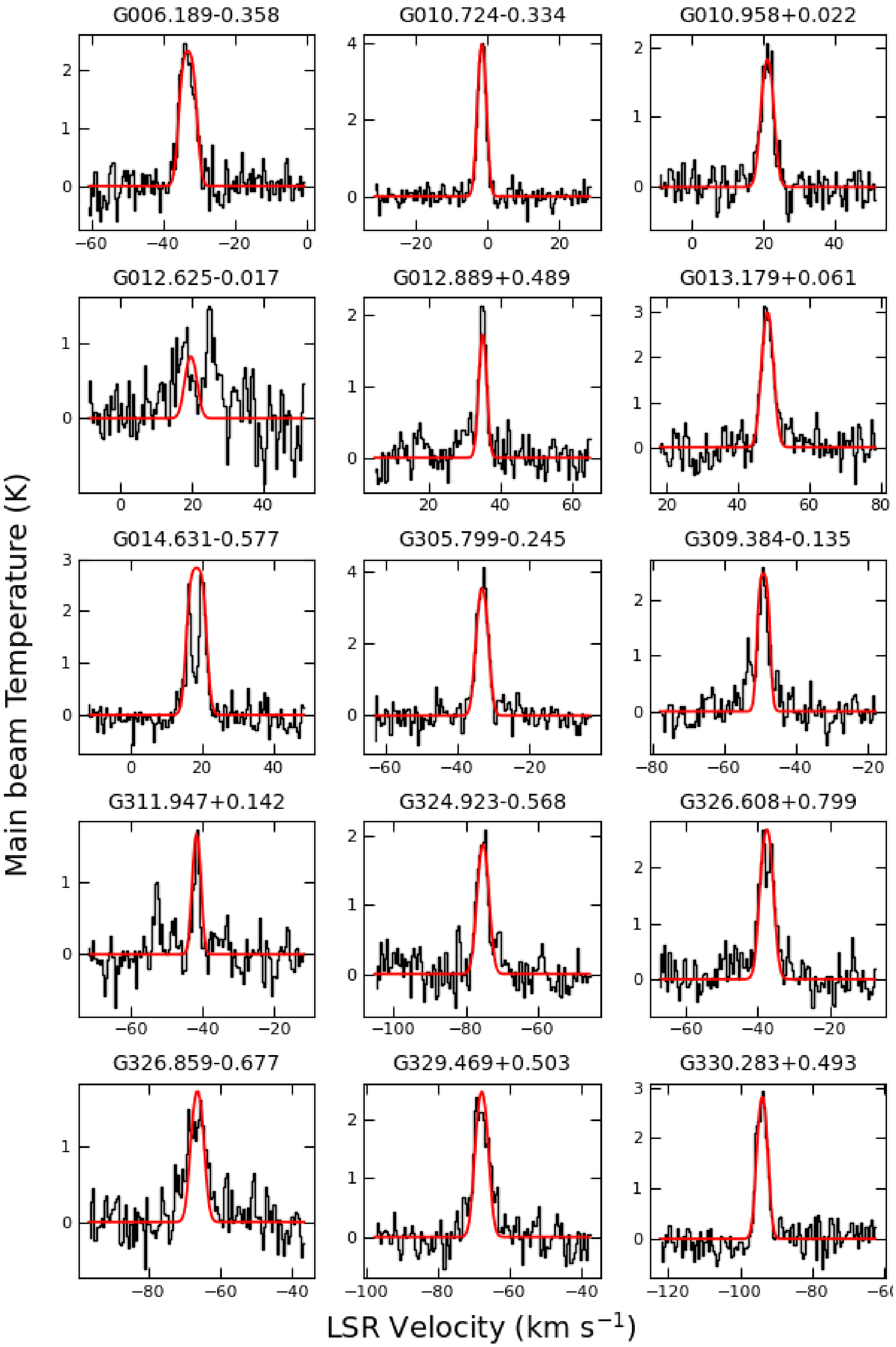

Figure B.14: Fits to HCO$^+$ spectra towards the brightest pixel of each source.

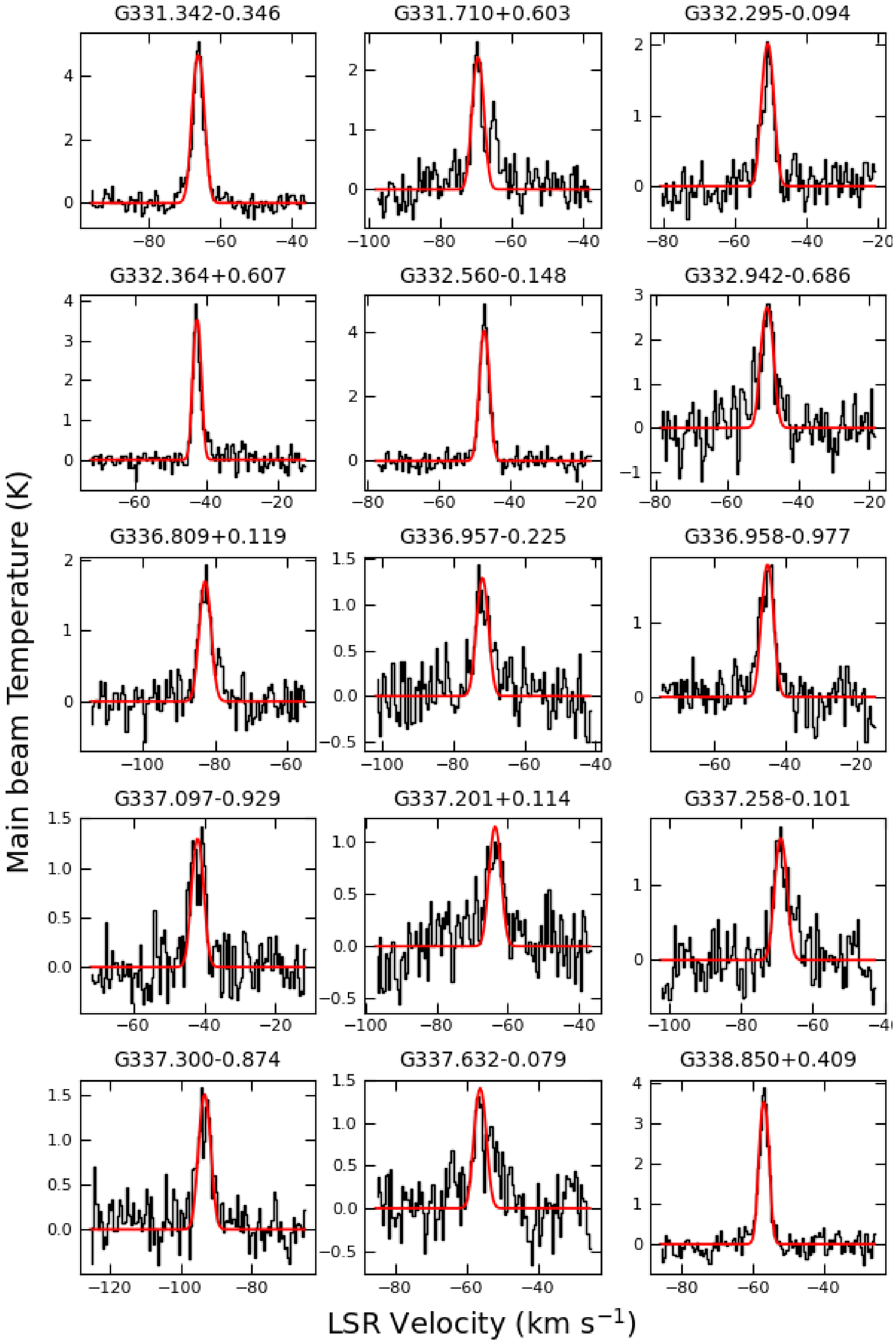

Continued from previous page.

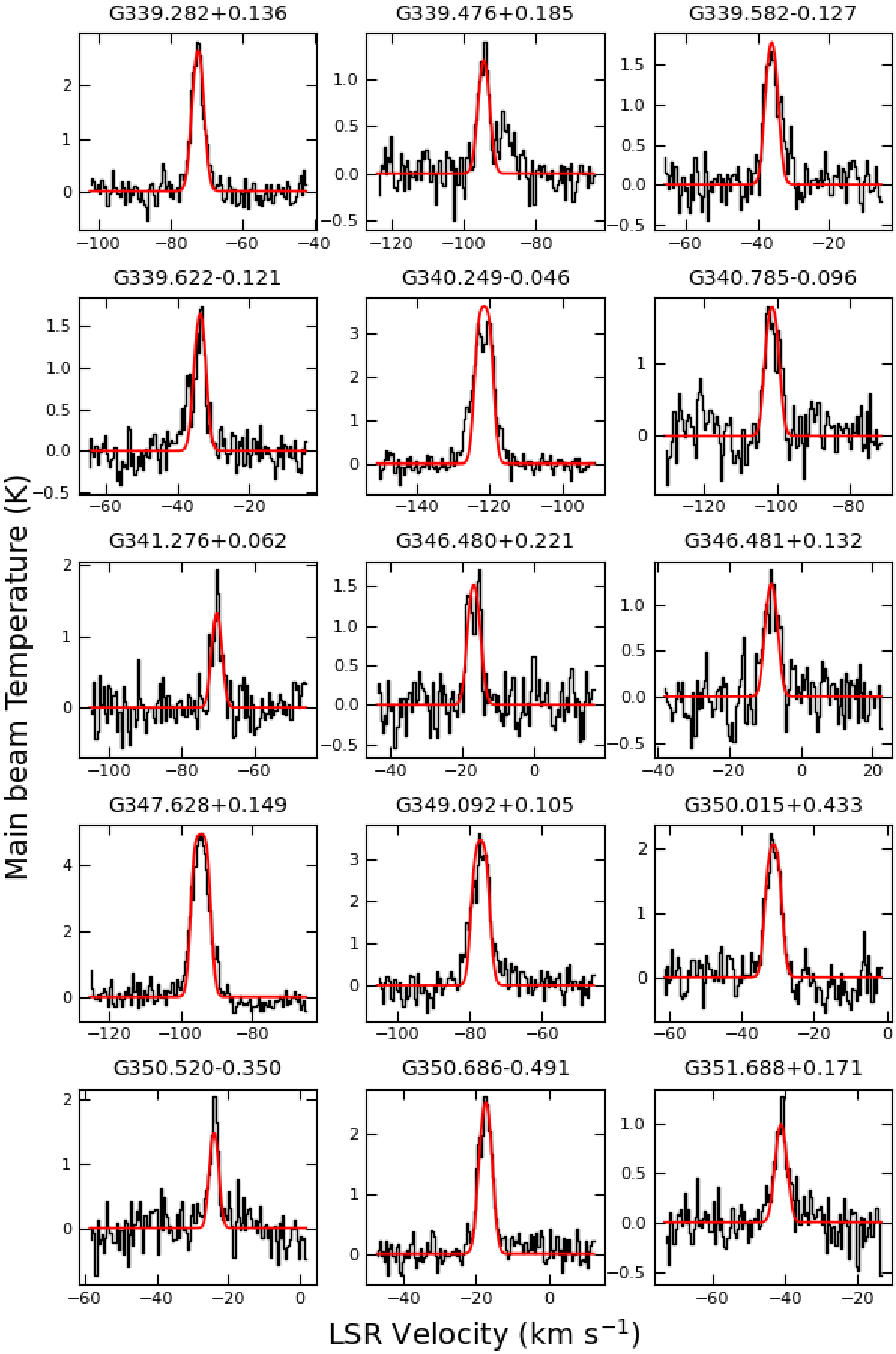

Continued from previous page.

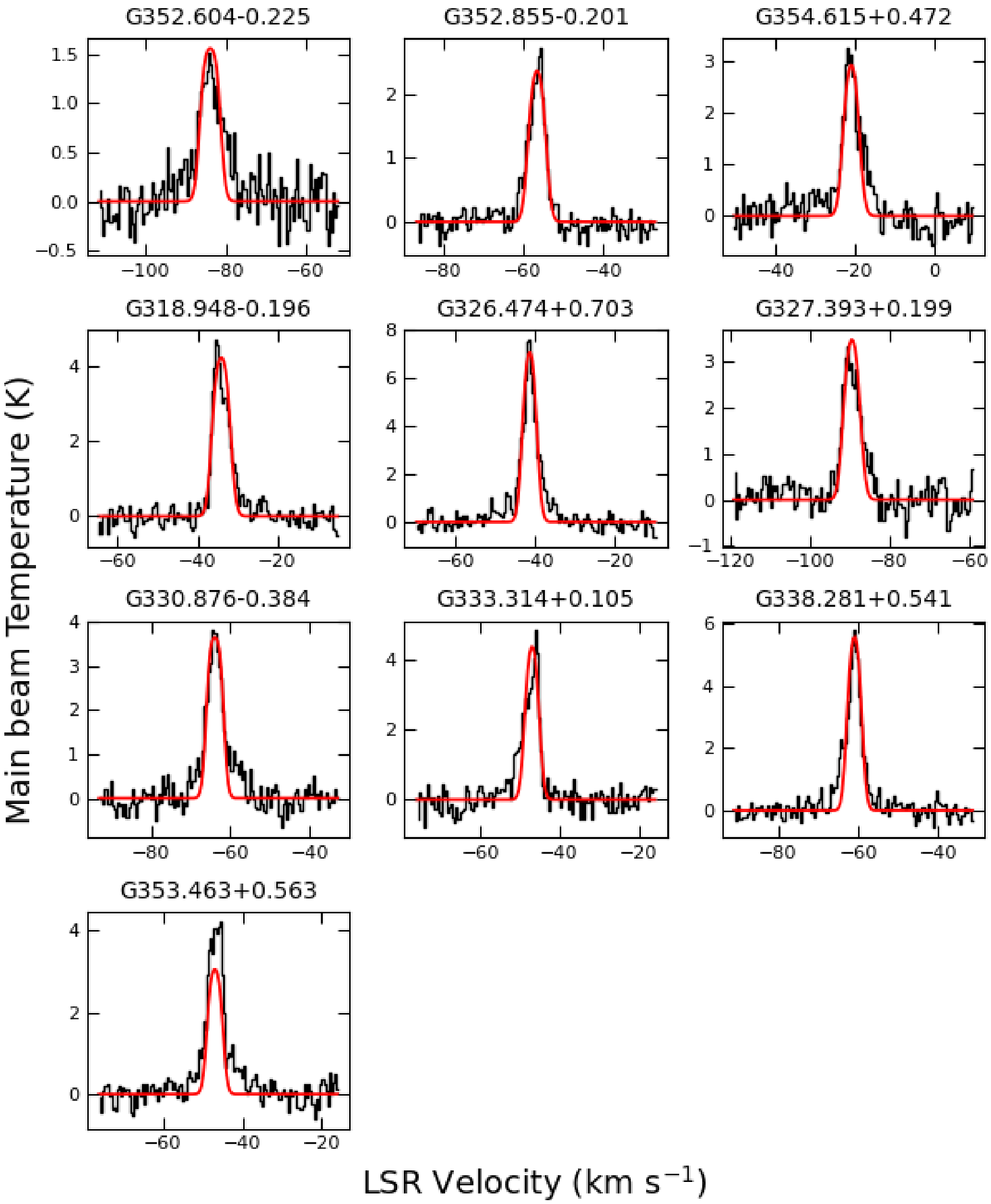

Continued from previous page.